Flow Behavior of Sparsely Branched Metallocene-Catalyzed Polyethylenes

Phillip J. Doerpinghaus, Jr.

Dissertation submitted to the Faculty of the
Virginia Polytechnic Institute and State University
in partial fulfillment of the requirements for the degree of

DOCTOR OF PHILOSOPHY
IN
CHEMICAL ENGINEERING

Advisory Committee:

Dr. Donald G. Baird, Chairman
Dr. Richey M. Davis
Dr. Timothy E. Long
Dr. Peter Wapperom
Dr. Garth L. Wilkes

August 8, 2002
Blacksburg, VA

Keywords: metallocene, polyethylene, rheology, melt fracture, contraction flow behavior

Flow Behavior of Sparsely Branched Metallocene-Catalyzed Polyethylenes

Phillip J. Doerpinghaus

(ABSTRACT)

This work is concerned with a better understanding of the influences that sparse long-chain branching has on the rheological and processing behavior of commercial metallocene polyethylene (mPE) resins. In order to clarify these influences, a series of six commercial polyethylenes was investigated. Four of these resins are mPE resins having varying degrees of long-chain branching and narrow molecular weight distribution. The remaining two resins are deemed controls and include a highly branched low-density polyethylene and a linear low-density polyethylene. Together, the effects of long-chain branching are considered with respect to the shear and extensional rheological properties, the melt fracture behavior, and the ability to accurately predict the flow through an abrupt 4:1 contraction geometry.

The effects that sparse long-chain branching ($M_{branch} > M_c$) has on the shear and extensional rheological properties are analyzed in two separate treatments. The first focuses on the shear rheological properties of linear, sparsely branched, and highly branched PE systems. By employing a time-molecular weight superposition principle, the effects of molecular weight on the shear rheological properties are factored out. The results show that as little as 0.6 LCB/10^4 carbons (<1 LCB/molecule) significantly increases the zero-shear viscosity, reduces the onset of shear-thinning behavior, and increases elasticity at low deformation rates when compared to linear materials of equivalent molecular weight. Conversely, a high degree of long-chain branching ultimately reduces the zero-shear viscosity. The second treatment focuses on the relationship between long-chain branching and extensional strain-hardening behavior. In this

study, the McLeish-Larson molecular constitutive model is employed to relate long-chain branching to rheological behavior. The results show that extensional strain hardening arises from the presence of LCB in polyethylene resins, and that the frequency of branching in sparsely branched metallocene polyethylenes dictates the degree of strain hardening. This observation for the metallocene polyethylenes agrees well with the proposed mechanism for polymerization.

The presence of long-chain branching profoundly alters the melt fracture behavior of commercial polyethylene resins. Results obtained from a sparsely branched metallocene polyethylene show that as few as one long-chain branch per two molecules was found to mitigate oscillatory slip-stick fracture often observed in linear polyethylenes. Furthermore, the presence and severity of gross melt fracture was found to increase with long-chain branching content. These indirect effects were correlated to an early onset of shear-thinning behavior and extensional strain hardening, respectively. Conversely, linear resins exhibiting a delayed onset of shear-thinning behavior and extensional strain softening were found to manifest pronounced slip-stick fracture and less severe gross melt fracture. The occurrence of surface melt fracture appeared to correlate best with the degree of shear thinning arising from both molecular weight distribution and long-chain branching.

The ability to predict the flow behavior of long-chain branched and linear polyethylene resins was also investigated. Using the benchmark 4:1 planar contraction geometry, pressure profile measurements and predictions were obtained for a linear and branched polyethylene. Two sets of finite element method (FEM) predictions were obtained using a viscoelastic Phan-Thien/Tanner (PTT) model and an inelastic Generalized Newtonian Fluid (GNF) model. The results show that the predicted profiles for the linear PE resin were consistently more accurate than those of the branched PE resin, all of which were within 15% of the measured vales.

Furthermore, the differences in the predictions provided by the two constitutive models was found to vary by less than 5% over the range of numerical simulations obtained. In the case of the branched PE resin, this range was very narrow due to loss of convergence. It was determined that the small differences between the PTT and GNF predictions were the result of the small contraction ratio utilized and the long relaxation behavior of the branched PE resin, which obscured the influence of extensional strain hardening on the pressure predictions. Hence, it was expected that numerical simulations of the 4:1 planar contraction flow for the mildly strain hardening metallocene polyethylenes would not be fruitful.

Acknowledgments

The author wishes to thank Professor Donald G. Baird for his support and guidance resulting in the completion of this work. In addition, the author would like to thank all members of his research committee (past and present): Dr. Davis, Dr. Dillard, Dr. Long, Dr. Sullivan, Dr. Wapperom, and Dr. Wilkes.

The author wishes to acknowledge the following persons:

- His parents and siblings for their continued support throughout this process.
- Professor Brian P. Grady at the University of Oklahoma for the encouragement to pursue a graduate degree.
- Dr. Robert T. Young for his assistance, advice, and friendship.
- All members of the Polymer Processing Lab he has had the honor of serving with: Thomas, Mike, Robert, Monty, Sujan, Jianhua, Frank, Bort, Eric, Wade, Matt, and Caroline.
- Those members of department staff who have made this work easier over the years: Diane, Chris, Riley and Wendell.

Original Contributions

The following are considered to be significant original contributions of this research:

1. A clearer understanding of the influence of sparse long-chain branching in metallocene-catalyzed polyethylenes on their shear rheological properties is established. Once the effects of weight-average molecular weight have been removed, the degree of zero-shear viscosity enhancement, normal stress difference enhancement, and reduced onset of shear-thinning behavior becomes more evident.

2. The ability to correlate extensional strain-hardening behavior in sparsely branched metallocene polyethylenes to long-chain branching frequency is identified using the McLeish-Larson "pom-pom" constitutive model. This treatment is shown to be consistent with the proposed polymerization mechanism for metallocene polyethylenes.

3. It is demonstrated that the fluid relaxation behavior dominates the pressure profile predictions of the abrupt 4:1 planar contraction geometry within the range of numerical convergence. For the case of branched polyethylenes, the small extensional strains encountered and the slow relaxation behavior of the fluid negates any effects on the pressure profiles arising from extensional strain hardening.

4. The identification that increased degrees of shear thinning and extensional strain-hardening behavior arising from long-chain branching mitigates slip-stick fracture and augments gross melt fracture in commercial polyethylenes, respectively.

Table of Contents

List of Figures

Chapter 5.0

Chapter 6.0

Chapter 7.0

List of Tables

Chapter 7.0

1.0 Introduction

1.0 Introduction

Polymers have played an increasingly important role in everyday life over the past 50 years. Many household items are now made of plastic or plastic composite materials, replacing age-old materials like metal, glass and wood. One of the most prolific of all commercial plastics has been polyethylene. Polyethylene (PE), a thermoplastic polymer, is currently the largest volume selling commodity resin worldwide and owes much of its success to its inherent versatility. The key to this success has been the evolution of polyethylene's molecular structure.

During the past five decades four major generations of polyethylene materials have emerged, each time providing new solutions for consumer needs. Figure 1 provides a general schematic of the evolution of molecular structure during each of the four generations. The first generation of polyethylene was discovered by ICI (England) in 1933 [McMillan (1979)]. This particular form of PE, now known as low-density polyethylene (LDPE), is generated under high-temperature, high-pressure conditions yielding a highly branched structure. LDPE has an

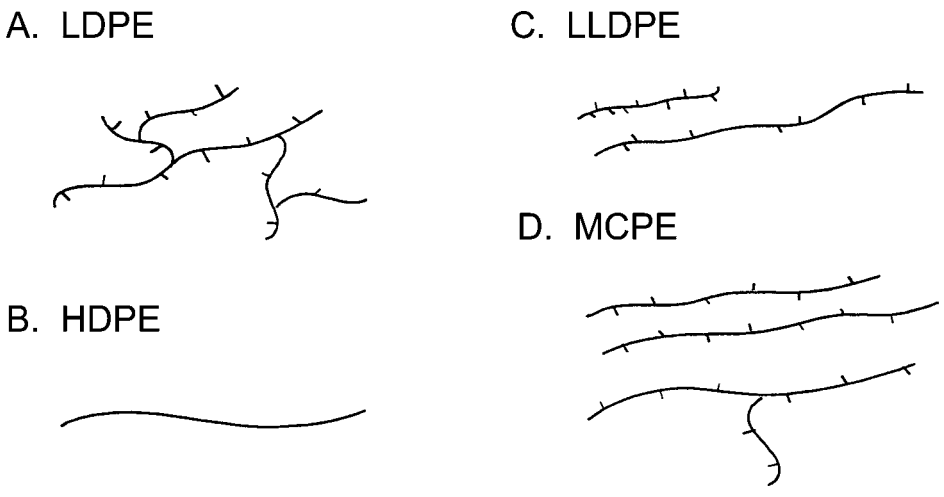

Figure 1.1: Molecular Structures of Polyethylene [Kim *et al*. (1996)]

average bulk density between 0.910 and 0.940 g/cm^3 and an average melting point of 110 °C. Due to the high degree of branching, the overall degree of crystallinity is low and as a consequence reduces the polymer's performance and properties. Fortunately, the high degree of long-chain branching (LCB) that does exist in LDPE greatly enhances the processability of the molten resin.

The second generation of polyethylene developed from major discoveries in organometallic chemistry. During the 1950's, a substantial amount of work was done with transition metal salts and oxides that led to the development of coordination catalysts, namely the Ziegler-Natta (Z-N) [Ziegler *et al*. (1955), Natta (1955)] and Phillips (Petroleum Co.) [Hogan and Banks (1958)] catalysts. These new catalysts required substantially lower operating temperatures and pressures and could generate linear polymer structures. The homo-polymerization of ethylene using coordination catalysts gives a linear polyethylene known as high-density polyethylene (HDPE), see Figure 1. HDPE has an average bulk density in excess of 0.94 g/cc and a higher melting point than that of LDPE. The increased density and enhanced mechanical properties are associated with the higher degree of crystallinity. Unfortunately, HDPE is more difficult to melt process than its branched counterpart and because of the high degree of crystallinity suffers from environmental stress cracking (ESC). The copolymerization of small fractions of α-olefins (1-butene, 1-hexene, etc.) with ethylene has proven successful in alleviating ESC, but α-olefin uptake was generally limited in early polymerization processes.

The third generation of polyethylene appeared almost twenty years after the second and was more an evolution of process engineering than polymer chemistry. Although coordination catalysts could produce higher strength ethylene/alpha-olefin copolymers they could not initially overtake the early lead, economics, and production capacity established for LDPE by the free-

radical process. This changed dramatically in 1977 with the introduction of Union Carbide's Unipol™ gas-phase process [Miller (1977)]. The gas-phase process provided an economical, versatile route to producing linear polyethylene with up to 10 wt% alpha-olefin content. The increased comonomer content increased the degree of short-chain branching (SCB) and decreased the resin bulk density to between 0.915 and 0.925 g/cm^3. This new resin was decidedly known as linear low-density polyethylene (LLDPE) because of its linear structure and LDPE-like density. Although melt processing of LLDPE resins was generally easier than HDPE it was still inferior to that of LDPE.

The recent development of metallocene and single-site catalyst technology has begun the fourth generation of the polyethylene. Since its introduction in the 1980's and commercialization in the 1990's, metallocene-catalyzed polyethylenes (MCPE) have generated a substantial amount of industrial and academic research. Commercial MCPE resins generally have narrower molecular weight distributions, high comonomer content, and narrower comonomer composition distribution than any of the previous generations of polyethylene. Metallocene catalysts also permit the introduction of small amounts of long-chain branching (LCB) into the molecular structure. All of these advancements have improved the processability and mechanical properties of MCPE resins over the "conventional" resins discussed above.

Most of the industrial fascination with metallocene catalysts has been the ability to "tailor" MCPE resins to customer's needs. The ability to "tailor" resins largely depends on the ability to manipulate the molecular structure of the resin. Figure 1.2 illustrates the degree of molecular architecture control attained during each of the four generations. The discrete control of molecular architecture provides the ability to adjust important physical properties such as: melting point, modulus, clarity, toughness and elasticity. At the same time, molecular

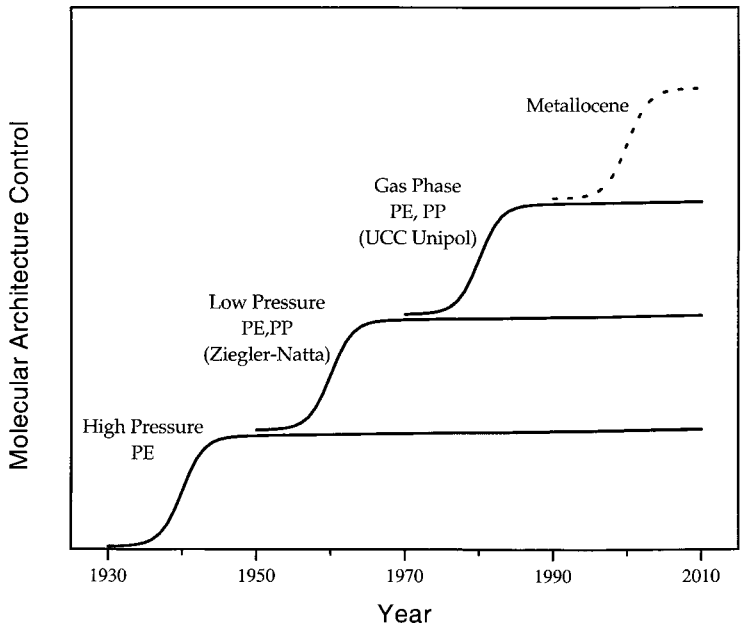

Figure 1.2: Evolution of Molecular Control (adapted from [Montangna and Floyd (1993)])

architecture can also have a significant effect on resin processability. Often times, improvements in mechanical properties can occur at the expense of resin processability, and vice-versa.

The duality between mechanical properties and processability is well recognized in PE processing. High molecular weight resins with narrow molecular weight distributions exhibit exceptional mechanical properties. However, they are the most difficult to melt process due to their lower shear sensitivity. This results in higher operating pressures, lower output rates and process instabilities. Previous attempts to improve resin rheology have focused on polymer modification. Modification is often performed through the use of polymer/polymer blending or the addition of processing aids and additives. While modification can alleviate most processing difficulties, it requires an additional processing step and is usually suited to one particular application.

Although MCPE resins can suffer from the same processing limitations as conventional PE resins, the addition of low degrees of long-chain branching, e.g. less than 1 branch per chain,

can markedly affect the processability of the resin. With the use of constrained-geometry [metallocene] catalysts (CGC) like those developed using Dow Chemical Company's INSITE™ Technology it is possible to incorporate and control sparse amounts of LCB into the molecular architecture [Lai *et al*. (1993)]. Figure 1.1 has shown examples of linear and branched mPE molecules. Sparse levels of LCB can greatly enhance the zero-shear viscosity and shear sensitivity of the MCPE resin while maintaining the exceptional mechanical properties. This provides the ability to rapidly modify resin rheology for whatever processing scheme is desired.

Resin rheology greatly affects the processability of a given polymer. Improved processability can reduce rejects and downtime, increase line speeds and productivity, and produce thinner gauge products without sacrificing performance. In order to determine what rheological properties are important, the kinematics associated with a given processing scheme must be known. One common processing scheme used for producing packaging grade film is film blowing. The film blowing process consists of shear dominated and extensional dominated deformations. A relatively low viscosity polymer melt may lead to reduced pumping requirements and greater throughput, but the ability to effectively draw the material is compromised. Rather, a polymer melt exhibiting a higher viscosity at low shear rates and substantial shear-thinning behavior is most desired. This combination of properties maintains low pumping requirements, but provides needed melt strength during the drawing operation. Therefore, resin rheology, and the influence that molecular structure has on it, will be important for improving processability.

Quite often product quality and productivity can be affected by flow instabilities. Two types of instabilities commonly seen during the film blowing of PE resins are melt fracture and bubble instability. Melt fracture can be a periodic or irregular distortion of the extrudate surface

arising from the extrusion die itself. This type of distortion greatly reduces product clarity, and during extreme cases can impact mechanical properties as well. The second type of instability is known as bubble instability. It is a free surface instability that adversely affects film dimensions and process control during the film blowing operations. There are many types of bubble instabilities, all of which reduce product quality and often lead to catastrophic failure during processing. Although bubble instability is a rather intriguing phenomenon, this study will be limited to investigating the melt fracture phenomenon.

The onset of melt fracture often represents the limiting rate of production. Further increases in capacity lead to reduced product quality and performance. The degree of melt fracture is often dependent on the polymer being processed as well as the extrusion geometry. As mentioned above, polyethylene resins are known for their susceptibility to melt fracture. All PE resins can exhibit melt fracture at high processing rates, but the molecular architecture of the resin plays an important role in the type and severity of the observed instability. The flow geometry can also affect the melt fracture behavior. The prior flow history, die dimensions and material of construction can all have a significant impact on the form and severity of the extrudate distortion [Baird and Collias (1995)]. Therefore, it is important to fully understand how the resin characteristics and flow geometry can impact the melt fracture phenomenon.

Given the rheological properties of a particular MCPE melt, it would be of great benefit to predict the flow behavior and stability of the resin during typical processing scenarios. This would limit the costly trial-and-error method of resin matching and mold design. Although typical processing scenarios are quite complex and have elaborate flow histories, ideal complex flow geometries, like abrupt planar and axisymmetric contractions (Fig. 1.3), are easy to construct and provide valuable information about the process. Abrupt contractions produce

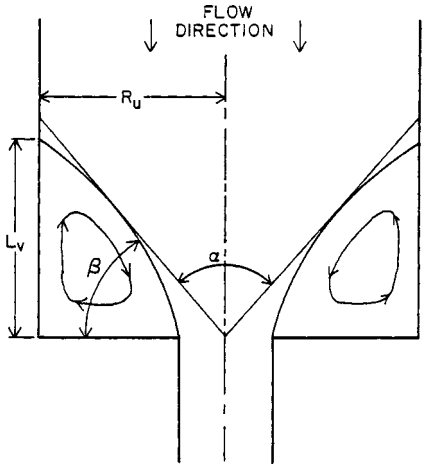

Figure 1.3: Entry Flow Pattern [White (1987)]

complex flow kinematics consisting of shear and extensional deformations, exhibit non-Newtonian flow characteristics, and better represent typical processing situations than do viscometric flows. This *experimental relevance* can lead to a more accurate description of the flow behavior in less ideal flow situations. However, the ability to accurately predict the flow behavior relies upon the proper choice of numerical method as well.

The success of any numerical simulation depends on its ability to predict *real* flow behavior. One of the most important factors is the choice of constitutive equation. The constitutive equation must be able to accurately predict the flow behavior under the desired processing conditions. If the constitutive model is not adequate then erroneous results or lack of convergence will occur. Because we have chosen to investigate the flow behavior around an abrupt contraction, our chosen constitutive equation must address both shear and extensional material responses. Three constitutive equations that have shown promise are the Phan-Thien and Tanner (PTT) [Phan-Thien and Tanner (1977)], K-BKZ [Kaye (1962), Bernstein *et al*. (1963)] and Pom-pom [McLeish and Larson (1998), Inkson *et al*. (1999)] models. The PTT model is one of very few constitutive equations capable of predicting extensional behavior

independent of shear behavior. The PTT model is extremely versatile providing multiple response modes and kinematic specific parameters. The K-BKZ model also has the ability to accurately describe uniaxial extensional properties and has received much attention over the years. Unfortunately, it is limited in planar extensional deformations, which are of interest here. The pom-pom model is very unique in that it has been specifically designed to address the effects of a branched architecture on rheological response. The presence of branching in LDPE and some MCPE resins makes the pom-pom model an appropriate choice.

The ability to describe and predict the flow behavior of sparsely branched MCPE resins requires a thorough knowledge of the resin characteristics and processing scenario. Although a substantial amount of research has been performed on previous generations of PE resins, many questions remain unanswered. These questions include the specific effects of sparse degrees of long-chain branching on resin rheology and flow stability, and whether the flow behavior of long-chain branched polyethylene resins can be accurately modeled through numerical simulations. This study will attempt to address these questions through three main objectives. The first will be to investigate and quantify the effects of sparse long-chain branching on the shear and extensional rheological properties of the polymer melt. The second objective will elucidate and identify the influence that resin rheology, arising from breadth of distribution and long-chain branching, has on the onset and form of melt fracture instability during extrusion. The final objective will determine the ability of numerical simulations to accurately predict the flow of linear and long-chain branched polyethylenes through an abrupt contraction geometry with special emphasis on the hydrodynamic pressure predictions. The results of these objectives should provide a clearer understanding of the flow behavior of sparsely branched metallocene-catalyzed polyethylene resins.

1.1 References

Baird, D.G. and D.I. Collias, *Polymer Processing: Principles and Design*, Butterworth-Heinemann, Boston, 1995

Bernstein, B., E. Kearsley and L. Zapas, *Trans. Soc. Rheol*., **7**, 391-410 (1963)

Hogan, J.P. and R.L. Banks, U.S. Patent 2 825 721 (to Phillips Petroleum Co.), March 4, 1958

Inkson, N.J., T.C.B. McLeish, O.G. Harlen and D.J. Groves, *J. Rheol*., **43**, 873 (1999)

Kaye, A., College of Aeronautics, Cranfield, *Note* No. 134 (1962)

Kim, Y.S., C.I. Chung, S.Y. Lai, and K.S. Hyun, *J. Appl. Polym. Sci*., **59**, 125 (1996)

Lai, S.-Y., J.R. Wilson, G.W. Knight, J.C. Stevens and P.-W. S. Chum, U.S. Patent 5 272 236 (to The Dow Chemical Company), December 21, 1993

McLeish, T.C.B. and R.G. Larson, *J. Rheol*., **42**, 81 (1998)

McMillan, F.M., *The Chain Straighteners*, The MacMillan Press Ltd., London, 1979

Miller, A.R., U.S. Patent 4 003 712 (to Union Carbide), January 18, 1977

Montagna, A. and J.C. Floyd, Proc. of Worldwide Metallocene Conf., MetCon '93, Houston, TX, 171 (1993)

Natta, G., *J. Polym. Sci*., **16**, 143 (1955)

Phan-Thien, N. and R.I. Tanner, *J. Non-Newt. Fluid Mech.*, **2**, 255 (1977)

White, S.A., PhD Dissertation, Virginia Tech, Blacksburg, VA (1987)

Ziegler, K., E. Holzkamp, H. Breil and H. Martin, *Angew. Chem*., **67**, 541 (1955)

2.0 Literature Review

Preface

This chapter provides a review of literature pertinent to this research project. The key topics discussed in this chapter include: structures of polyethylene, effects of molecular structure on resin rheology, melt fracture phenomena, and numerical simulation methods.

2.0 Literature Review

In this chapter, previous research that is relevant to the experimental characteristics and numerical simulation of linear and branched polyethylenes will be reviewed. In section 2.1, the various molecular structures of polyethylene will be discussed, and a brief introduction to the chemistry and mechanical properties will be provided. Section 2.2 will focus on the rheological characterization of linear and branched polyethylenes, and section 2.3 will review the typical melt fracture behavior of polyethylenes under fast flow conditions. The final review section will focus on numerical simulations of viscoelastic flow and review some of the deficiencies plaguing their accuracy and robustness. The research objectives of the this study conclude the chapter.

2.1 Structure of Polyethylene

Polyethylene (PE) is the generic name for a class of thermoplastic, semi-crystalline polymers made from the homo-polymerization or co-polymerization of ethylene. All polyethylene resins contain continuous carbon-carbon backbones and all are made from two elemental sources, carbon (C) and hydrogen (H). However, not all polyethylene resins are the same. One of the most fascinating attributes of polyethylene is its "polymorphic" nature. Despite its inherent chemical simplicity, PE can exist in several different forms, each form possessing different physical, chemical, and mechanical properties.

During the past 70 years, the desire to understand, and ultimately control, the structure of PE has initiated a substantial amount industrial and academic research. This research has lead to the development of four major generations of PE resins. Each generation has improved upon its predecessors and each is characterized by its own unique molecular structure. The ability to control resin architecture has developed largely from dramatic discoveries in the areas of

polymer science and engineering. Together, these discoveries have defined the evolution of PE from an intellectual curiosity to a global, diversified commodity plastic.

2.1.1 Low-Density Polyethylene

The birth of polyethylene occurred in the research labs of Imperial Chemical Industries (ICI) in March 1933. The event was marked by confusion rather than excitement because the results were unexpected, a serendipitous occurrence. Research continued through the mid-1930s and the process for making "polythene" was patented by ICI in September 1937 [Fawcett (1937)]. Polythene, the archaic name for low-density polyethylene (LDPE), is a highly branched polymer formed from the free-radical polymerization of ethylene at extremely high pressures. Although the initial applications of this new plastic material were limited, especially during the Great Depression, LDPE found application in radar cable insulation during World War II [McMillan (1979)].

Low-density polyethylene, also known as high-pressure polyethylene, is manufactured in high pressure stirred autoclave or tubular reactors. LDPE is commercially produced at pressures ranging from 100 – 300 MPa and temperatures ranging from 150 – 325 °C [Doak and Schrage (1965)]. The high capital costs and engineering problems associated with high-pressure technology are one of the major disadvantages of LDPE production.

The bulk polymerization of supercritical ethylene occurs via the free-radical mechanism. The relevant free-radical polymerization reactions are outlined in Figure 2.1. The initiation, propagation, and termination reactions are classical free-radical addition reactions. Commonly used initiators are *tert*-butyl peroxybenzoate and di-*tert*-butyl peroxide. Due to the high reaction pressures and temperatures additional side-reactions can occur. Some of the most common side-

Initiation

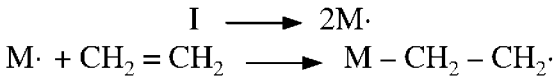

Propagation

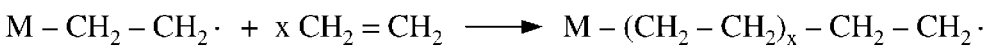

Termination

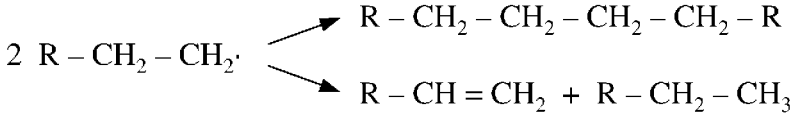

Transfer to Monomer

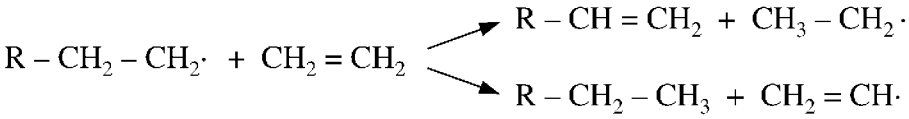

Intra-molecular Chain Transfer

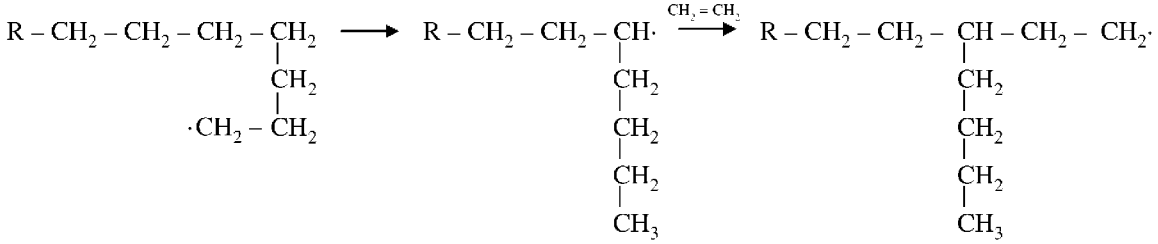

Inter-molecular Chain Transfer

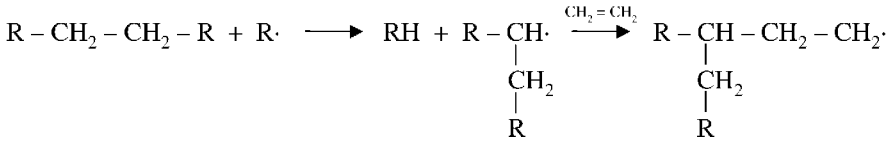

Figure 2.1: Free-radical polymerization reactions [adapted from Hill and Doak (1965)]

reactions are molecular chain transfer reactions. Molecular chain transfer reactions can occur through two pathways: intra-molecular and inter-molecular chain transfer. *Intra-molecular* chain transfer, also known as "backbiting", generates short-chain branches that have very few repeat units, typically 2 – 8 units [Dorman *et al.* (1972)]. *Inter-molecular* chain transfer, on the other hand, generates long-chain branches through the reaction of a growing chain with an existing chain [Roedel (1953)]. Long-chain branches, unlike short-chain branches, are considered large enough to interact or entangle with neighboring molecules. Therefore, the molecular weight of the branch (M_b) itself is considered greater than the critical molecular weight for entanglement (M_c).

Commercially produced LDPE resins typically have weight-averaged molecular weights on the order of $10^2 – 10^5$ g/mol [Pebsworth (1999)]. The molecular weights of these resins are often crudely referenced using a melt flow index [ASTM D1238] or precisely measured using gel-permeation chromatography (GPC). Increasing the reaction pressure and/or decreasing the reaction temperature can increase chain length, but the most predominate method of molecular weight control is through chain transfer agents. Commonly used chain transfer agents include hydrogen, propylene and isobutylene. The molecular weight distribution (MWD) of LDPE resins is typically very broad. The MWD, or polydispersity index, is defined as the ratio of the weight-averaged and number-averaged molecular weights, M_w/M_n. Commercial LDPE resins have polydispersity indices of 10 – 20, depending on reactor type and reactor conditions [Doak (1990)]. Kiparissides and co-workers (1993) have shown that the primary reason for such broad distributions is due to the long-chain branching mechanism.

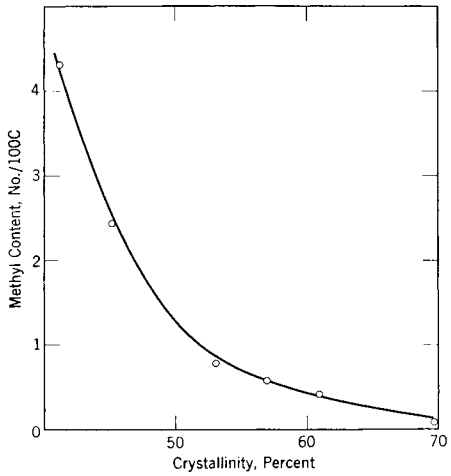

Figure 2.2: SCB vs. Crystallinity [Faucher and Reding (1965)]

The unique feature of LDPE is the intrinsic presence of both short- and long-chain branches in the molecular architecture. The high degree of branching that exists distinguishes LDPE from the remaining substantially linear polyethylene resins. Short-chain branching that is formed during "backbiting" reactions primarily affects the overall degree of crystallinity. Figure 2.2 demonstrates the pronounced effect of short-chain branching on crystallinity. The number of short-chain branches in commercial LDPE resins varies from 10 – 50 per 1000 carbons, depending on reaction conditions [Faucher and Reding (1965)]. The bulk density and degree of crystallinity are often related by the following formula,

$$C = \frac{\rho_c}{\rho} \frac{\rho - \rho_a}{\rho_c - \rho_a} \qquad (2.1)$$

where C is the weight percent crystallinity, ρ is the measured polymer density, ρ_a is the amorphous density, and ρ_c is the crystalline density. The crystalline density of polyethylene is usually taken as 1.00 g/cm^3 and the amorphous density as 0.855 g/cm^3. Commercial LDPE resins have densities of 0.915 – 0.940 g/cm^3, corresponding to 50 – 65 percent crystallinity. The

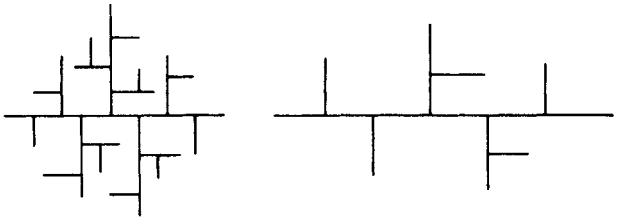

Figure 2.3: Long chain branching in LDPE: (A) autoclave product, (B) tubular product (no short-chain branches shown) [Kuhn and Kromer (1982)]

fact that density, or degree of crystallinity, is closely correlated to bulk mechanical, chemical and physical properties illustrates the importance of short-chain branching in polyethylene resins.

In addition to SCB, LDPE has a substantial amount of LCB as well. Long-chain branching occurs primarily through intermolecular chain transfer reactions (discussed earlier) and the branching frequency has been estimated to vary between 0.6 – 4.1 branches per 1000 carbons [Bovey *et al.* (1976), Axelson *et al.* (1979)]. The branching frequency is very sensitive to reactor conditions and residence time distribution. Long-chain branching increases with polymer concentration and temperature and decreases with pressure. Additionally, broad residence time distributions increase the degree of LCB. Figure 2.3 shows the variation in structure of LDPE resins polymerized in stirred autoclave reactors versus tubular reactors. Stirred autoclave reactors typically lead to broad residence time distributions that promote long-chain branching, while tubular reactors have narrower residence time distributions and consequently fewer long-chain branches.

2.1.2 High-Density Polyethylene

Historically, conventional high-density polyethylene (HDPE) has been defined as an ethylene homopolymer or ethylene copolymer having a bulk density of 0.94 g/cm^3 or greater.

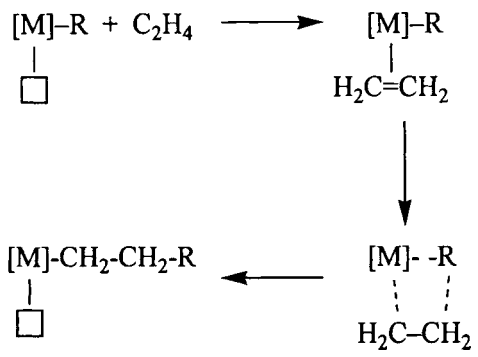

Figure 2.4: Coordination polymerization of ethylene (Cossee-Arlman mechanism); [M] active metal center, (-R) alkyl chain [Janiak (1998)]

HDPE is a substantially linear polyethylene resin prepared using transition-metal polymerization catalysts based on molybdenum [Zletz (1952)], chromium [Hogan and Banks (1955,1958)], or titanium [Ziegler *et al.* (1960)]. Commercial production of HDPE was started in 1956 by Phillips Petroleum Co. in the United States and by Hoechst AG in the FRG. During the past 40 years, the production of HDPE resins has grown dramatically and the current worldwide capacity has eclipsed 14 million tons per year.

The polymerization of high-density polyethylene proceeds via the coordination polymerization of ethylene using transition metal based catalysts. Coordination polymerization is a unique form of addition polymerization that requires the sequential coordination and complexation of the monomer to a active transition metal center prior to intramolecular chain insertion. Figure 2.4 illustrates the coordination polymerization of ethylene using a transition metal catalyst system. The active center of polymerization is believed to be either a transition metal-carbon bond or a base metal-carbon bond, with most experimental research indicating the former as the main site of activity [Boor (1979)]. Details of the various proposed polymerization mechanisms are not the focus of this research project and can be found elsewhere [Boor (1979), Friedlander (1965)].

There are currently two heterogeneous catalyst systems used for producing conventional high-density polyethylene. The first is known as the Phillips chromium catalyst and has historically been the most dominant catalyst for producing HDPE. The Phillips chromium catalyst consists of a chromium (VI) oxide complex bound to either a silica-alumina or silica support. The chromium oxide catalyst exhibits very high activity (3-10 kg polymer/g catalyst) and produces linear high-density polyethylene with little or no branching. The addition of 1-butene as a comonomer is used to increase short-chain branching and reduce overall crystallinity. The Phillips catalyst is used exclusively to make polyethylene and ethylene copolymers.

The second heterogeneous catalyst is simply known as the Ziegler-Natta (Z-N) catalyst system [Zeigler *et al.* (1960), Natta *et al.* (1957)]. The Z-N catalyst system differs from the Phillips catalyst in that it requires two compounds: a transition metal halide and an organometallic cocatalyst. Titanium (IV) chloride is probably the most widely used transition metal halide, although vanadium chlorides have shown utility in ethylene polymerization. The co-catalyst functions primarily as an alkylating agent for the transition metal halide prior to polymerization, and triethyl aluminum is most often used for that purpose. The Z-N catalyst system also exhibits high activity and can produce high molecular weight polymer. The biggest difference between the Phillips and Z-N catalyst systems is versatility. The Z-N catalyst is capable of polymerizing higher α-olefin monomers (primarily propylene) with desirable stereoregularity.

The polymerization of HDPE resins requires lower reaction temperatures and pressures than those required for LDPE production. HDPE resins produced using the Phillips catalyst require reaction temperatures of 85 – 110 °C and operating pressures of 3 MPa in a light hydrocarbon solvent. HDPE resins produced using the Ziegler-Natta catalyst system require

reaction temperatures of 70 – 100 °C and reaction pressures of 0.1 – 2 MPa. The Z-N polymerization reaction can be carried out in an inert liquid medium or in the gas phase.

Commercially produced HDPE resins typically have weight-averaged molecular weights on the order of 10^2 – 10^6 g/mol. This corresponds to melt indices ranging from 500 (low molecular weight waxes) to 0.001 (ultra-high molecular weight resins) dg/min. The molecular weights of HPDE resins produced by Phillips catalysts are determined exclusively by reaction temperature, while those produced by Z-N catalyst systems are determined by reaction temperature and/or the presence of chain transfer agents [Boor (1979)]. The molecular weight distributions of HDPE resins are generally narrower than LDPE resins, but the catalyst system used has a large effect. Phillips HPDE resins have polydispersity indices as low as 6 – 8 or as high as 10 – 18 depending on the support used and catalyst activation [Pullukat *et al.* (1983)]. Z-N HDPE resins can have polydispersity indices from 5 – 10 for supported catalysts and 20 – 30 for unsupported Ziegler catalysts [Zucchini and Cecchin (1983)].

The greatest difference between HDPE and LDPE resins is the relative lack of chain branching in HDPE resins. HDPE resins have very few short-chain branches (SCB) and no long-chain branches (LCB). The homo-polymerization of ethylene using either catalyst system generates substantially linear polyethylene with very little branching. The degree of short-chain branching stemming from homo-polymerization is as low as 0.5 – 3 branches per 1000 carbons, and is usually attributed to traces of higher olefins in the ethylene feed. Commercial HDPE copolymers have at most 5 – 10 branches per 1000 carbons, corresponding to an overall crystallinity of 60 – 80 percent [Kissin (1999a)]. The intentional addition of small quantities of α-olefins as a comonomer is often performed to further reduce the degree of crystallinity and mitigate the effects of environmental stress cracking (ESC). The most common comonomer is 1-

butene because of its low cost. The lack of long-chain branching in HDPE resins can be ascribed to the controlled method of polymerization using transition metal catalysts.

2.1.3 Linear Low-Density Polyethylene

Linear low-density polyethylene (LLDPE) is designated as the linear analog to low-density polyethylene (LDPE). LLDPE is a substantially linear polymer characterized by a high degree of short-chain branching arising from the copolymerization of ethylene with higher α-olefin comonomers. The single largest impact on the production and commercial viability of LLDPE was the introduction of the gas-phase, fluidized bed polymerization process by Union Carbide in 1977. The gas-phase Unipol® process [Levine and Karol (1977)], as it is called, was licensed worldwide for use in the production of LLDPE, a replacement for LDPE resins. During the past 20 years, the LLDPE resins using the Unipol ® and other polymerization processes have gained a significant share of the polyethylene market.

Although LLDPE is a close sibling to HDPE, the commercial viability of LLDPE resins was not attained until the late 1970's. Prior to 1977, linear polyethylene resins of low density could not be efficiently made using the existing polymerization processes, namely slurry and solution processes. Slurry processes caused excessive swelling of the polymer at bulk densities below 0.93 g/cm^3, and solution processes were limited by the high viscosities arising from high molecular weight species. The equipment required for separation of residual solvent and low molecular weight species from the polymer proved too costly and prevented economic viability. The development of the gas-phase Unipol ® process in 1977 overcame these problems and provided the means to economically produce LLDPE. The gas-phase process avoids the solubility and viscosity problems inherent to solution- or slurry-based processes, eliminates

solvent storage and recovery, and allows easy conversion between LLDPE and HDPE production.

Linear low-density polyethylenes are polymerized using the same heterogeneous catalysts used for producing HDPE resins. The molecular weight range of commercial LLDPE resins is relatively narrow and is on the order of 10^4 and 10^5 g/mol. This corresponds to melt indices of 0.1 – 5 dg/min. The primary reason for such a narrow product range is simply because most LLDPE resins are used in film blowing processes where low melt index materials are desirable. The molecular weight distributions of LLDPE resins are similar to those of HDPE and can be as narrow as 2.5 – 4.5 and as broad as 10 – 35. The molecular weight and MWD are most affected by reactor conditions and choice of catalyst system.

The most significant difference between LLDPE and HDPE resins is the type and degree of short-chain branching present in the polymer. A typical HDPE resin contains less than one mole percent of a α-olefin (usually 1-butene), while a typical LLDPE resin may contain 2 – 4 mole percent. The increased amount of comonomer incorporation reduces the bulk density of the LLDPE resin to 0.915 – 0.940 g/cm^3 and the overall degree of crystallinity to 30 – 60 percent. This reduction in crystallinity corresponds to an increase in the degree of short-chain branching to approximately 10 – 20 branches per 1000 carbons. Commercial LLDPE products, unlike HDPE products, are also available as ethylene copolymers of 1-butene, 4-methyl-1-pentene, 1-hexene, or 1-octene. The choice of comonomer is primarily dependent upon process compatibility, cost and product properties. Figure 2.5 demonstrates the effect of short-chain branch length on LLDPE film toughness.

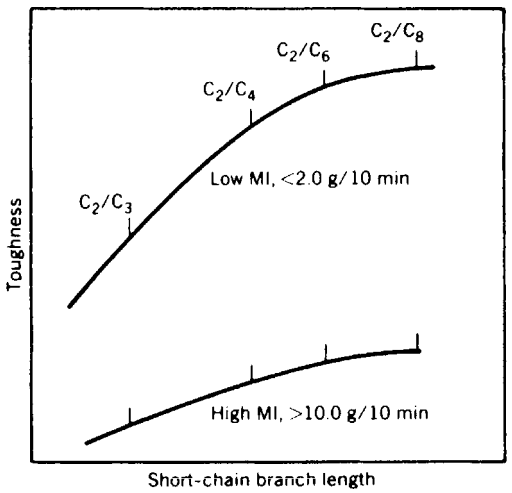

Figure 2.5: Short-chain branch length vs. LLDPE film toughness [James (1990)]

In addition to the number of short-chain branches, the compositional uniformity of short-chain branches is also important. Most commercially produced LLDPE resins have very broad, or nonuniform, branching distributions. The low molecular weight fractions generally have a greater composition of comonomer than the high molecular weight fractions due to variations in site activity associated with heterogeneous catalyst systems. This degree of nonuniformity is often measured using temperature-rising elution fractionation (TREF) [Pigeon and Rudin (1994)] or differential scanning calorimetry. The degree of nonuniformity can have a significant effect on the physical and mechanical properties of the LLDPE resin. Resins lacking compositional uniformity often require a greater fraction of comonomer to reduce the bulk density and melting temperature, and often contain greater amounts of extractables that may be detrimental to end use properties.

2.1.4 Metallocene-Catalyzed Polyethylenes

Metallocene-catalyzed polyethylenes (MCPE) are the latest, and most interesting, generation of polyethylene resins. The importance of metallocene catalysts has been made

obvious by the more than 600 patents issued in the field since 1980 [Tzoganakis *et al.* (1989)]. The major advantage of metallocene and other single site catalysts is their versatility in tailoring polymers with well-defined molecular structures (M_w, MWD, LCB). This desirable capability allows plastic manufactures to "design" resins for specific applications. At present, the production of metallocene-catalyzed polyethylene resins has reached 3.5 million tons per year, which accounts for almost 10% of the worldwide PE capacity [Benedikt and Goodall (1998)].

Metallocene-catalyzed polyethylenes are produced from metallocene and other single-site catalysts. Interestingly, metallocene catalysts are similar in composition and mechanism to traditional heterogeneous Ziegler-Natta catalyst systems. Both catalyst systems feature active transition metal centers, coordinate and complex monomers prior to chain insertion, and require co-catalysts for enhanced activity. Metallocene catalysts also operate at reaction temperatures and pressures similar to those of conventional Ziegler-Natta catalysts. In fact, metallocene catalysts have been historically known as soluble or homogeneous Ziegler-Natta catalysts since their discovery by Kealy and Pauson (1951). However, their initial use was limited to mechanistic studies due to their low catalyst activity [Breslow and Newburg (1957)].

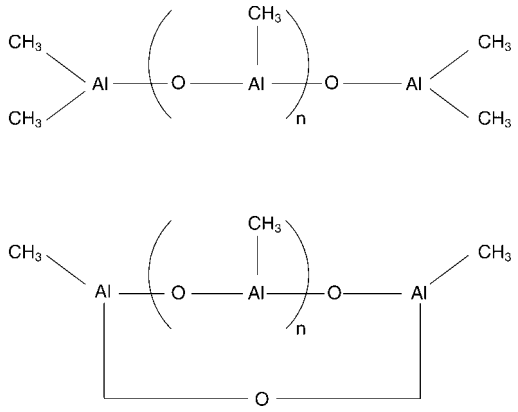

Figure 2.6: Linear and cyclic structures of aluminoxane [adapted from Kaminsky and Stieger (1988)]

The organometallic world changed dramatically in 1980 when Sinn and Kaminsky (1980) found that small amounts of water could greatly enhance the polymerization activity of metallocene/alkylaluminum catalyst systems. The formation of oligomeric alkylaluminoxane from alkylalumnium and water greatly enhanced the activity of the catalyst. Although the actual structure of alkylaluminoxane is not known in detail, Kaminsky and Steiger (1988) found that each active site must consist of 6 – 20 aluminum atoms. This single discovery led to a substantial increase of research in the field and the development of a new class of soluble catalysts known collectively as metallocene or single-site catalysts.

Three types of metallocene catalysts are currently used for polyethylene production: Kaminsky catalysts, ionic combination catalysts, and constrained geometry catalysts (Figure 2.7). The Kaminisky catalyst is the original metallocene catalyst system consisting of methylaluminoxane (MAO) and a metallocene complex of zirconium, titanium or hafnium "sandwiched" between two cyclopentadienyl rings [Sinn and Kaminsky (1980), Sinn *et al.* (1980)]. Kaminisky catalysts exhibit high activity comparable with conventional Z-N catalysts, however this degree of activity requires extremely high concentrations of MAO. MAO is a rather expensive compound and can represent a large portion of the catalyst cost. One successful alternative to alkylaluminoxane co-catalysts has been the development of non-coordinating anion (NCA) compounds [Jordan (1991)]. Perflourinated aromatic boron compounds have been found to be the most effective NCA replacements for MAO. The necessary concentration of NCA compounds is much lower than that of MAO, and the catalytic activity is comparable. The ionic combination catalysts make use of NCA compounds along with a corresponding cationic bis(cylopentadienyl) metallocene complex. Because ionic catalysts do not contain MAO the

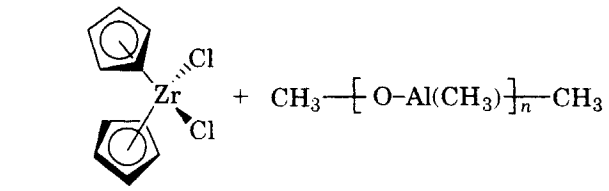

(a)

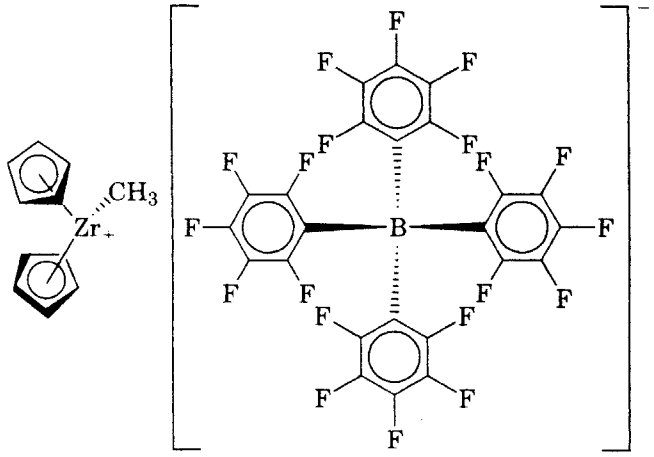

(b)

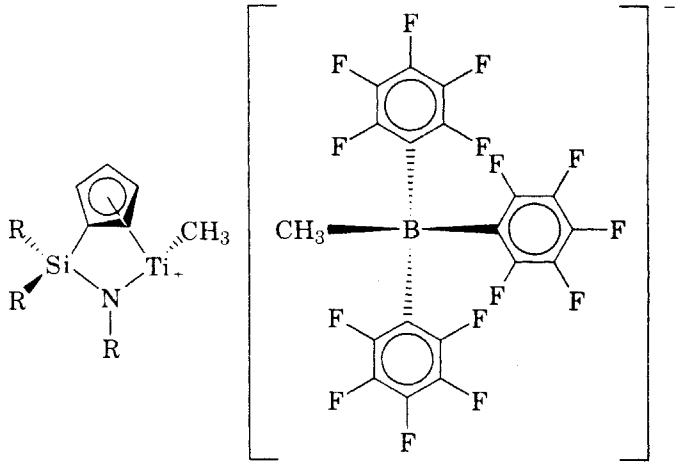

(c)

Figure 2.7: Commercial metallocene catalyst systems: (a) Kaminsky catalyst, (b) ionic combination catalyst, and (c) constrained geometry catalyst (CGC) [Kissin (1999b)]

monomer purity must be high in order to prevent catalyst poisoning from water and oxygen. Ionic combination catalysts exhibit exceptional polymerization activity.

The third metallocene catalyst system is known as the constrained-geometry catalyst (CGC) system. This catalyst is marketed by The Dow Chemical Company under the INSITE® Technology trade name. CGC catalysts are similar to ionic combination catalysts, but the cationic metallocene complex contains only one cyclopentadienyl ring coupled to the titanium center by a silane bridge [Stevens and Neithamer (1991)]. This particular conformation greatly reduces the steric hindrance associated with the bis(cyclopentadienyl) ring systems. The increased accessibility to the active transition metal center greatly enhances the catalyst activity and allows easier incorporation of higher α-olefins and high molecular weight macromonomers to growing polymer chain [Lai *et al.* (1993)].

Metallocene-catalyzed polyethylenes can be produced with a wide range of weight-averaged molecular weights, M_w. Ultra high molecular weight resins (10^6 g/mol) or low molecular weight waxes (10^2 g/mol) can be polymerized using single site catalysts. The reaction temperature, type of catalyst, and presence of chain transfer agents can be varied to control the molecular weight. Because metallocene catalysts have a single type of active site, they can produce resins with a high degree of molecular *uniformity*. The molecular weight distributions of MCPE resins are narrow, having polydispersity indices around 2.0. The comonomer distribution, or compositional uniformity, of MCPE resins is also homogenous. MCPE resins, unlike Z-N PE resins, exhibit random comonomer distribution across the entire molecular weight distribution. Figure 2.8 compares the compositional uniformity of metallocene-catalyzed versus conventional Z-N PE resins. The high degree of uniformity found in MCPE resins leads to

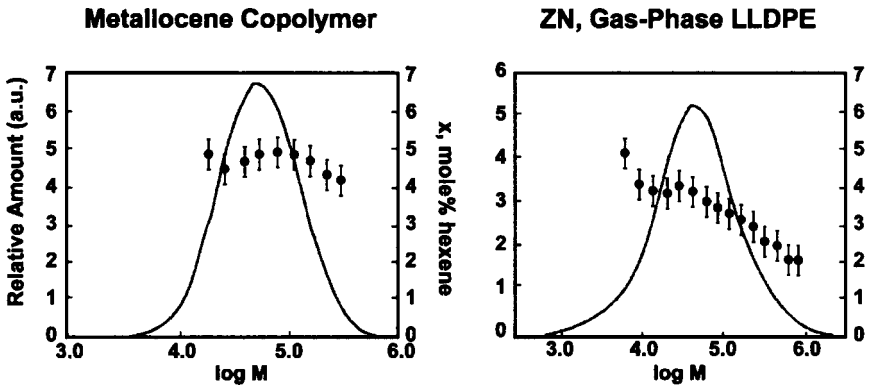

Figure 2.8: Comonomer composition distribution of metallocene and Ziegler-Natta polymerized linear low-density polyethylene resins [adapted from Brant and O'Malley (1999)]

favorable physical, mechanical, and optical properties while reducing the presence of extractables.

One of the unique features of MCPE resins is the ability to incorporate long-chain branching into the molecular structure. The use of CGC catalysts provides the ability autocopolymerize large, vinyl-terminated molecules with growing chains, thereby forming branched structures. CGC catalysts are ideal because of their "open" structure that allows macromonomers access to the active transition metal center. Currently, homo- and co-polymerized MCPE resins made with CGC catalysts can have 0.01 – 3 long-chain branches per 1000 carbons [Soares and Hamielec (1998)]. The degree of branching is primarily influenced by the polymer concentration and reaction temperature during polymerization. Table 2.1 illustrates some of the possible structures available using metallocene catalysts.

Solution processes are preferred for producing long-chain branched MCPE resins for several reasons. Macromonomers with terminal, vinyl unsaturation are formed at high rates in solution processes at elevated temperatures. The key elimination reactions leading to terminal unsaturation during coordination polymerization are summarized in Figure 2.9. The dissolved

Table 2.1: Various long-chain branched structures [Koch and Volkenburgh (1998)]

Molecule Type	Description	LC Branched Counterpart
	Homopolymer: High melting point, stiff, poor optics	
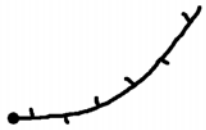	Copolymer: Medium melting point and optics, excellent mechanical properties. Used for tie molecules.	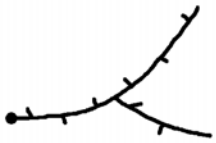
	Elastomer: Soft, elastic, low melting point, transparent, low crystallinity, high impact elastomer	
	LDPE: Medium melting point, optics and mechanical properties, excellent processability	

macromonomers are mobile and have relatively free access to the CGC catalyst. The use of continuous stirred tank reactors (CSTR) provides the ability control the polymer concentrations and the rate of long-chain branching. Furthermore, the broad residence time distributions associated with CSTRs favor the formation of long-chain branching.

(1) Vinyl Unsaturation

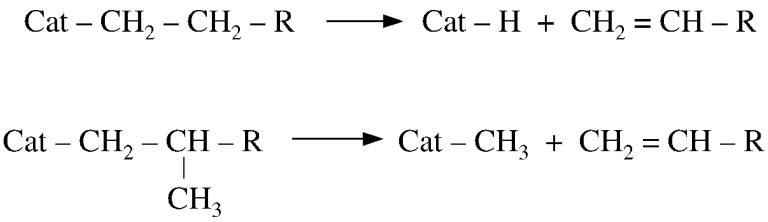

(2) Vinylidene Unsaturation

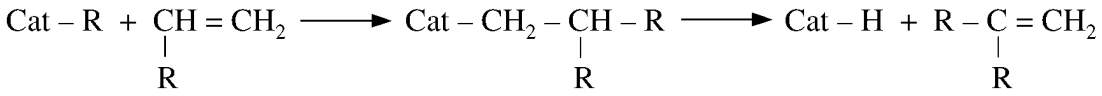

(3) Trans Unsaturation

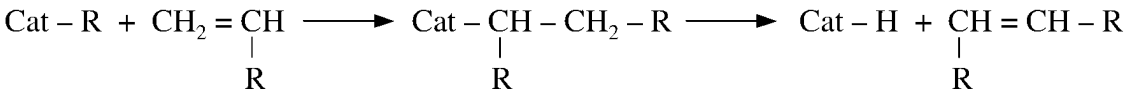

Figure 2.9: Sources of aliphatic unsaturation [adapted from Soares and Hamielec (1998)]

2.2 Rheological Effects of Molecular Structure

We have seen in the previous section that polyethylene can have an array of molecular structures. Four key molecular parameters have been identified to describe the molecular structure of the polyethylene resins: molecular weight (M_w), molecular weight distribution (MWD) or polydispersity, degree and uniformity of short-chain branching (SCB), and the degree and uniformity of long-chain branching (LCB). In the following subsections, the rheological implications of each parameter will be discussed and, where possible, quantitative descriptions applied.

However, before discussing the varying rheological effects of molecular architecture one must first understand the basic principles and methods of rheology. Subsection 2.2.1 will begin with a brief review of the basic concepts of rheology and will introduce the reader to the material functions used to describe the rheological behavior of polymer melts and liquids. With a good understanding of the kind of fluid responses characteristic of polymeric materials, the review of research on the effects of molecular architecture in later subsections will become more meaningful.

2.2.1 Material Functions for Viscoelastic Fluids

Rheology, simply stated, is the study of flow and deformation of materials. This ubiquitous term has been historically reserved for liquids, but also applies to solids and gases. Although most plastics are solids at room temperature, many must be "melted" at higher temperatures prior to fabrication. Therefore, the rheological characterization of polymeric liquids and melts is an important area of research in both industrial and academic settings. One

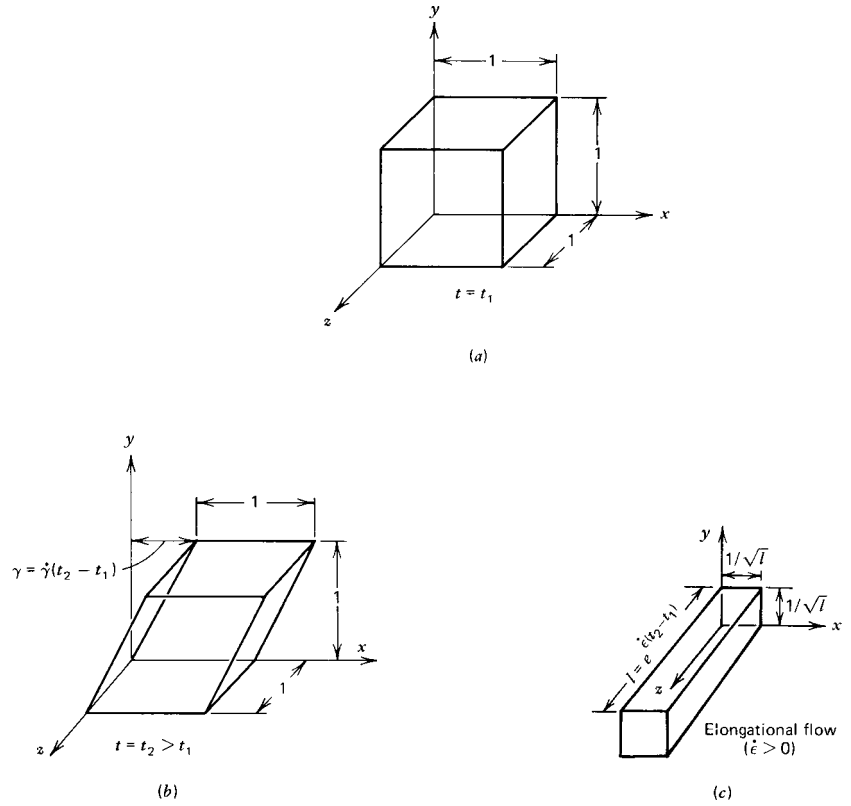

Figure 2.10: Deformation of (a) unit cube of material in (b) steady simple shear flow and (c) steady simple shear-free flow [adapted from Bird et al. (1986)]

of the main goals of polymer rheology is to relate the measurable viscoelastic properties of the polymer melt to the underlying macromolecular structure.

The two basic types of flow most often used to characterize polymeric melts and liquids are *shear* and *shear-free* flows. We will see that the molecular motions arising from each type of deformation are quite dissimilar, and as a result, will provide distinctly different material information. The two types of deformations are depicted in Figure 2.10. Material functions are used to relate the kinematics of a particular flow to the stress field required to sustain the motion. The material information gained from these material functions can be used to quantify differences between polymer melts.

Shear Flows

Simple shear flows are given by the following velocity field

$$v_x = \dot{\gamma}_{yx} y$$
$$v_y = v_z = 0 \qquad (2.2)$$

where $v_{x,y,z}$ are the rectilinear scalar velocities, and $\dot{\gamma}_{yx}$ is the velocity gradient. This type of flow is easily generated between two parallel plates and is analogous to shearing a deck of playing cards. This type of flow is distinguished by an imposed rate of deformation tensor that has two independent, non-zero components and is uniform throughout the material. The rate of deformation tensor in simple shear flow takes the following form:

$$\dot{\boldsymbol{\gamma}}_{ij} = \dot{\gamma}(t)\begin{pmatrix} 0 & 1 & 0 \\ 1 & 0 & 0 \\ 0 & 0 & 0 \end{pmatrix} \qquad (2.3)$$

where $\dot{\gamma}(t)$ may be constant or a function of time. An additional characteristic of steady shear flows is that the distance between two neighboring fluid particles is determined by the following equation:

$$l = l_0\sqrt{1+(\dot{\gamma}\Delta t)^2} \sim l_0\dot{\gamma}\Delta t \qquad (2.4)$$

where l is the final distance between particles, l_0 is the initial distance between particles, $\dot{\gamma}$ is the velocity gradient, and Δt is the time interval. Therefore neighboring particles appear to separate linearly in time for large Δt. This distinguishing feature has led many to describe shearing flows as *weak* flows because of the weak time dependence.

Various types of shear flow experiments are used to characterize polymeric melts and liquids [Bird *et al.* (1986), Baird and Collias (1998)]. One of the most common flow experiments is known as steady shear flow. Steady shear flow is characterized by a constant shear rate, $\dot{\gamma}(t) = \dot{\gamma}_0$, and gives rise to three common material functions:

$$\tau_{xy} = -\eta(\dot{\gamma})\dot{\gamma}_0$$
$$\tau_{xx} - \tau_{yy} = N_1 = -\Psi_1(\dot{\gamma})\dot{\gamma}_0^2 \qquad (2.5)$$
$$\tau_{yy} - \tau_{zz} = N_2 = -\Psi_2(\dot{\gamma})\dot{\gamma}_0^2$$

where $\eta(\dot{\gamma})$ is the shear viscosity, N_1 and N_2 are the primary and secondary normal stress differences, respectively, and Ψ_1 and Ψ_2 are the primary and secondary normal stress coefficients, respectively. The shear viscosity represents a measurement of the viscous nature of the polymeric liquid, while the normal stress difference coefficients correlate to the elastic nature.

In addition to steady shear flow, other commonly used flow experiments include small-amplitude oscillatory and creep flow experiments. Oscillatory shear flow employs a transient, sinusoidally varying velocity gradient, $\dot{\gamma}(t) = \dot{\gamma}_0 \cos \omega t$. For polymeric materials, the shear stress oscillates with the imposed frequency ω, but is not in phase with either the shear strain or shear rate. This phase shift is due the viscoelastic nature of polymer materials. The relevant material functions can be written as:

$$\tau_{xy} = -G'(\omega)\gamma_0 \sin \omega t - G''(\omega)\gamma_0 \cos \omega t$$
$$\tau_{xy} = -\eta'(\omega)\dot{\gamma}_0 \cos \omega t - \eta''(w)\dot{\gamma}_0 \sin \omega t \qquad (2.6)$$

where G' and G'' are the storage and loss modulus, respectively, and η' and η'' are the real and imaginary portions of the complex viscosity, $\eta^* = \eta' - i\eta''$, respectively. Creep flow is similar to steady shear flow except that the applied shear stress is held constant and the resulting shear strain is measured. This particular test measures the "give" or compliance of the sample. The relevant material function appears as:

$$\gamma_{yx}(t) = -J(t, \tau_0)\tau_0 \qquad (2.7)$$

where $\gamma_{yx}(t)$ is the measured shear strain, J is the shear creep compliance, and τ_0 is the applied shear stress.

Shear-free Flows

The remaining basic type of flow is known as shear-free flow. Simple shear-free flows are given by the following velocity field:

$$\begin{aligned} v_x &= -\frac{1}{2}\dot{\varepsilon}x \\ v_y &= -\frac{1}{2}\dot{\varepsilon}y \\ v_z &= +\dot{\varepsilon}z \end{aligned} \qquad (2.8)$$

where $v_{x,y,z}$ are the rectilinear scalar velocities and $\dot{\varepsilon}$ is the elongation rate. The rate of deformation tensor contains three, non-zero components and takes the following form for simple shear-free flows:

$$\dot{\gamma}_{ij} = \dot{\varepsilon}(t)\begin{pmatrix} -1 & 0 & 0 \\ 0 & -1 & 0 \\ 0 & 0 & 2 \end{pmatrix} \qquad (2.9)$$

where $\dot{\varepsilon}(t)$ is a constant or a function of time. One of the most obvious differences between shear and shear-free flows is the rate of particle separation. Particle separation during simple shear-free flow is determined by the following equation:

$$l = l_0 e^{\dot{\varepsilon}(\Delta t)} \qquad (2.10)$$

where l and l_0 are the final and initial distances between fluid particles, $\dot{\varepsilon}$ is the time-independent elongation rate, and Δt is the time interval. One can see that particle separation occurs at an exponential rate with respect to time, rather than at a linear rate seen in shear flows. Due to the strong time dependence, shear-free flows are often described as *strong* flows.

The shear-free flow experiments used to determine shear-free material functions are very similar to those discussed for shear flows. The two most common shear-free flow experiments are steady simple shear-free and elongational creep flows. Steady simple shear-free flow is characterized by a constant elongational rate, $\dot{\varepsilon}(t) = \dot{\varepsilon}_0$, and gives rise to the following material function:

$$\tau_{zz} - \tau_{xx} = -\eta_e(\dot{\varepsilon})\dot{\varepsilon}_0 \qquad (2.11)$$

where τ_{zz} and τ_{xx} are the principal normal stresses in the direction of and orthogonal to the direction of flow, respectively, and η_e is the elongational viscosity. Elongational creep flow is characterized by a constant applied tensile stress. The resulting material function is:

$$\varepsilon(t) = -D(t, \sigma_0)\sigma_0 \qquad (2.12)$$

where $\varepsilon(t)$ is the measured tensile strain, D is the elongational creep compliance, and σ_0 is the applied tensile stress.

2.2.2 Molecular Weight

The zero-shear viscosity of various polymer melts has been studied extensively [Berry and Fox (1968), Minoshima *et al.* (1980), Yamane and White (1982)], and is known to have a pronounced dependence on weight-average molecular weight. As the molecular weight of the polymer melt increases, the number of chain segments whose motion must coordinate during deformation increases. Once a critical molecular weight is attained, the presence of entanglement coupling between neighboring molecules causes a marked increase in the viscosity dependence on molecular weight. Figure 2.11 demonstrates this seemingly universal phenomenon. At lower molecular weights, the slope of the curve is near unity, but beyond the critical molecular weight

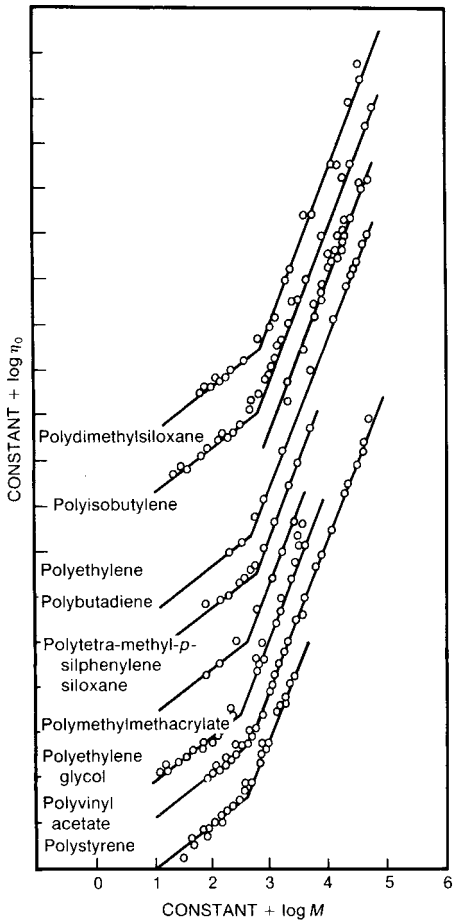

Figure 2.11: Typical zero-shear viscosity, η_0, versus molecular weight dependence for molten linear polymers [adapted from Berry and Fox (1955)]

for entanglement, M_c, the slope increases to approximately 3.4. This behavior can be described by the following relationship:

$$\eta_0 = \begin{cases} aM^{\alpha} & \text{at } M < M_c \\ bM^{\beta} & \text{at } M \geq M_c \end{cases} \qquad (2.13)$$

where a and b are polymer-specific constants, α is approximately unity, β is approximately 3.4-3.6, M is taken as the weight-average molecular weight, and M_c is the critical molecular weight for entanglement coupling. Bueche (1952) developed a theory that explains equation 2.13 and agrees surprisingly well with experimental data. The theory predicts two straight lines, below M_c the slope is unity and above M_c the slope is 3.5.

Although many polymers are well described by the above relationship, there has been considerable disagreement over the viscosity-molecular weight relationship in polyethylene. Raju *et al.* (1979) studied the linear viscoelastic behavior of fractionated monodisperse samples of HDPE. They generated what has become the standard zero-shear viscosity molecular weight relation for linear polyethylene at 190 °C (eq 2.14).

$$\eta_0 (Pa\,s) = 3.4 \times 10^{-15} \left(M_w\right)^{3.6} \qquad (2.14)$$

Although many have observed similar results for polyethylene [Fleissner (1981), Wood-Adams and Dealy (2000)], others have found that the exponent can be much higher. Kume *et al.* (1980) and Minoshima and White (1986) found exponents of 3.8 and 3.9, respectively, while Schreiber and Bagley (1962) found a power law dependence of 4.2 for linear HDPE fractions. More recently, Vega *et al.* (1996) confirmed the findings of Raju *et al.* for conventional HDPE resins, but found an exponent of 4.2 for narrow molecular weight, metallocene-catalyzed ethylene homopolymers. The reason for the higher exponent is not entirely clear but may be associated with the breadth of the molecular weight distribution and/or the effect of long-chain branching [Bueche (1960), Saeda *et al.* (1971), Vega *et al.* (1998)]

In addition to the zero-shear viscosity, the creep compliance and the onset of non-Newtonian behavior are also affected by the molecular weight. The steady state creep compliance (J_S^0) of a polymer melt, which is a measure of its elasticity, is found to be linearly dependent on molecular weight below a critical molecular weight and independent of molecular weight above the critical value [Ferry (1980)]. The following relationship summarizes the observations seen in monodisperse polymer melts:

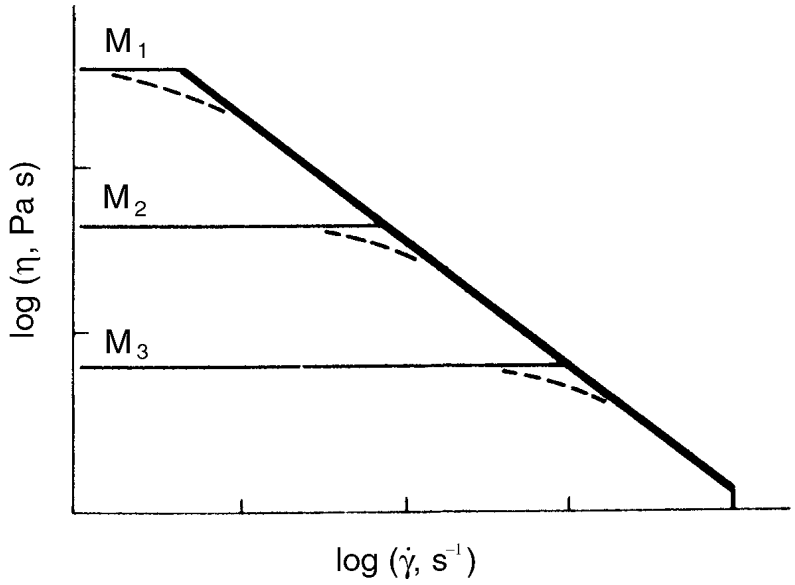

Figure 2.12: The effect of molecular weight on the terminal relaxation time, or onset of shear-thinning, in monodisperse polymer systems. [Ferry (1980)]

$$J_S^0 = \begin{cases} \dfrac{2}{5}\dfrac{M}{\rho RT} & \text{at } M < M_c' \\ \dfrac{2}{5}\dfrac{M_c'}{\rho RT} & \text{at } M \geq M_c' \end{cases} \qquad (2.15)$$

where M is taken as the weight average molecular weight, ρ is the melt density, R is the gas constant, T is the absolute temperature, and M_c' is a characteristic critical molecular weight. Above M_c' the melt acts as a rubber crosslinked by entanglements, with a molecular weight between "crosslinks" determined by M_c'.

The onset of non-Newtonian behavior is also affected by molecular weight. At relatively high shear rates the entangled polymer molecules do not have time to respond completely to the applied stress. This response arises from the entanglement coupling between neighboring polymer molecules and leads to a lowering of the viscosity. As the molecular weight increases, the degree of entanglement coupling also increases. Therefore, the individual polymer molecules

require more *time* to fully respond to the imposed local stress. This effectively increases the retardation or relaxation time of the polymer liquid. For this reason, the higher the molecular weight, the lower the shear rate at which a reduced viscosity is expected. Figure 2.12 demonstrates the nature of this phenomenon. Bueche's (1954) treatment of this effect leads to the following equation:

$$\tau_1 = \frac{12\eta_0 M}{\pi^2 \rho RT} \tag{2.16}$$

where τ_1 is the retardation time, η_0 is the zero-shear viscosity, M is taken as the weight-average molecular weight, ρ is the melt density, R is the gas constant, and T is the absolute temperature. Although Bueche's treatment provides qualitative agreement with experimental results, the model strictly applies to monodisperse samples with correspondingly acute shear-thinning behavior.

Although the material properties measured during shear deformations are a very important characteristic of polymer melts, they are not the only ones. In addition to the shear viscosity, the extensional viscosity of polymer melts is also important, especially during shear-free deformations. From linear viscoelasticity, the elongational viscosity is three (3) times the zero-shear viscosity, also known as the Trouton ratio. Therefore, one might expect that the extensional viscosity, in the limit of low strains and low strain rates, will scale with the same molecular weight dependence as the zero-shear viscosity. And experiments do in fact show this relationship. Munstedt (1980) found that the low shear rate elongational viscosity of polystyrene varied with the 3.5 power of the molecular weight, while Frank and Meissner (1984) found that similar polystyrene samples varied with an exponent of 3.6. These results compare well with those observed from shear experiments.

2.2.3 Molecular Weight Distribution

The manner, or degree, in which shear thinning occurs in polymeric fluids is often dependent upon the molecular weight distribution (MWD) or polydispersity. The onset of shear thinning is quite sharp for monodisperse polymers. Conversely, the onset becomes more diffuse with an increasing, or broadening, MWD. Figure 2.13 illustrates this behavior. The transition to non-Newtonian flow behavior is a relaxation effect that depends on the form of the relaxation spectrum, $H(\tau)$. The relaxation spectrum, in turn, is determined by the molecular weight distribution and hence the apparent relationship between molecular structure and rheological response. One can imagine that high molecular weight components, representing longer relaxation times, will transition to a "rubbery" state first, followed by lower molecular weight components, representing shorter relaxation times, at higher shear rates. Consequently, this mechanism gives more shear rate dependent behavior than seen in monodisperse samples.

Wissbrun (1986) fit data obtained from a previous investigation [Graessley (1967)] to a modified Cross equation in order to relate the MWD to viscosity-shear rate function parameters.

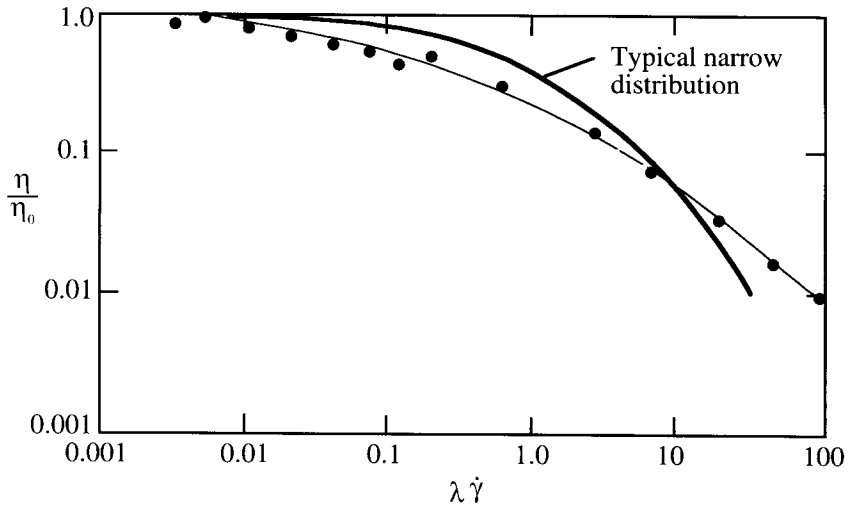

Figure 2.13: Reduced viscosity versus reduced shear rate for narrow and broad molecular weight distribution polyethylenes [Macosko (1994)]

The modified Cross equation appears as:

$$\eta\left(\dot{\gamma}\right) = \frac{\eta_0}{1 + \left[\lambda_f \eta_0 J_S^0\left(M_c'\right)\dot{\gamma}\right]^m} \tag{2.17}$$

where $\eta(\dot{\gamma})$ is the rate-dependent viscosity, η_0 is the zero-shear viscosity, J_s^0 is the steady-state compliance, λ_f is a fitting parameter which shifts the curve along the shear-rate axis, $\dot{\gamma}$ is the shear rate, and m is a fitting parameter which is related to the slope or degree shear-thinning in the non-Newtonian region. Wissbrun found that broadening the MWD reduces the onset of shear-thinning behavior to lower shear rates and decreases the degree, or acuteness, of shear thinning. Furthermore, the onset of shear-thinning was much more sensitive to MWD, varying with $(M_w/M_n)^3$, than the degree of shear-thinning, varying with $(M_w/M_n)^{0.25}$. These predictions agree well with experimental observations.

The steady-state compliance and other representations of melt elasticity, such as normal stress differences, extrudate swell, capillary end corrections are also extremely sensitive to molecular weight distribution (MWD) [Dealy and Wissbrun (1990)]. The steady-state compliance has been shown to be a linear function of molecular weight below M_c' and independent of molecular weight above it. However, when two samples of different molecular weights yet similar compliances are blended, the resulting compliance of the blend can be much greater than either component [Graessley (1984)]. Figure 2.14 demonstrates this peculiar behavior. This behavior has been estimated using the following relations:

$$J_S^0 = J_S^0\left(M_c'\right) f\left(MWD\right) \tag{2.18}$$

$$f\left(MWD\right) = \frac{M_Z M_{Z+1}}{M_w^2} \tag{2.19}$$

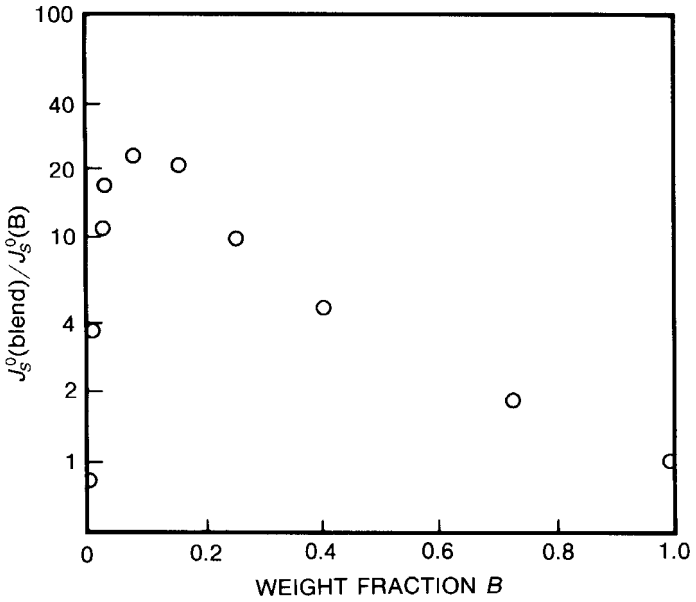

Figure 2.14: Reduced steady-state compliance versus bimodal distribution [Ferry (1980)]

$$f(MWD) = \left(\frac{M_Z}{M_W}\right)^2, 2 < a < 3.7 \qquad (2.20)$$

where M_z and M_{z+1} are higher moments of the molecular weight distribution. One can see from Figure 2.14 and the above equations that high molecular weight fractions are very important rheologically. This behavior has also been observed for normal stress difference values. In the linear viscoelastic limit the first normal stress difference can be written as:

$$N_1 = 2J_S^0\sigma^2 \qquad (2.21)$$

where N_1 is the primary normal stress difference, J_s^0 is the steady-state compliance, and σ is the applied shear stress. Therefore, one would expect the primary normal stress difference to be as sensitive to molecular weight distribution as well.

A significant amount of work has been conducted in the past to study the effects of molecular weight distribution on the viscous and elastic behavior of polyethylenes. Many have shown that the MWD has a pronounced effect on the non-Newtonian shear flow behavior of

polyethylenes. Minoshima and White (1986) performed a comprehensive study of linear and branched polyethylenes of different molecular weights and molecular weight distributions. They found that broadening the MWD broadened the transition between the Newtonian plateau and the shear-thinning power law region and also increased the magnitude and scope of the primary normal stress difference. The authors concluded that the presence of high molecular weight fractions has a dramatic impact on the rheological properties, which is consistent with the above predictions. Others have observed comparable results for the onset of shear-thinning [Graessley (1974), Kazatchkov *et al.* (1999), Wood-Adams and Dealy (2000)] and normal stress difference behavior [Oda et al (1978), Minoshima *et al.* (1980)] in polyethylenes. Studies on polypropylene [Zeichner and Patel (1980), Minoshima *et al.* (1980), Tzongankis *et al.* (1999)] and polystyrene [Yamane and White (1982)] have yielded similar results.

The elongational flow behavior of polymers is equally affected by molecular weight distribution. Munstedt (1980) performed a series of extensional measurements on polystyrene samples and found that the presence of high molecular weight fractions in the molecular weight distributions causes pronounced strain-hardening behavior. Figure 2.15 shows the transient extensional stress growth response of two PS samples. PS-I shows little strain hardening and approaches three-times the zero-shear viscosity at high strains. This observation is generally consistent with narrow MWD linear resins [Munstedt (1975), Laun and Schuch (1989), Ide and White (1978)]. PS-II, however, shows pronounced strain-hardening behavior and only reaches steady state at the lowest extension rate. Although PS-II is considered a narrow molecular weight sample, the presence of a small fraction of high molecular weight material greatly enhances the cooperative nature of the entangled melt leading to a higher extensional viscosity. Munstedt and Laun (1981) and Linster and Meissner (1986) have found similar results for

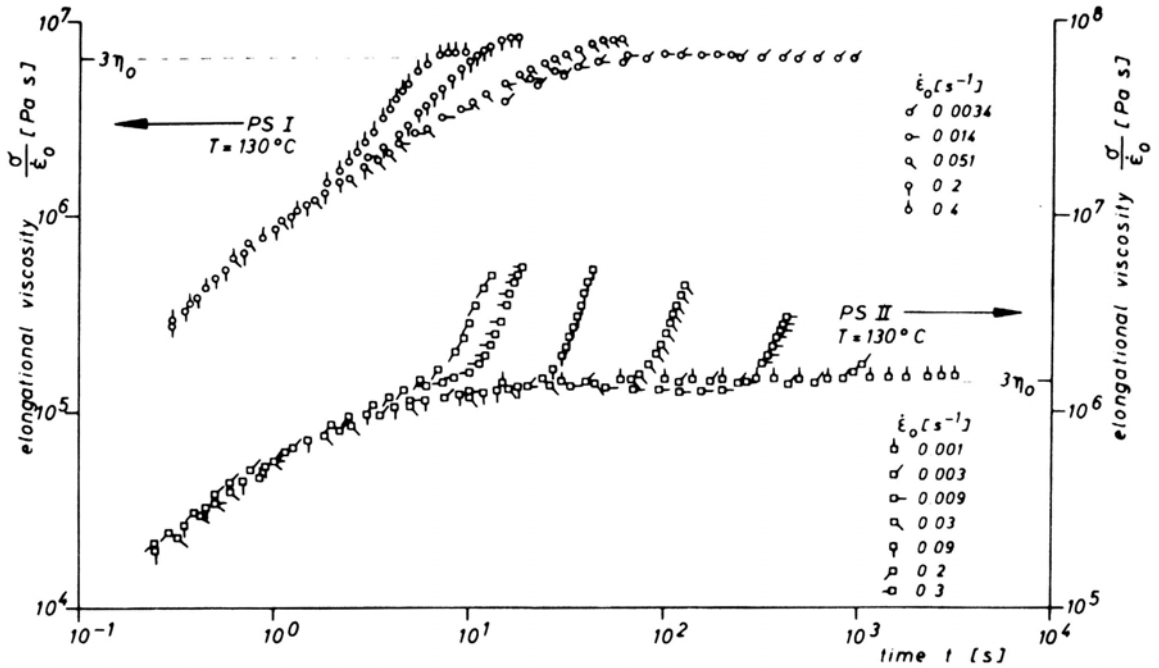

Figure 2.15: Transient elongational viscosities of two polystyrenes with a low molecular weight. PS-I, narrow MWD; PS-II, narrow MWD, high MW tail [Munstedt (1980)]

polydisperse HDPE resins. Both groups concluded that the presence of high molecular weight fractions has an un-proportional effect on the steady-state extensional responses.

2.2.4 Short-Chain Branching

The presence of short-chain branching (SCB) in polyethylene resins is known to have a dramatic effect on the physical, mechanical and chemical properties. Nevertheless, all of these properties are measured at or below the melting point of the resin. Above the melting point, the rheological properties of the melt dominate. It could be reasoned that the presence of short-chain branches would increase the free volume of the melt and lead to a lower density, less viscous melt [Peticolas and Watkins (1959)]. However, experimental evidence has shown little variation in melt density with SCB content in low-density and high-density polyethylene resins [Marshall (1956), Nielsen (1954)]. On the other hand, it is conceivable that short-chain branching could

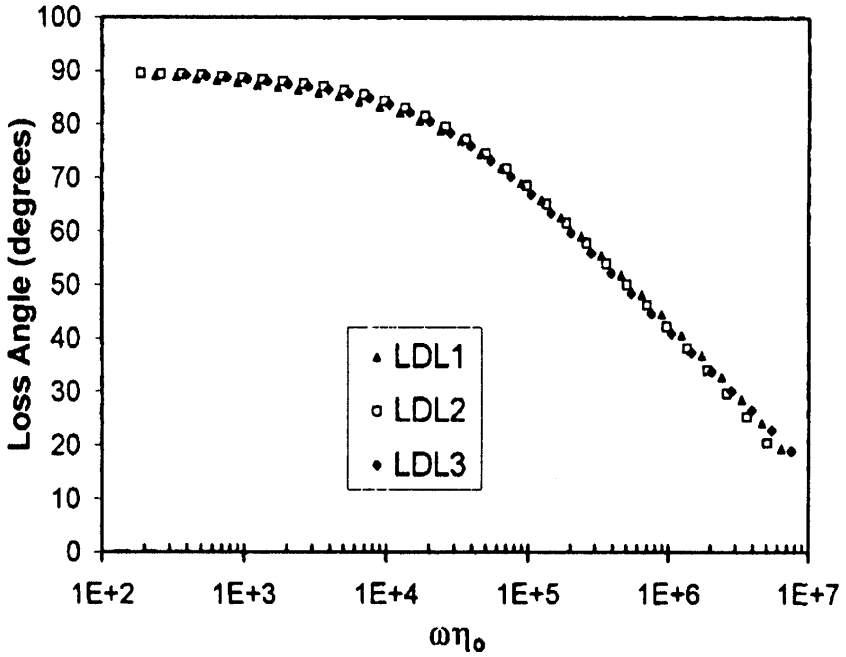

Figure 2.16: Loss angle versus reduced frequency of ethylene-butene copolymers. LDL1, 11 wt% butene; LDL2, 17 wt% butene; LDL3, 21 wt% butene [Wood-Adams and Dealy (2000)]

have significant influence on rheological properties near the melting point, where there may in fact be differences in melt density [Peticolas (1962), Moore and Schulken (1965)].

One of the strongest arguments against any rheological effects of short-chain branching is the lack of entanglement coupling between branches or other polymer chains. Short-chain branches, by definition, have branch molecular weights that are much less than the critical molecular weight for entanglement, M_c. For polyethylene resins this value lies between 2000-5000 g/mol [Vinogradov and Malkin (1980)]. Therefore, any branch less than M_c would not be expected to enhance or reduce the shear or extensional properties of the melt. Kim *et al.* (1996) and Sukhadia *et al.* (2000) investigated the effects of comonomer type, or branch length (i.e. ethyl, butyl, or hexyl branch), in conventional linear low-density polyethylenes and metallocene-catalyzed LLDPE, respectively, and found little dependence on shear viscosity. Furthermore, Wood-Adams and Dealy (2000) studied a series of ethylene-butene copolymers prepared using

metallocene catalysts. They found that the degree of branching, or branch content, had no effect on the shear viscosity or the measured loss angle (Figure 2.16) for copolymers containing up to 21 wt% 1-butene.

2.2.5 Long-Chain Branching

If the length of a side chain is comparable in length to that of the backbone, then one may consider it capable of entanglement coupling with neighboring molecules. This particular type of side chain is appropriately known as a *long-chain branch* (LCB). Because the molecular weight of the LCB is comparable to that of the backbone, and at least greater than M_c, then it is reasonable to expect that branched architecture should have a strong influence on the relaxation behavior, and thus rheological properties, of the polymer melt. Unfortunately, determining the relationship between LCB and rheology has been notoriously difficult. The degree, length and topology (i.e. random, star, comb, etc.) of branching can influence the rheological behavior. Moreover, many studies involving branched resins have been further complicated by the presence of broad molecular weight distributions (i.e. LDPE). As a result, most of the fundamental knowledge concerning the LCB-rheology relationship has been acquired from model systems in which branching has be varied independently of other molecular variables.

Shear Rheology

The presence of long-chain branching has a significant effect on the zero-shear viscosity, η_0. The apparent deviation from the traditional η_0-M_w relationship is well recognized in model systems and appears to be very dependent on the branch dimensions. Initial investigations showed that random long-chain branching reduced the zero-shear viscosity of branched species

below that of linear species of the same molecular weight [Schaefgen and Flory (1948), Charlesby (1955), Fox and Allen (1962)]. Charlesby (1955) irradiated polydimethylsiloxane fluids for varying durations, thereby introducing controlled degrees of branching. The bulk viscosities of the irradiated samples were found to be lower than those of the linear samples with comparable molecular weights. On the other hand, later studies showed that sufficiently long branches could lead to increases in the melt viscosity. Long *et al.* (1964) compared the zero-shear viscosity of linear and comb-branched polyvinylacetate (PVAc) samples. They were able to conclude from their study that branching enhances the zero-shear melt viscosity, provided the long-chain branches are long enough to entangle with neighboring polymer chains. Later, Kraus and Gruver (1964) investigated the effect of molecular weight on the zero-shear viscosities of linear and star-branched polybutadienes (PB). They found that below a structurally-dependent characteristic molecular weight the η_0 of the branched samples was distinctly lower than that of the linear samples, and that above this characteristic molecular weight the zero-shear viscosity was greater (Figure 2.17). The authors explained this behavior by stating that at low molecular weights the reduced "coil radius", or radius of gyration, of the molecule leads to lower viscosities, while at high molecular weights the enhanced entanglement coupling between neighboring molecules causes a significant increase in viscosity.

Additional studies on model systems have shown that the structural arrangement and length of branches can have a significant effect on the rheological response of branched resins. Graessley *et al.* (1976) and Raju *et al.* (1979) have observed zero-shear viscosity enhancement of star-branched polyisoprene (PI) and hydrogenated polybutadiene (HPB) over the linear polymer of equivalent molecular size. Graessley and coworkers also showed that the degree of branching enhances the steady-state compliance in addition to the zero-shear viscosity. Roovers and

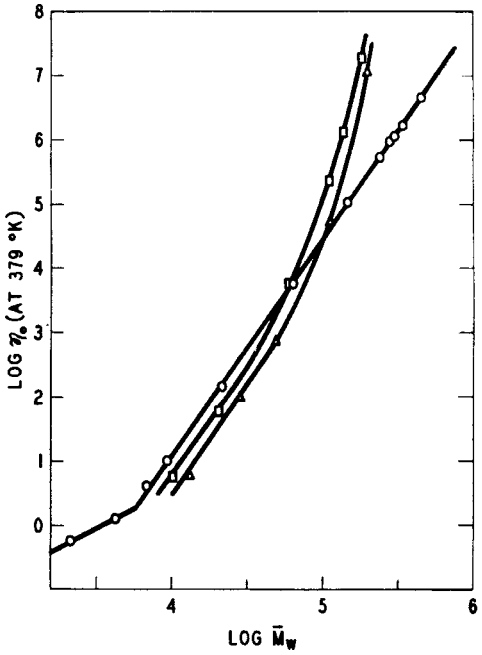

Figure 2.17: Zero-shear viscosity versus molecular weight of (○) linear, (□) trichain star, and (△) tetrachain star polybutadienes [Kraus and Gruver (1964)]

Graessley (1981) and Roovers (1984) investigated the effects of LCB in comb- and H-shaped polystyrenes. They also found viscosity enhancement in those branched polymers for a given radius of gyration. Furthermore, Roovers found that for the same number of entanglements per branch, H-shaped polymers exhibited a higher degree of viscosity enhancement than either three- or four-arm stars (Figure 2.18). The author explains this phenomenon by associating a long-time relaxation mechanism with the reptation of the central segment between branch points. This long retardation time associated with reptation may also explain the molecular weight dependence of the steady-state compliance, J_e^0, well above the M_c' for polystyrene and the apparent increase in melt elasticity.

Raju *et al.* (1979) also studied the impact of branch length on star-branched hydrogenated polybutadiene (HPB) resins. The authors observed the typical enhancement in the zero-shear viscosity, but also recognized an exponential dependence on the branch length. Similar results were observed by Carella et al (1986) and Fetters *et al.* (1993) for star-branched polybutadiene

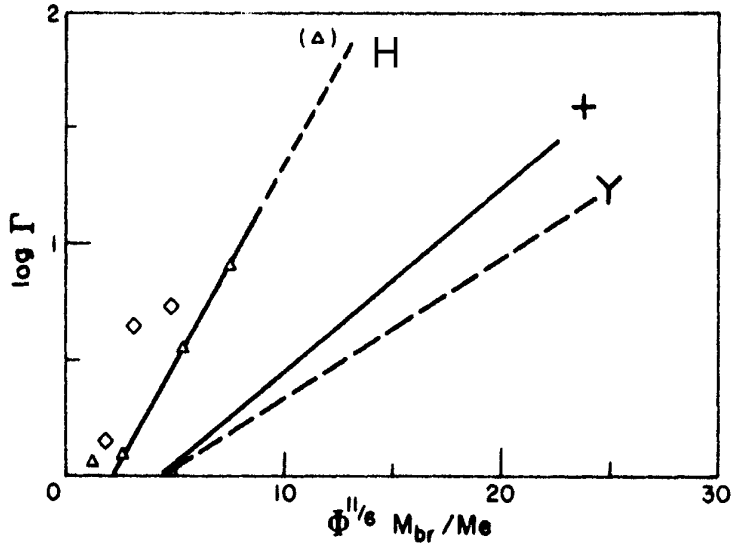

Figure 2.18: Zero-shear viscosity enhancement versus the number of entanglements per branch for H-shaped, 4-arm, and 3-arm polystyrene samples [Roovers]

and polyisoprene samples. Jordan *et al.* (1989) and Gell *et al.* (1997) examined the critical branch length for entanglement coupling. Jordan and coworkers investigated the diffusion nature of asymmetric three-arm polybutadiene stars and found that branch lengths exceeding twice the molecular weight between entanglements, $2M_e$, were considered *long-chain branches*. Gell and coworkers studied a similar series of asymmetric three-arm stars of poly(ethylene-alt-propylene) and found that branch lengths exceeding $2.4M_e$ led to separate relaxation modes for the branches and backbone. Furthermore, they found that the relaxation spectrum rapidly broadens with branch length.

Although work with model branched polymers has greatly enhanced our understanding of the effects of long-chain branching on rheology, the structures of these materials are quite different from those of industrial materials. Studies on the melt flow properties of commercial polymer systems have proven to be of considerable practical value in predicting processability. Wild *et al.* (1976) analyzed the melt flow behavior of fractionated and unfractionated low-density polyethylenes. They found that high degrees of long-chain branching caused a

significant reduction in η_0, while sparse degrees of branching led to a noticeable enhancement of η_0 for a given molecular weight. Studies by Graessley (1977) and Mendelson *et al.* (1970) have shown similar results, all of which compare well with work performed on model systems.

Bersted *et al.* (1981) studied the effect of long-chain branching on the shear-rate dependence of polyethylene resins. They found that the viscosity flow curve of polyethylenes could be accurately described by treating the material as a blend of branched and linear material. Using the ideas of reduced radius of gyration from branching and a logarithmic rule of mixtures, the authors were able to predict the viscosity curve of HDPE/LDPE blends and sparsely branched HDPE resins. At high degrees of LCB, the zero-shear viscosity is reduced for an equivalent molecular weight (M_w), and the shear sensitivity is greatly increased over that of the linear material. At low degrees of LCB, the zero-shear viscosity is increased above that of the linear analog while maintaining much of the shear sensitivity. Hingmann and Marczinke (1994) have witnessed similar results for peroxide-induced branched polypropylene resins.

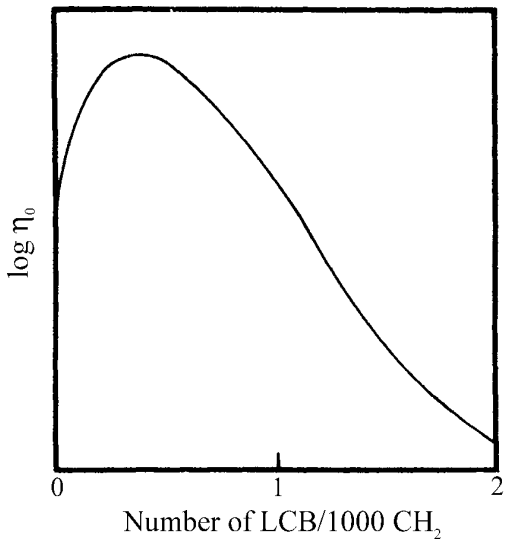

Figure 2.19: Zero-shear viscosity vs. branch content in sparsely branched polyethylene samples of similar M_w [adapted from Bersted et al. (1981)]

Additionally, Bersted and coworkers found that their treatment predicts a maximum in the η_0-LCB relationship, which agrees well with the results obtained by Wild *et al*. (1976).

Long-chain branched polymers often exhibit higher activation energies of flow, E_a, than linear polymers with the same chemical structure. In polyethylene resins, particularly, one often sees an increase in E_a from around 6.5 kcal/mol K for linear HDPE to approximately 14 kcal/mol K for highly branched LDPE [Dealy and Wissbrun (1990), Laun (1987)]. Bersted (1985) measured the activation energy of an HDPE resin before and following peroxide-induced decomposition. He found that the activation energy increased from 5.5 kcal/mol for linear HDPE to about 7.4 kcal/mol for the branched PE polymer containing 0.52 LCB/10^4 CH_2 (NMR). More recently, Kim et al (1996) studied the temperature sensitivity of various metallocene-catalyzed ethylene-α-olefin copolymers and also found that the presence of branching, even at low concentrations, caused a marked increase in the activation energy.

One of the most difficult tasks associated with branched polymers has been the ability to accurately quantify the degree of long-chain branching. This is certainly true for commercial polymer systems where random branching occurs. Conventional methods of characterization, such as dilute solution measurements or NMR, are often limited when the long-chain branch content is very small (< 0.3 LCB/10^3 CH_2) or when short-chain branching (SCB) is also present [Schroff and Mavridis (1999)]. As a result, more consideration is being given to rheological characterization as a sensitive indicator of LCB content. Schreiber and Bagley (1962) first attempted to quantify LCB content according to the exponential dependence of the η_0-M_w relationship. Unfortunately, their proposed method was limited in that it could not determine absolute branching values, but rather relative values for a given series of materials. Later studies have focused on the varying relationships between zero-shear viscosity, intrinsic viscosity,

characteristic relaxation time, and activation energy as a source of differentiating branched samples [Locati and Gargani (1976), Lai *et al.* (1994), Vega *et al.* (1998), Schroff and Mavridis (1999), Wood-Adams and Dealy (2000)].

More recently, Janzen and Colby (1999) have proposed a method for determining long-chain branch content from η_0-M_w data. Their technique employs a phenomenological description developed by Lusignan and coworkers (1996,1999) for determining the number of branch points, or vertices, in randomly branched polymer systems. The phenomenological description proposed for capturing the molecular weight dependence of the zero-shear viscosity in the presence of branching is

$$\eta_0 = AM_b\left[1+\left(\frac{M_b}{M_c}\right)^{2.4}\right]\left(\frac{M_w}{M_b}\right)^{s/\gamma} \qquad (2.22)$$

where A is a numerical prefactor having units of (Pa s mol)/g and is specific to a given polymer at a given temperature, M_b is the molecular weight between branch points, M_c is the critical

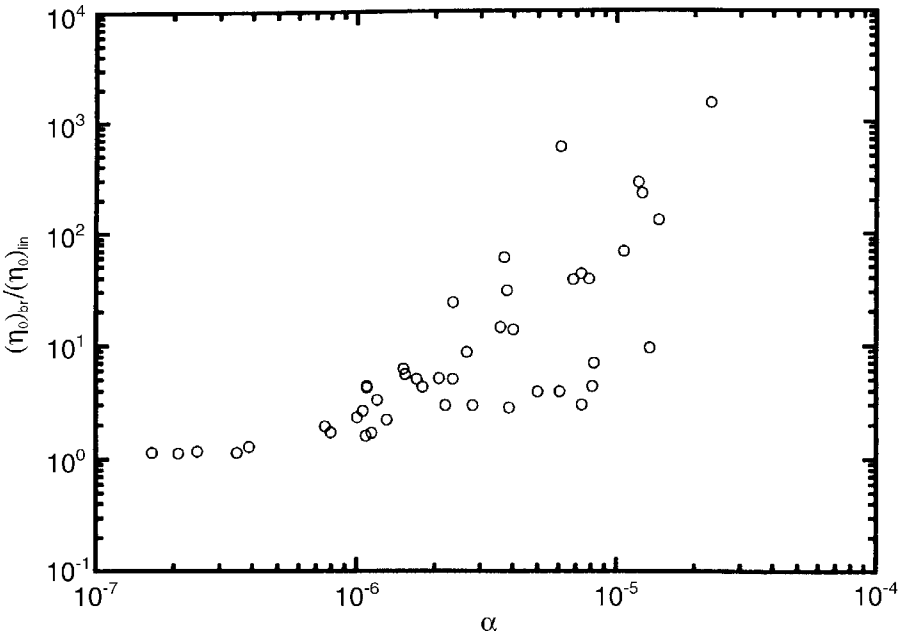

Figure 2.20: Zero-shear viscosity enhancement vs. the fraction of branch vertices, α [adapted from Janzen and Colby (1999)]

molecular weight for entanglements, M_w is the weight-average molecular weight, and s/γ is the exponent given by

$$s/\gamma = \max\left[1, \frac{3}{2} + \left(\frac{9}{8}\right) B \ln\left(\frac{M_b}{90 M_{Kuhn}}\right)\right] \qquad (2.23)$$

where B (~ 6.0 for PE) is a material specific constant, and M_{Kuhn} (~ 146 g/mol for PE) is the molecular weight of a statistical Kuhn segment. Janzen and Colby found that the zero-shear viscosity enhancement exhibited by peroxide-induced, long-chain branched polyethylenes is primarily a function of the molecular weight between branch points or branch vertexes, M_b. The authors claim that their method can distinguish as few as one long-chain branch per million (10^6) carbons atoms, levels simply too low for conventional characterization techniques to detect.

Extensional Rheology

One of the most striking effects of LCB on the melt rheology of polyethylenes can be seen during extensional deformations. The presence of LCB has a pronounced effect on the stress growth behavior and rate dependence of extensional viscosity. During the past forty years, the extensional-thickening nature of long-chain branched polymer systems has been a subject of intensive research. Despite the inherent difficulties associated with measuring extensional properties [Dealy and Wissbrun (1990)], the extensional-thickening, and/or strain-hardening, behavior can have significant processing implications during free surface deformations (i.e. film blowing, fiber spinning, etc.).

Meissner (1972) was one of the first researchers to compare the shear and extensional behavior of long-chain branched polyethylenes. Figure 2.20 shows the data collected for an LDPE sample with a melt index of 1.4 and density of 0.918 g/cm^3. One can see that the

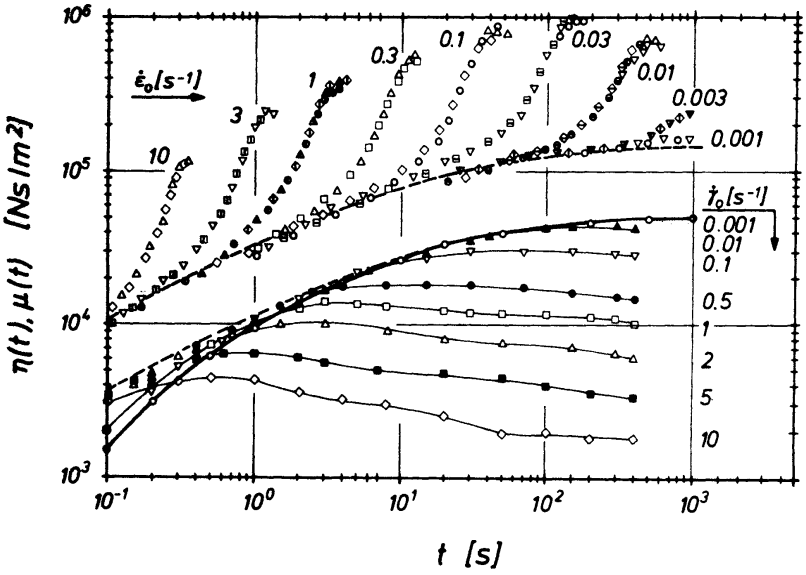

Figure 2.21: Strain-hardening effect in long-chain branched LDPE resins [Meissner (1984)]

maximum shear viscosity is attained at the lowest shear rate, and that further increases in shear rate lead to a reduction of both transient and steady state shear viscosities. The extensional viscosities, on the other hand, exhibit the opposite trend. The minimum steady-state extensional viscosity is attained at the lowest extension rate, and further increases in rate lead to pronounced strain-hardening behavior. It is interesting to note that the linear viscoelastic limit of $3\eta_0$ is well obeyed at lowest shear and extension rates.

Laun and Munstedt (1976, 1978, 1981) performed a series of constant tensile stress and constant extension rate tests on both low- and high-density polyethylene resins. They found that the presence of long-chain branching and a broad molecular weight distribution leads to significant strain-hardening behavior in LDPE resins. Furthermore, the authors found that the greater the degree of branching (and broader the MWD), the greater the rise in steady-state extensional viscosity above the Trouton ratio of $3\eta_0$. In Figure 2.21, the steady-state extensional viscosities of two LDPE and one HDPE resins as a function of tensile stress (or extension rate) are compared. Despite the three PE resins having similar Trouton viscosities (~ 10^5 Pa s), the

LDPE 6 resin, having the greatest degree of branching (30 CH_3/ 10^3 CH_2), shows pronounced rate hardening over the less-branched LDPE 9 (15 CH_3/ 10^3 CH_2) and HDPE 3 (0 CH_3 / 10^3 CH_2) resins. Although the authors concluded that molecular weight distribution might have a significant effect on the extensional behavior of PE resins, Laun and Schuch (1989) later found that broad MWD polystyrene fractions did not show significant strain- or rate-hardening behavior and that LCB must the primary source of nonlinearity.

Recent studies by Bin Wadud and Baird (2000) on metallocene-catalyzed linear low-density polyethylenes (mLLDPE) and Hingmann and Marczinke (1994) and Kurzbeck *et al.* (1997) on branched polypropylene resins have convincingly proven the substantial role of LCB on polymer melt extensional properties. Bin Wadud and Baird investigated a set of mLLDPE resins with similar MWD and varying degrees of long-chain branching. They found that in addition to zero-shear viscosity enhancement (see above), the presence of sparse branching led to

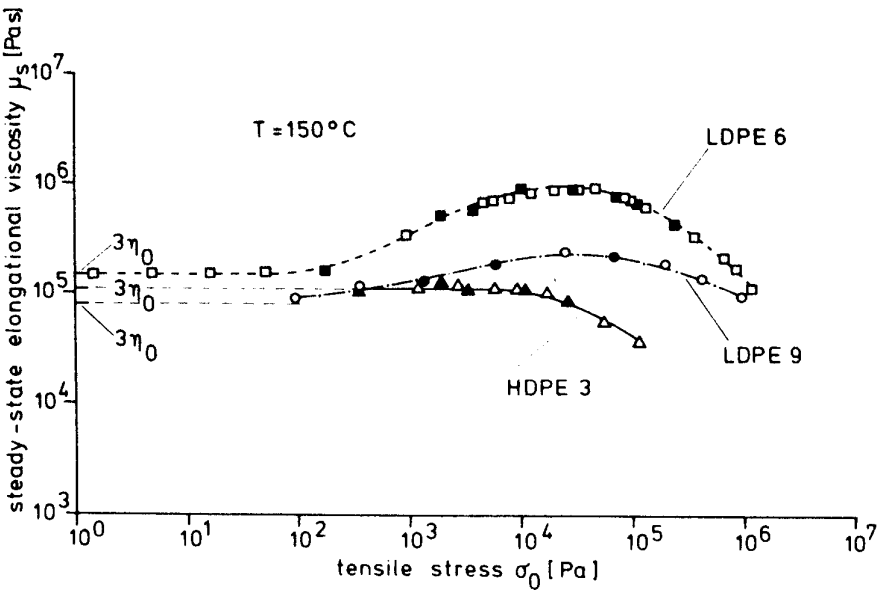

Figure 2.22: Steady-state elongational viscosities of linear and branched PE resins [adapted from Laun and Munstedt (1980)]

noticeable strain-hardening behavior during uniaxial extensional deformation, and which was consistent with LCB content determined from dilute solution measurements. On the other hand, Hingmann and Marczinke performed shear and extensional testing on linear and branched polypropylene resins with similar molecular weight distributions. They found that linear polypropylene shows both shear- and extensional-thinning with increasing deformation rate, while branched polypropylenes exhibit significant extensional-thickening behavior. Kurzbeck and coworkers also investigated the extensional stress growth of commercial linear and branched polypropylenes. The authors observed similar findings (Figure 2.22), with substantial strain and rate hardening of branched polypropylenes and little or no strain hardening in the linear PP resin.

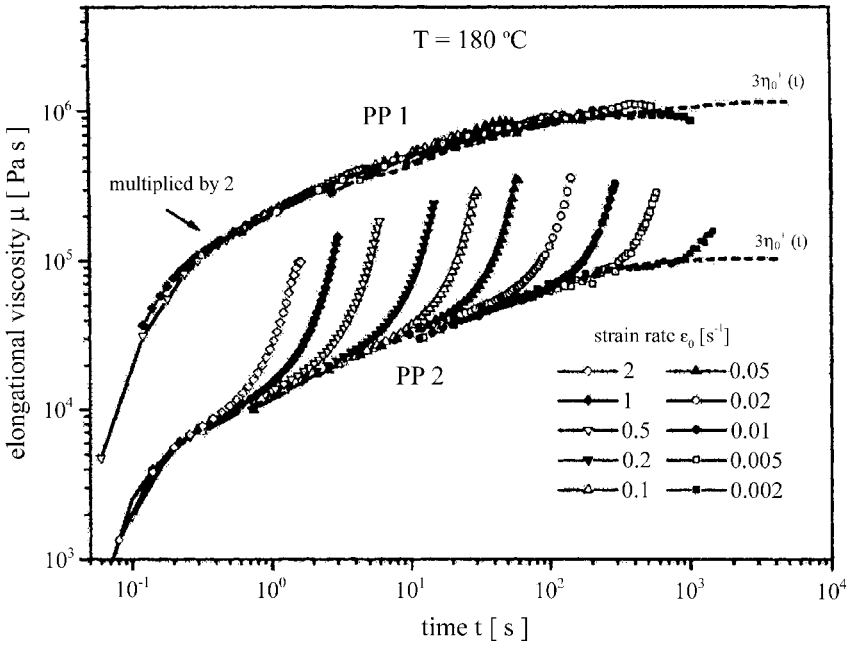

Figure 2.23: Extensional viscosities of linear and branched PP resins [Kurzbeck, *et al*. (1997)]

2.3 Melt Fracture Phenomena

Melt fracture (MF) is a very important phenomenon that is known to affect the quality and rate of production of many polymer products. The term *melt fracture* [Tordella (1956)] is loosely applied to describe any type of extrudate distortion that results in a variation in shape along the length of the extrudate. Melt fracture is generally classified into three major types: surface melt fracture, slip-stick or spurt fracture, and gross melt fracture. Surface melt fracture, also known as *matte* or *sharkskin*, is characterized by fine scale surface irregularities, with variations of less than 10% of the mean extrudate diameter. Surface melt fracture is normally observed during steady flow conditions and is generally viewed as an aesthetic nuisance. Slip-stick fracture is described by oscillating pressure gradients and extrusion rates during constant velocity and constant pressure conditions, respectively. Slip-stick fracture is often associated with the unusual discontinuity in shear stress – shear rate flow curves at high flow rates. Gross melt fracture, also known as *wavy* fracture, is characterized by severe distortions, typically on the on order of the mean extrudate diameter itself. Gross fracture often leads to excessive deformity, and can adversely affect the extrudate mechanical properties.

The first official observation of the melt fracture phenomenon was reported by Nason (1945), who found that extruded polystyrene became wavy at high flow rates. Subsequent studies [Spencer and Dillon (1948,1949)] further showed that the observed instability occurred at a constant wall shear stress of 10^5 Pa, a value that has become synonymous with melt fracture. In the 55 years that have followed those initial observations, a significant amount of research has been performed on many different polymer systems in an attempt to better understand the observed phenomena. A comprehensive review of the early experimental work was first

provided by Tordella (1969), while more recent reviews by Petrie and Denn (1976) and Larson (1992) include the majority of the contemporary research.

The intent of the current section is not to duplicate existing reviews of melt fracture phenomena, but rather to focus on the melt fracture behavior of polyethylene and similar systems. The current section will begin with a review of the relevant experimental observations. Specifically, the melt fracture behavior of low-density PE (LDPE), high-density PE (HDPE), linear low-density PE (LLDPE), and metallocene-catalyzed PE (MCPE) will be discussed. A brief summary of some of the proposed mechanisms of melt fracture will follow. Finally, the specific effects of molecular structure on melt fracture behavior will be reviewed.

2.3.1. Experimental Observations

LDPE

Low-density polyethylene, unlike its linear homologs, does not exhibit all three types of melt fracture. Rather, LDPE is generally observed to transition from a smooth extrudate directly to a grossly deformed one above an apparent critical wall shear stress, τ_c. This critical shear stress is of the order of 10^5 Pa, but the exact value may be mildly influenced by die geometry, polymer molecular weight, or extrusion temperature [Tordella (1969)]. Figure 2.24 depicts the typical melt fracture behavior of LDPE at a melt temperature of 150 °C. One can see that prior to the onset of gross melt fracture the first two polymer specimens are of uniform diameter. Following the onset of fracture, the degree of fracture increases with flow rate (specimens 3-8) as denoted by the apparent *waviness* of the extrudate.

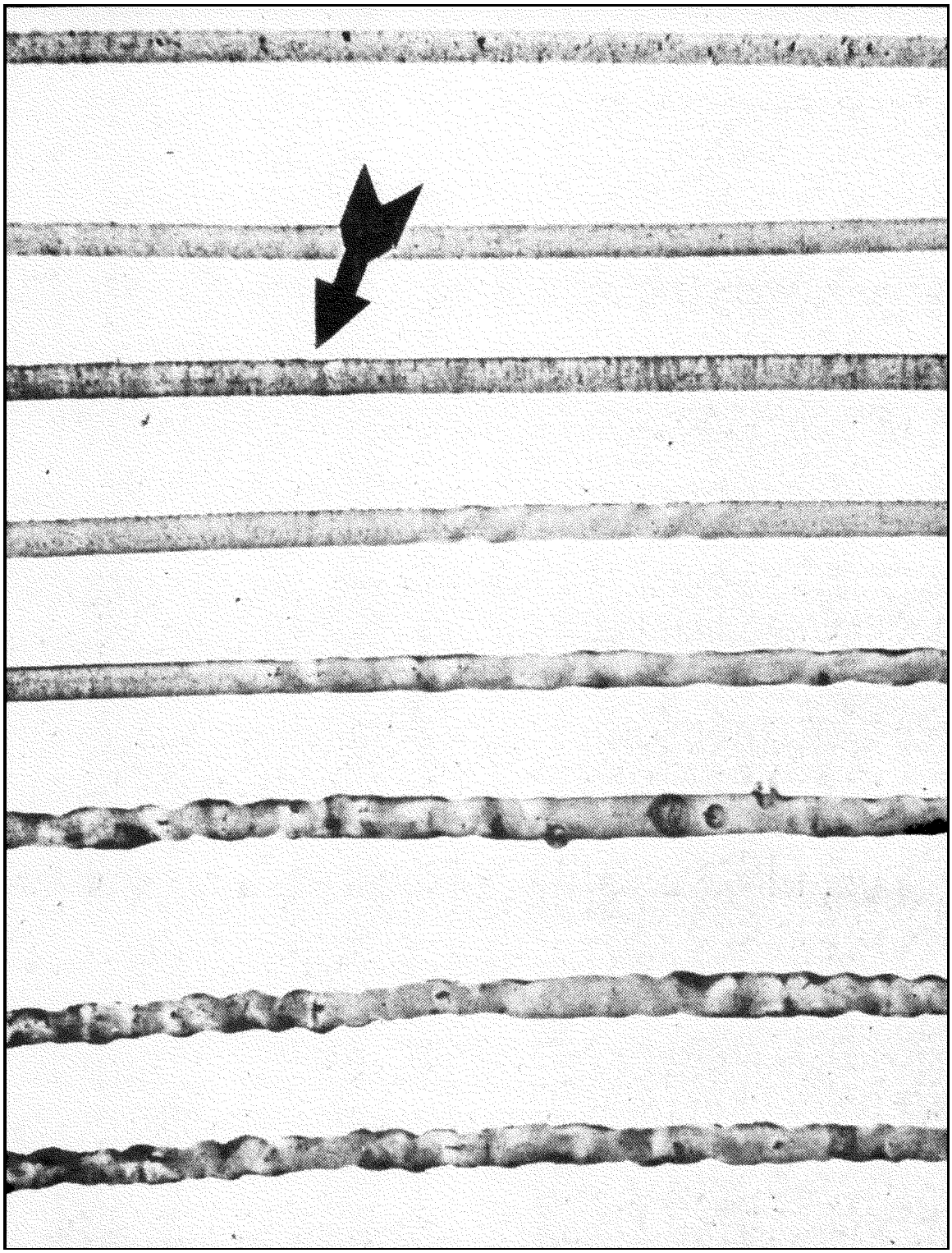

Figure 2.24: Melt fracture behavior of LDPE [adapted from Tordella (1957)]

Prior to the onset of gross melt fracture in LDPE, vortices are observed to form in the entry region of the die, creating what is affectionately known as the "wine glass stem" entry pattern. Flow visualization studies [Bagley and Birks (1960), den Otter (1970), Ballenger and White (1971)] have shown that linear polymers fill the available space preceding the flow contraction, while branched polymers exhibit a large dead space filled by these recirculating vortices. This concept is shown schematically in Figure 2.25. The mere presence of recirculating vortices is indicative of viscoelastic materials that exhibit extensional strain-hardening behavior [White and Baird (1986)]. The noticeable "tapering" of the flow field into the die entrance serves to reduce the extensional strain rate felt by the polymer melt and therefore mitigates the effects of strain-hardening behavior. As we have seen in previous sections of this literature review, LDPE exhibits a substantial degree of strain hardening due the presence and high degree of long-chain branching.

At the onset of gross melt fracture, the symmetry of the entry flow is lost and periodic surging of melt material from the recirculating regions into the primary flow region occurs. Flow visualization studies [Tordella (1957,1963)] have demonstrated that trapped material

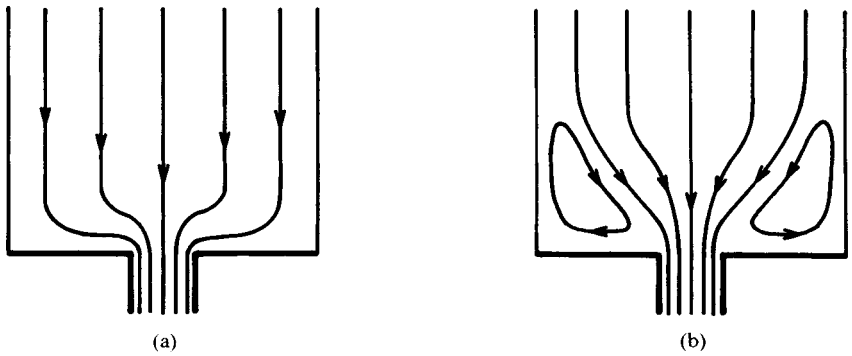

Figure 2.25: Entry flow patterns of (a) linear and (b) branched polyethylenes [Dealy and Wissburn (1990)]

within the vortices intermittently surge into the main flow, thereby causing unbalanced flow ahead of the die entrance. Flow birefringence experiments [Tordella (1969)] have further shown that the unsteady flow ahead of the die entrance is preceded by asymmetry of the stress field in the entry region. The onset of asymmetry typically occurs at a constant wall shear stress of 10^5 Pa, regardless of die geometry or even indication of melt fracture. Interestingly, although local surging was observed near the die entrance, no surging was detected in the land of the die.

Studies of the effect of die geometry on the gross melt fracture of LDPE have shown that the severity of fracture is most influenced, while the actual onset of fracture remains unaffected. Tordella (1969) found that the degree of distortion of the emerging stream at and above the critical shear stress decreases with increasing capillary length. He attributed this behavior to the stress relaxation in the polymer as it passes through the die land. Therefore, the longer the die land, the greater the degree of relaxation, and consequently less severe melt fracture. Several researchers [Bagley (1957), Bagley and Schreiber (1961)] found that the use of conically tapered or "streamlined" inlet geometries also reduced the severity of fracture. Contoured inlets reduce the rate of acceleration of the melt near the die entrance and effectively mimic the natural "tappering" of the melt stream seen in abrupt contraction geometries. The resulting loss, or at least reduction, of recirculating vortices leads to a greater degree of flow symmetry at higher shear rates. It should be reiterated that neither increasing the die length nor streamlining the inlet appreciably affects the onset of melt fracture, but rather delays the onset of *detectability* to higher shear rates.

HDPE

The melt fracture behavior of high-density polyethylene (HDPE) differs considerably from that of LDPE. As mentioned earlier, HDPE exhibits all three modes of fracture, namely surface, slip-stick, and gross melt fracture behavior. This apparent difference in fracture behavior is often attributed to the lack of long-chain branching in linear HDPE resins. The presence of surface and slip-stick melt fracture introduces a new mechanism of fracture, which expands the scope of instability beyond the die entry. One of the major qualitative differences between HDPE and LDPE is the characteristic discontinuity in the flow curve of HDPE. Figure 2.26 depicts the typical flow curve of HDPE and demonstrates this concept. This discontinuity, first noted by Bagley, Cabott and West (1958), leads to the observed flow oscillations that are often associated with slip-stick melt fracture. Surprisingly, despite the inherent differences in molecular architecture and observed differences in fast flow behavior, the onset of melt fracture remains essentially constant at a critical wall shear stress of approximately $1x10^5$ Pa.

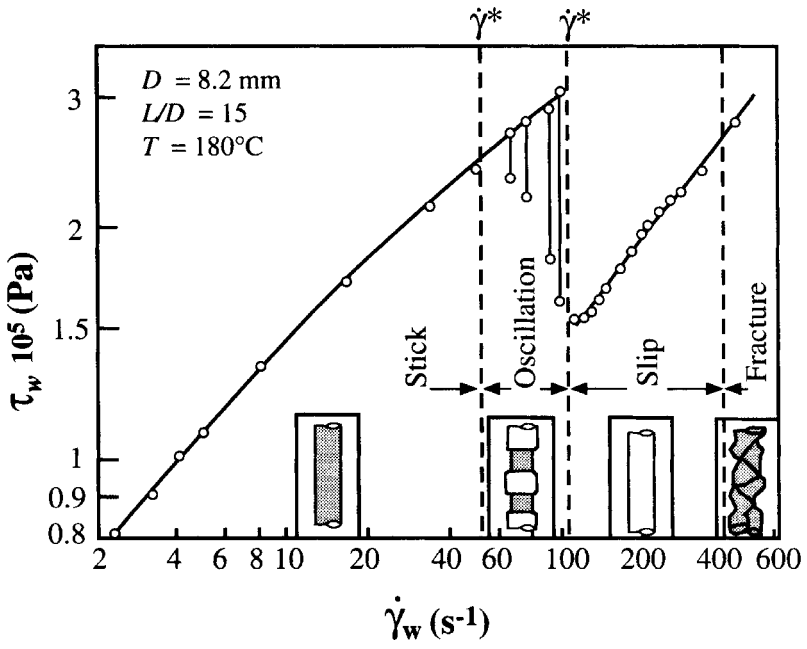

Figure 2.26: Melt fracture behavior of HDPE [adapted from Uhland (1979)]

The onset of melt fracture in HDPE occurs with the presence of fine-scale, high frequency distortions known as surface melt fracture (SMF). This differs from the wavy distortions seen in LDPE resins. SMF is usually observed at a wall shear stress of 10^5 Pa and flow remains otherwise steady with a constant pressure drop across the die. The most significant difference between SMF and gross fracture is the site of instability. Whereas gross fracture is associated with the die entrance region, SMF is generally associated with die exit region [Petrie and Denn (1976)]. Benbow and Lamb (1963) convincingly demonstrated this idea in their experiments with a Wood's metal die. They were able to show that sharkskin is initiated at the die exit, and that flow within die land remains steady. Later studies by Vinogradov *et al.* (1972) confirmed this notion by showing that SMF was accompanied by high local stresses at the point where the melt parts from the die. Interestingly, despite the presence of extrudate distortion, SMF of HDPE has been largely ignored because of the minor impact on product properties during blow molding and injection molding operations.

The most significant difference between the melt fracture behaviors of LDPE and HDPE resins is the apparent discontinuity in the flow curve of HDPE during slip-stick fracture. As we have seen in Figure 2.26, Uhland (1979) noted flow oscillations in HDPE at a wall shear stress of approximately 2.2 x 10^5 Pa and an apparent shear rate of 50 s^{-1}. These oscillations continued up to a shear rate of approximately 110 s^{-1} and were accompanied by a 50% decrease in wall shear stress. Tordella (1969) analyzed the same phenomena under controlled stress conditions and developed the generalized flow curve plotted in Figure 2.27. Tordella found that at shear stresses below point A, flow is steady and without distortions. Between points A and B, flow remains steady but the presence of SMF is observed. At the discontinuity in the flow curve, the shear rate (flow rate) becomes double valued and slip-stick fracture is observed. The value of

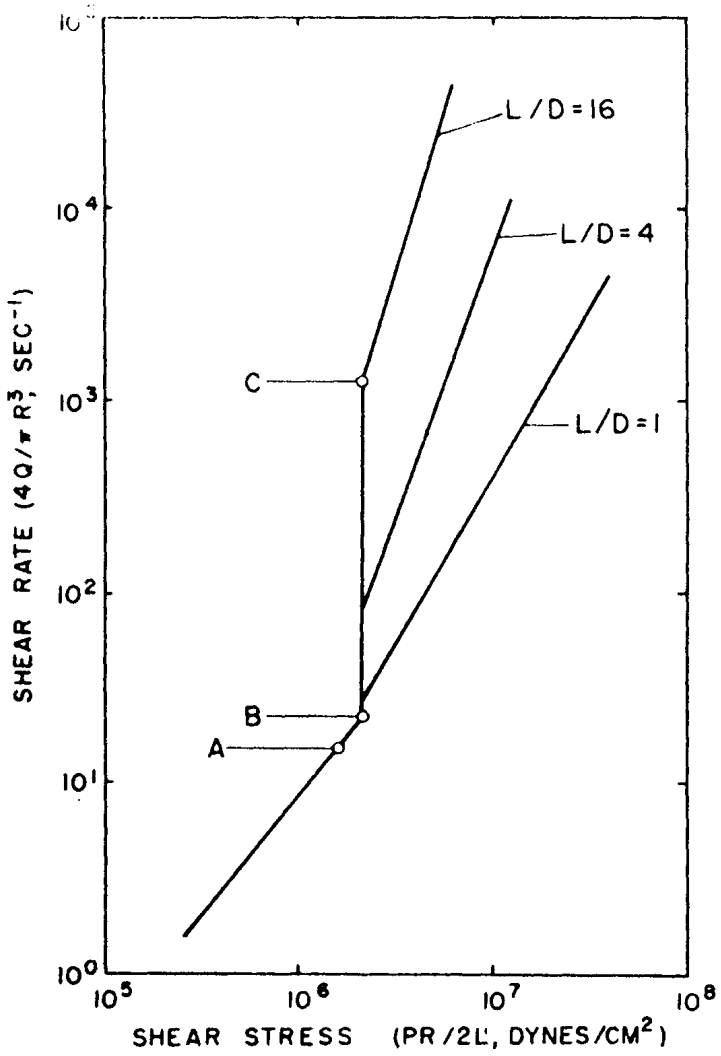

Figure 2.27: Flow curve discontinuity during slip-stick fracture [Tordella(1957)]

the higher rate becomes larger with increasing L/D (or L/R) of the capillary die. This observation indicates that increasing the die length will exacerbate the instability, unlike that observed in LDPE. Ballenger *et al.* (1971) observed similar results.

During slip-stick fracture, the extrudate obtains a "bamboo-like" appearance. As the flow rate oscillates between points B and C, the specimen's surfaces change accordingly, from rough ("sticking" on lower curve) to smooth ("slipping" on upper curve). The rough portion of the extrudate is associated with SMF, while the smooth portion is associated with slippage of the

melt as it passes through the die. The role of slip will become move obvious later in this section. The frequency of the observed oscillations increases as the volume of melt in the reservoir decreases [Hatzikiriakos and Dealy (1992)]. This dependency arises from the slight compressibility of the melt in the upstream reservoir [Lupton and Register (1965)]. Therefore, as suggested, melt compressibility is a prerequisite for unstable flow during slip-stick fracture.

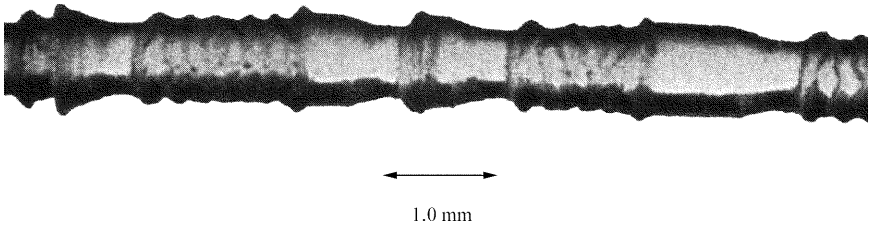

Figure 2.28: Slip-stick fracture extrudate [adapted from Kalika and Denn (1987)]

Following slip-stick fracture, the flow curve in Figure 2.26 follows a monotonic increase in shear stress with shear rate. The extrudate becomes smooth again between shear rates of 100 and 400 s^{-1} and at higher rates transitions to a gross melt fracture form. The smooth extrudate appears so locally, however a larger scale, regular, helical shape is usually present. At higher rates, the extrudate becomes grossly deformed and often exhibits sharp-edged helical or chaotic forms. Although HDPE resins do not exhibit pronounced recirculating vortices in abrupt contraction dies [Ballenger *et al.* (1971)], the inlet region may become more important at the higher flow rates.

LLDPE

The study of the melt fracture behavior of linear low-density polyethylene (LLDPE) has been an important, and controversial, research topic since the late 1980's. LLDPE is very similar to HDPE in melt fracture behavior [Kalika and Denn (1987)], however most of the emphasis in literature has been placed on the surface melt fracture (SMF) behavior. This is not surprising since the main application of LLDPE resins are in blown film markets, where optical clarity is vital. Therefore, this review will focus on the SMF behavior of LLDPE and the influential variables governing its manifestation.

As the reader has already learned, surface melt fracture or sharkskin is the first form of extrudate distortion encountered with increasing shear rate. Surface melt fracture in LLDPE occurs under steady flow conditions and ranges in details from loss of specular gloss to a more severe form known as sharkskin. The only rheological indication of SMF is a slight change in slope of the nominal shear rate versus shear stress flow curve, beginning at the onset of sharkskin [Kurtz (1984)]. This concept is illustrated in Figure 2.29. From the data depicted, the power law index n changes from a value of 0.56 in the stable flow region to an apparent value of 0.43 during SMF. The remainder of the flow curve is very similar to that of HDPE. As mentioned earlier, the locus of failure is believed to be the die exit region.

Many studies over the years have greatly enhanced the knowledge base concerning the SMF of LLDPE resins. One of the most extensive and publicized studies was that performed by Ramamurthy (1986). In his study, the influence of extrusion temperature, die geometry, and material of die construction were investigated. The results of the capillary studies showed that, of the parameters studied, only the material of construction had any significant impact on the SMF behavior of LLDPE. The most interesting result of Ramamurthy's study was the presence

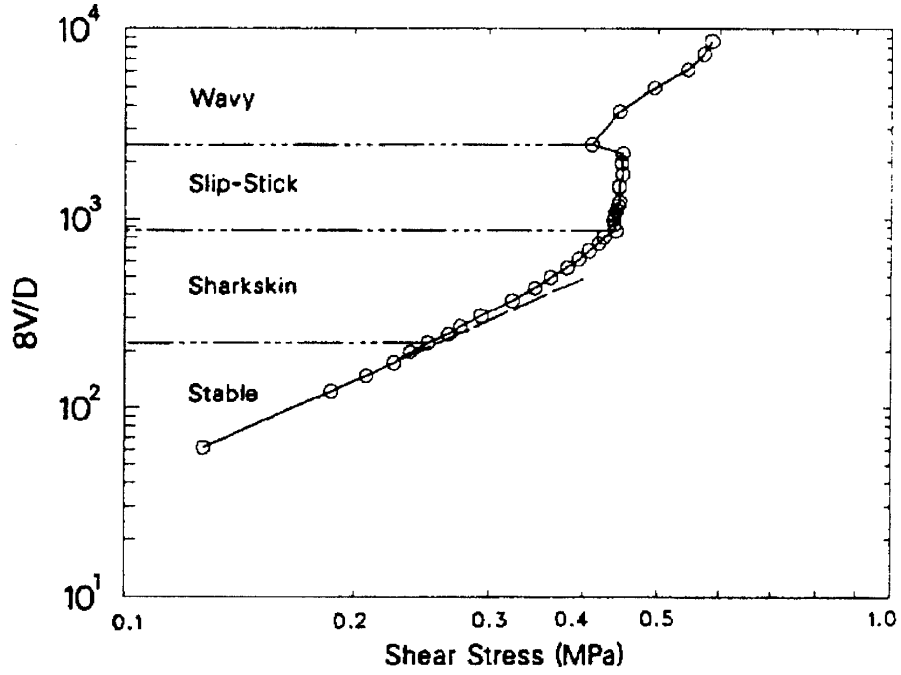

Figure 2.29: LLDPE flow curve [Kalika and Denn (1987)]

of a non-zero wall slip velocity at a wall shear stress of 0.1 MPa (10^5 Pa) and greater. Following the method Lupton and Regester (1965), Ramamurthy used a Mooney analysis to estimate the apparent wall slip velocities. This observation was coincident with the presence of SMF. Later work by Kalika and Denn (1987) also confirmed the presence of wall slip during SMF.

Later studies by Piau *et al.* (1990) and Moynihan *et al.* (1990) found that die geometry can affect the onset and severity of SMF. Piau *et al.* found that the shape of the outlet region of the die can increase the onset of SMF to high wall shear stresses. Round-edged die exits increased the critical wall shear stress over sharp-edged die exits and generally decreased the severity of fracture. The authors concluded that round-edged die exits decrease the degree SMF exhibited by LLDPE resins by reducing the degree of acceleration and stretching seen by the melt as it exits the die. Moynihan *et al.* (1990) found that the critical wall shear stress for sharkskin was dependent upon the L/D ratio in short capillary dies. They concluded that the die

inlet region influences the SMF behavior through pre-stressing, and that increasing the length of the die reduces the severity of fracture.

Moynihan *et al*. (1990) also showed that the presence of a fluoro-elastomer (FE) coating in the exit region of the die eliminates surface melt fracture behavior and "unequivocally" isolates the exit region as the source of SMF. Visual observations and flow birefringence experiments demonstrate that the presence of slip at the melt/die interface functions to eradicate fracture. Figure 2.30 demonstrates the dramatic effect of FE on the melt fracture behavior of extruded LLDPE. Similar studies [Hatzikirikos and Dealy (1993), Varennes and Schreiber (1994), Wang *et al.* (1997)] using polymer processing additives (PPA) and/or other low energy surfaces have shown commensurate results in LLDPE resins.

MCPE

The relatively recent introduction of metallocene-catalyzed polyethylenes (MCPE) prevents an extensive literature review on the subject of melt fracture behavior. Most of the available literature on MCPE resins revolves around the rheological characterization of those resins. However, based on their molecular architecture (Section 2.1.4), one might expect the melt fracture behavior to vary between that of LDPE (highly branched) and LLDPE or HDPE (linear), depending the degree of long-chain branching present. Interestingly, the MF behavior of commercial MCPE resins is ultimately more similar to linear PE than branched PE resins.

Initial studies by Vega *et al*. (1996) reported that linear metallocene-catalyzed HDPE resins exhibited both surface and slip-stick melt fracture, as expected. They found that the onset of SMF occurred at a wall shear stress of 0.18 MPa, and the onset of slip-stick fracture occurred at wall shear stress of 0.25 MPa. Vega *et al.* also found that above the slip-stick transition the

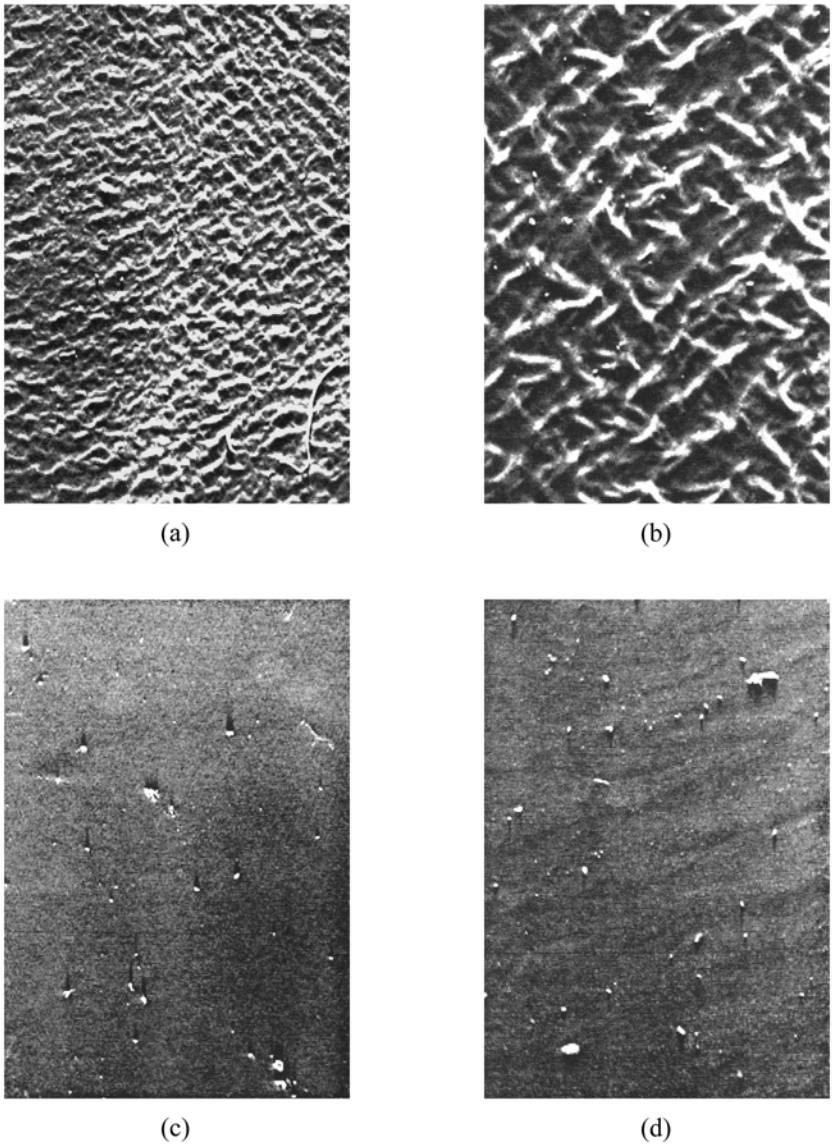

Figure 2.30: Effect of FE coating on extrudate distortion: uncoated (a) $\dot{\gamma}_a = 42\ s^{-1}$, (b) $\dot{\gamma}_a = 52\ s^{-1}$, and coated (c) $\dot{\gamma}_a = 44\ s^{-1}$, (d) $\dot{\gamma}_a = 55\ s^{-1}$ [Moynihan, *et al.* (1990)]

flow curves at different temperatures collapse upon one another, thereby giving an apparent activation energy E_a of zero. They attributed this behavior to plug-like flow in the capillary. The presence of a gross melt fracture regime at higher shear rates was not addressed.

Later work by Hatzikirakos and coworkers (1997) reported the rheological and melt fracture behavior of linear and sparsely branched metallocene LLDPE resins. Their results showed many idiosyncrasies not previously observed in conventional linear polyethylenes. The

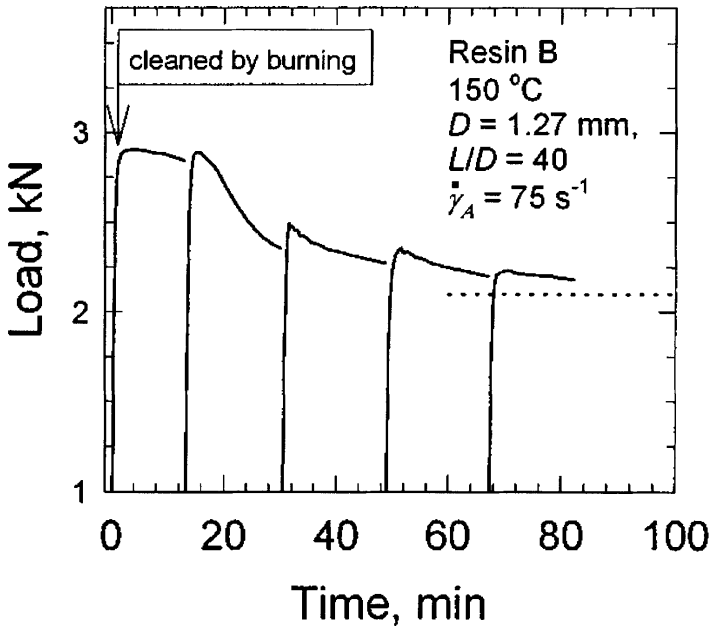

Figure 2.31: Effect of melt/die interaction on the pressure response during capillary extrusion [Hatzikirikos, et al. (1997)]

most obvious anomaly was the presence of a very long induction time prior to steady-state flow. Figure 2.31 illustrates this transient behavior. The authors found that the SMF existed over a very narrow range of flow rates and that slip-stick fracture was only present in the linear mLLDPE resin. The authors concluded that the anomalous extrusion behavior of the mLLDPE resins might be due to physico-chemical changes in the die surface leading to slip and the atypical melt fracture behavior observed.

More recently, Perez-Gonzalez *et al*. (2000) studied the die geometry and temperature dependence of MF on a commercial linear MCPE resin. Their studies focused on the slip-stick fracture behavior, and did not report any information on SMF or gross fracture. They found that the critical shear stress for the onset of unstable "spurt" flow decreased with die length and varied nonlinearly with extrusion temperature. They also reported that the amplitude of

oscillation increased with capillary length, similar to that of conventional LLDPE and HDPE. The authors concluded that the nonlinear, nonmonotonic temperature dependence might have been influenced by flow-induced crystallization near the melting temperature of resin.

2.3.2. Proposed Mechanisms of Fracture

Gross Melt Fracture

The onset of gross melt fracture in linear and branched polyethylenes has typically been associated with a critical value of the recoverable shear strain, S_R. The recoverable shear strain is defined as the ratio of the wall shear stress to the characteristic elastic shear modulus of the polymer melt, $S_R = \tau_w/G$. The reported values for S_R generally lie between values of 1 and 10, with the majority being between 5 and 8 [Petrie and Denn (1976)]. If one assumes that the elastic shear modulus can be approximated by η_0/λ, then $S_R \approx \dot{\gamma}\lambda$, which is roughly equal to the Weissenberg number, We. This relationship implies that gross melt fracture only occurs when the elastic nature of polyethylene melts becomes significant, and is therefore an elastic phenomenon.

Tordella (1957) first suggested that the onset of gross melt fracture would occur at the critical S_R and would lead to rupture or "fracture" of the polymer melt. This mechanism would occur through shear rupture, rather than tensile rupture, and would therefore not exhibit void formation. Tordella added that the high stress concentration near the die wall could then cause the rupture to propagate into macroscopic flow disturbances. In a contradictory viewpoint, Everage and Ballman (1974) argued that the correlation of the onset of melt fracture with measurments in shearing flows is inconsistent with experimental observations. They suggested that the recoverable extensional strain, ε_R, would be a more appropriate indicator due the

extensional deformations associated with converging flows near the die inlet. Their proposed theory of gross melt fracture cited tensile rupture of the melt, at a critical value of ε_R, as the primary mechanism of fracture. This claim appears to be supported by Vinogradov (1975), in which the tensile rupture of narrow MWD polybutadiene was found to occur at a tensile stress of 10^5 Pa, a stress comparable with the onset of gross melt fracture during extrusion.

In a later work, Tordella (1969) presented a mechanism for gross melt fracture based on a molecular mechanism. This theory models polymer molecules as semi-discrete clusters that are formed under the influence of flow. At high flow rates, these "rolling" clusters are unable to effectively transmit the imposed stresses between clusters and therefore lead to localized failure at a melt-melt interface. The onset of localized failure was deemed to be microscopic shear rupture between fluid layers at or near the die wall, and that fracture occurs in regions of high elastic deformation. Tordella reasoned that the die surface was quite rough and that failure at the melt-die interface was not likely.

Slip-Stick Fracture

Before proceeding with the following subsection, a clarification of the chosen classification of melt fracture phenomena is in order. Historically, slip-stick melt fracture has been grouped with the inlet-type of fracture described previously, and together have been collectively labeled as "gross melt fracture" [Tordella (1969), Petrie and Denn (1976)]. However, the observed melt fracture phenomena exhibited by branched and linear polyethylene resins would imply that two separate mechanisms are occurring. In fact, linear polyethylenes often undergo inlet-type melt fracture following slip-stick fracture. This practice has undoubtedly led to some confusion. Therefore, this author has decided to separate the inlet-type

gross melt fracture from slip-stick fracture in an attempt to address each more accurately and more thoroughly.

One of the simplest explanations for the observed discontinuity in the flow curves of linear polyethylenes has been the presence of an inherent constitutive instability [Huseby (1966), Lin (1985)]. A constitutive instability is believed to occur if the constitutive relationship between shear stress and shear rate is non-monotonic as depicted in Figure 2.32. This behavior will lead to multiple shear rates for a given shear stress, and qualitatively describes the observed flow oscillations during slip-stick fracture. Vinogradov and coworkers (1984) have described this event as a sharp transition from "a fluid to a high-elastic state". Interestingly enough, stability analysis using the Doi-Edwards molecular theory for entangled polymers has shown that a constitutive instability will occur when the recoverable shear strain reaches a value of 2 [McLeish and Ball (1986), Deiber and Schowalter (1991)]. Furthermore, McLeish and Ball (1986) have been able to quantitatively predict features of the slip-stick fracture seen in high molecular weight, monodisperse polybutadiene. Unfortunately, no physical evidence has been provided for linear polyethylenes that would suggest that a constitutive instability is cause of

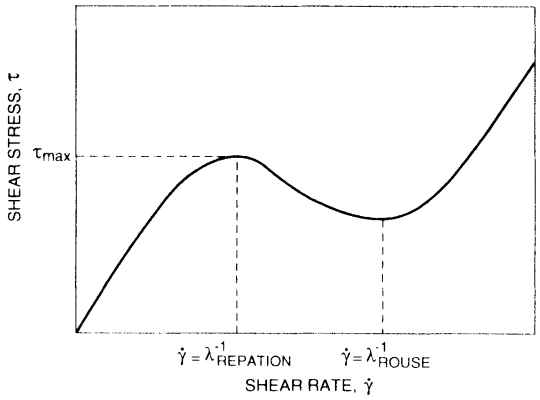

Figure 2.32: Hypothesized relationship between shear stress and shear rate for highly entangled polymeric fluids [Larson (1992)]

slip-stick fracture [Hatzikiriakos and Dealy (1992)].

Another popular mechanism that has been proposed for slip-stick fracture is that of adhesive failure at the melt/die interface. The presence of wall slip prior to and following slip-stick fracture strongly suggests that the adhesion between the die and adsorbed polymer chains may be affected by the imposed shear stress. Lupton and Regester (1965) first reported the presence of wall slip on the lower branch of the flow curve using the Mooney analysis technique. Later studies by Ramamurthy (1986), Kalika and Denn (1987), and Hatzikirikos and Dealy (1992) confirmed these findings. Furthermore, Lupton and Regester also found evidence of slip on the upper branch of the flow curve, with slip velocities more than an order of magnitude higher than those of the lower branch. The proposed mechanism generally involves a buildup of shear stress to a critical value, followed by a large increase in flow rate and decrease in shear stress upon adhesive failure. The resulting extrudate initially exhibits sharkskin SMF and then transitions to a smooth or wavy extrudate during "slipping". The apparent dependence of capillary length on slip-stick behavior appears to support the idea that slip at the wall, and the resulting melt fracture, will depend on the slip area.

More recently, several other theories for explaining the slip-stick fracture behavior of linear PE resins have been suggested. One of the most convincing mechanisms has been advanced by Yang *et al.* (1998). They propose that the sharp stick-slip discontinuity occurs through a chain-chain entanglement/disentanglement process arising from a coil-stretch transition [Wang and Drda (1996)]. The entanglement/disentanglement process occurs at a critical value of the wall shear stress, which leads to localized slip (Figure 2.33). Yang *et al*. have also shown that the presence of a low energy surface could eliminate slip-stick fracture by introducing bulk slip and therefore minimizing the chain-chain entanglement/disentanglement

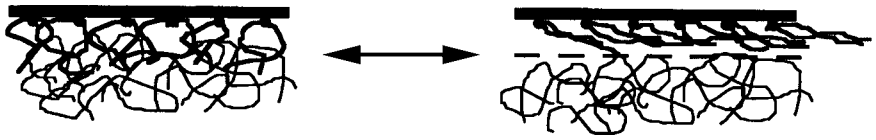

Figure 2.33: Entanglement/Disentanglement Process [Yang et al. (1998)]

process. Alternatively, Hatzikirikos and Dealy (1992) have speculated that slip-stick fracture occurs through bulk cohesive failure between fluid layers near the die wall. The jump to the high-flow branch occurs when cohesive failure occurs, at an upper critical shear stress, while the fall to the low-flow branch occurs when "adhesion" is established at the fracture surface, at a lower critical shear stress.

Surface Melt Fracture

The mechanisms proposed for surface melt fracture are, in many ways, similar to those of slip-stick fracture. One explanation involves a constitutive instability while the other focuses on adhesive failure at the die-melt interface. However, the localization of SMF to the die exit and the apparently steady flow conditions under which it occurs precludes it from the more severe forms of slip-stick melt fracture. Therefore, this review will focus on the short-range mechanisms proposed for SMF in linear polyethylene resins.

One of the first theories put forth to explain SMF was by Howells and Benbow (1962) and later Cogswell (1977). They hypothesized that the polymer literally fractures due to high stresses and high stretching rates which develop at the exit of the die. Visual observations by Bergem (1976) and Piau *et al.* (1988) appeared to support this idea. Kurtz (1984) later proposed a two-step mechanism that expanded upon Cogswell's theory. The first step involved 'pre-stressing' the melt along the wall region of the die land, and the second step required a critical

acceleration of the 'pre-stressed' material as it exited the die. The rapid acceleration of the melt from a near zero velocity at the wall boundary to a finite plug velocity resulted in the brittle fracture of the material on the extrudate surface. Moynihan *et al*. (1990) observed similar results, adding that 'pre-stressing' in the short capillaries could be accomplished in the die entry.

In a contrary view, Ramamurthy (1986) and Kalika and Denn (1987) suggested that SMF is due to the adhesive breakdown of the melt/die interface in the die land. This loss of adhesion would then lead to wall slip and SMF. Figure 2.34 illustrates the nonzero wall slip velocities (nonzero slope) measured by Ramamurthy as a function of wall shear stress. Arguments supporting the presence of slip during SMF are based on the flow curves for LLDPE. As mentioned earlier, it has been suggested that the change in slope prior to the onset of SMF, and well before slip-stick fracture, is a direct result of wall slip. Furthermore, Ramamurthy

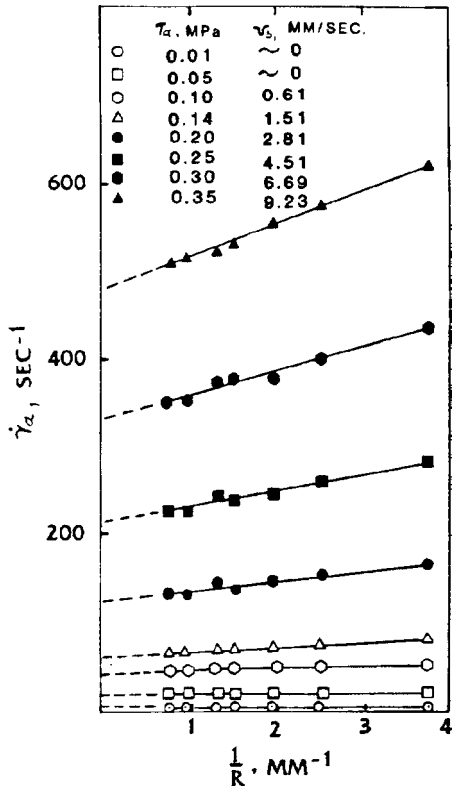

Figure 2.34: Wall slip measurements for LLDPE at 220 °C [Ramamurthy (1986)]

demonstrated that changing the material of die construction could influence the critical shear stress for the onset of SMF, a clear indication of the significance of the die-metal interface. Hill *et al*. (1990) showed that solid-state peel testing of LLDPE below the melting processing temperature could be used to predict the onset of slip and melt fracture.

Finally, two other explanations for SMF have recently been suggested. Flow analysis of inelastic fluids shows that high stresses at the die exit produce negative hydrostatic pressure in a small zone extending a few microns from the die lip. Tremblay (1991) has argued that cavitation should then occur in a manner similar that of crazing. The bubbles then coalesce to form the characteristic surface cracks of sharkskin. Alternatively, Barone *et al.* (1998) suggest an interfacial mechanical instability (IMI) similar to that seen in slip-stick fracture [Yang *et al.* (1996)]. The only exception is that the characteristic entanglement/disentanglement process occurs locally at the die exit. The corresponding oscillation of the exit wall boundary condition leads to cycles of local stress relaxation and growth and to periodic perturbation of the extrudate swell in the form of sharkskin-like SMF.

2.3.3. Molecular Structure Effects

Molecular Weight

We have seen in previous sections that the molecular weight (M_W) of the polymer has a significant and fairly predictable effect on the viscosity behavior. The characteristic power law relationship between M_W and η_0 is well established and is best described by entanglement network theory. Therefore, one would expect that at high flow rates the cooperative nature of entangled polymer melt might affect the melt fracture behavior.

One of the most comprehensive works examining the effect of molecular weight on the melt fracture behavior of polyethylene melts was presented by Blyler and Hart (1970). The authors examined five different linear polyethylenes with M_W ranging between 40,000 to 200,000 g/mol. The results showed that the onset of slip-stick fracture was insensitive to molecular weight, when it occurred, and that the wall slip velocity increased with M_W. Furthermore, the magnitude of the discontinuity at τ_{c2} increased with molecular weight (Figure 2.35). This effect is similar to that of increasing the L/D ratio of the die. It is important to note that the effect of M_W is only evident below the critical shear stress, and that above it the flow curves generally collapse upon one another. Later work by Lim and Schowalter (1989) and Vinogradov *et al*. (1984) presented similar results for polybutadiene melts.

Venet and Vergnes (1997) found that molecular weight also affects the sharkskin behavior of polyethylene melts. In their study, they found that the amplitude and period of

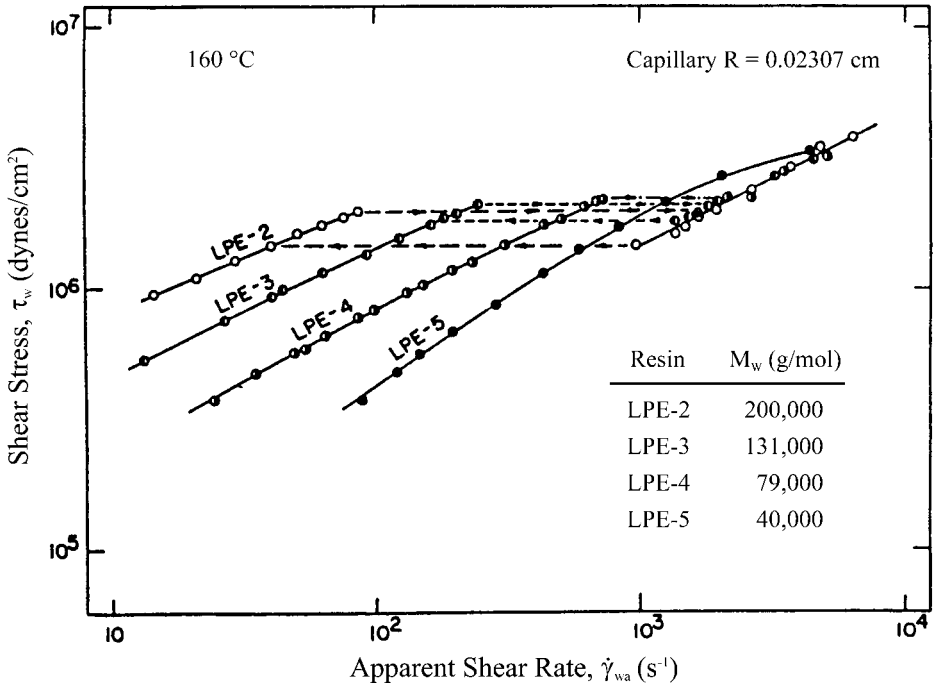

Figure 2.35: Effect of M_w on flow curves [adapted from Blyler and Hart (1970)]

oscillation of the fine-scale surface distortions increased with M_W for a given wall shear stress. They concluded that high molecular weight *linear* polyethylene resins with sufficiently narrow molecular weight distributions exhibit the most severe sharkskin distortion. These results agree well with previous observations [Dennison (1967), Bergem (1976), El Kissi and Piau (1990)].

In a statistical treatment by Middleman (1977), he found that the critical wall shear stress for severe fracture could be correlated to the weight-average molecular weight (M_w) and the absolute temperature during processing. The trends exhibited by branched polyethylenes were similar to those of linear polyethylenes, however the linear resins always exhibit a higher critical shear stress for severe fracture. The empirical expressions were found to be:

$$\tau_{cr}/T_{abs} = 131.7 + 1.0 \times 10^7/M_W \qquad \text{(branched PE)} \qquad (2.24)$$

$$\tau_{cr}/T_{abs} = 171.7 + 2.7 \times 10^7/M_W \qquad \text{(linear PE)} \qquad (2.25)$$

One should note that the onset of severe fracture in LDPE is classified as gross melt fracture, while that of HDPE and LLDPE is slip-stick fracture.

Molecular Weight Distribution

In addition to molecular weight, the molecular weight distribution has a significant effect on the melt fracture behavior of polyethylenes. Blyler and Hart (1970) found that the addition of small amount of low molecular polyethylene wax (M_w ~ 1600 g/mol) to a linear, high molecular weight polyethylene resin caused a noticeable reduction in the degree of slip-stick fracture. For their studies, polymer blends of 10, 20 and 30 wt% PE wax were prepared. The flow curve for the pure high MW PE resin showed a large discontinuity at a wall shear stress of 2×10^5 Pa. The addition of PE wax first reduced the magnitude of the discontinuity, and then eliminated the discontinuity all together at the highest concentration. Blyler and Hart also found that above a

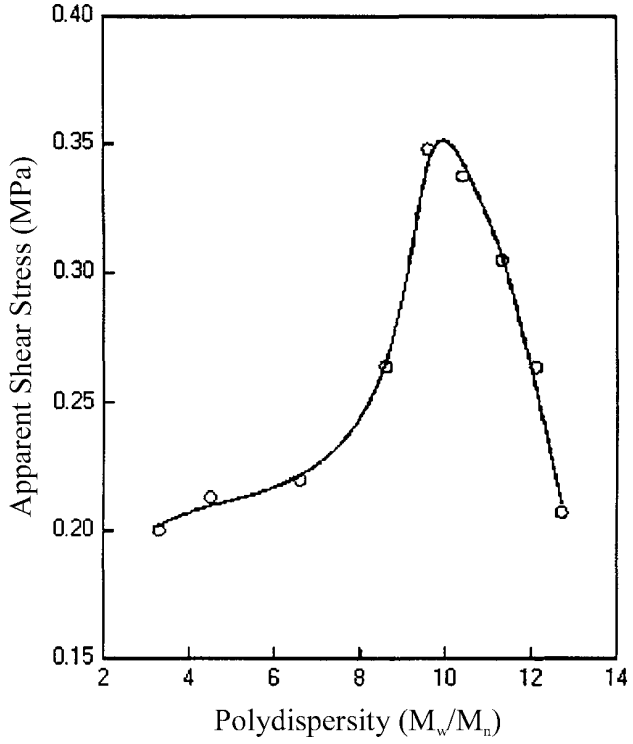

Figure 2.36: Effect of MWD on Critical Wall Shear Stress [Goyal et al. (1997)]

30 wt% fraction of PE wax, no wall slip was witnessed. However, the onset of distortion was found to be insensitive to the presence of low molecular weight component.

Goyal *et al.* (1997) found that over a wide range of polydispersities, the onset of slip-stick fracture in LLDPE is greatly affected. They investigated a series of LLDPE resins with similar M_W and variable MWD. As seen in Figure 2.36, their results show that the critical wall shear stress slowly increases as the polydispersity is broadened from three (3) to about eight (8). Then, between 8 and 10, a precipitous rise in critical wall shear stress is observed. Any further increase in MWD again reduces the τ_{c2}. The authors reasoned that the proper balance between melt viscosity and elasticity are required to maximize the critical wall shear stress.

In addition to polydisperity index, Vlachopoulos and Alam (1972) correlated the recoverable shear strain to higher moments of the molecular weight distribution. They

investigated the melt fracture behavior of several polymers and obtain the following equation for the critical recoverable shear strain at fracture

$$S_R = 2.65 \, (M_z \, M_{z+1} / M_w^2) \qquad (2.26)$$

where M_z and M_{z+1} are consecutively higher moments of the molecular weight distribution. One can imply from their correlation that monodisperse polymers will fracture at critical recoverable shear strains of 2.65, regardless of molecular weight.

Long-Chain Branching

When considering the melt fracture behavior of LDPE and HDPE or LLDPE, it is tempting to attribute the difference in behavior to the presence of long-chain branching. While similar distinction hold for some materials (e.g. linear vs. branched polydimethylsiloxanes), it does not for others [den Otter (1970, 1971)]. Neither polypropylene [Vinogradov *et al*. (1970)] nor linear silicones [Benbow and Lamb (1963)] exhibit the characteristic flow curve discontinuity of linear polyethylene, and low molecular weight silicone oils can exhibit recirculating vortices in the die entry [den Otter (1971)]. As a result, the direct correlation of melt fracture behavior to molecular topology must be treated with appropriate caution.

Blyler and Hart (1970) concluded their study on linear polyethylenes by blending high molecular weight HDPE with relatively high molecular weight LDPE. The goal of the study was to better understand the significance of long-chain branching on melt fracture behavior. The results of their work are summarized in Figure 2.37. The HDPE and LDPE whole polymers exhibit typical melt fracture behavior. However, the presence of increasing amounts of long-chain branched fractions affects the blends in two ways. First, the magnitude of the flow curve discontinuity is decreased, and second, the critical shear stress for the onset of fracture is

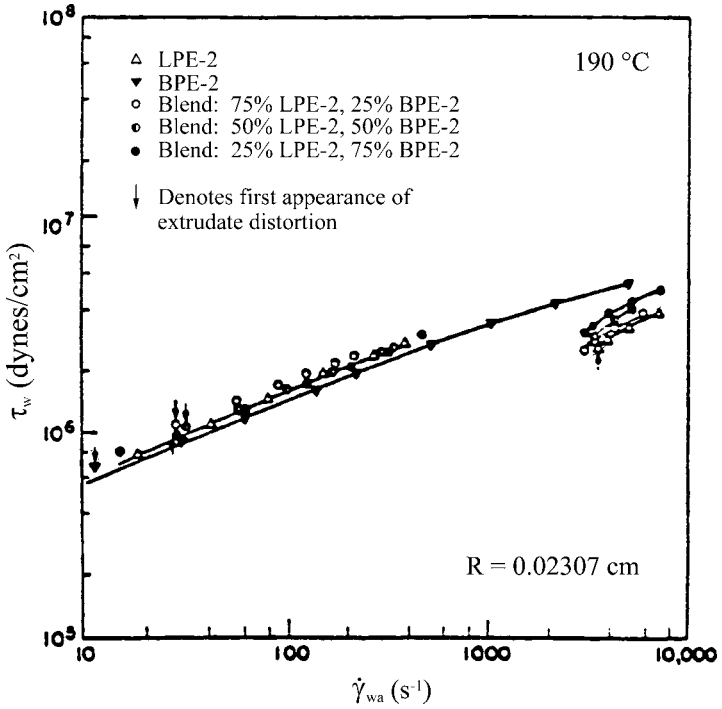

Figure 2.37: Effect of LCB on flow curves (adapted from Blyler and Hartt(1970)]

increased. The degree of change appears to scale in proportion to the content of each. The authors conclude that although LDPE fractions undergo gross melt fracture at a similar critical wall shear stress, the inlet-type mechanism provides *strain* relief to the remaining linear material that typically undergoes slip-stick fracture.

More recently, Venet and Vergnes (1997) have shown that the presence sparse degrees of long-chain branching in LLDPE resins can drastically alter SMF behavior. In their studies, Venet and Vergnes compared three LLDPE resins (A, C and D) with increasing M_w and decreasing MWD, respectively. Resin C was generated from the γ-irradiation of resin A to generate sparse degrees of long-chain branching. The results show that resin D, with highest M_W and narrowest MWD, exhibits the most severe SMF behavior with the greatest amplitude and period of oscillation (Figure 2.38), as expected. Surprisingly, resin C exhibits the least severe sharkskin behavior of the three resins tested. Despite having a greater M_W and narrower MWD

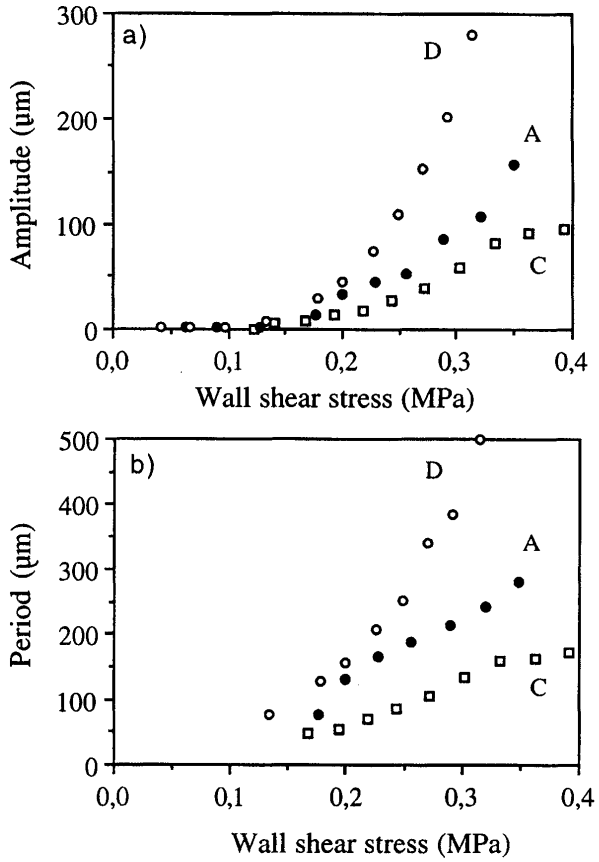

Figure 2.38: Amplitude and Period of SMF defects [Venet and Vergnes (1997)]

than resin A, the presence of LCB helps alleviate some of the instability present during SMF. The authors conclude that the reduced severity of sharkskin in resin C is due to enhanced extensional strain-hardening behavior arising from LCB.

2.4 Numerical Simulations of Viscoelastic Flow

A large number of the polymer-processing operations currently employed involve either isothermal or, more often, non-isothermal flow of polymer melts and solutions through complex geometries. The rate of deformation and deformation history experienced by these polymer fluids does vary considerably between processes. Furthermore, the nature of the polymer itself will determine its processability during forming operations and may lead to peculiar phenomena (i.e. melt fracture, die swell, etc.). In the case of polyethylene, the molecular architecture can have significant effect on the rheological properties. Therefore, the ability to analyze and predict the flow behavior of viscoelastic fluids using numerical simulations has become important, now more than ever. In the following section, the basic components required for numerical simulations along with the limitations associated with such complex computations will be reviewed.

2.4.1. Governing Equations

Any attempt to simulate flow processes must first be preceded by a description of the mathematical model, as if the problem were to be solved analytically. The ingredients of any mathematical description include the field equations, also known as the conservation equations, which are the same for all flow processes, the constitutive equations that describe the specific properties of the fluid at hand, and the relevant boundary conditions. The following subsection will review the governing field equations, provide a general introduction to constitutive equations, and comment on the implications of boundary conditions during numerical simulations.

Field Equations

The field equations are used to describe the basic laws of conserved quantities of a continuum. These laws include the conservation of mass, momentum and energy. Therefore, a general flow problem will consist of solving the following field equations:

$$\text{Mass:} \qquad \frac{D\rho}{Dt} + \rho(\nabla \cdot \boldsymbol{v}) = 0 \tag{2.27}$$

$$\text{Momentum:} \qquad \frac{D(\rho \boldsymbol{v})}{Dt} + \nabla \cdot \pi - \rho \boldsymbol{g} = 0 \tag{2.28}$$

$$\text{Energy:} \qquad \frac{DU}{Dt} + \nabla \cdot \boldsymbol{q} + \pi : \nabla \boldsymbol{v} = 0 \tag{2.29}$$

where D/Dt is the material derivative, ρ is the fluid density, $\boldsymbol{v}$ is the velocity vector, π is the total stress tensor, $\boldsymbol{g}$ is the body force, U is the internal energy, $\boldsymbol{q}$ is the heat flux, and $\nabla \boldsymbol{v}$ is the velocity gradient. It is well recognized that under "real" flow situations, the above equations are coupled and highly nonlinear in nature.

Generally, most numerical simulations of polymeric fluids occur under steady, isothermal, incompressible, creeping flow (no inertia) conditions. This approach greatly simplifies the numerical formulation, and provides a first approximation to real flow conditions. The simplified equation set appears as:

$$\text{Mass:} \qquad \nabla \cdot \boldsymbol{v} = 0 \tag{2.30}$$

$$\text{Momentum:} \qquad \nabla \cdot \pi - \rho \boldsymbol{g} = 0 \tag{2.31}$$

Because we have assumed the flow incompressible, the total stress tensor can be decomposed into an indeterminate pressure term and an extra stress tensor, $\pi = p\delta + \tau$. Furthermore, due to the isothermal nature of the flow, the energy equation (2.29) reduces to a trivial solution of zero.

Constitutive Equations

The field equations above govern the basic fundamental principles of a continuum. However, one can quickly determine that the 17 unknown quantities arising from three-dimensional application of the field equations (2.27 – 2.29) are described by only 5 equations. In order to close the mathematical system formed by the field equations, one must also specify the necessary *equations of state*. In this case, a rheological constitutive equation describing the stress components and a thermal equation of state describing the heat flux components.

Limiting ourselves to incompressible, isotropic fluids, the simplest equations of state are described by Newton's law of viscosity and Fourier's law of heat conduction, i.e.

Viscosity: $$\tau_{ij} = -\mu\left(\frac{dv_j}{dx_i} + \frac{dv_i}{dx_j}\right) \tag{2.32}$$

Conduction: $$q_i = -k\frac{\partial T}{\partial x_i} \tag{2.33}$$

where μ is the constant fluid viscosity and k is the constant thermal conductivity. Index notation has been used to denote the nine equations arising from the rheological constitutive equation and the three equations arising from the thermal constitutive equation. When combined with the field equations the mathematical system is closed and becomes solvable. However, in order to arrive at a unique solution one must also specify suitable boundary conditions.

Boundary Conditions

In order to complete the mathematical description of a transport process, one must specify appropriate boundary conditions. The nature of those boundary conditions is intimately connected to the mathematical nature of the governing equations. In the following section we will restrict our discussion to boundary conditions related to isothermal flowing media because

of its relevance to this research project. However, similar approaches can be taken for heat and mass transport processes.

The selection of appropriate boundary conditions is important for both analytical and numerical calculations. The problem solution is very dependent upon the manner and quantities used in describing the boundary conditions. In the case of a Newtonian fluid, the extra stress is substituted out of the equation of motion leading to four unknowns: v_i (i=1,2,3) and P. It is sufficient to specify the velocity or surface force components over the boundary of the domain of interest. For elastic liquids this specification is insufficient on account of fluid memory. The strain history or stress field entering the domain must be known *a priori*. In practice, assuming "fully-developed flow conditions" often inadvertently satisfies the boundary condition requirements, which essentially implies knowledge of the flow field upstream.

2.4.2. Constitutive Equations for Viscoelastic Fluids

The selection of the constitutive equation is obviously a critical step in the modeling of viscoelastic flows. A large number of constitutive models have been developed to describe the rheological behavior of polymeric fluids. The simplest constitutive equation capable of capturing some of the viscoelastic nature of polymeric melts is the upper-convected Maxwell (UCM) model. It has the following form,

$$\tau + \lambda \tau_{(1)} = -\eta \dot{\gamma} \qquad (2.34)$$

where λ is the fluid relaxation time, η is the fluid shear viscosity, $\dot{\boldsymbol{\gamma}}$ is the rate-of-strain tensor, and $\tau_{(1)}$ is the upper-convected, or contravariant, derivative of the stress tensor, with the form

$$\tau_{(1)} = \frac{\partial \tau}{\partial t} + \boldsymbol{v} \cdot \nabla \tau - \tau \cdot (\nabla \boldsymbol{v})^{\dagger} - (\nabla \boldsymbol{v}) \cdot \tau \qquad (2.35)$$

The upper-convected derivative of the stress tensor introduces strain history dependence into the *quasi-linear* version of the original Maxwell model. Although the UCM model is often used in numerical stability analysis, it is a poor choice for modeling "real" polymer flow. The constant shear viscosity and unbounded extensional viscosity at finite values of the rate-of-strain tensor makes its application very unrealistic. Therefore, the choice of the constitutive model should be dictated by the rheological behavior of the polymeric fluid under the flow kinematics of interest.

Several constitutive equations with more realistic behavior for modeling polymer flow have been developed over the years. For the most part, these constitutive equations are presented as empirical relations that are designed so that a wide variety of experimental data can be described. Interestingly, some of these models are derived from, or at least inspired by, molecular theory. In the present case, the ability to accurately model the flow behavior of branched and linear polyethylenes is highly desirable. Three models that have emerged over the years for describing branched polymers include the Phan-Thien and Tanner (PTT) model, the K-BKZ single integral model, and more recently, the McLiesh-Larson "Pom-Pom" model. Therefore, the nature and predictions of these constitutive models must be understood in light of need for prediction accuracy.

Phan-Thien and Tanner (PTT) Model

The Phan-Thien and Tanner model [Phan-Thien and Tanner (1977), Phan-Thien (1978)] is a differential model derived from Lodge-Yamamoto type network theory [Lodge (1968), Yamamoto (1956)] for polymeric fluids that incorporates the idea of nonaffine deformation of network junctions into its formulation. In the PTT model, it is assumed that there is a certain degree of slip within the network and that there is a dynamic equilibrium of network junctions

that depend upon the average extension of the network strands. Through this approach, two adjustable parameters arise that provide near-independent control over the shear and extensional deformation predictions. The multi-mode representation of the PTT model appears as,

$$\tau = \sum_i \tau_i \tag{2.36}$$

$$Z(\mathrm{tr}\,\tau_i)\tau_i + \lambda_i \tau_{i(1)} + \frac{\lambda_i \xi}{2}\left(\dot{\gamma}\cdot\tau_i + \tau_i\cdot\dot{\gamma}\right) = -\eta_i\dot{\gamma} \tag{2.37}$$

where λ_i and η_i are individual modes taken from the discrete relaxation spectrum, ξ describes the non-affine nature of the network, and $Z(\mathrm{tr}\,\tau_i)$ is a function that describes the local creation and destruction of network junction points and has two possible forms,

$$Z(\mathrm{tr}\,\tau_i) = 1 - \frac{\varepsilon\lambda_i}{\eta_i}\mathrm{tr}\,\tau_i \tag{2.38}$$

$$Z(\mathrm{tr}\,\tau_i) = \exp\left(-\frac{\varepsilon\lambda_i}{\eta_i}\mathrm{tr}\,\tau_i\right) \tag{2.39}$$

where tr τ_i is the trace of extra stress tensor, and ε is a characteristic parameter determined from extensional measurements. The two different forms of $Z(\mathrm{tr}\,\tau_i)$ predict different extensional behavior (Figure 2.39). The most realistic response is provided by the exponential form, which predicts the Trouton ratio ($3\eta_0$) at low extension rates and then passes through a maximum at higher extension rates. The magnitude of this maximum is determined by the extensional dependent parameter ε. This particular shape of the extensional viscosity versus strain-rate curve has been observed for polyethylene melts and is used most frequently [Munstedt (1979)].

Analytical expressions for shear-flow predictions of the PTT model often require an assumption concerning the nonlinear contribution of the $Z(\mathrm{tr}\,\tau_i)$ term. If the magnitude of the network strain is assumed to be small, then its influence as a whole should be relatively small.

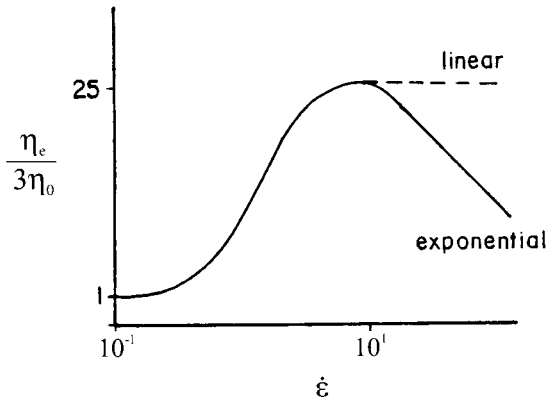

Figure 2.39: Effect of Z(tr τ) function on extensional viscosity predictions [White (1987)]

This is a reasonable assumption for shear flows and eliminates the nonlinear exponential function. As a result, the predictions of the model in steady simple shear flow are given by,

$$\eta = \frac{\eta_i}{1+\xi(2-\xi)(\lambda_i\dot{\gamma})^2} + O(\varepsilon) \tag{2.40}$$

$$\Psi_1 = \frac{2\eta_i\lambda_i}{1+\xi(2-\xi)(\lambda_i\dot{\gamma})^2} + O(\varepsilon) \tag{2.41}$$

$$\Psi_2 = -\frac{\xi}{2}\Psi_1 \tag{2.42}$$

where Ψ_1 and Ψ_2 are the primary and secondary normal stress difference coefficients. For larger degrees of network strain, the contribution from the exponential term $O(\varepsilon)$ should be addressed. In small amplitude oscillatory shear flow the predictions are,

$$G' = \frac{\eta_i\lambda_i\omega^2}{1+(\lambda_i\omega)^2} \tag{2.43}$$

$$G'' = \frac{\eta_i\lambda_i\omega}{1+(\lambda_i\omega)^2} \tag{2.44}$$

where G' and G'' are the storage and loss moduli, respectively, and ω is the applied angular frequency.

For the case of extensional flow, it is no longer possible to obtain an analytical solution for the rheological material functions. This arises from the $Z(\text{tr}\,\tau_i)$ term which is no longer neglected in large strain deformations. Therefore, in order to determine the steady-state extensional viscosity η_e, or the transient tensile stress growth function σ_e^+, it is necessary to solve a coupled set of differential equations. For steady-state, simple (uniaxial) extensional flow, these equations become,

$$\exp\left[-\frac{\varepsilon\lambda_i}{\eta_i}\left(\tau_{xx,i}+\tau_{yy,i}+\tau_{zz,i}\right)\right]\tau_{xx,i}+\lambda_i\left(1-\xi\right)\dot{\varepsilon}\tau_{xx,i}=\eta_i\dot{\varepsilon} \tag{2.45}$$

$$\exp\left[-\frac{\varepsilon\lambda_i}{\eta_i}\left(\tau_{xx,i}+\tau_{yy,i}+\tau_{zz,i}\right)\right]\tau_{yy,i}+\lambda_i\left(1-\xi\right)\dot{\varepsilon}\tau_{yy,i}=\eta_i\dot{\varepsilon} \tag{2.46}$$

$$\exp\left[-\frac{\varepsilon\lambda_i}{\eta_i}\left(\tau_{xx,i}+\tau_{yy,i}+\tau_{zz,i}\right)\right]\tau_{zz,i}-2\lambda_i\left(1-\xi\right)\dot{\varepsilon}\tau_{zz,i}=-2\eta_i\dot{\varepsilon} \tag{2.47}$$

One of the greatest advantages of the PTT model is its relatively simple formulation. The PTT model is easily implemented into numerical simulations, and it can provide excellent rheological predictions when used in the multi-mode form. The explicit material functions for shear deformations makes parameter fitting straightforward, the only exception being the extensional parameter. One of the biggest disadvantages associated with the PTT model is maintaining a monotonic function of shear stress at all shear rates. Implementation of a retardation term or an extremely fast relaxation mode of appropriate strength into the formulation will usually circumvent this limitation [Crochet and Bezy (1979), Keunings and Crochet (1984)].

Factorized K-BKZ Integral Model

The factorized K-BKZ integral model is a nonlinear single integral model born from the original K-BKZ integral equation first proposed in the early 1960s [Kaye (1962), Bernstein *et al*.

(1963)]. The original K-BKZ model was developed from thermodynamic-mechanical arguments that address the solid behavior of polymers at short times and their liquid nature at long times. These two concepts are related by the strain and strain-rate history experienced by the material in question. A more general class of this nonlinear single integral model has been advanced by Rivlin and Sawyers (1971), but the functional form is quite similar to the K-BKZ model and requires no additional explanation. The factorized K-BKZ integral model appears as,

$$\tau(t) = \int_{-\infty}^{t} M(t-t') \left[\frac{\partial W(I_1, I_2)}{\partial I_1} \gamma_{[0]} + \frac{\partial W(I_1, I_2)}{\partial I_2} \gamma^{[0]} \right] dt' \qquad (2.48)$$

where $\gamma_{[0]}$ and $\gamma^{[0]}$ are the relative Finger and Cauchy finite strain tensors, respectively, I_1 and I_2 are the first and second invariants of the Finger strain tensor, $W(I_1,I_2)$ is a scalar potential function of the invariants, and M(t-t') is the viscoelastic memory function which is often expressed in terms of the Lodge network model,

$$M(t-t') = \sum_{i=1}^{n} \frac{\eta_i}{\lambda_i^2} \exp\left(-\frac{t-t'}{\lambda_i} \right) \qquad (2.49)$$

where n is the number of relaxation modes, and λ_i and η_i are obtained from the discrete relaxation spectrum.

The I_1-differentiated scalar potential function of the strain invariants $W(I_1,I_2)$ is generally referred to as the nonlinear damping function and many forms have been proposed by various researchers [Bird *et al.* (1987), Larson(1988)]. The form of the nonlinear damping function proposed by Papanastasiou, Scriven and Macosko (1983) is presented here because of its excellent ability to fit steady and transient material functions of linear and branched polyethylenes. Papanastasiou and coworkers observed that step strain data suggested a sigmoidal form of the damping function. Their results recommend the following form,

$$\frac{\partial W(I_1, I_2)}{\partial I_1} = \frac{\alpha}{(\alpha - 3) + \beta I_1 + (1 - \beta) I_2} \tag{2.50}$$

where α and β are adjustable parameters, with β only affecting extensional flow predictions. They did not recommend a form for the I_2-differentiated scalar function.

Due to the presence of a nonlinear integrand, explicit analytical solutions for the material functions are difficult, if not impossible, to obtain. Numerical integration is often required to arrive at a solution. If one writes the material functions in a general form, steady simple shear material functions become,

$$\eta = \int_0^\infty M(s) s (\phi_1 + \phi_2) ds \tag{2.51}$$

$$\Psi_1 = \int_0^\infty M(s) s^2 (\phi_1 + \phi_2) ds \tag{2.52}$$

$$\Psi_2 = -\int_0^\infty M(s) s^2 \phi_2 ds \tag{2.53}$$

where $s = t-t'$, and $\phi_j = \partial W / \partial I_j$. One should note that using the PSM damping function alone and letting ϕ_2 equal zero leads to a non-existent N_2. However, considering its relatively small value this result is acceptable. In small amplitude dynamic oscillatory, the material functions are

$$G' = \int_0^\infty M(s)(1 - \cos \omega s) ds \tag{2.54}$$

$$G'' = \int_0^\infty M(s) \sin \omega s ds \tag{2.55}$$

and the uniaxial extensional viscosity can be written as

$$\eta_e = \frac{1}{\dot{\varepsilon}} \int_0^\infty M(s)[\phi_1 (e^{2\dot{\varepsilon}s} - e^{-\dot{\varepsilon}s}) + \phi_2 (e^{\dot{\varepsilon}s} - e^{-2\dot{\varepsilon}s})] ds \tag{2.56}$$

One of the biggest deficiencies of the factorized K-BKZ model is its inability to discriminate shear and planar extension behavior [Samurkas *et al*. (1989)]. This kinematic flaw arises from the strict dependence of the damping function upon the two strain invariants, I_1 and

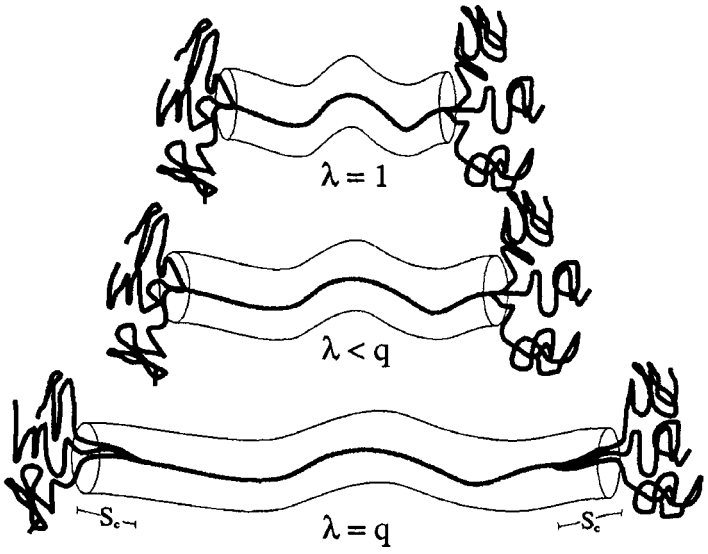

Figure 2.40: The structure of the pom-pom polymer [McLeish and Larson (1998)]

I_2. For both shearing and planar extension deformation, $I_1 = I_2$ identically, and therefore the predicted behaviors are similar. This contradicts experimental measurements of branched polyethylenes that show both shear-thinning and planar extensional strain-hardening behavior. Therefore, judicious choice of fitting data and avoidance of combined shear and planar extensional deformations is usually required.

McLeish-Larson 'Pom-Pom' Model

The "pom-pom" model of McLeish and Larson (1998) is a rheological constitutive equation developed from the Doi-Edwards tube model [Doi and Edwards (1978)] for linear molecules and extended to pom-pom shaped molecules. The pom-pom model presents a theoretical approach to the behavior of macromolecular segments that lie between the multiple branch points of large branched molecules like low-density polyethylene. For their studies, McLeish and Larson greatly simplified their approach by considering model architectures. The pom-pom molecule is an idealized branched polymer consisting of a backbone (or crossbar) that

ends in two branch points consisting of *q* arms. This pom-pom polymer is illustrated in Figure 2.40. The pom-pom model is based upon two key molecular processes, segment stretch and orientation. These two concepts are translated into the following formulation of the pom-pom model,

$$\sigma(t) = \frac{15}{4} G_0 \phi_b \left(\phi_b \lambda^2(t) + \frac{2qs_c(t)}{2qs_a + s_b} \right) \boldsymbol{S}(t) \tag{2.57}$$

where G_0 is the plateau modulus, ϕ_b is the fraction of the molecular weight contained in the backbone, $\lambda(t)$ is a measure of the backbone stretch, q is the number of branch point arms, $s_c(t)$ is a measure of the arm withdrawal into the backbone tube, s_a is a measure of the length of the branch arms, s_b is a measure of the length of the backbone, and $\boldsymbol{S}(t)$ is the orientation tensor. The orientation tensor, degree of backbone stretch, and degree of arm withdrawal are determined from the following set of equations,

$$\boldsymbol{S}(t) = \frac{1}{\tau_b} \int_{-\infty}^{t} \exp\left(\frac{t - t'}{\tau_b} \right) \boldsymbol{Q}(t') dt' \tag{2.58}$$

$$\frac{\partial \lambda}{\partial t} = \lambda (\boldsymbol{K} : \boldsymbol{S}) - \frac{1}{\tau_s} (\lambda - 1) \tag{2.59}$$

$$\frac{\partial s_c}{\partial t} = \left(q \frac{s_b}{2} + s_c \right) \boldsymbol{K} : \boldsymbol{S} - \frac{1}{2\tau_a} \tag{2.60}$$

where τ_b is the backbone orientation relaxation time, $\boldsymbol{Q}$(t') is the universal strain measure of Doi and Edwards (1978), $\boldsymbol{K}$ is the deformation rate tensor, and τ_a is the arm spectrum relaxation time. Due to the complexity of the formal pom-pom model formulation, the authors also provide a simpler, differential form of the model which simplifies the orientation tensor to

$$\boldsymbol{S}(t) = \frac{\boldsymbol{A}(t)}{\mathrm{tr}\, \boldsymbol{A}(t)} \tag{2.61}$$

where $\boldsymbol{A}(t)$ is determined from the equation

$$\frac{\partial}{\partial t}\boldsymbol{A}(t) = \boldsymbol{K}\cdot\boldsymbol{A} + \boldsymbol{A}\cdot\boldsymbol{K}^{T} - \frac{1}{\tau_b}\left(\boldsymbol{A} - \frac{1}{3}\boldsymbol{I}\right) \tag{2.62}$$

Furthermore, the effects of backbone withdrawal $s_c(t)$ on the stress tensor are generally neglected due to its small contribution in comparison to the backbone segment itself.

The obvious complexity of the pom-pom model prevents the derivation of explicit forms of the material functions. In light of this fact, the authors prepared a series of figures describing the predictions under steady and transient flows. Figure 2.41 summarizes the time-dependent shear viscosity and first normal stress difference for shear startup flows using the model parameters: q=5, s_a=3, and s_b=30. The model predicts excellent qualitative behavior, with overshoot and shear thinning behavior of both shear viscosity and first normal stress difference coefficient. Figure 2.42 summarizes the transient extensional viscosity response for the same model parameters listed above. The strain hardening viscosity is unmistakable and clearly captures the rheological behavior of branched polymers like branched polyethylenes. Recently,

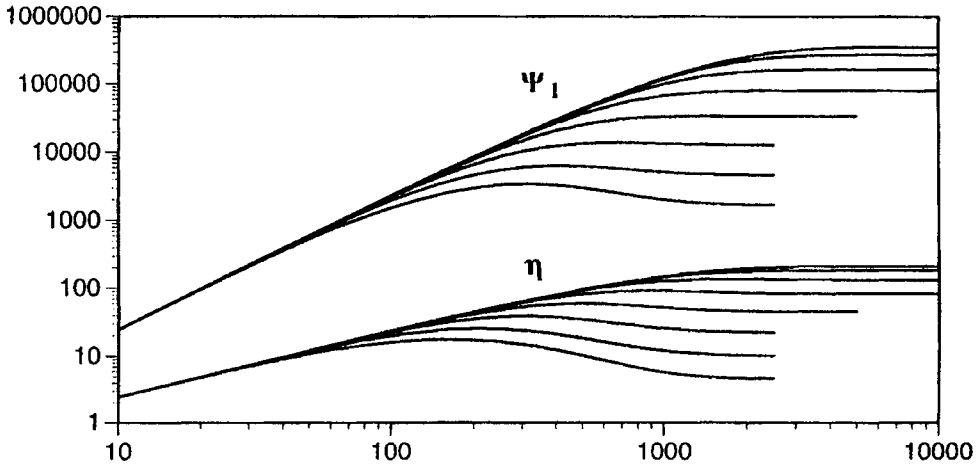

Figure 2.41: Pom-pom model shear predictions [McLeish and Larson (1998)]

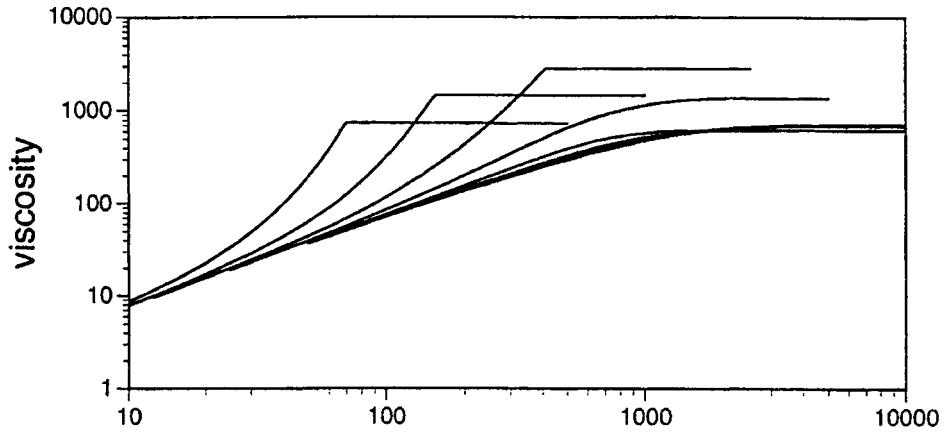

Figure 2.42: Pom-pom model extensional viscosity predictions [McLeish and Larson (1998)]

Inkson *et al.* (1999) and Blackwell *et al.* (2000) have shown that a multi-mode approach *can* quantitatively capture the shear and extension behavior of highly branched LDPE. In addition to the excellent shear and uniaxial deformation predictions, the pom-pom model can also predict planar extensional strain hardening, unlike the K-BKZ model.

2.4.3. The Finite Element Method

The finite element method (FEM) is a numerical method that can be used to solve a variety of complex engineering problems. The method was first developed in the 1960s [Argyris and Kelsey (1960), Clough (1960)] as a technique for structural analysis. Since that time, and in parallel with the advances in computing power, it has become a powerful numerical technique for solving a wide range of problems, including Newtonian and non-Newtonian fluid dynamics. Over the years, numerous texts providing general introductions to the finite element method [Hinton and Owen (1980), Reddy (1984)] and their application to flow problems [Chung (1978), Crochet *et al.* (1984), Crochet (1994)] have been presented.

The basic principle of the finite element method is to approximate the solution of a complicated problem by replacing it with a simpler one. This is accomplished by discretizing the continuum domain into smaller subdivisions called "finite elements". Within each element, the field equations are locally approximated by simple functions (generally polynomials). The error of the approximation is then minimized through simultaneous solution of element equations. In the case of non-Newtonian flows, the approximating system is first linearized and then solved iteratively. The following section will review some of the key steps involved in formulating a FEM solution including: discretization of the flow domain, approximation and simplification of the field equations, and numerical techniques used for nonlinear systems.

Domain Discretization

The discretization of the domain into finite elements is the first step in a finite element method formulation. For flow problems, one needs to discretize the velocity components, pressure, and extra stress components. This is accomplished by replacing the *whole* solution region with an assemblage of smaller elements. Figure 2.43 illustrates this concept of domain discretization. The number, shape, size, and density of elements used in a given problem depend on a number of considerations, but should be chosen to best simulate the original domain.

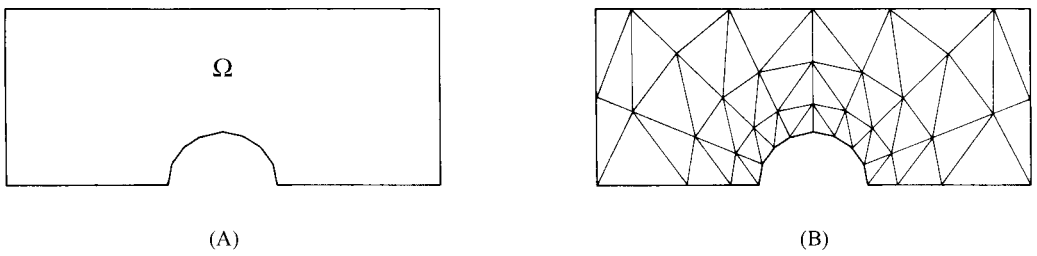

Figure 2.43: Domain Discretization, (A) original flow region Ω, (B) discretized flow region using triangular-shaped elements.

The most popular element shapes used in two-dimensional representations are the triangle and quadrilateral. These shapes can be used separately or in combination with one another to describe a given flow region. The number of nodes in each element is generally determined by the order of the interpolating polynomial used. The boundaries of the elements can be straight (linear) or curved (quadratic or greater). The number and size of the elements influence the convergence and accuracy of the solution, but also increase the computational expense. The density of the elements should be refined insure that steep gradients of the solution are accurately calculated. In general, knowledge of the qualitative behavior of the problem combined with engineering judgment should be used to determine the geometric factors and degree of refinement involved in mesh generation.

Element Equations

The first step in the formulation of the element equations is the approximation of the field variables across the element subdomain. If one assumes a finite element is associated with a number of nodes, the nodal values represent discrete values of the field variable at that point. The variation in the values between nodal points is determined by a shape function chosen for that given element. The finite element representation of the field variable becomes,

$$u = \sum_{i=1}^{n} U_i \psi_i \qquad (2.63)$$

where u is the finite element representation of a continuous function, U_i is the nodal value of u at the i-th node, ψ_i is the shape function, and n is the number of nodes in the element. The shape function ψ_i is a piecewise, continuous polynomial function with a value of unity at node i, and a value of zero at all other non-corresponding nodes. This approximation can be easily extended to a multi-dimensional representation of the field variables introduced earlier, i.e.

$$v_\alpha = \sum_{i=1}^{n} V_{\alpha i}\psi_i \tag{2.64}$$

$$\tau_{\alpha\beta} = \sum_{i=1}^{n} T_{\alpha\beta i}\varphi_i \tag{2.65}$$

$$p = \sum_{i=1}^{n} P_i\pi_i \tag{2.66}$$

where $V_{\alpha i}$, $T_{\alpha\beta i}$, and P_i are the nodal values of the individual components of the velocity vector, extra stress tensor, and isotropic pressure, respectively, at the i-th node. The shape functions for each variable need not be the same.

The second step in the formulation is the approximation of the field equations. Due to the approximate nature of finite element method, there exists a finite amount of error between the numerical and exact solution. This error is generally referred to as the residual error or simply the residual. The most common technique for reducing this error is known as the weighted residual method. In this treatment, the governing equations are multiplied by a weighting function and integrated over the element subdomain. If one applies this technique to the simplified governing equations developed earlier, then the weighted equations become,

$$\int_{\Omega_e} (\nabla \cdot \boldsymbol{v}) w_j \, d\Omega = 0 \tag{2.67}$$

$$\int_{\Omega_e} (\nabla p + \nabla \cdot \tau) y_j \, d\Omega = 0 \tag{2.68}$$

$$\int_{\Omega_e} (\boldsymbol{h}\{\tau, \dot{\gamma}, \boldsymbol{v}\}) z_j \, d\Omega = 0 \tag{2.69}$$

where w_i, y_i and z_i are the weighting functions, and $\boldsymbol{h}$ is any arbitrary rheological constitutive equation. If the divergence theorem is then applied to the above equations, the *weak* form of the equations can be realized. The weak form of the momentum equation (2.68) is written as,

$$\int_{\Omega_e} \left(p \nabla y_j + \tau \cdot \nabla y_j \right) d\Omega = \int_{\Gamma_e} y_j (\pi \cdot \boldsymbol{n}) d\Gamma \qquad (2.70)$$

where $\boldsymbol{n}$ is the unit outward normal vector along the boundary surface Γ. The weak form reduces the degree of differentiation upon the field variables by passing it along to the weighting functions. Obviously the weighting functions must be of sufficient order to prevent a trivial solution of zero.

Once the weak form of the equations has been derived and the field variables have been approximated, the element equations can be developed. Using the approximated field variables (equations 2.64-66) and equation 2.70 the element equation becomes,

$$\sum_{i=1}^{n} \int_{\Omega_e} \left(P_i \pi_i y_{j,\alpha} + T_{\beta\alpha i} \varphi_i y_{j,\beta} \right) d\Omega = \sum_{i=1}^{n} \int_{\Gamma_e} y_j \left(T_{\beta\alpha i} \pi_i n_i \right) d\Gamma \qquad (2.71)$$

For the sake of simplicity, Einstein index notation has been used in place of symbolic notation. In the above formulation, the shape functions and weighting functions have been treated as separate functions. However, one of the most popular formulations, known as the Galerkin method, allows the global shape function and the weighting function to equal one another, $\pi_i = y_i$. This method has also become quite popular in computational fluid dynamics. On the other hand, if $\pi_i \neq y_i$ and the functions are linearly independent then one has the Petrov-Galerkin formulation. Interestingly, the Petrov-Galerkin method does not work well for viscoelastic flow.

Non-linear systems

In a complex flow problem, it is common to encounter several thousand unknown nodal variables or degrees of freedom. For solving these types of systems, one must choose an appropriate iterative algorithm together with a linearization technique. For example, given a solution vector $\mathbf{X}_n$ one wishes to linearize in terms of the increment $\delta\mathbf{X}$ defined by

$$\boldsymbol{X}_{n+1} = \boldsymbol{X}_n + \delta\boldsymbol{X} \tag{2.72}$$

The simplest technique for iterating is called the Picard method. This consists of rewriting a set of non-linear equations as follows, with an appropriate selection of function G and g,

$$G(\boldsymbol{X})\boldsymbol{X} - g(\boldsymbol{X}) = 0 \tag{2.73}$$

One can then linearize the system as follows

$$G(\boldsymbol{X}_n)\boldsymbol{X}_{n+1} - g(\boldsymbol{X}_n) = 0 \tag{2.74}$$

In this case, the solution $\mathbf{X}_{n+1}$ for the next iteration is solved using the functions G and g evaluated at the previous solution $\mathbf{X}_n$. Unfortunately, the rate of convergence of the Picard algorithm is linear at best. It is primarily used in the calculation of generalized Newtonian fluid flow problems where the shear rate dependent viscosity is calculated on the basis of the current velocity field [Crochet *et al.* (1984)].

If the above function is generalized by the function F($\mathbf{X}$) and expanded around $\mathbf{X}_n$ using a Taylor series one can arrive at the following form,

$$F(\boldsymbol{X}_{n+1}) = F(\boldsymbol{X}_n + \delta\boldsymbol{X}) = F(\boldsymbol{X}_n) + \nabla F(\boldsymbol{X}_n)\cdot\delta\boldsymbol{X} + \ldots \tag{2.75}$$

Claiming that $F(\mathbf{X}_{n+1})$ vanishes, we may therefore require that

$$\nabla F(\boldsymbol{X}_n)\cdot\delta\boldsymbol{X} = -F(\boldsymbol{X}_n) \tag{2.76}$$

and obtain a linear system in the unknown vector $\delta\mathbf{X}$ and subsequently a solution to the original function $F(\mathbf{X}+\delta\mathbf{X})$. This method is known as Newton's method. It has considerable advantages over the Picard method. The greatest advantage is the fact that it is endowed with terminal quadratic convergence that allows one to verify the existence of numerical solution up to machine accuracy. Newton's method is most often used in viscoelastic fluid flow because of its fast convergence behavior in the presence of considerable computational expense.

2.4.4. High Weissenberg Number Problem (HWNP)

Despite significant advances over the last four decades, obtaining accurate numerical solutions at high values of the Weissenberg (or Deborah) number remains a challenge. The high Weissenberg number problem (HWNP) is associated with the divergence of conventional iterative schemes or loss of solution stability beyond some critical value of the Weissenberg number, We_{crit}. The major difficulty in the early years of numerical simulation of viscoelastic flow was the lack of understanding of the *pathology* of loss of convergence, making it difficult to apply an appropriate remedy. In order to understand the causes of HWNP, one must first focus on the set of algebraic equations obtained after discretization. In the following section, the underlying causes for numerical loss of convergence will be reviewed.

Manifestation

The loss of convergence of numerical solutions can be manifested in several ways. The qualitative behavior of a solution family can be quite rich in view of the nonlinear character of the governing algebraic equations. The possible causes of loss of convergence are illustrated in Figure 2.44. With the exception of (A), all involve irregular points in the solution family. Of course, the solution family arising from continuous integro-partial differential equations may not translate into the same solution family for the discretized FEM formulation.

The solution family associated with (A) exhibits a single-valued function of We and the flow is locally unique. This situation describes a well-conditioned problem that rarely ever exists in complex numerical simulations. Case (B) describes a solution family that varies rapidly at We_{crit}. Although the solution family is continuous and single-valued, conventional Picard and Newtonian iterative schemes may experience convergence difficulties due to the steep gradient

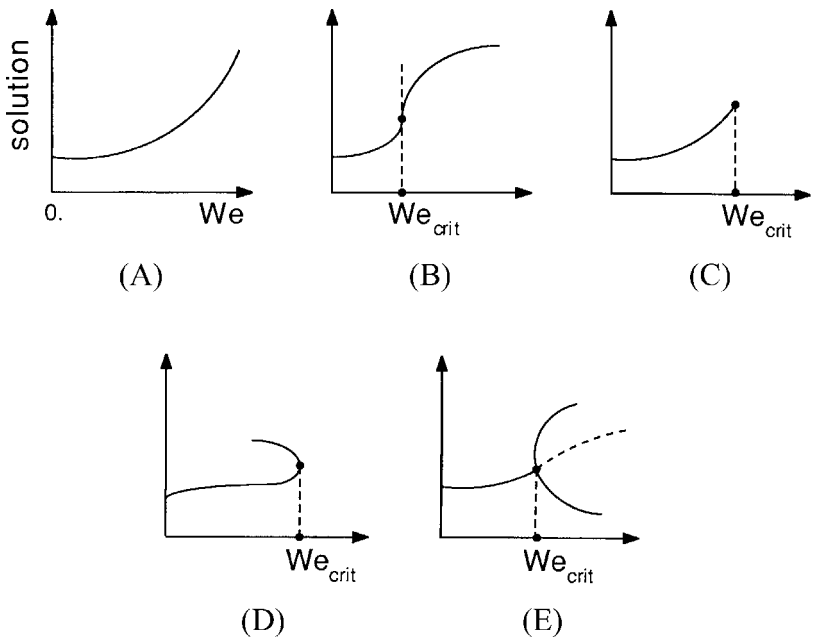

Figure 2.44: Qualitative behavior of the numerical solution family at high We [Keunings (1989)]

in the solution [van Schaftingen and Crochet (1985)]. Cases (C) and (D) describe limit points of the solution family. Limit points may be described by local loss of solution [Beris *et al.* (1984)] or a solution family that turns back on itself [Menon *et al.* (1988)], respectively. In either situation, a solution does not exist beyond a critical We. The final case (E) depicts a bifurcation point. At We_{crit} the solution family becomes doubled value [Keller (1977)]. The bifurcating branches may consist of steady-state solutions, however the lack of a unique solution destroys the integrity of the numerical simulation.

Intrinsic Property or Approximation Error

The root of the HWNP is the nature of the loss of convergence. The irregular points that arise at high Weissenberg numbers could be intrinsic to the analytical solution families or induced by excessive approximation error. Mendelson *et al.* (1982) were the first to suspect the presence of irregular point in viscoelastic simulations. Their initial hypothesis on the subject has

led to additional research over the years. The current consensus is that numerical approximation is the main source of irregular points in numerical simulations, however some evidence does suggest that certain constitutive equations may inherently contain irregular points.

Beris *et al.* (1984) discovered the existence of turning and bifurcation points in their finite element simulations of the journal-bearing problem with the second-order fluid model. The second-order fluid model is generally not recommended for use in practical simulations, however it is very useful for assessing the capabilities of numerical techniques. The authors found that the exact solution of the problem did not yield any turning or bifurcation points. The numerical solutions, on the other hand, did predict a turning point for the case of moderate eccentricity [Beris *et al.* (1986)]. This implies that the observed turning point was clearly a numerical artifact. Similar conclusions were reached by Josse and coworkers (1986) for their numerical simulations of plane Poiseuille flow of an upper-convected Maxwell fluid. Furthermore, Beris and coworkers (1984,1986) showed in their studies that the critical We number could be increased with mesh refinement, a clear indication of approximation error.

On the other hand, Yeh *et al.* (1984) were the first to find a turning point in mixed finite element solutions of the flow of an upper-convected Maxwell (UCM) fluid through an abrupt axisymmetric contraction. The location of the turning point was found to be relatively insensitive to mesh refinement. Keunings (1986) found similar results for the flow of an upper-convected Maxwell fluid through an abrupt planar contraction. He also found that the location of We_{crit} was insensitive to mesh refinement. Conversely, Keunings found that the Giesekus model exhibited a substantial amount of mesh dependence. Together, these two studies imply that the Maxwell model may have an intrinsic turning point. However, one should note that spurious

oscillations in the stress field always preceded We_{crit}, and the presence of boundary singularities in the chosen flow geometries may have affected the results [Keunings (1989)].

Causes for Excessive Approximation Error

The presence of limit and turning points are responsible for the HWNP in various simulations with coupled mixed methods. In most of these studies, the turning points are induced by excessive discretization error. Spurious bifurcation points also arise in simulations with coupled governing equations, but they do not cause divergence. Cleary, the task is to identify the underlying causes for numerical approximation errors. It is generally believed that there are three basic sources of approximation error: the presence of boundary layers or singularities, the hyperbolic character of the governing equations, and nonlinear coupling between stress and velocity unknowns.

The presence of normal stresses gives rise to very thin stress boundary layers in complex flows. This phenomena leads to high stress gradients near the boundary layer. Similarly, boundary singularities can also lead to steep stress gradients. The existence of boundary layers has been clearly demonstrated for the journal-bearing problem and stress singularities are known to occur at the re-entrant corner of abrupt contraction flows. The high stress gradients in each of these cases are detrimental to the accuracy of the stress calculations in the mixed method approach. Furthermore, intensive mesh refinement does not eliminate the numerical difficulties in the presence of a stress singularity.

As is well known, it is a challenge to construct a finite element technique capable of higher-order accuracy *and* good stability properties for hyperbolic equations. The hyperbolic character of the full set of conservation and constitutive equations can give rise to even more

challenging numerical problems than seen in Newtonian flows. Hyperbolicity usually arises from the use of differential constitutive equations containing convected derivatives, i.e.

$$\lambda \boldsymbol{v} \cdot \nabla \tau = B(\tau, \nabla \boldsymbol{v}) \qquad (2.77)$$

where B is a model-dependent tensor function and $\boldsymbol{v}\cdot\nabla\tau$ represents the first-order hyperbolic portion of the constitutive equation. For many constitutive models, the hyperbolic nature is associated with the vorticity of the deformation field. Numerical techniques designed for elliptic problems (e.g. Galerkin method) are likely to be inappropriate for problems with local changes of type. The development of the streamline upwinding Petrov-Galerkin (SUPG) interpolation method [Hughes and Brooks (1982)], the Explicitly Elliptic Momentum Equation (EEME) [King *et al.* (1988)], and the Elastic-Viscous Split Stess (EVSS) method [Rajagopolan *et al.* (1990)] have been used to combat the deleterious effects of hyperbolicity in numerical simulations.

The nonlinear coupling between stress and velocity unknowns is just as enigmatic. Using mixed FEM methods, which require simultaneous solution of velocity, pressure and extra stress unknowns, leads to unusual numerical interactions that may cause divergence or loss of stability of the solution. Many believe that these interactions arise from the choice of interpolation polynomials used to describe the velocity and extra-stress unknowns. In general, typical mixed interpolation polynomials for the Newtonian case include biquadratic polynomials for velocity and bilinear or biquadratic polynomials for extra-stress. Marchal and Crochet (1987) devised a special element that further divided the 9-node Lagrangian element for the velocity field into a set of 4x4 bilinear subelements for the extra-stresses. This method provided excellent results in the absence of stress singularities. Unfortunately, the presence of stress boundary layers or hyperbolicity of the equation set limits the application of the 4x4 subelement without the use streamline upwinding or other techniques.

2.5 Research Objectives

The previous sections of this chapter have shown that molecular architecture can have a significant effect on the flow behavior of polyethylene resins. These variations in molecular architecture arise from the polymorphic nature of polyethylene and the catalysts and polymerization processes used to produce them. The highly branched, broad molecular weight distribution of low-density polyethylene (LDPE) contrasts with the linear, narrower molecular weight distribution of high-density polyethylene (HDPE) and linear low-density polyethylene (LLDPE). The significance of these differences is manifested in the flow behavior of each of these resins, which has a large impact on the processability during typical forming operations.

The development of metallocene-catalyzed polyethylenes has bridged the gap between highly branched and linear polyethylenes through the introduction of sparse amounts of long-chain branching. Long-chain branching (LCB) in MCPE resins is expected to enhance the melt strength and shear sensitivity of the polymer melt, while maintaining excellent mechanical properties arising from their characteristic narrow molecular weight distribution. Previous work on model systems and recent work with MCPE resins indicates that this concept is in fact true. Unfortunately, most of these studies have failed to isolate the influence that random LCB has on shear rheological properties and have overlooked the influence that sparse LCB has on extensional flow characteristics. Both of which greatly affect industrial forming processes.

Melt fracture in polyethylene resins is manifested in many different forms. Surprisingly, the type and severity of fracture is largely determined by the underlying molecular structure of the PE melt. For LDPE, having a high degree of long-chain branching and a broad molecular weight distribution, gross melt fracture is the only form of fracture observed. Conversely, linear PE resins with narrower molecular weight distributions also exhibit surface and slip-stick

fracture prior to gross fracture. With this wide variation in molecular structure, it is difficult isolate the specific influences of long-chain branching and molecular weight distribution on the melt fracture behavior of commercial PE resins. The development of metallocene PE resins may provide the means to discriminate these effects.

One of the most difficult problems facing polymer rheologists and process developers is the ability to accurately model the flow behavior of polyethylene resins. Due to the complex flow geometries typical of industrial processing operations, flow modeling must often be determined numerically using techniques such as the finite element method. Even simple geometries like the 4:1 contraction require the use of complex numerical algorithms to solve the governing transport equations. Furthermore, differential and single-integral rheological constitutive equations capable of describing both the shear and extensional flow properties of these materials must be considered. The PTT model has demonstrated exceptional ability at describing the shear and extensional properties of polyethylene melts, but its ability to accurately predict macroscopic pressure measurements has been overlooked. A feature that is critical to die design and optimization.

Because a large number of questions remain concerning the effects of long-chain branching on the processing behavior of metallocene-catalyzed polyethylenes, and the ability to accurately model those resins under complex flow, the research to be performed will investigate the following three objectives:

1. **Establish the specific role that sparse long-chain branching has on the shear and extensional rheological properties of commercial metallocene polyethylenes.**

2. **Identify the effects that long-chain branching and molecular weight distribution have on the melt fracture behavior of commercial polyethylenes.**

3. **Determine the ability of numerical simulations to accurately predict the flow of linear and branched polyethylene resins. Furthermore, assess the significance of the constitutive equation model employed on the range and validity of the predictions.**

A review of the literature relevant to describing the flow behavior of sparsely long-chain branched metallocene-catalyzed polyethylenes has been presented in this chapter. An emphasis has been placed on flow phenomena that have historically shown sensitivity to long-chain branching. In the next chapter, a detailed account of the experimental procedures used to address the above research objectives will be presented. The remaining chapters will address the results obtained from each these objectives.

2.6 References

Argyris, J.H. and S. Kelsey, *Energy Theorems and Structural Analysis*, Butterworth Sci. Publications, London, 1960.

Axelson, D.E., G.C. Levy and L. Mandelkern, *Macromolecules*, **12**, 41 (1979)

Baird, D.G. and D.I. Collias, *Polymer Processing: Principles and Design*, Butterworth-Heinemann, Boston, 1995.

Bagley, E.B. and A.M. Birks, *J. Appl. Phys*., **31**, 556 (1960)

Bagley, E.B., *J. Appl. Phys*., **28**, 264 (1957)

Bagley, E.B. and H.P. Schreiber, *Trans. Soc. Rheol*., **5**, 341 (1961)

Bagley, E.B., I.M. Cabott, and D.C. West, *J. Appl. Phys*., **29**, 109 (1958)

Ballenger, T.F. and J.L. White, *J. Appl. Polym. Sci*., **15**, 1949 (1971)

Ballenger, T.F., I.J. Chen, J.W. Crowder, G.E. Hagler, D.C. Bogue, and J.L. White, *Trans. Soc. Rheol*., **15**, 195 (1971)

Barone, J.R., N. Plucktaveesak, and S.Q. Wang, *J. Rheol*., **42**, 813 (1998)

Benbow, J.J. and P. Lamb, *S.P.E. Trans*., **3**, 7 (1963)

Benedikt, G.M. and B.L. Goodall, eds., *Metallocene-Catalyzed Polymers: Materials, Properties, Processing & Markets*, Plastics Design Library, New York, 1998.

Bergem, N., in *Proc. 7th International Congress of Rheology*, 50, Swedish Society of Rheology, Gothenberg (1976)

Beris, A.N., R.C. Armstrong and R.A. Brown, *J. Non-Newt. Fluid Mech*., **16**, 141-172 (1984)

Beris, A.N., R.C. Armstrong and R.A. Brown, *J. Non-Newt. Fluid Mech*., **19**, 323-347 (1986)

Bernstein, B., E. Kearsley and L. Zapas, *Trans. Soc. Rheol*., **7**, 391-410 (1963)

Berry, G.C. and T.G. Fox, *Adv. Polym. Sci.*, **5**, 261 (1968)

Bersted, B.H., J.D. Slee and C.A. Richter, *J. Appl. Polym. Sci*., **26**, 1001 (1981)

Bersted, B.H., *J. Appl. Polym. Sci*., **30**, 3751 (1985)

Bird, R.B., R.C. Armstrong and O. Hassager, *Dynamics of Polymeric Liquids. Volume 1: Fluid Mechanics*, 2nd ed., John Wiley & Sons, New York, 1987.

Bin Wadud, S.E. and D.G. Baird, *J. Rheol*., **44**, 1151 (2000)

Blackwell, R.J., T.C.B. McLeish and O.G. Harlen, *J. Rheol*., **44**, 121-136 (2000)

Blyler, L.L. and A.C. Hart, *Polym. Eng. Sci*., **10**, 193 (1970)

Boor, Jr., J., *Ziegler-Natta Catalysts and Polymerization*, Academic Press, New York, 1979.

Bovey, F.A., F.C. Schilling, F.L. McCrackin and H.L. Wagner, *Macromolecules*, **9**, 76 (1976)

Brant, P. and J.J. O'Malley, "Advances in Polyolefins Through Catalysis" (1999)

Breslow, D.S. and N.R. Newburg, *J. Am. Chem. Soc*., **79**, 5073 (1957)

Brooks, A.N. and T.J.R. Hughes, *Comput. Meth. Appl. Mech. Eng*., **32**, 199 (1982)

Bueche, F., *J. Chem. Phys*., **20**, 1959 (1952)

Bueche, F., *J. Chem. Phys*., **22**, 1570 (1954)

Bueche, F., *J. Polym. Sci*., **43**, 527 (1960)

Carella, J.M., J.T. Gotro and W.W. Graessley, *Macromolecules*, **19**, 659 (1986)

Charlesby, A., *J. Polym. Sci*., **17**, 379 (1955)

Chung, T.J., *Finite Element Analysis in Fluid Dynamics*, McGraw-Hill, New York, 1978.

Clough, R.W., *J. Struct. Div. ASCE*, Proc. 2nd Conf. Electr. Comp. 345 (1960)

Cogswell, F.N., *J. Non-Newtonian Fluid Mech*., **2**, 37 (1977)

Crochet, M.J., "Numerical Simulation of Viscoelastic Flow", in *Non-Newtonian Fluid Mechanics*, Lecture Series 1994-03, von Karman Institute for Fluid Dynamics, Belgium, 1994.

Crochet, M.J., A.R. Davies and K. Walters, *Numerical Simulation of Non-Newtonian Flow*, Elsevier, New York, 1984.

Crochet, M.J. and M. Bezy, *J. Non-Newt. Fluid Mech*., **5**, 201 (1979)

Dealy, J.M. and K.F. Wissbrun, *Melt Rheology and Its Role in Plastics Processing: Theory and Applications*, Van Nostrand Reinhold, New York, 1990.

Deiber, J.A. and W.R. Schowalter, *J. Non-Newt. Fluid Mech*., **40**, 141 (1991)

den Otter, J.L., *Plastics Polymers*, **38**, 155 (1970)

den Otter, J.L., *Rheol. Acta*, **10**, 200 (1971)

Dennison, M.T., *Trans. J. Plast. Inst*., **37**, 803 (1967)

Doak, K.W., "Low Density Polyethylene (High Pressure)", in *Enyclopedia of Polymer Science and Engineering*, Vol. 6, ed. R.I. Kroschwitz, Wiley-Interscience, New York, 1990.

Doak, K.W. and A. Schrage, "Polymerization and Copolymerization Processes", in *Crystalline Olefin Polymers*, eds. R.A.V. Raff and K.W. Doak, Interscience Publishers, New York, 1965.

Doi, M. and S.F. Edwards, *J. Chem. Soc. Faraday Trans*., **11**, 1802-1817 (1978)

Dorman, D.E., E.P. Otocka and F.A. Bovey, *Macromolecules*, **5**, 574 (1972)

El Kissi, N. and J.M. Piau, *J. Non-Newt. Fluid Mech*., **37**, 55 (1990)

Everage, A.E. and R.L. Ballman, *J. Appl. Polym. Sci*., **18**, 933 (1974)

Faucher, J.A. and F.P. Reding, "Relationship Between Structure and Fundamental Properties", in *Crystalline Olefin Polymers*, eds. R.A.V. Raff and K.W. Doak, Interscience Publishers, New York, 1965.

Fawcett, E.W., R.O. Gibson, M.W. Perrin, J.G. Paton, and E.G. Williams, Brit. 471 590, to Imperial Chemical Industries, Ltd., Sept. 6, 1937.

Ferry, J.D., *Viscoelastic Properties of Polymers*, 3rd ed., John Wiley and Sons, New York, 1980.

Fetters, L.J., A.D. Kiss, D.S. Pearson, G.F. Quack, F.J. Vitus, *Macromolecules*, 26, 647 (1993)

Fleissner, M., *Ang. Makromol. Chem*., **94**, 197 (1981)

Fox, T.G. and V.R. Allen, paper presented to Division of Polymer Chemistry, 141st Meeting, American Chemical Society, Washington, D.C., March 1962.

Frank, A. and J. Meissner, *Rheol. Acta*, **23**, 117 (1984)

Friedlander, H.N., "Mechanism of Polymerization on Transition Metal Oxide Solid Catalysts", in *Crystalline Olefin Polymers*, eds. R.A.V. Raff and K.W. Doak, Interscience Publishers, New York, 1965.

Gell, C.B., W.W. Graessley, V. Efstratiadis, M. Pitsikalis and N. Hadjichristidis, *J. Polym. Sci. Polym. Phys*., 35, 1943 (1997)

Goyal, S.K., I.B. Kazatchkov, N. Bohnet, and S.G. Hatzikiriakos, SPE ANTEC (1997)

Graessley, W.W., *J. Chem. Phys*., **47**, 1942 (1967)

Graessley, W.W., *Adv. Polym. Sci*., **17**, 70 (1974)

Graessley, W.W., *Acc. Chem. Res*., **10**, 332 (1977)

Graessley, W.W., "Viscoelasticity and Flow in Polymer Melts and Concentrated Solutions", Chapter 3 in *Physical Properties of Polymers*, J.E. Mark ed., American Chemical Society, Washington, D.C. (1984)

Graessley, W.W., T. Masuda, J.E.L. Roovers and N. Hadjichristidis, *Macromolecules*, **9**, 127 (1976)

Hatzikiriakos, S.G. and J.M. Dealy, *J. Rheol*., **36**, 845 (1992)

Hatzikirakos, S.G. and J. M. Dealy, *Int. Polym. Process*., VIII, **36** (1993)

Hatzikirakos, S.G., I.B. Kazatchkov, and D. Vlassopoulous, *J. Rheol*., **41**, 1299 (1997)

Hill, A. and K.W. Doak, "Mechanism of Free-Radical Polymerization of Ethylene" in *Crystalline Olefin Polymers*, eds. R.A.V. Raff and K.W. Doak, Interscience Publishers, New York, 1965.

Hill, D.A., T. Hasegawa, and M.M. Denn, *J. Rheol*., **34**, 891 (1990)

Hingmann, R. and B.L. Marczinke, *J. Rheol*., **38**, 573 (1994)

Hinton, E. and D.R.J. Owen, *A Simple Guide to Finite Elements*, Pineridge Press, Swansea, U.K., 1980.

Hogan, J.P. and R.L. Banks, Belg. Patent 530 617, to Phillips Petroleum Co., January 24, 1955

Hogan, J.P. and R.L. Banks, U.S. Patent 2 825 721, to Phillips Petroleum Co., March 4, 1958

Howells, E.R. and J.J. Benbow, *Trans. J. Plast. Inst*., **30**, 240 (1962)

Huseby, T.W., *J. Rheol*., **10**, 181 (1966)

Ide, Y. and J.L. White, *J. Appl. Polym. Sci*., **22**, 1061 (1978)

Inkson, N.J., T.C.B. McLeish, O.G. Harlen, and D.J. Groves, *J. Rheol*., **43**, 873-896 (1999)

Janiak, C., "Metallocene Catalysts for Olefin Polymerization", in *Metallocenes: synthesis, reactivity, applications*, eds. A. Togni and R. Halterman, Wiley-VCH, Weinheim, 1998.

James, D.E., "Linear Low Density Polyethylene", in *Enyclopedia of Polymer Science and Engineering*, Vol. 6, ed. R.I. Kroschwitz, Wiley-Interscience, New York, 1990.

Janzen, J. and R.H. Colby, *J. Mol. Struct*., **485**/**486**, 569 (1999)

Jordan, E.A., A.M. Donald, L.J. Fetters, and J. Klein, *J. ACS Polym. Prepr*. **30**, 63 (1989)

Jordan, R.F., *Adv. Organomet. Chem*., **32**, 325 (1991)

Josse, S.L., K.C. Lee, and B.A. Finlayson, *J. Non-Newt. Fluid Mech*., **20**, 257-269 (1986)

Kalika, D.S. and M.M. Denn, *J. Rheol*., **31**, 815 (1987)

Kaminsky, W. and R. Steiger, *Polyhedron*, **7**, 2375 (1988)

Kaye, A., College of Aeronautics, Cranfield, *Note* No. 134 (1962)

Kazatchkov, I.B., N. Bohnet, K. Goyal and S.G. Hatzikiriakos, *Polym. Eng. Sci*., **39**, 804 (1999)

Kealy, T.J. and P.L. Pauson, *Nature*, **2**, 1039 (1951)

Keller, H.B., "Numerical Solution of Bifurcation and Nonlinear Eigenvalue Problems", in *Applications of Bifurcation Theory*, P.H. Rabinowitz, ed., Acadmeic Press, New York, 359-384,1997.

Keunings, R. and M.J. Crochet, *J. Non-Newt. Fluid Mech*., **14**, 279 (1984)

Keunings, R., *J. Non-Newt. Fluid Mech*., **20**, 209-226 (1986)

Keunings, R., "Simulation of Viscoelastic Flow", in *Fundamentals of Computer Modeling for Polymer Processing*, C.L. Tucker, ed., Hanser Publishers, Munich, 403-469, 1989.

Kim, Y.S., C.I. Chung, S.Y. Lai and K.S. Hyun, *J. Appl. Polym. Sci*., **59**, 125 (1996)

King, R.C., M.R. Apelian, R.C. Armstrong and R.A. Brown, *J. Non-Newt. Fluid Mech*., **29**, 147 (1988)

Kissin, Y.V., "High Density Polyethylene", in *Encyclopedia of Chemical Technology*, vol. 17, ed. R.I. Kroschwitz, Wiley-Interscience, New York, 1999a.

Kissin, Y.V. "Linear Low Density Polyethylene", in *Encyclopedia of Chemical Technology*, vol. 17, ed. R.I. Kroschwitz, Wiley-Interscience, New York, 1999b.

Kiparissides, C., G. Verros and J.M.S. Rex, *Macromol. Chem. Phys*., C33, 437 (1993)

Koch, K.C. and W.V. Volkenburgh, "Enhancing Polyethylene Performance with INSITE® Technology and Molecular Design", in *Metallocene-Catalyzed Polymers: Materials, Properties, Processing & Markets*, eds. G.M. Benedikt and B.L. Goodall, Plastics Design Library, New York, 1998.

Kraus, G. and J.T. Gruver, *J. Polym. Sci. Part A*, **3**, 105 (1965)

Kuhn, R. and H. Kromer, *Colloid Polym. Sci*., **260**, 1083 (1982)

Kume, K., M. Takahashi, T. Masuda and S. Onogi, *Nihon Reoriji Gakkaishi*, **8**, 18 (1980)

Kurtz, S.J., in *Advances in Rheology* (Proc. IX Intl. Congress Rheol.), Vol. 3, B.Mena, A. Garcia-Rejon, and C. Rangel-Nafaile, eds., Univ. Nacional Autonoma Mexico, Mexico City 1984.

Kurzbeck, S., H. Munstedt, L. Egersdorfer and F. Oster, Proc. of the 13th Annual PPS Meeting, 8-A (1997)

Lai, S.-Y., J.R. Wilson, G.W. Knight, J.C. Stevens and P.-K. Chum, U.S. Patent 5 272 236 (to The Dow Chemical Company), December 21, 1993

Lai, S., T.A. Plumley, T.I. Butler, G.W. Knight and C.I. Kao, SPE Antec Tech. Papers, **40**, 1814 (1994)

Larson, R.G., *Constitutive Equations for Polymer Melts and Solutions*, Butterworth, New York, 1988.

Larson, R.G., *Rheol. Acta*, **31**, 213 (1992)

Laun, H.M., *Prog. Colloid Polym. Sci*., **75**, 111 (1987)

Laun, H.M. and H. Munstedt, *Rheol. Acta*, **15**, 517 (1976)

Laun, H.M. and H. Munstedt, *Rheol. Acta*, **17**, 415 (1978)

Laun, H.M. and H. Schuch, *J. Rheol*., **33**, 119 (1989)

Levine, I.J. and F.J. Karol, U.S. Patent 4 011 382 (to Union Carbide), March 8, 1977

Lim, F.J. and W.R. Schowalter, *J. Rheol*., **33**, 1359 (1989)

Lin, Y.-H., *J. Rheol*., **29**, 605 (1985)

Linster, J.J. and J. Meissner, *Makromol. Chem*., **190**, 599 (1989)

Locati, G. and L. Gargani, Proc. 7th Intl. Congr. Rheol., 520 (1976)

Lodge, A.S., *Rheol. Acta*, **7**, 379-392 (1968)

Long, V.C., G.C. Berry and L.M. Hobbs, *Polymer*, **5**, 517 (1964)

Lupton, J.M. and J.W. Regester, *Polym. Engr. Sci*., **5**, 235 (1965)

Lusignan, C.P., T.H. Mourey, J.C. Wilson and R.H. Colby, *Phy. Rev. E*, **52**, 6271 (1995)

Lusignan, C.P., T.H. Mourey, J.C. Wilson and R.H. Colby, *Phy. Rev. E*, **60**, 5657 (1999)

Macosko, C.W., *Rheology: Principles, Measurements, and Applications*, Wiley-VCH, New York, 1994.

Marshall, D.T., paper presented at the 130th National Meeting of the American Chemical Society, Atlantic City, N.J., 1956.

McLeish, T.C.B. and R.C. Ball, *J. Polym. Sci.: Polym. Phys. Ed*., **24**, 1735 (1986)

McLeish, T.C. B. and R.G. Larson, *J. Rheol*., **42**, 81-110 (1998)

McMillan, F.M., *The Chain Straighteners*, The MacMillan Press Ltd., London, 1979.

Meissner, J., *J. Appl. Polym. Sci*., **16**, 2877 (1972)

Meissner, J., *Chimia*, **38**, 65 (1984)

Mendelson, M.A., P-W. Yeh, R.A. Brown and R.C. Armstrong, *J. Non-Newt. Fluid Mech*., **10**, 31-54 (1982)

Mendelson, R.A., W.A. Bowles and F.L. Finger, *J. Polym. Sci. A-2*, **8**, 105 (1970)

Menon, R.K., M.E. Kim-E, R.C. Armstrong, R.A. Brown, and J.F. Brady, *J. Non-Newt. Fluid Mech*., **27**, 265-297 (1988)

Middleman, S., *Fundamentals of Polymer Processing*, McGraw-Hill, New York, 1977

Minoshima, W., J.E. Spruiell and J.L. White, *Polym. Eng. Sci*., **20**, 1166 (1980)

Minoshima, W. and J.L. White, *J. Non-Newt. Fl. Mech*., **19**, 251 (1986)

Moore, Jr., L.D. and R.M. Schulken, Jr., "Rheological Properties", in *Crystalline Olefin Polymers*, eds. R.A.V. Raff and K.W. Doak, Interscience Publishers, New York, 1965.

Moynihan, R.H., D.G. Baird, and R. Ramanathan, *J. Non-Newt. Fluid Mech*., **36**, 255 (1990)

Munstedt, H., *Rheol. Acta*, **14**, 1077 (1975)

Munstedt, H., *Trans. Soc. Rheol*., **23**, 421 (1979)

Munstedt, H., *J. Rheol*., **24**, 847 (1980)

Munstedt, H. and H.M. Laun, *Rheol. Acta*, **20**, 211 (1981)

Nason, H.K., *J. Appl. Phys*., **16**, 338 (1945)

Natta, G., P. Pino, G. Mazzanti and R. Lanzo, *Chim. Ind. (Milan)*, **39**, 1032 (1957)

Nielson, L.E., *J. Appl. Phys*., **25**, 1210 (1954)

Oda, K., J.L. White and E.S. Clark, *Polym. Eng. Sci*., **18**, 25 (1978)

Papanastasiou, A.C., L.E. Scriven, C.W. Macosko, *J. Rheol*., **27**, 387 (1983)

Pebsworth, L. W., "Low Density Polyethylene", in *Encyclopedia of Chemical Technology*, Vol. 17, ed. R.I. Kroschwitz, Wiley-Interscience, New York, 1999.

Perez-Gonzalez, J. and L. de Vargas, *J. Rheol*., **44**, 441 (2000)

Peticolas, W.L., *J. Polym. Sci*., **58**, 1405 (1962)

Peticolas, W.L. and J.M. Watkins, *J. Am. Chem. Soc*., **79**, 5083 (1959)

Petrie, C.J.S. and M.M. Denn, *A.I.Ch.E. J*., **22**, 209 (1976)

Phan-Thien, N. and R.I. Tanner, *J. Non-Newt. Fluid Mech*., **2**, 353-365 (1977)

Phan-Thien, N., *J. Rheol*., **22**, 259-283 (1978)

Piau, J.M., N. El Kissi, F. Toussaint, and A. Mezghani, *Rheol. Acta*, **34**, 40 (1995)

Piau, J.M., N. El-Kissi, and B. Tremblay, *J. Non-Newt. Fluid Mech*., **30**, 198 (1988)

Pigeon, M.G. and A. Rudin, *J. Appl. Polym. Sci*., **51**, 303 (1994)

Pullukat, T.J., M. Shida and R.E. Hoff, "Titanium Modified Chromium Catalysts for Ethylene Polymerization", in *Transition Metal Catalyzed Polymerizations: Alkenes and Dienes*, ed. R.P. Quirk, Harwood Academic Publishers, New York, 1983.

Rajagopolan, D., R.C. Armstrong and R.A. Brown, *J. Non-Newt. Fluid Mech*., **36**, 135 (1990)

Raju, V.R., G.G. Smith, G. Marin and J.R. Knox, *J. Polym. Sci*.: *Polym. Phys*., **17**, 1183 (1979)

Raju, V.R., H. Rachapudy and W.W. Graessley, *J. Polym. Sci*.: *Polym. Phys*., **17**, 1223 (1979)

Ramamurthy, A.V., *J. Rheol*., **30**, 337 (1986)

Reddy, J.N., *An Introduction to the Finite Element Method*, Mc-Graw Hill Book Company, New York, 1984.

Rivlin, R.S. and K.N. Sawyers, *Ann. Rev. Fluid Mech*., **3**, 117-146 (1971)

Roedel, M.J., *J. Am. Chem. Soc*., **75**, 6110 (1953)

Roovers, J., *Macromolecules*, **17**, 1196 (1984)

Roovers, J. and W.W. Graessley, *Macromolecules*, **14**, 766 (1981)

Samurkas, T., R.G. Larson and J.M. Dealy, *J. Rheol*., **33**, 559-578 (1989)

Schaefgen, J.R. and P.J. Flory, *J. Am. Chem. Soc*., **70**, 2709 (1948)

Schreiber, H.P. and E.B. Bagley, *J. Polym. Sci*., **58**, 29 (1962)

Schroff, R.N. and H. Mavridis, *Macromolecules*, **32**, 8454 (1999)

Sinn, H. and W. Kaminsky, *Adv. Organomet. Chem*., **18**, 99 (1980)

Sinn, H., W. Kaminsky, H.-J. Vollmer and R. Woldt, *Angew. Chem.*, **19**, 390 (1980)

Saeda, S., T. Suzuki and K. Yamaguchi, *J. Appl. Polym. Sci*., **15**, 277 (1971)

Soares, J.P. and A.E. Hamielec, "Semicrystalline Polyolefins – Narrow MWD and Long Chain Branching: Best of Both Worlds", in *Metallocene-Catalyzed Polymers: Materials, Properties, Processing & Markets*, eds. G.M. Benedikt and B.L. Goodall, Plastics Design Library, New York, 1998.

Spencer, R.S. and R.E. Dillon, *J. Coll. Sci*., **3**, 163 (1948)

Spencer, R.S. and R.E. Dillon, *J. Coll. Sci*., **4**, 241 (1949)

Stevens, J.C. and D.R. Neithamer, U.S. Patent 5 064 802, to The Dow Chemical Company, November 12, 1991

Tordella, J.P., *J. Appl. Phys*., **27**, 454 (1956)

Tordella, J.P., *Trans. Soc. Rheol*., **1**, 203 (1957)

Tordella, J.P., *J. Appl. Polym. Sci*., **7**, 215 (1963)

Tordella, J.P. "Unstable Flow of Molten Polymers", in *Rheology*, F.R. Eirich, ed., Vol. V, Academic Press, New York (1969)

Tremblay, B. *J. Rheol*., **35**, 985 (1991)

Tzoganakis, C., J. Vlachopoulos, A.E. Hamielec and D.M. Shinozaki, *Polym. Eng. Sci*., **29**, 390 (1989)

Uhland, E., *Rheol. Acta*, **18**, 1 (1979)

Van Schaftingen, J.J. and M.J. Crochet, *J. Non-Newt. Fluid Mech*., **18**, 335-251 (1985)

Varennes, S. and H.P. Schreiber, *J. Adhes*., **46**, 3 (1994)

Vega, J.F., A. Munoz-Escalona, A. Santamaria, M.E. Munoz and P. Lafuente, *Macromolecules*, **29**, 960 (1996)

Vega, J.F. A. Munoz-Escalona, A. Santamaria, and P. Lafuente, *Macromolecules*, **31**, 3639 (1998)

Venet, C. and B. Vergnes, *J. Rheol*., **41**, 873 (1997)

Vinogradov, G. V. and A.Y. Malkin, *Rheology of Polymers*, Springer-Verlag, Berlin, 1980.

Vinogradov, G.V., A. Y. Malkin, Y.G. Yanovskii, E.K. Borisenkova, B.V. Yarlykov, and G.V. Berezhnaya, *J. Polym. Sci*., A2, **10**, 1061 (1972)

Vinogradov, G.V., *Rheol. Acta*, **14**, 942 (1975)

Vinogradov, G.V., V.P. Protasov, and V.E. Dreval, *Rheol. Acta*, **23**, 46 (1984)

Vinogradov, G.V., M.L. Friedman, B.V. Yarlykov, and A. Ya. Malkin, *Rheol. Acta*, **9**, 323 (1970)

Vlachopoulos, J. and M. Alam, *Polym. Eng. Sci*., **12**, 184 (1972)

Wang, S.Q., P.A. Drda, and A. Baugher, ANTEC, 1006 (1997)

Wang, S.-Q. and P.A. Drda, *Macromolecules*, **29**, 2627 (1996)

White, S.A. and D.G. Baird, *J. Non-Newt. Fl. Mech*. **29**, 245 (1988)

Wild, L., R. Ranganath and D.C. Knobeloch, *Polym. Eng. Sci*., **16**, 811 (1976)

Wissbrun, K.F., *J. Rheol*., **30**, 1143 (1986)

Wood-Adams, P.M. and J.M. Dealy, *Macromolecules*, **33**, 7481 (2000a)

Wood-Adams, P.M. and J.M. Dealy, *Macromolecules*, **33**, 7489 (2000b)

Yamamoto, M., *J. Phys. Soc. Jpn*., **11**, 413 (1956)

Yamane, H. and J.L. White, *Polym. Eng. Rev*., **2**, 167 (1982)

Yang, X., H. Ishida, and S.-Q. Wang, *J. Rheol*., **42**, 63 (1998)

Yeh, P.W., M.E. Kim-E, R.C. Armstrong and R.A. Brown, *J. Non-Newt. Fluid Mech*., **16**, 173-194 (1984)

Zeichner, G.R. and O. Patel, *Proc. of 2nd World Congress of Chemical Eng*., **6**, 333 (1980)

Ziegler, K., H. Breil, H. Martin and E. Holzkamp, Ger. Patent 973 626, to Karl Ziegler, April 14, 1960.

Zletz, A., U.S. Patent 2 692 257, to Standard Oil Co. (Indiana), May 17, 1952

Zucchini, U. and G. Cecchin, *Adv. Polym. Sci*., **51**, 101 (1983)

3.0 Experimental and Numerical Methods

Preface

This chapter provides additional information regarding the experimental and numerical methods used for this research. The information contained within is meant to supplement the brief descriptions provided in later chapters (manuscripts) and provide a guide for future Polymer Processing Laboratory personnel.

This chapter presents relevant details regarding the materials studied, the experimental apparatus and procedure followed, and the numerical methods utilized to fulfill the research objectives identified in the previous chapter. Section 3.1 identifies the polyethylene resins that are used during the course of this work. Section 3.2 presents the rheometric test methods used to characterize each of the polyethylene resins. Sections 3.3, 3.4, and 3.5 summarize the experimental apparatus and methods used for the melt fracture analysis, flow visualization, and pressure profiling, respectively. Lastly, section 3.6 will review the hardware and software used for performing numerical simulations as well as the software execution procedure.

3.1 Materials Studied

This work focuses on the rheology and flow behavior of two classes of polyethylene resins. The first class of resins is the crux of this research project and consists of sparsely long-chain branched and linear metallocene-catalyzed polyethylenes (MCPE). These materials are compared and contrasted in order to understand the subtle effects of sparse degrees of long-chain branching on the flow behavior of narrow molecular weight distribution polyethylene resins. The second class of materials includes the ``conventional'' PE resins. Specifically, highly branched LDPE and strictly linear LLDPE are included in this particular classification. These resins serve as branched and linear controls with which to compare to the MCPE resins, and thus gauge their *processability*.

Table 3.1: Polyethylene Resin Data

Resin	$\mathbf{M_w}$	$\mathbf{M_w/M_n}$	$\mathbf{M_z}$	*LCB* /10^4 C
Exact 0201	88 700	2.14	158 900	0.79
Exact 3132	111 000	2.04	180 400	—
Affinity PL1840	87 400	2.43	160 200	0.57
Affinity PL1880	115 800	2.12	183 700	0.18
NTX101	122 700	3.44	319 700	—
NA952	235 500	17.1	2 619 300	39[a]

[a]: C^{13} NMR measurement

3.1.1 Metallocene-Catalyzed Polyethylenes

The metallocene-catalyzed polyethylene resins are divided into two groups. The first group consists of sparsely long-chain branched resins and the second consists of strictly linear resins. The reasons for having both groups is to understand the overall significance of long-chain branching on rheology and flow behavior, and to better quantify the sensitivity of flow properties to branch content. All of the MCPE resins analyzed in this study are commercially available resins developed for film blowing applications. Furthermore, none of these film-grade resins contains processing aids or slip/antiblock agents that might alter their inherent melt flow behavior.

All of the MCPE resins have been characterized by researchers at Dow Chemical (Freeport, TX) using high-temperature gel permeation chromatography (GPC) coupled with dilute solution low-angle laser light scattering (LALLS). The theoretical basis for this particular technique can be found elsewhere [Zimm(1949)]. This combined-technique method provides typical molecular weight distribution curves, but also gives an indication of the long-chain branch content. The molecular characteristics of each of the MCPE resins are tabulated in Table

3.1. All of the MCPE resins used in this study have narrow molecular weight distributions (MWD ~ 2), characteristic of metallocene-catalyzed polyolefins.

The sparsely branched MCPE resins contain different degrees of long-chain branching content. They include the Dow Affinity PL1840, Dow Affinity PL1880 and ExxonMobil Exact 0201 resins. The Dow Affinity resins have been produced using the Dow constrained-geometry [metallocene] catalyst (CGC) technology spoken of in Section 2.1, while the Exact resin has been produced using the EXXPOL® catalyst technology. Table 3.1 shows that the Affinity PL1880 resins contains the lowest branch content of the three resins at 0.18 LCB/10000 carbons, but has the highest weight-averaged molecular weight (M_w) at 115,800 g/mol. Conversely, the Exact 0201 resin has the highest branch content at 0.79 LCB/10^4 carbons, yet one the lowest M_w. The Affinity PL1840 is similar in molecular weight to the Exact 0201 resin, but has an intermediate degree (0.57 LCB/10^4 carbons) of long-chain branching. All of the branched MCPE resins described are ethylene-octene copolymers.

The linear MCPE resin used for this study is the Exact 3132 resin. Exact 3132 is manufactured using the EXXPOL® catalyst technology. The linear MCPE resin has been characterized in a similar manner to the branched MCPE resins and the results can be found in Table 3.1. The molecular analysis confirms that no long-chain branches are present, as expected. The molecular weight and MWD are similar in value to the branched Affinity PL1880 resin. Finally, the Exact 3132 resin is an ethylene-hexene copolymer.

3.1.2 Conventional Polyethylenes

In addition to the MCPE resins, a set of conventional polyethylene resins has been investigated. The conventional resins include a high-temperature, high-pressure autoclave

produced low-density polyethylene (LDPE) manufactured by Equistar, and a Ziegler-Natta polymerized ethylene-hexene copolymer produced by ExxonMobil. The conventional LDPE is commercially designated as NA952 and has a melt flow index of 2.0; the conventional LLDPE is commercially designated as NTX101 and has a melt flow index of 0.9. Furthermore, the molecular characteristics of each of these resins can also be found in Table 3.1. Neither resin has processing aids nor slip/antiblock agents that might obscure their true melt flow behavior. Although these resins represent more complex fluids, with broader molecular weight distributions than the MCPE resins, they embody the typical responses of branched and linear polyethylenes, respectively. Therefore, these conventional resins will serve as experimental controls with which to compare the branched and linear MCPE resins.

3.2 Rheological Characterization

In order to realize the effects arising from molecular structure, and more specifically from long-chain branching, the rheological properties of these resins must first be measured. Rheological characterization is generally divided into two separate flow kinematics: shear and shear-free flows. The kinematic arguments and relevant equations are presented earlier (Section 2.2.1). In this section, the apparatus used to perform rheological measurements and the operating procedures used to acquire kinematic specific data will be presented.

3.2.1 Shear Rheology

The shear rheological measurements can be further divided into two categories. These two categories are homogeneous and nonhomogeneous shearing flows. Homogenous flows are characterized by deforming stresses that are independent of position, while nonhomogeneous

flows exhibit spatial dependence. This comparison is the same as that between drag flows and pressure-driven flows. In this study, a torsional rheometer has been used to obtain homogeneous rheological data and a capillary rheometer has been used to obtain nonhomogeneous rheological data. Although both methods provide shear viscosity, the versatility and range of data available differs.

Torsional Rheometry

Steady shear and small-amplitude dynamic oscillatory experiments are performed using a Rheometrics Mechanical Spectrometer Model 800 (RMS-800). The RMS-800 is a controlled strain torsional rheometer capable of steady angular rotation and dynamic oscillatory displacements. A dual range force rebalance transducer (FRT) is used to measure both torque and normal force response during testing. Each test is performed within an inert nitrogen environment using cone-and-plate test fixtures having a plate diameter of 25mm and a cone angle of 0.1 radians. This particular configuration provides the most accurate rheological data due to the homogeneous deformation field.

The RMS-800 provides viscoelastic data in the range of 0.001 to 100 s^{-1}. Steady shear deformation provides shear viscosity (η) and primary normal stress difference (N_1) data in the range of 0.001 to 1.000 s^{-1}. Small-strain dynamic oscillatory deformations provide complex viscosity (η^*), storage modulus (G'), and loss modulus (G") data in the range of 0.1 to 100 rad/s. In most cases, the Cox-Merz rule has been assumed to hold true ($\omega = \dot{\gamma}$).

Capillary Rheometry

Nonhomogeneous steady shear experiments at shear rates greater than 10 s^{-1} are performed using a Goettfert Rheograph 2001 (RG2001). The RG2001 is a controlled displacment capillary rheometer capable of volumetric displacements of 3.5 cm^3/s and applied loads of 20 kN. The dies used for rheological analysis are tungsten carbide steel capillaries with die diameters of 1 mm and lengths of 10, 20, and 30 mm. Furthermore, each of the dies has a 180° included entry angle (flat entrance) and a barrel-to-capillary contraction ratio of 15.

The RG2001 provides steady shear viscosities (η) in the range of 10 to 1000 s^{-1}. Because of the nonhomogeneous flow field the steady state shear viscosity is the only relevant quantity. The limits of accuracy are determined by the sensitivity of the mounted pressure transducer at low rates and the onset of melt fracture at high rates. Due to the large contraction ratio, a Bagley end analysis is typically performed to correct the effects of entrance pressure loss on the wall shear stress and shear viscosity. Furthermore, the Rabinowitsch correction is also utilized to correct for non-parabolic flow profiles within the capillary.

3.2.2 Extensional Rheology

Uniaxial extensional measurements are carried out using a Rheometrics Extensional Rheometer Model 9000 (RER-9000). The RER-9000 is based on the original design by H. Munstedt (1979) in which a homogeneous molded cylindrical sample is suspended in a heated oil bath and fixed between a stationary platform and a mobile drawing arm. Figure 3.1 represents a basic schematic of the device. The density of the oil (Dow Corning Fluid 200) is so chosen to match the resin density at the test temperature, therefore creating a neutrally buoyant environment. The applied force resulting from deformation is measured using a linear variable

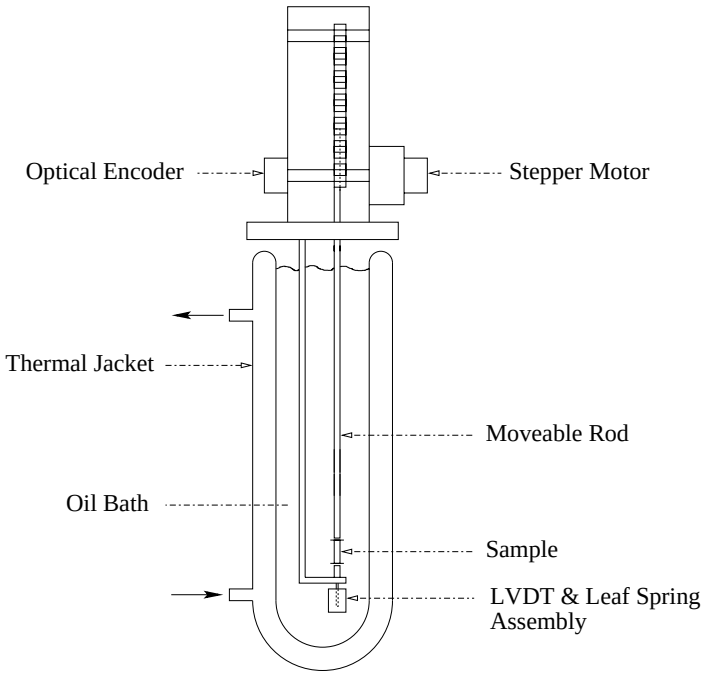

Figure 3.1: RER9000 Schematic

differential transformer (LVDT). A viewing window is used to assure that homogeneous deformation of the sample occurs.

The RER-9000 provides homogeneous uniaxial deformation at a specified applied strain rate or stress. The instrument is capable of applying extensional strain rates from 0.001 to 5 s^{-1}, however the practical limit is generally found to be 1 s^{-1}. The maximum strain, using 22 mm samples, is typically found to be 3.0 strain units. Because the presence of a free surface often leads to nonhomogeneous or nonuniform deformation, many duplicate tests are performed. Those samples that ``appear" to deform uniformly are averaged to obtain a statistical response for a given strain rate and strain.

3.3 Melt Fracture Analysis

The experiments examining the melt fracture behavior of metallocene and conventional polyethylene resins were found to require two key components. The first component consists of

a pumping device capable of accurately metering polymer melt at a desired flow rate. The second component is an imaging device that can resolve both gross and fine features of extruded samples. In the following section, the chosen apparatus and operating procedures used to perform the melt fracture studies will be outlined.

3.3.1 Apparatus

The Goettfert Rheograph 2001 (RG2001) capillary rheometer (see Section 3.2.1) was chosen as the metering device for this study. The RG2001 is a positive displacement pump that provides very accurate metering of polymer melt through round capillary dies. The RG2001 is fitted with a pre-contraction pressure transducer port that is used to measure transient and steady-state driving pressures. Additionally, a high-speed data acquisition system consisting of a 12-bit A/D acquisition card (Model ADM12-11) by Quatech and an IBM-compatible personal computer (PC) are utilized to rapidly measure pressure fluctuations during slip-stick flow conditions.

The imaging device chosen for this study is either a Cambridge Instruments Stereoscan Model 200 scanning electron microscope (SEM) or a Leo 1550 field emission scanning electron microscope (FE-SEM). An SEM was found to be most versatile because it can provide both coarse and fine resolution micrographs of the extruded melt fracture samples. Furthermore, scanning electron microscopy provides greater image contrast than optical microscopy when imaging semi-transparent materials like polyethylene.

3.3.2 Operating Procedure

In the next two subsections, detailed instructions for obtaining and imaging melt fracture specimens using the apparatus described earlier are provided.

Sample Collection

1. Prepare the Rheograph 2001 for operation according to the instrument user manual. This step includes setting the operating temperature, installing the capillary die, and installing and calibrating the pressure transducer.
2. Enter the desired piston rate (0.0001 to 20 mm/s) and activate the servo-hydraulic system.
3. Allow the driving pressure to equilibrate. If unsteady flow conditions occur, attach the high-speed data acquisition system to the chart recorder input leads and capture the sinusoidal pressure response.
4. Obtain multiple samples of the extrudate and quench in water.
5. Document the extrusion temperature, capillary dimensions, and pressure reading for each sample collected.
6. Repeat steps 2-5 for each subsequent piston rate.
7. Repeat steps 1-6 for each extrusion capillary used.

Imaging

1. Securely mount each sample onto a separate specimen stage using conductive tape.
2. Sputter coat the specimens with 10nm thick layer of gold.

3. Prepare the Leo 1550 for operation according to the instrument user manual. This step includes mounting the specimen stages, evacuating the imaging chamber, and positioning each specimen stage for imaging.
4. Obtain micrographs at 20x & 50x magnification.
5. Label the micrograph(s) appropriately and document relevant imaging parameters.
6. Repeat steps 4-5 for each melt fracture specimen.

3.4 Flow Visualization

The flow visualization experiments are very complex studies that consist of a large number of components and require precise measurement of experimental quantities. The current section will provide an overview of the apparatus and operating procedure used to obtain isochromatic fringe patterns and particle streak patterns.

3.4.1 Apparatus

The flow visualization studies rely upon three key component systems: the polymer delivery system, the visualization die, and the optical imaging system. The following three subsections will summarize the individual devices that make up the component systems.

Polymer Delivery System

The polymer delivery system has been designed to provide pulseless, precisely metered molten polymer at near isothermal conditions. This is accomplished using a 25.4mm plasticating laboratory extruder (Killion) and 1.752 cc/rev gear pump (Zenith, HPB-5556). The gear pump is driven by a 1/4 horsepower AC motor (US Electric Motors) that operates between 11 and 113

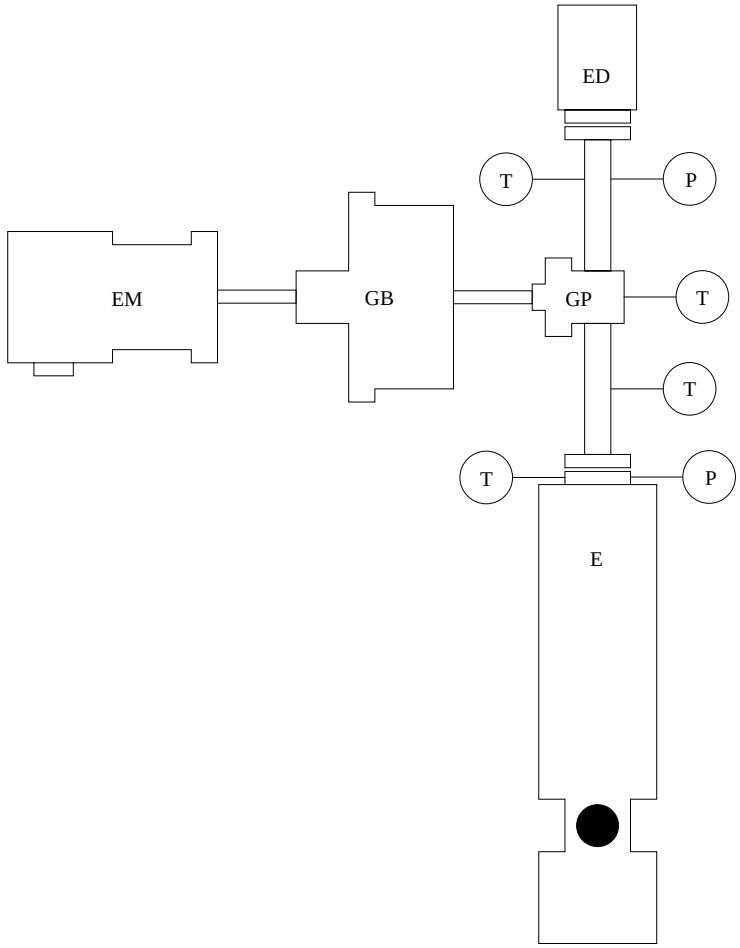

Figure 3.2: Polymer Delivery System. E – Extruder, GP – Gear Pump Assembly, EM – Electric Motor, GB – Gearbox Reducer (optional), ED – Extrusion Die, T – Temperature Probe, P – Pressure Probe.

rpm. Lower flow rates are obtained by placing a gear-reducing unit (Reynolds Ltd.) between the motor and gear pump. The gear reduction ratio is 21.4:1. High-pressure conduit connects the extruder and gear pump assemblies while a high-pressure conduit fitted with a Kenics static mixer connects the gear pump to downstream equipment. The static mixing element is used to thermally and mechanically homogenize the polymer melt.

The primary operating variables are flow rate and melt temperature. The flow rate is manually adjusted by first varying the gear pump drive speed and then adjusting the extruder screw speed to maintain acceptable back pressure on the gear pump inlet. An optical tachometer

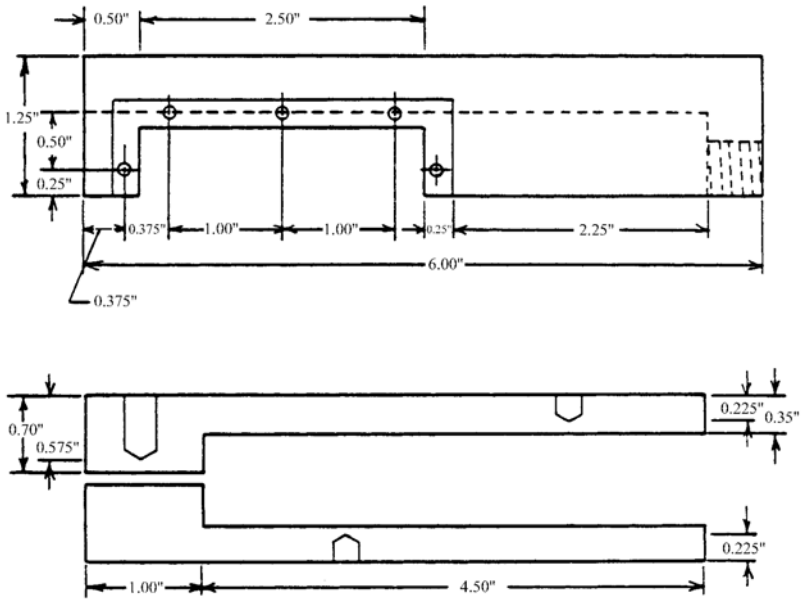

Figure 3.3: Visualization die schematics [White (1987)].

is linked to the gear pump drive shaft to determine the volumetric flow rate. The melt temperature is controlled by 4 sets of heating elements. The first set is found in the extruder, the second on the extruder-gear pump connecting conduit, the third on the gear pump assembly, and the fourth on the static mixer assembly. All four regions are regulated around a desired set point via PID controllers.

Visualization Die

The visualization die used for this study is a planar contraction die originally designed and constructed by S. White [White (1987)]. The basic features and dimensions of the die are found in Figure 3.3. The die is machined from 316 stainless steel and features insert slots that can be used to vary the contraction geometry. This study employs the previously machined 8:1 planar contraction geometry inserts. The upstream slit dimensions are 25.4 x 20.3 x 114.3 mm (WxHxL) and the downstream slit dimensions are 25.4 x 2.54 x 25.4 mm. The machining

tolerance is 0.026mm. Heating of the die is accomplished using three, independently controlled sets of strip resistance heaters (Industrial Heater Co.).

The most unique features of the visualization die are the optical windows. Two rectangular windows are positioned on opposite sides of the contraction region. The optical windows are made from commercial grade quartz (Dell Optics) and have dimensions of 25.4 x 31.7 x 63.5 mm (WxHxL). The thickness was specifically chosen to withstand the large hydrostatic pressures present at high flow rates. The windows are secured using silicone gasket material and steel retaining brackets.

Optical Imaging System

The optical system is used to *illuminate* the flow field. The specific attributes and components are determined by the particular study. For flow birefringence studies, the generation of isochromatic fringe patterns requires a monochromatic light source, polarization optics, and imaging device [Janeschitz-Kriegle (1983)]. The monochromatic light source chosen for this study is an unpolarized 0.5 mW He-Ne laser (Spectra Physics). The characteristic wavelength is 632.8 nm. Because the beam diameter is only 0.9mm, it is expanded using a 10x objective lens (Tower) and 76.2 mm collimating lens (Oriel). The expanded beam is then passed through a ``polarizer'' with its optic axis rotated 45 degrees from the flow direction. The polarized beam passes through the visualization die and proceeds through the ``analyzer''. The analyzer is a matched polarizing optic with its optic axis orthogonal to the ``polarizer''. The resulting beam is then focused using a 76.2 mm focusing lens (Oriel) and imaged using a digital camera (Sony TRV900). All optic components are mounted to an optic rail to maintain alignment.

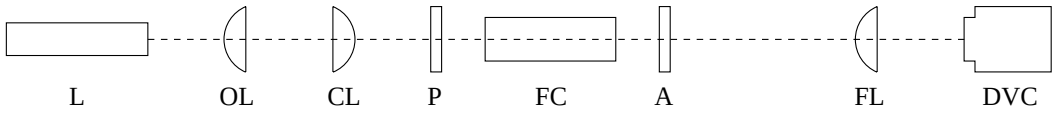

Figure 3.4: Optial Rail Assembly. L – Laser, OL – Objective Lens, CL – Collimating Lens, P – Polarizer (Plane or Circular), FC – Flow Cell, A – Analyzer (Plane or Circular), FL – Focusing Lens, DVC – Digital Video Camera.

The "polarizer" and "analyzer" can be either plane or circular polarizers. Plane polarizers simply polarize the incident beam along the optic axis. Plane polarization gives rise to dark field patterns which represent whole order fringes (N=0,1,2,...). On the other hand, circular polarization combines a plane polarizer with a quarter wave plate. This combination yields a retarded wave and gives rise to light field patterns which represent half order fringes (N=1/2, 3/2, 5/2, …). The mathematical details pertaining to flow birefringence can be found in Appendix G.

The particle streak patterns are produced using a much simpler setup. White light illuminates the flow cell at a 45 degree angle and reflects off of solid particles dispersed in the melt stream. These particles are generated by adding 0.5% by weight of powdered nickel or iron to the extruder feed. Generally, a small amount of mineral oil is added to better disperse the powdered metal and prevent settling in the extruder throat. A digital camcorder (Sony TRV900) is used to record the streaming particles. The recorded flow patterns are then manipulated using Adobe Photoshop 5.0 to obtain time-lapsed streak patterns.

3.4.2 Operating Procedure

In the next three subsections, detailed instructions for obtaining isochromatic fringe patterns and particle streak patterns are provided. A procedure common to both experiments will be provided first, followed by experiment specific instructions.

System Initialization

1. Turn on extruder and temperature controllers.
2. Set temperature setpoints and allow one hour soak time.
3. Set the zero and gain (80\% scale) of all pressure transducer indicators.
4. Feed polymer pellets into the extruder hopper and initiate screw rotation at 10 rpm.
5. Once considerable backpressure is observed (~1000 psi), reduce screw speed and initiate gear pump motor (setting 0).
6. Bring gear pump motor to desired speed and adjust extruder screw speed to maintain 1000 psi back pressure on extruder pressure transducer.
7. Allow 30 minute purge period to remove resident polymer melt.

Isochromatic Fringe Patterns

8. Install and align the optic components as illustrated in Figure 3.4. Assure that the expanded, collimated beam is centered around the contraction entrance along the neutral flow axis (z-axis).
9. Obtain dark field stress patterns by placing the plane polarizers along the optical rail. Insure that the polarization axes are crossed.
10. Replace the plane polarizers with the circular polarizers and obtain the light field pattern. Insure that the quarter wave plates are facing each other and that the polarization axes remain crossed.
11. Repeat steps 8 and 9 for each flow rate.
12. Extract still images for each flow rate using digital video software (MiroVideo 200).

Particle Streak Patterns

8. Add the powdered metal tracers to the feed polymer and allow sufficient time for complete dispersal of tracer particles across the viewing region.
9. Align the digital video camera with the visualization die and orient the light source to get maximum reflection and contrast of the embedded tracer particles.
10. Record the flow from 5 to 20 minutes, depending on the imposed flow rate.
11. Repeat step 9 for each flow rate.
12. Extract the full motion video for each flow rate and generate streak patterns using image manipulation software.

3.5 Pressure Profiling

The pressure profiling studies investigate the effects of an abrupt planar contraction on the flow behavior of polyethylene melts. Specifically, the observed pressure drop along the flow axis will be measured. The following section will summarize the key components of the apparatus used, and the operating procedure used to perform the studies.

3.5.1 Apparatus

The pressure profiling apparatus is similar to that of the flow visualization studies. The same polymer distribution system described previously is also used for metering polymer melt to pressure profiling die. The main difference is that of the extrusion die utilized. The profiling die was fabricated specifically for this study. The relevant dimensional schematics can be found in Figures 3.5 and 3.6. The profiling die is machined from 440C stainless steel and consists of six pressure transducer ports machined along the slit flow path. Four of these ports are placed

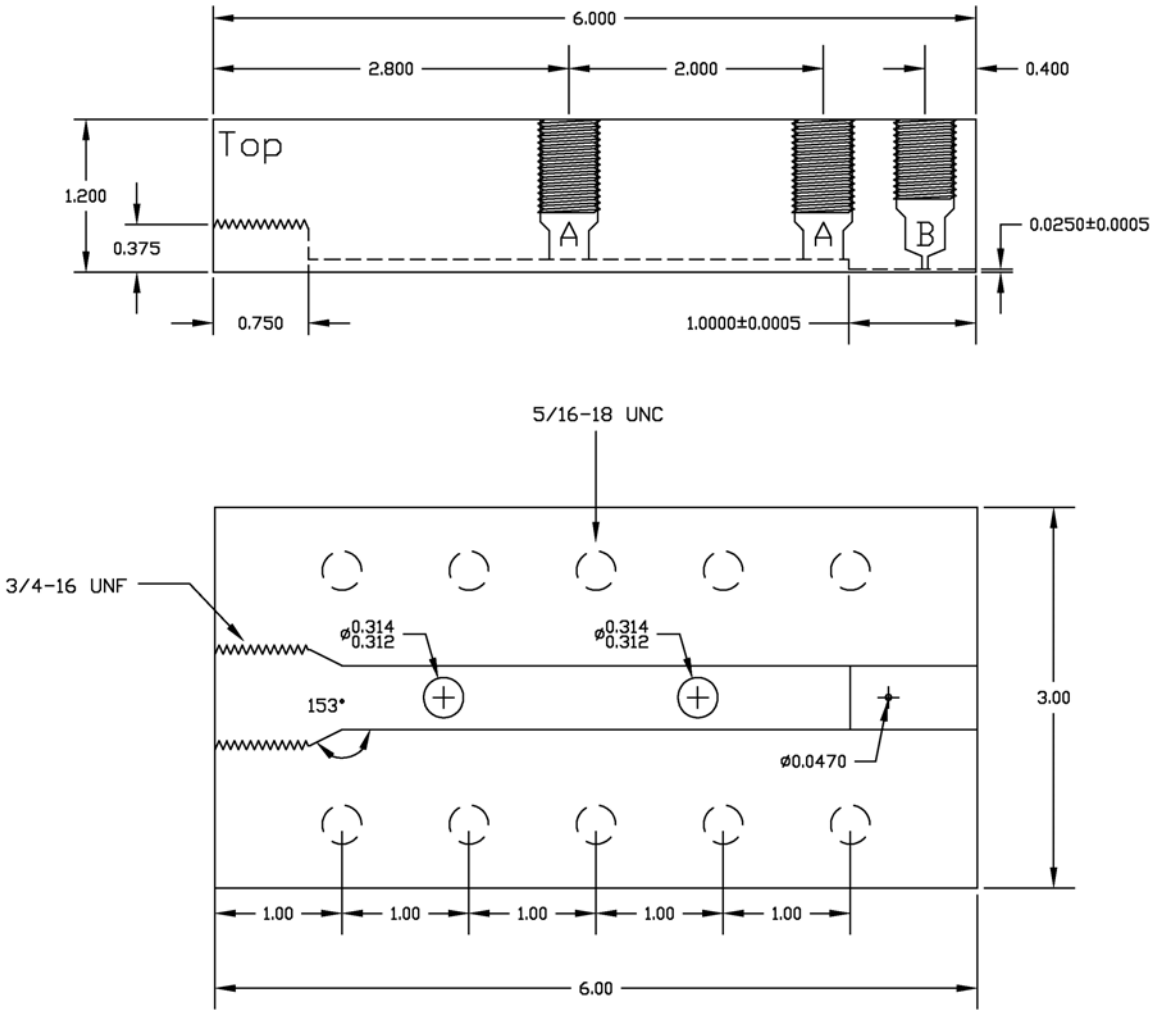

Figure 3.5: Profiling Die (Top half)

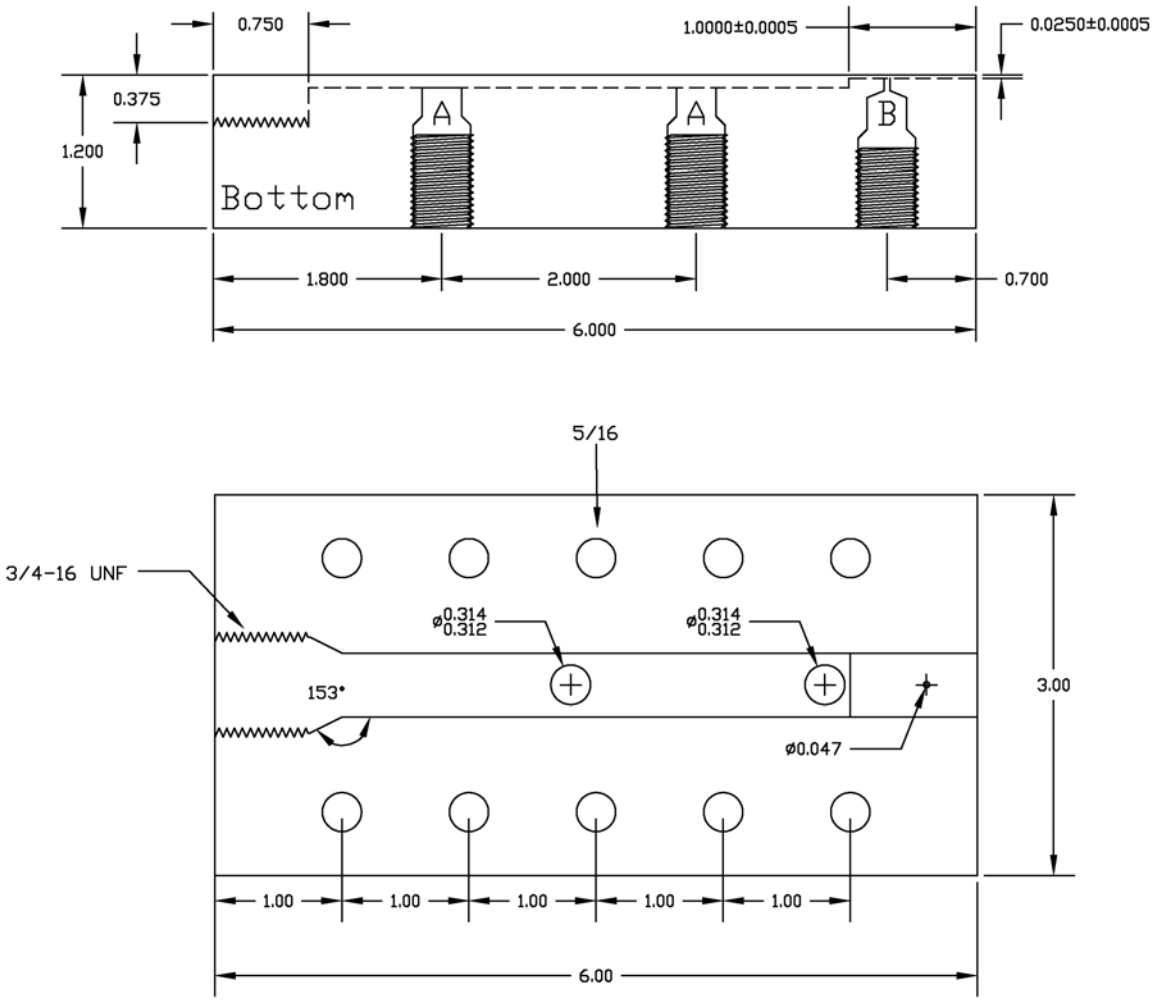

Figure 3.6: Profiling Die (Bottom Half)

upstream of the abrupt 4:1 planar contraction, the remaining two ports are found downstream. The upstream slit dimensions are 12.7 x 2.54 x 108.0 mm (WxHxL) and the downstream dimensions are 12.7 x 0.635 x 25.4 mm (WxHxL). These dimensions were chosen in order to augment the maximum achievable shear rate to approximately 100 s^{-1}.

The pressure measurements were obtained using melt pressure transducers (Dynisco PT422A) with maximum pressure ranges from 34.5 to 103.4 bars (500 to 1500 psi). Calibration of these transducers was performed using a dead weight tester (Model No. 23-1) manufactured by Chandler Engineering (Tulsa, OK). Practical pressure measurements were obtained using scaled pressure indicators (Dynisco ER478) or the Quatech A/D data acquisition card described earlier.

Temperature control of the die is accomplished using two enclosing aluminum heating plates that are securely fastened to the top and bottom faces of the die. The aluminum plates have been pre-drilled to accept twelve 150W 6.35 x 38.1 mm (0.25 x 1.5 in.) cartridge heaters. Combined with appropriate temperature controllers (Omega CN9000), these heating plates provide near isothermal flow conditions within the profiling die.

3.5.2 Operating Procedure

The current subsection provides instructions for initializing the polymer delivery system, preparing the profiling die for use, and obtaining pressure measurements during operation.

System Initialization

1. Turn on extruder and temperature controllers.
2. Set temperature setpoints and allow one hour soak time.

3. Set the zero and gain (80\% scale) of all pressure transducer indicators.
4. Feed polymer pellets into the extruder hopper and initiate screw rotation at 10 rpm.
5. Once considerable backpressure is observed (~1000 psi), reduce screw speed and initiate gear pump motor (setting 0).
6. Bring gear pump motor to desired speed and adjust extruder screw speed to maintain 1000 psi back pressure on extruder pressure transducer.
7. Allow 30 minute purge period to remove resident polymer melt.

Pressure Measurements

8. While the polymer distribution system components are heating: attach the heating plates, install the pressure transducers, and initiate heating of the profiling die. Allow a one-hour soak and then set the zero and gain (80% scale) for all pressure transducer indicators.
9. During operation, record the indicated pressure for each of the six melt transducers.
10. Repeat step 9 for each subsequent flow rate.

3.6 Numerical Simulations

Numerical simulations are performed to assess the ability to predict the flow behavior of the metallocene and conventional polyethylene resins under complex flow conditions. The computational method and capacity greatly determine the practical limits of computational efficiency. In the following subsections, the hardware and software packages used to perform numerical simulations, and the numerical procedure used to obtain flow predictions are summarized.

3.6.1 Hardware & Software

All of the numerical simulations undertaken in this project were performed using a Silicon Graphics Inc. (SGI) Origin 200 server. The Origin 200 is a deskside, entry level workgroup server supporting one to four MIPS processors. Currently, the Origin 200 is fitted with two 270 MHz IP27 RISC processors and 512 MB of main memory. The installed 64-bit operating system is IRIX 6.5.10f. In addition to the numerical simulations, the curve and parameter fitting calculations are performed using a personal Pentium III 733 MHz computer.

The software used for this study can be divided between two classifications, parameter fitting applications and finite element method simulations. The parameter fitting software is self-written and coded in the Fortran 90 conventions. Absoft Pro Fortran 6.0 (academic) is used to compile the source code into an executable format. Fitting programs for the Generalized Newtonian Fluid (GNF), Phan-Thien and Tanner (PTT) and McLeish-Larson Pom-Pom models have been written. Furthermore, IMSL numerical subroutines, available from Visual Numerics, are used to solve ordinary and partial differential equations as well as numerical integration calculations. A complete listing of all relevant Fortran 90 source code is found in Appendix D.

The finite element method simulation software used for this study is Polyflow 3.8 (Fluent). This particular version is written for the IRIX operating system and therefore used on the SGI Origin 200 server. The Polyflow 3.8 software suite consists of four discrete applications: GAMBIT, Polydata, Polyflow, and FlPost. The GAMBIT application is used to define and mesh the desired flow region. Polydata is used to specify simulation parameters: the flow boundary conditions, the chosen constitutive equation, the interpolation techniques, and local and global convergence criteria. Polyflow is the finite element method solver and actually

performs the simulation calculations. The final application, FlPost, is a postprocessor application and provides visualization of the simulation results in a convenient, graphical manner.

3.6.2 Procedure

The procedure used for obtaining accurate numerical simulations does not follow a strict "operating procedure", but rather a methodology. In this section, a *method* for performing numerical simulations that are derived from physical experiments and calculated from available rheological data is outlined. Although this approach may not be deemed the most accurate or the most efficient, it has been determined to be the most consistent one across many different fluid descriptions.

Parameter Fitting

Parameter fitting is arguably the most important step involved in obtaining accurate numerical predictions. It is during this step that experimentally measured data is translated into a considerably smaller set of constitutive parameters. Therefore, it is very important to understand the flow kinematics and range of applicability associated with the rheological measurements in comparison to that of the simulated geometry. Excessive extrapolation of rheological properties beyond experimentally measured bounds may lead to significant inaccuracies in the resulting numerical predictions.

The parameter fitting method consists of three steps. The first step is fitting available linear viscoelastic data to obtain the discrete relaxation spectrum. Linear viscoelastic data is usually comprised of G', G'', and η in the zero-shear viscosity plateau. The discrete relaxation spectrum, composed of a finite number of relaxation times and strengths, is calculated using the

fitting programs. The general rule of thumb is one relaxation time per decade of data. The fitting algorithms implement non-linear least squares minimization to obtain the relaxation strengths at each user-supplied relaxation time.

The second step involves the fitting of the nonlinear shear parameters found within each of the constitutive equations investigated. Because all of the parameters in the GNF model are nonlinear shear parameters, nonlinear regression is used to obtain the model parameters by reducing the sum of the squared errors. For the PTT model, the ξ parameter is the nonlinear shear parameter, while for the Pom-Pom model τ_s is the respective nonlinear parameter. The difference between each of these parameters is the source of rheological data used for fitting. ξ is generally determined from manual shifting of $\eta(\dot{\gamma})$ to overlay on $\eta'(\omega)$ data. Therefore numerical fitting is not utilized. τ_s is significantly more difficult to obtain from shear data alone and is often determined with the use of extensional data as well. The combination of the nonlinear shear parameter and discrete relaxation spectrum provides more accurate predictions during *pure* shear deformations.

The final step is fitting extensional viscosity growth data to obtain the shear-free parameter. For the PTT model, ε is the nonlinear shear-free parameter, while for the Pom-pom model, q is the nonlinear shear-free parameter. In addition to the relevant rheological data, the use of the discrete relaxation parameter and non-linear shear parameters is also required. Because of the strain-hardening nature of branched PE resins, it is very difficult to obtain steady extensional viscosities. Therefore, most of the available data is transient extensional viscosity data.

Polyflow Simulations

The Polyflow numerical simulations follow are very straightforward method for performing finite element method calculations on user-defined flow domains. As mentioned in the ``Hardware \& Software" section, there are four discrete applications used to setup, execute, and analyze the numerical simulations. Figure 3.7 illustrates the process for carrying out numerical simulations using the Polyflow software suite. A comprehensive description of each application can be found in the respective Polyflow manuals [Polyflow (1998)].

The first application is the GAMBIT mesh generation package. This software application generates two- or three-dimensional, structured or unstructured, finite element meshes. Furthermore, triangular or quadrilateral element geometries are available for 2-D meshes. The user-supplied information includes the mesh dimensions and boundary types. The resulting mesh file is known as a GAMBIT neutral (NEU) file. This mesh file is utilized by the Polydata software application.

The next user-activated application is Polydata. Polydata is used to specify simulation parameters, including: boundary conditions, constitutive equations, variable interpolation techniques, and convergence criteria. Polydata uses the NEU mesh file described above and converts it to a Polyflow compatible MSH file. Polydata then uses this mesh file to map appropriate boundary conditions. The simulation data file (DAT) produced by Polydata is then used as primary input for the finite element solver, Polyflow.

Polyflow is the actual FEM solver. This software application uses the Polydata DAT file as input and generates various output files. The primary outputs are the Fluent mesh (FLUM) and Fluent result (FLUR) files. These files contain the nodal solutions for each independent variable (pressure, velocity, and stress). Furthermore, the Fluent output files are also output for

each evolutive step of the simulation. This is very useful for analyzing the flow development as a function of flowrate or viscoelastic character. Optionally, result probe files (PRB) can be used to monitor variable values at specific locations or nodes within the flow geometry.

The final application is the simulation postprocessor, FlPost. FlPost uses the Fluent output files from Polyflow to visualize the results. Flpost provides pressure, velocity, stress, and streamline contours across the flow domain. These contour patterns can be saved in a graphic format (EPS, TIFF) or printed for future use. Additionally, nodal values can be plotted and/or saved to disk for later use as well.

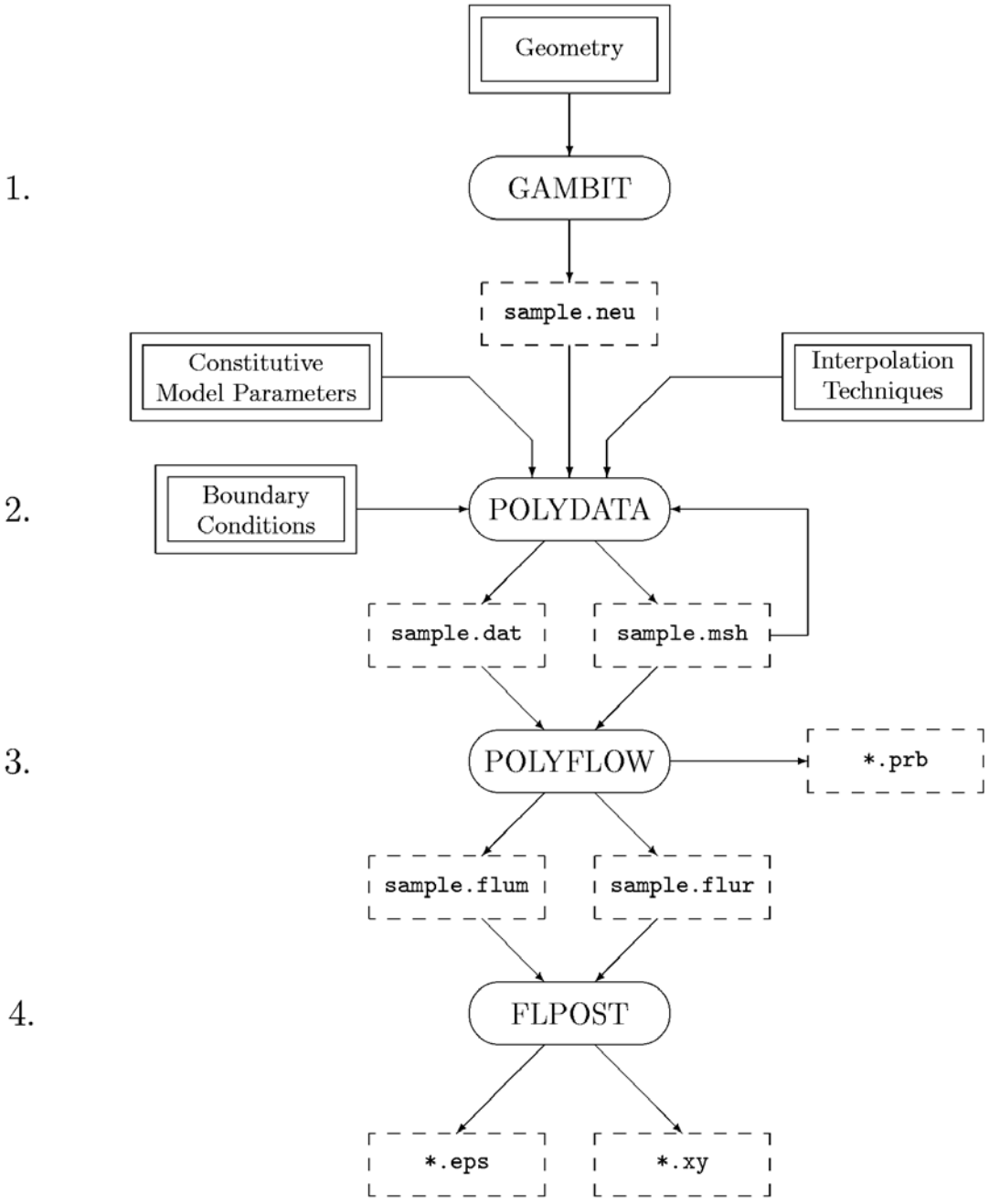

Figure 3.7: Polyflow Simulation Procedure

3.7 References

Janeschitz-Kriegl, H., *Polymer Melt Rheology and Flow Birefringence*, Springer-Verlag, New York, 1983.

Münstedt, H., *J. Rheol*., **23**, 421 (1979).

Polyflow S.A., Belgium, *Polyflow 3.8*, 2000.

White, S.A., *The Planar Entry Flow Behavior of Polymer Melts: Experimental and Numerical Analysis*, Ph.D. Dissertation, Virginia Tech, Blacksburg, VA, 1987.

Zimm, B.H. and H.W. Stockmayer, *J. Am. Chem. Soc*., **17**, 1301 (1949).

4.0 Effects on Shear Rheological Properties

Preface

This chapter addresses the first objective of the research. Specifically, the effects of sparse long-chain branching on the shear rheological properties of metallocene-catalyzed polyethylenes are examined. These rheological properties include the zero-shear viscosity, the onset of shear-thinning behavior, the dynamic storage modulus, and the primary normal stress difference coefficient (Ψ_1). This chapter is organized as a manuscript for future publication.

Separating the effects of sparse long-chain branching from those due to molecular weight in polyethylenes

Phillip J. Doerpinghaus and Donald G. Baird

Department of Chemical Engineering, Virginia Polytechnic Institute and State University Blacksburg, VA 24061-0221

Synopsis

The ability to differentiate the effects of sparse long-chain branching in metallocene-catalyzed polyethylenes from those of molecular weight is evaluated in this study. The time-molecular weight superposition principle is applied to a series of polyethylene resins having differing degrees of long-chain branching and weight-average molecular weights. Four metallocene polyethylenes with degrees of long-chain branching as determined from dilute solution measurements ranging from zero (linear) to 0.79 LCB/10^4 CH_2, along with a conventional Ziegler-Natta polymerized LLDPE, and a tubular free-radical polymerized LDPE are investigated. The results show that long-chain branching can increase the zero-shear viscosity by a factor of six at low concentrations, but contributes to a significant reduction in η_0 at high concentrations (densely branched). Furthermore, the dynamic storage modulus G' shows similar enhancement at low frequencies, while the primary normal stress difference coefficient $\Psi_{1,0}$ exhibits a 20% greater dependence on long-chain branching than that predicted from the zero-shear viscosity enhancement. Surprisingly, a small amount of sparse long-chain branching can reduce the onset of shear thinning by a factor of 100 when compared to a linear polyethylene with the same weight-average molecular weight. Furthermore, the observed viscosity enhancement is qualitatively in agreement with the predicted viscosity enhancement obtained

from the Janzen and Colby viscosity relation evaluated using dilute solution long-chain branching measurements.

4.1 Introduction

The combined effects of molecular weight, molecular weight distribution, and long-chain branching all contribute to the rheological properties of polyethylene resins [Laun and Schuch (1989)]. The development of metallocene polyethylenes (mPE) may provide the ability to distinguish the individual contributions arising from molecular structure because of their narrow molecular weight distribution and controlled levels of sparse long-chain branching. Of most interest is the subtle effect that sparse long-chain branching has on the steady and dynamic oscillatory shear properties of mPE resins. Prior studies on mPE resins have begun to elucidate the influence of sparse long-chain branching on shear rheology[Vega *et al*. (1998), Bin Wadud and Baird (2000), Wood-Adams and Dealy (2000)], but additional interest in quantifying these effects on shear viscosity, dynamic moduli, and normal stresses remains. Therefore, this paper is concerned with addressing those interests.

Long-chain branching in polyethylenes refers to branches having a molecular weight greater than the critical molecular weight for entanglements, M_c. It is then reasonable to expect that LCB should have a strong influence on the relaxation behavior, and thus the rheological properties, of the polymer melt. This influence has long been postulated for the case of low-density polyethylene (LDPE), which has a high degree of long-chain branching. Unfortunately, the free-radical polymerization process by which LDPE is manufactured also gives rise to a broad molecular weight distribution (MWD) [Kiparissides *et al*. (1993)]. Therefore, this convolution with MWD has obscured the distinct effects of LCB.

Metallocene polyethylenes

Metallocene polyethylenes do not suffer from the convolution of LCB and MWD. Branched mPE resins made using constrained geometry catalysts [Lai *et al*. (1993)] have controlled amounts of random, sparse long-chain branching while retaining a relatively narrow molecular weight distribution of approximately two. In this case, sparse branching in mPE resins generally refers to less than one branch per molecule. This differs significantly from the highly branched structure of LDPE resins. As a result, mPE resins now allow researchers to focus exclusively on the effects of long-chain branching independent of other molecular factors.

Recent work with random, sparsely branched metallocene PE resins indicates that long-chain branching does have a discernable effect on shear rheology. Wood-Adams *et al*. (2000) performed a comprehensive study on the rheological implications of molecular structure and observed that the zero-shear viscosity, breadth of the relaxation spectrum, and dynamic loss angle δ were most sensitive to the presence of sparse long-chain branching. Similar results were observed by Kim *et al*. (1996), Koopmans (1997), and Malmberg *et al*. (1998). Kim *et al*. (1996) and Bin Wadud and Baird (2000) studied the temperature dependence of mPE resins and found the flow activation energy (E_a) to be sensitive to the presence of low levels of random long-chain branching. However, Bin Wadud and Baird were unable to distinguish the level of branching from E_a alone. Instead, Bin Wadud and Baird found that nonlinear viscoelastic measurements of the transient primary normal stress difference (N_1^+) and transient extensional viscosity (η_E^+) were more sensitive to the degree of branching found in the sparsely branched mPE systems they studied. These relatively few results represent a significant step in understanding the influence of random branching on the rheology of commercial polyethylene resins.

Model polymer systems

Prior to metallocene polyethyene systems, most of the fundamental knowledge regarding long-chain branching was garnered from research on systematically branched model polymer systems and carefully prepared commercial materials. Studies on monodisperse, anionically polymerized polymers show that the number of branches, the length of branches, and the topology (i.e. linear, star, comb, etc.) can all affect the shear rheological properties. Here a brief review of those findings is presented in this section.

One of the first studies employing systematically branched polymers was performed by Kraus and Gruver (1964). They found that above a characteristic molecular weight three- and four-arm star-branched polybutadiene (PB) resins exhibited zero-shear viscosity enhancement over their linear PB equivalents. That is, the viscosity of the branched species was greater than that of the linear species for the same weight-average molecular weight. Kraus and Gruver hypothesized that enhanced entanglement coupling was occurring between neighboring molecules above the characteristic molecular weight. Similar studies by Graessley *et al*. (1976) and Raju et al. (1979a) on polyisoprene (PI) and hydrogenated polybutadiene (HPB) systems, respectively, have yielded similar results.

In addition to the number of branches, the length of branches was also investigated. Several researchers have found that the zero-shear viscosity of star-branched polymers depends exponentially upon the arm molecular weight M_a above a critical molecular weight [Raju *et al*. (1979a), Carrella *et al*. (1986), Fetters *et al*. (1993)]. Furthermore, in studies by Jordan *et al*. (1989) and Gell *et al*. (1997) it was found that the length of the shortest arm in asymmetric PB and poly(ethylene-alt-propylene) (PEP) three-arm stars must exceed the critical molecular weight

for entanglement, M_c, in order to manifest zero-shear viscosity enhancement. This finding certainly reiterates the importance of entanglement coupling as the mode of enhancement.

Perhaps the most interesting studies on model branched systems were performed by Roovers and Graessley (1981) and Roovers (1984). These authors investigated the effects of topology on the zero-shear viscosity behavior of comb and H-shaped polystyrenes (PS). Roovers (1984) observed that H-shaped polystyrene molecules exhibit a substantially greater degree of viscosity enhancement than either three or four-arm stars of equivalent molecular weight. This observation is believed to be due to a long-time relaxation mechanism associated with the central segment between branch points. Therefore, one assumes that the number of branch points per molecule may have an additional influence on shear rheological properties.

Influence of molecular weight

Model branched systems clearly exhibit greater dependence upon weight-average molecular weight than their linear counterparts. This is evidenced by the observed zero-shear viscosity enhancement for the branched species at a given M_w. As a result, the influences of M_w and LCB on the shear rheological properties are not explicitly separate. Although careful synthesis and fractionation of model branched systems can remove unwanted dependency upon M_w, this approach is much too tedious and yields very little material for practical purposes. Therefore, an appropriate method for removing M_w dependence on the shear rheological properties is more desirable.

One such method is the time-molecular weight (TMW) superposition principle. This principle is obeyed by polymers having similar, narrow molecular weight distributions [Vinogradov (1980)]. The principles for TMW superposition are quite simple and are formed

from linear viscoelasticity and experimental observations. First, the observed shift in the zero-shear viscosity η_0 with M_w follows the classical relationship presented by Berry and Fox (1968) for linear, flexible chain molecules above their critical molecular weight for entanglement, M_c. This relationship appear as,

$$\eta_0 = KM_w^{3.4} \tag{4.1}$$

where K is a prefactor that is dependent upon molecular composition and temperature. Second, the longest relaxation time τ_1 is observed to be directly proportional to the product of the steady-state compliance J_s^0 and the zero-shear viscosity as given in Eq. 4.2 [Ferry (1980)],

$$\tau_1 \propto J_s^0 \eta_0 \tag{4.2}$$

Because the steady-state compliance is often found to be independent of M_w above $2M_c$ [Ferry (1980)], the resulting relationship for the longest relaxation time yields the same M_w dependence as the zero-shear viscosity. Therefore, combining these concepts leads to equivalent shifting along the time, or rate, axis and the viscosity axis. The actual superposition is then applied using the shift factor a_M, given as,

$$a_M = \frac{\eta_0(M)}{\eta_0(M_{ref})} \tag{4.3}$$

where $\eta_0(M)$ refers to the zero-shear viscosity at a given M_w, and $\eta_0(M_{ref})$ refers to the zero-shear viscosity at the reference M_w. Applying this principle to linear materials with similar, narrow molecular weight distributions should shift rheological data obtained at different M_w to a single master curve. Therefore, any deviations from a single master curve for metallocene PE resins are expected to be due to long-chain branching.

Relating molecular structure to rheology

One of the greatest limitations to working with randomly branched systems is the uncertainty associated with the molecular structure. Conventional methods of characterization, such as dilute solution low-angle laser light scattering (LALLS) and C^{13} NMR measurements, are often limited when the degree of long-chain branching is small (< 0.3 LCB/1000 C) or short-chain branching (SCB) is also present [Schroff and Mavridis (1999), Randall (1980)]. As a result, consideration is being given to rheological characterization as a sensitive indicator of LCB content. Lai *et al*. (1996), Schroff and Mavridis (1999), and Wood-Adams and Dealy (1999) have each developed methods that rely solely on rheological data or a combination of rheological data and molecular weight data to predict branching content. Although these empiricisms can be useful, they are all limited to materials that have sparse, random long-chain branching. In the case of highly branched resins, such as LDPE, they appear to be less useful.

One notable exception is the method developed by Janzen and Colby (1999). Janzen and Colby proposed a method of determining random long-chain branching in polyethylenes from η_0-M_w data. Their technique employs a phenomenological description developed by Lusignan and coworkers (1996, 1999) for randomly branched, flexible chain polymers combined with the assumed branching structure of a Cayley tree. Together, the number of branch points, or branch vertices, can be deduced from the degree of zero-shear viscosity enhancement observed. The phenomenological description appears in Eqs. 4.4 and 4.5,

$$\eta_0 = AM_b\left[1+\left(\frac{M_b}{M_c}\right)^{2.4}\right]\left(\frac{M_w}{M_b}\right)^{s/\gamma} \qquad M_c \le M_b \le M_w \qquad (4.4)$$

Here, A is a numerical pre-factor having units of (Pa s mol)/g and is specific to molecular composition and temperature, M_b is the molecular weight between branch points, M_c is the

critical molecular weight for entanglements, M_w is the weight-average molecular weight, and s/γ is an exponent that depends logarithmically on M_b as shown in Eq. 4.5,

$$s/\gamma = \max\left[1, \frac{3}{2} + \frac{9B}{8}\ln\left(\frac{M_b}{90M_{Kuhn}}\right)\right] \tag{4.5}$$

where B is a material specific constant, and M_{Kuhn} is the molecular weight of a statistical Kuhn segment. Janzen and Colby observed that the zero-shear viscosity of peroxid-induced, random long-chain branched polyethylene was very sensitive to the degree of long-chain branching. Using the observed enhancement, the degree of branching could then be calculated. Bin Wadud and Baird (2000) extended this treatment to sparsely branched mPE resins and found that the predicted degree of long-chain branching agreed qualitatively with estimates obtained from dilute solution measurements. However, the predicted magnitudes were a factor of three smaller than dilute solution measurements.

Conversely, the degree of enhancement can be predicted using the Janzen and Colby relation knowing the branching content. Janzen and Colby found that the zero-shear viscosity enhancement is primarily a function of the molecular weight between branch points, M_b. The value of M_b can be calculated using the following equation if the number of branch points α is known,

$$M_b = \left[\frac{2\alpha}{M_1} + M_w^{-1}\right]^{-1} \tag{4.6}$$

where M_1 is the repeat unit molecular weight. Significant zero-shear viscosity enhancement is observed at large values of M_b (i.e. low degrees of LCB), and pronounced viscosity reduction at low values of M_b. Surprisingly, the authors found that as few as one LCB per 10^6 carbon backbone segments gives rise to measurable η_0 enhancement in sparsely branched polyethylenes.

This striking observation clearly identifies shear rheological properties as being very sensitive to the effects of long-chain branching.

In the current study, a series of six commercially available PE resins will be analyzed to better understand the effects of long-chain branching on steady and dynamic oscillatory shear rheology. Four of these resins are narrow molecular weight distribution metallocene-catalyzed polyethylenes, of which three are sparsely long-chain branched. The remaining two resins are conventional LLDPE and LDPE resins that will serve as comparative resins throughout the study. The molecular weight distributions and long-chain branching have been obtained from dilute solution characterization measurements. The goal of this study is to investigate the effects that sparse long-chain branching has on the steady and dynamic shear rheological properties of polyethylenes. In order to focus exclusively on the effects of LCB, the role of M_w will be removed using the time-molecular weight superposition approach outlined earlier. This should allow for a more accurate depiction of the role of sparse long-chain branching on the rheology of commercial mPE resins.

4.2 Experimental

4.2.1 Materials

A series of six commercial polyethylene resins were chosen for this study. These resins typify the range in molecular structure found in commercial polyethylenes and afford a sufficient quantity of material to perform complete rheological analysis. Furthermore, each of the resins analyzed has a melt index close to one. The use of resins with similar melt indices provides an industrial measure with which to compare these resins, as well as expose the deficiencies of

using the melt index as a measure of rheological response. The particular resins chosen for this study and their relevant indices are tabulated in Table 4.1.

The first four resins listed in Table 4.1 are metallocene-catalyzed polyethylene (mPE) resins. The mPE resins were specifically chosen to compare the effects of level of sparse long-chain branching on melt rheology. The Affinity PL1840 and PL1880 resins are manufactured by Dow Chemical using INSITE® catalyst technology. These two resins are solution polymerized ethylene-octene copolymers. The Exact 0201 and 3132 resins are manufactured by ExxonMobil Chemical using EXXPOL® catalyst technology. The Exact 0201 resin is an ethylene-octene copolymer while the Exact 3132 is an ethylene-hexene copolymer. The Affinity PL1840, Affinity PL1880, and Exact 0201 resins were identified as having sparse long-chain branching by their respective manufactures. The Exact 3132 was specified as a strictly linear mPE copolymer. All four resins have melt indices between 1.0 and 1.2. The densities of these materials are also similar and imply equivalent comomoner content.

The remaining two resins listed in Table 4.1 are conventional linear low-density polyethylene (LLDPE) and low-density polyethylene (LDPE). The NTX101 resin is an ethylene-hexene copolymer manufactured by ExxonMobil using a Zielger-Natta gas-phase polymerization process. The NA952 resin is an ethylene homopolymer manufactured by Equistar using a high-pressure, high-temperature tubular free-radical polymerization process. The NTX101 was chosen as a linear reference material, while the NA952 resin was chosen as a densely branched reference material.

Table 4.1: Materials properties.

Resin	Density g/cm^3	MFI dg/min
Exact 0201	0.902	1.1
Exact 3132	0.900	1.2
Affinity PL1840	0.909	1.0
Affinity PL1880	0.902	1.0
NTX101	0.917	0.9
NA952	0.919	2.0

4.2.2 Analytical Methods

Molecular weight distribution information was obtained using combined high temperature gel permeation chromatography (GPC), intrinsic viscosity measurements, and low angle laser light scattering (LALLS) measurements. This triple-detector technique provides absolute molecular weight determination and can be used to determine branch content in the sparsely branched mPE resins. The degree of sparse branching is calculated using the Mark-Houwink and Zimm-Stockmayer relations [Flory (1953), Zimm and Stockmayer (1949)]. In the case of the highly branched NA952 resin, C^{13} NMR measurements were used to quantify the branch content. The major limitation to using this method with LDPE is that it cannot distinguish branches having lengths greater than six carbon atoms ($M_{branch} > 85$ g/mol) [Axelson (1979)]. Therefore, one may expect some short-chain branches (85 g/mol $< M_{branch} < M_c$) to be counted with the long-chain branches. Thus, the reported branching value is most likely larger than the true number of long-chain branches. All of the molecular characterization of these resins was performed by researchers at Dow Chemical (Freeport,TX).

All measurements of the shear viscoelastic properties were performed using a Rheometrics Mechanical Spectrometer Model 800 (RMS-800). A set of 25mm diameter parallel plate fixtures was used for the small-amplitude dynamic oscillatory measurements while a set of 25 mm cone and plate fixtures was used for all steady shear measurements. The cone angle used for all steady shear measurements was 0.1 radians. All testing was performed within an inert nitrogen atmosphere to prevent thermo-oxidative degradation. The test samples were prepared by compression molding preforms at 170 °C under nominal pressure and allowing them to cool slowly under no pressure. This method provides homogenous samples with minimal residual stress. The shear rheometry results represent the average of at least three runs using different

samples each run. All testing was performed at a melt temperature of 150 °C. The calculated errors for the dynamic oscillatory and the steady shear viscosity measurements were found to be less than ±5 and ±10%, respectively.

4.3 Results and Discussion

4.3.1 Molecular Characterization

The results of the molecular characterization are tabulated in Table 4.2. The weight average molecular weight, molecular weight distribution, z-average molecular weight, and long-chain branching content are reported for each resin. The weight average molecular weights vary between 87,400 g/mol for the Dow Affinity PL1840 resin to 235,500 g/mol for the Equistar NA952 resin. The molecular weight distribution of the metallocene resins are relatively narrow at approximately two. The NTX101 has a broader MWD at 3.44, and the NA952 has the broadest molecular weight distribution at 17.1. The z-average molecular weights have been provided to further quantify the full distribution curves featured in Figure 4.1. The most important parameter for this study is the degree of long-chain branching. The mPE resins vary in long-chain branching content from zero for the linear Exact 3132 resin to 0.79 LCB/10^4 carbons for the Exact 0201 resins. The Affinity PL1840 and PL1880 resins yield intermediate values. The NTX101 resin is also linear and contains no long-chain branches, while the densely branched NA952 contains 39 branches/10^4 carbons. Although short-chain branching may be included in the value for the NA952 resin, the high degree of branching is confirmed by the very broad molecular weight distribution.

Table 4.2. Molecular weight distribution and LCB.

Resin	M_w	M_w/M_n	M_z	LCB /10^4 C
Exact 0201	88 700	2.14	158 900	0.79
Exact 3132	111 000	2.04	180 400	—
Affinity PL1840	87 400	2.43	160 200	0.57
Affinity PL1880	115 800	2.12	183 700	0.18
NTX101	122 700	3.44	319 700	—
NA952	235 500	17.1	2 619 300	39[a]

[a]: C^{13} NMR measurement

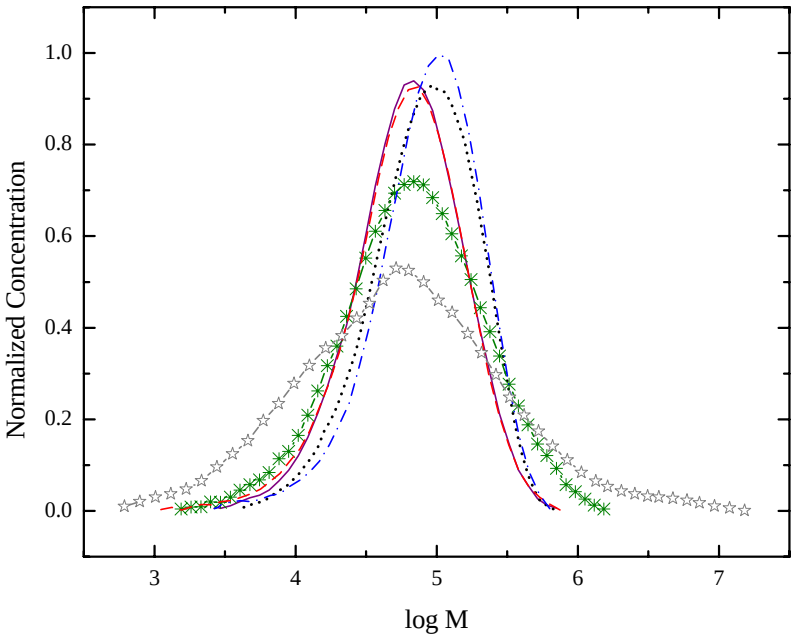

Figure 4.1: Molecular weight distribution curves for Exact 0201 (——), Exact 3132 (· · ·), Affinity PL1840 (– – –), Affinity PL1880 (—·—), NTX101 (–✳–), and NA952 (–☆–).

4.3.2 Shear Viscosity

The shear viscosity flow curves for each of the six resins are plotted in Figure 4.2. Each flow curves consists of steady shear and dynamic oscillatory data. The steady shear data covers the shear rate range of 0.001 – 0.1 s^{-1} and the dynamic oscillatory covers the frequency range of 0.1 – 100 rad s^{-1}. The low frequency intersection between steady and dynamic oscillatory data is in good agreement for all resins and implies that the Cox-Merz rule holds at low shear rates [Cox and Merz (1958)]. Data collected at higher shear rates using a capillary rheometer (but not shown here for clarity) suggest that the Cox-Merz rule holds true for the branched resins but deviates slightly for the linear resins [Doerpinghaus (2002)].

Analysis of the shear viscosity curves indicates that the zero-shear viscosity, onset of shear-thinning behavior, and degree of shear thinning are influenced by molecular structure. The Affinity PL1840, Affinity PL1880, Exact 0201, and NA952 resins all exhibit a common zero-shear viscosity plateau of approximately 45,000 Pa s. The NTX101 and Exact 3132 resins exhibit lower zero-shear viscosities at 22,000 and 15,000 Pa s, respectively. The NA952 resin transitions to non-Newtonian flow behavior at shear rates as low as 0.01 s^{-1}, while the sparsely branched mPE resins begin shear thinning at 0.05 s^{-1}. The onset of shear-thinning behavior in the linear resins appears to be influenced by molecular weight distribution. The NTX101 exhibits a broad transition to non-Newtonian flow beginning at $\dot{\gamma}$ = 0.1 s^{-1}, while the transition for the linear mPE resin is much more acute at $\dot{\gamma}$ = 2 s^{-1}. The degree of shear thinning is most pronounced in the densely branched NA952 resin with a 98% reduction in shear viscosity over the five decades in shear rate investigated. The viscosity reduction in the sparsely branched resins is also notable at 95%. The NTX101 and Exact 3132 resins exhibit considerably less

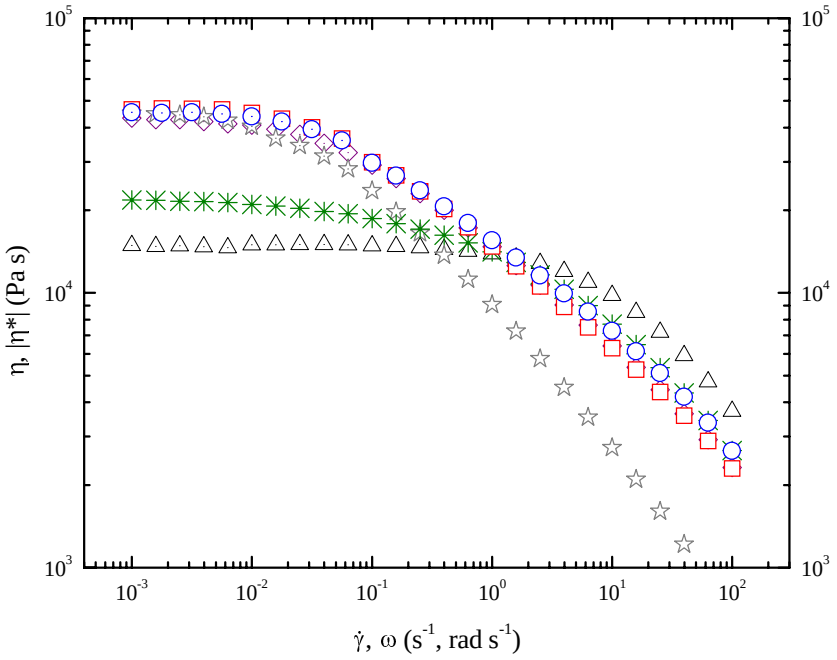

Figure 4.2: Steady shear and complex viscosities at 150 °C. (◇) Exact 0201, (△) Exact 3132, (☆) NA952, (✳) NTX101, (□) Affinity PL1840, (○) Affinity PL1880. Dotted symbols represent steady shear measurements; open symbols represent dynamic oscillatory measurements.

shear thinning than the branched resins with only an 8-fold and 4-fold decrease in shear viscosity, respectively.

Despite similarities in the shear viscosity curves of the sparsely branched mPE resins, the molecular structure of these materials is different. One of the most prominent differences is the weight-average molecular weight according to GPC-LALLS data tabulated in Table 4.2. Using the characteristic relationship between zero-shear viscosity and M_w for *linear* polyethylenes, it is proposed to normalize all of the viscosity flow curves by their respective M_w and shift to a reference molecular weight. The most logical reference material is the Exact 3132 resin because it is linear and of narrow molecular weight distribution. Application of the shift factor a_M should provide a clear picture of the individual contributions of sparse long-chain branching to the steady shear viscosity.

The shifted viscosity curves found in Figure 4.3 exhibit striking features. The most obvious feature is the separation of the branched resins. η_0 of the Exact 0201 and PL1840 resins are greater than six times η_0 of the Exact 3132 resin, compared to a factor of three before shifting. Furthermore, PL1880 shifts to an intermediate value that is less than three times η_0 of Exact 3132. Obviously, these differences in viscosity must be primarily attributed to the presence of long-chain branching. Fortuitously, the limiting viscosity of the conventional LLDPE falls directly on the linear mPE reference. This further strengthens the argument for LCB by proving that MWD does not significantly affect η_0. Quite surprisingly, the shear viscosity curve for NA952 is reduced precipitously from its original un-shifted value. This is certainly a consequence of its relatively large M_w.

The results obtained from the shifted flow curves in Figure 4.3 appear to agree well with the phenomenological theory of Janzen and Colby (1999). The sparsely branched resins exhibit

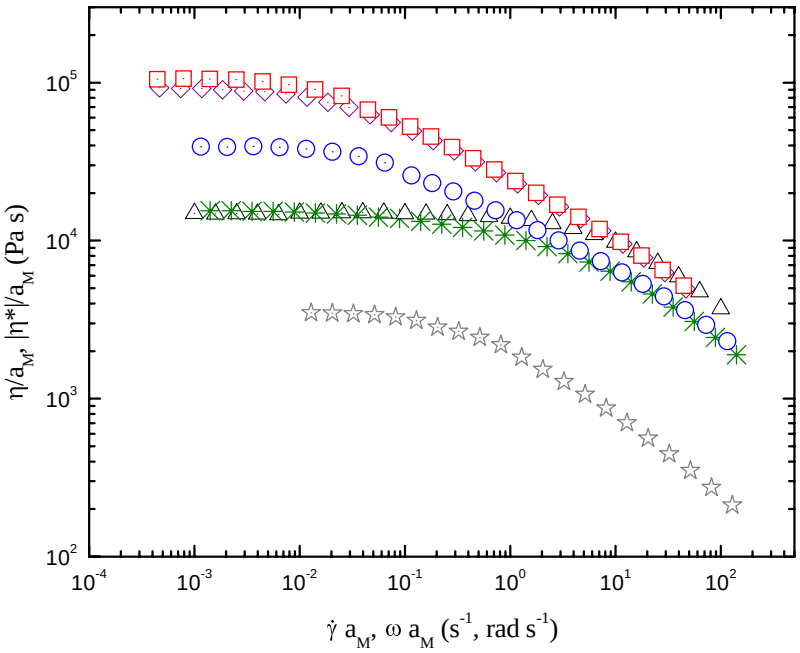

Figure 4.3: Shifted steady shear and complex viscosities, M_{ref} = 111 000 g/mol. (◇) Exact 0201, (△) Exact 3132, (☆) NA952, (✳) NTX101, (□) Affinity PL1840, (○) Affinity PL1880. Dotted symbols represent steady shear measurements; open symbols represent dynamic oscillatory measurements.

a noticeable degree of zero-shear viscosity enhancement, while the densely branched LDPE shows a significant reduction in the zero-shear viscosity. Figure 4.4 illustrates the predictions of Eqs. 4.4 and 4.5 for three different values of M_w. In all cases, the viscosity initially increases before reaching a maximum below one long-chain branch per molecule and then begins to decrease. The maximum degree of zero-shear viscosity enhancement and the point of no enhancement are determined by the M_w of the system. Using the dilute solution measurements for long-chain branching content combined with Eqs. 4.4, 4.5, and 4.6, the degree of viscosity enhancement can be predicted for each of the branched resins. The experimentally observed enhancement and the predicted enhancement are shown in Table 4.3. From the measured long-chain branching values, the predicted degrees of enhancement are considerably higher for the sparsely branched resins, and lower for the densely branched LDPE, than the observed enhancement. This may indicate that the dilute solution measurements are not sufficiently accurate measurements of the degree of long-chain branching in the metallocene resins or that the type of branches generated through peroxide-induced branching are different from the *in situ* branching created during CGC metallocene polymerization. On the other hand, the significant under prediction of the LDPE zero-shear viscosity is most likely a consequence of the over estimation of the degree of long-chain branching provided by C^{13} NMR characterization (which counts all branches > 6 carbons). Nevertheless, the observed enhancement for the sparsely branched resins and reduction for the densely branched resin is in qualitative agreement with the phenomenological treatment of Janzen and Colby.

Although enhancement is observed in the sparsely branched metallocene resins, the degree of enhancement does not scale with the measured degree of long-chain branching. More specifically, the Exact 0201 resin having 0.79 LCB/10^4 carbons does not show any additional

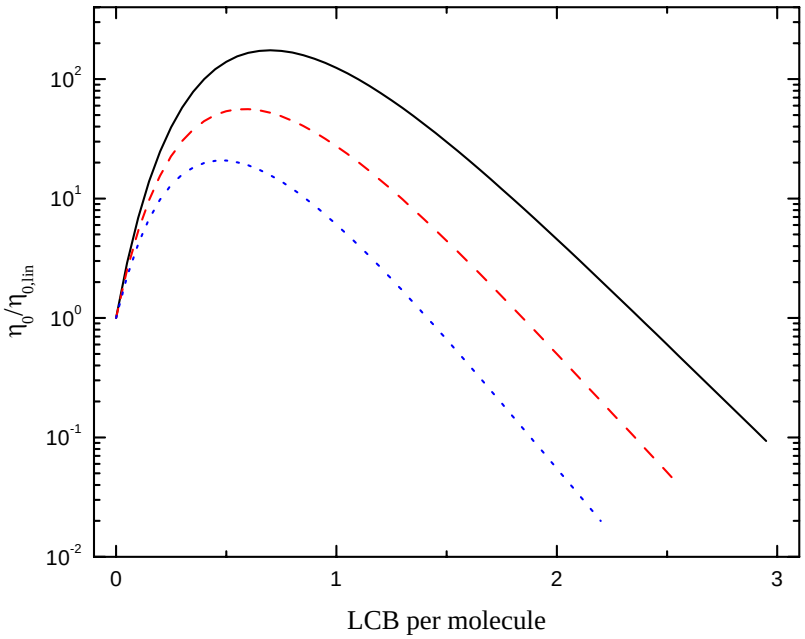

Figure 4.4: Predicted zero-shear viscosity versus long chain branches per molecule using the Janzen and Colby (1999) viscosity relation. [(——) M_w = 100,000 g/mol, (· · ·) M_w = 88,000 g/mol, (– – –) M_w = 120,000 g/mol]

Table 4.3. Observed η_0 enhancement Γ_{obs} versus the predicted η_0 enhancement Γ_{pred} from the Janzen and Colby viscosity relation.

Resin	Γ_{obs}	Γ_{pred}
Exact 0201	6.0	41
Exact 3132	1.0	1.0
Affinity PL1840	6.8	22
Affinity PL1880	2.5	8.0
NTX101	1.0	1.0
NA952	0.2	< 0.01

enhancement in the zero-shear viscosity over the Affinity PL1840 resin having 0.57 LCB/10^4 carbons. This lack of differentiation is believed to be due to one or more of three possible reasons. First, the dilute solution measurements may not be statistically different within experimental error. Thus, having similar M_w, MWD, and LCB will lead to the same shear rheological behavior. Second, the non-monotonic nature of zero-shear viscosity enhancement predictions from Janzen and Colby's treatment suggest that similar zero-shear viscosities can be observed for different degrees of long-chain branching. Finally, the distribution of molecular structures within the polymers may be different as a result of different catalysts and reaction conditions used. Numerical studies by Soares and Hamilec (1995,1997) predict that a distribution of molecules containing linear, star, and higher branched structures exist in sparsely long-chain branched metallocene polyethylenes. Because dilute solution measurements indicate an average number of branches, the exact concentration of linear and branched species within the whole polymer is unknown. From observations by Roovers (1984), polymer macromolecules containing two branch points exhibit much greater zero-shear viscosity dependence upon M_W than three-arm stars of comparable M_w. Therefore, one may infer that variations in the catalyst systems used by the respective manufactures may give rise to a different distribution of linear and branched species which is reflected in the zero-shear viscosity measurements. Not surprisingly, this apparent similarity between the Affinity PL1840 and Exact 0201 resins remains throughout most of this study.

In addition to zero-shear viscosity, the onset of shear thinning is also affected by shifting the viscosity flow curves. In an attempt to better visualize these effects, Figure 4.5 presents the normalized shear viscosities versus shifted shear rate for each resin. The results clearly identify the dramatic effect that long-chain branching has on the onset of shear-thinning in sparsely,

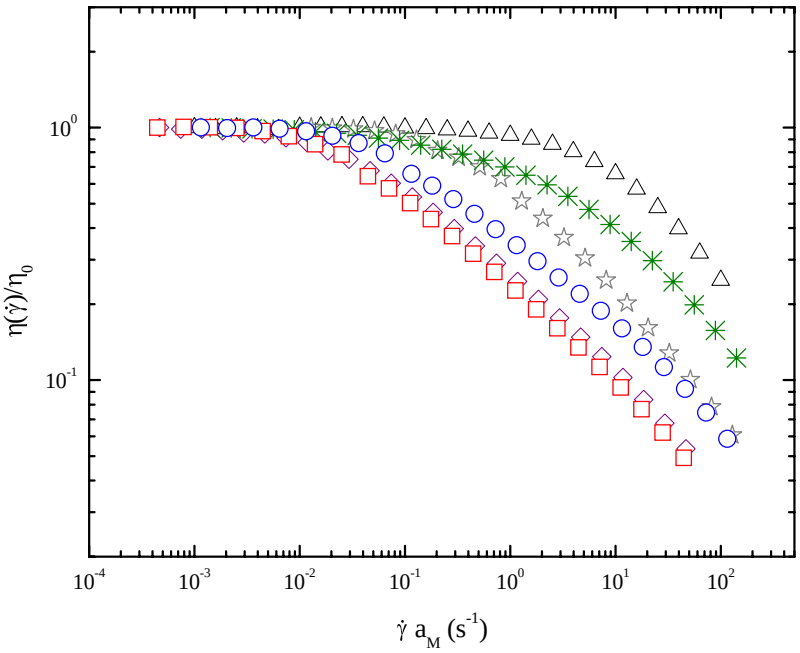

Figure 4.5: Normalized shear viscosities. (◇) Exact 0201, (△) Exact 3132, (☆) NA952, (✳) NTX101, (□) Affinity PL1840, (○) Affinity PL1880.

randomly branched systems. The onsets of shear-thinning behavior are shifted to $\dot{\gamma} = 0.02\ s^{-1}$ for PL1840 and Exact 0201, $0.06\ s^{-1}$ for PL1880, $0.15\ s^{-1}$ for NTX101, and $0.13\ s^{-1}$ for NA952. Surprisingly, this represents a two-order of magnitude decrease in the onset of shear thinning between the linear mPE resin and the sparsely branched mPE resins. The observed increase in the terminal relaxation time is considerably greater than the observed zero-shear viscosity enhancement and implies that the simple relation described by Eq. 4.3 does not hold for sparsely branched resins and that an additional dependency arising from long-chain branching exists. Furthermore, the linear NTX101 resin demonstrates the subtle effects of molecular weight distribution on the onset of shear thinning.

4.3.3 Dynamic Moduli

In addition to the shear viscosity, the dynamic moduli are also sensitive to the effects of sparse long-chain branching. Specifically, long-chain branching gives rise to increased elasticity. The dynamic storage and loss moduli for each resin over the frequency range of 0.1 – 100 rad/s are presented in Figures 4.6 and 4.7. The loss modulus, which dominates the magnitude of the material response over the low frequency range, appears in Figure 4.6. The results present a general trend of a monotonic growth in G'' for five of the six resins analyzed. The one exception is that of the NA952 resin. At higher rates, NA952 does not increase as rapidly with frequency as the other PE resins. Figure 4.7 presents the storage modulus as a function of frequency. In the low frequency range, G' appears to be a better indicator of molecular structure than G''. The differentiation between the branched PE resins, NTX101, and Exact 3132 possibly indicates a stronger dependence on the effects of long-chain branching

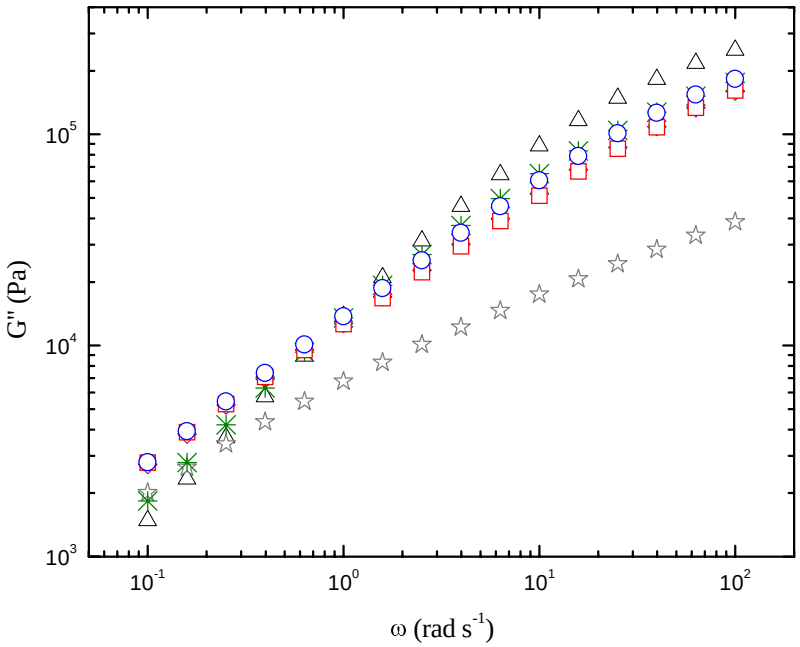

Figure 4.6: Dynamic loss moduli at 150 °C. (◇) Exact 0201, (△) Exact 3132, (☆) NA952, (✳) NTX101, (□) Affinity PL1840, (○) Affinity PL1880.

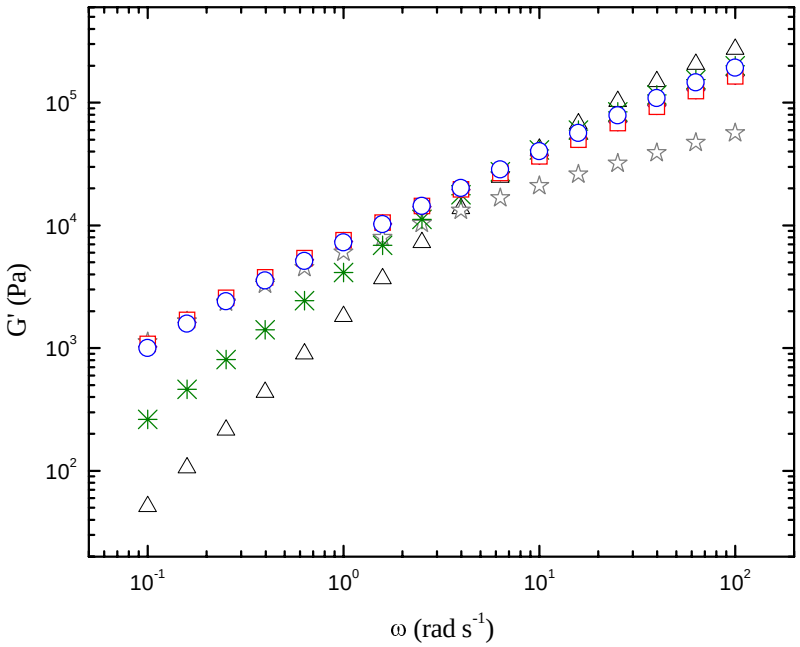

Figure 4.7: Dynamic storage moduli at 150 °C. (◇) Exact 0201, (△) Exact 3132, (☆) NA952, (✳) NTX101, (□) Affinity PL1840, (○) Affinity PL1880.

content and molecular weight distribution. At high frequencies, the storage moduli appear to converge with the exception of the highly branched LDPE resin.

Once again, the influence of molecular weight is convoluted with that of long-chain branching and molecular weight distribution. Application of the time-molecular weight superposition to the storage moduli leads to the results found in Figure 4.8. The shifted storage moduli also demonstrate the separability of long-chain branch content in mPE resins. As seen in the shear viscosity, the sparsely branched resins can be separated between the Affinity PL1880 and the pair of Affinity PL1840 and Exact 0201. This dependence of G' upon the degree of long-chain branching as obtained from dilute solution measurements appears consistent with previous studies [Wood-Adams (2000)]. On the other hand, the response of the densely branched NA952 resin is shifted to higher frequencies. This apparent reduction in storage modulus at a given frequency and M_W appears consistent with the concepts of reduced molecular dynamics and entanglement coupling stemming from a high degree of long-chain branching. Finally, direct comparison of the linear PE resins displays the subtle effect that molecular weight distribution has on the elastic properties at low frequencies. The NTX101 resin has a noticeably greater value of G' than the Exact 0201 resin in the lower frequency range.

4.3.4 Primary Normal Stress Difference

Along with the dynamic storage modulus, another strong indicator of elastic properties is the primary normal stress difference (N_1). N_1 typically exhibits greater dependence on M_w than η_0 [Vinogradov (1980)], and as such may be more sensitive to the presence long-chain branching. The measured values of N_1 are reported in Figure 4.9. The results indicate that NA952 exhibits the greatest value of N_1 at all rates examined, closely followed by the sparsely

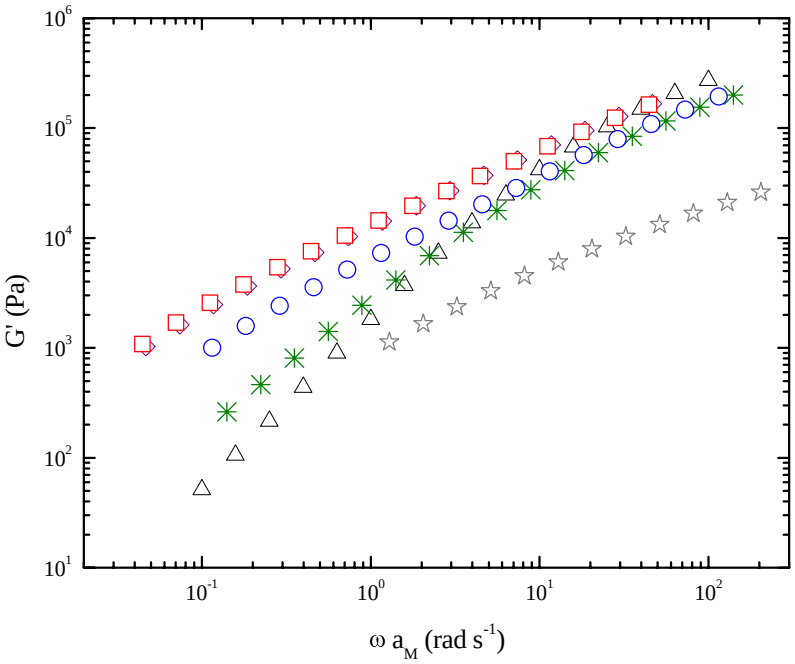

Figure 4.8: Shifted dynamic storage moduli, M_{ref} = 111 000 g/mol. (◇) Exact 0201, (△) Exact 3132, (☆) NA952, (✳) NTX101, (□) Affinity PL1840, (○) Affinity PL1880.

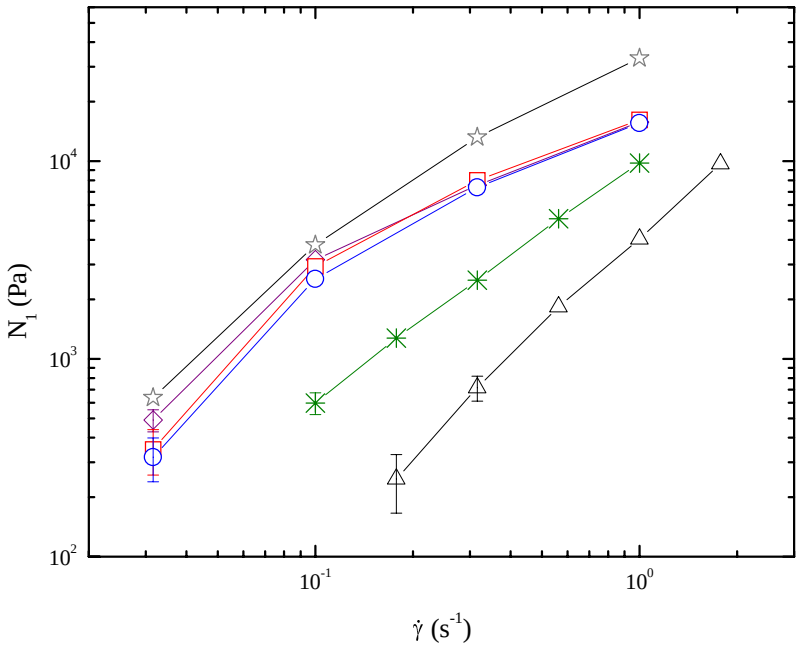

Figure 4.9: Primary normal stress differences (N_1) at 150 °C. (◇) Exact 0201, (△) Exact 3132, (☆) NA952, (✳) NTX101, (□) Affinity PL1840, (○) Affinity PL1880. Lines have been drawn to aid eye.

branched mPE resins. The linear mPE resin exhibits the lowest value of N_1 over the range tested. These observations appear to be consistent with shear viscosity results presented earlier. If the TMW shift procedure is applied, the differences between these resins become more evident. Figure 4.10 shows the shifted values of N_1. Once again, the sparsely branched mPE pair of Exact 0201 and PL1840 differentiate themselves from the less branched PL1880 resin. Next are the conventional LLDPE resin, the linear mPE resin, and finally the densely branched LDPE. As witnessed earlier, the broader molecular weight distribution found within the NTX101 contributes to additional elasticity. Although the range of available data is limited, the results agree well with G' data over the same interval.

A better illustration of the impact that long-chain branching has on the elastic properties of PE melts is the primary normal stress difference coefficient, Ψ_1. This measure has a similar response to the shear viscosity, and in the limit of infinitesimal deformation rates $\Psi_{1,0}$ becomes directly proportional to the square of the zero-shear viscosity, η_0^2 [Ferry (1980)]. The molecular weight invariant (shifted) values of Ψ_1 are plotted in Figure 4.11. Due to the limited amount data available for the Exact 3132 resin, an accurate determination of $\Psi_{1,0}$ is not possible. Nevertheless, the results exhibit some interesting trends. First, the degree of enhancement between the PL1880 and the remaining sparsely branched mPE resins has increased noticeably. In fact, the extrapolated degree of enhancement using available data is almost 20% greater than the zero-shear viscosity enhancement *squared*. This may represent an additional dependency or may include the effects of branching on the steady-state compliance, J_s^0. Second, all of the normal stress coefficient curves appear to converge at higher rates. This phenomenon has also been observed by Wood-Adams (2001), and implies that the effects of branching are most prominent in the low shear rate regime, as expected.

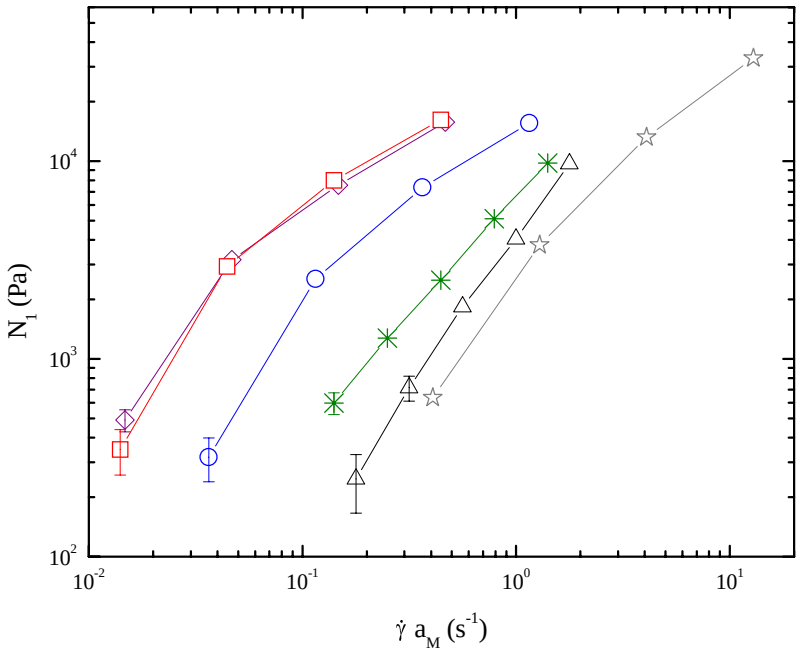

Figure 4.10: Shifted primary normal stress difference, M_{ref} = 111 000 g/mol. (◇) Exact 0201, (△) Exact 3132, (☆) NA952, (✳) NTX101, (□) Affinity PL1840, (○) Affinity PL1880. Lines have been drawn to aid eye.

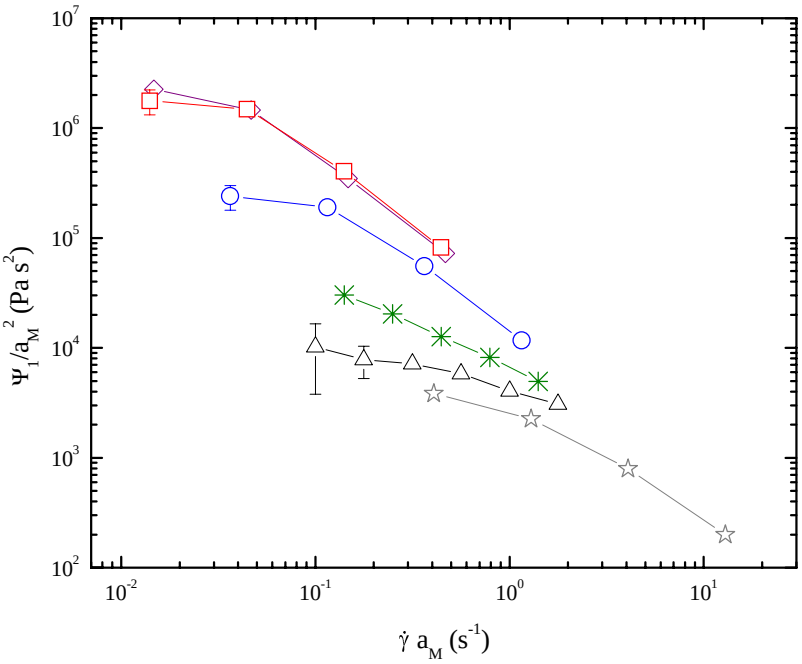

Figure 4.11: Shifted primary normal stress difference coefficient (Ψ_1), M_{ref} = 111 000 g/mol. (◇) Exact 0201, (△) Exact 3132, (☆) NA952, (✳) NTX101, (□) Affinity PL1840, (○) Affinity PL1880. Lines have been drawn to aid eye.

4.4 Conclusions

The application of a time-molecular weight superposition principle provides the ability to further differentiate the effects of molecular structure upon the shear rheological properties of polyethylene resins. The effects of long-chain branching and molecular weight distribution can be effectively separated from those due to weight-average molecular weight. In this case, the true enhancing effect of long-chain branching on the zero-shear viscosity, dynamic storage modulus, and primary normal stress difference are only realized after the overlying effects of weight-average molecular weight have been removed.

The molecular weight invariant analysis of the sparsely branched metallocene polyethylenes used in this study show a surprising degree of enhancement in steady and dynamic oscillatory shear rheological properties. The zero-shear viscosity of mPE resins was found to increase by a factor of six with as little as 0.6 LCB/10^4 carbons, yet densely branched LDPE was observed to decrease by a factor of four at much higher branching content. Furthermore, the onset of shear-thinning behavior is markedly shifted to lower shear rates because of sparse long-chain branching. The dynamic storage modulus shows that most of the elastic character resulting from sparse long-chain branching is evident at lower deformation rates, and that elasticity is only mildly sensitive to a broadening molecular weight distribution. The primary normal stress difference data agrees with the zero-shear viscosity and storage modulus results, but also suggests a stronger dependence on long-chain branching than either η_0 or G'.

Comparing the dilute solution and C^{13} NMR branching measurements, in combination with the Janzen and Colby treatment, to the observed rheological enhancement answers several questions concerning the influence of long-chain branching, but also raises others. A three-fold increase in long-chain branch content results in a zero-shear viscosity enhancement of 2.7

between the Affinity PL1840 and PL1880 resins. Conversely, an increase in LCB content from 0.57 to 0.79 LCB/10^4 carbons does not result in any additional effect on shear rheological properties. This may imply that dilute solution measurements of sparsely branched mPE resins are inaccurate, a compensating effect between enhanced entanglement coupling and reduced coil dimensions has been observed, or the distribution of linear and branched macromolecular species in the polymers are statistically different as a result of the different catalysts used in the synthesis of the metallocene-catalyzed polyethylene manufactures.

4.5 Acknowledgements

The authors would like to thank A. Willem deGroot and David Gillespie at the Dow Chemical Company for providing the LCB and MWD data as well as insightful information regarding the characterization techniques. The authors would also like to extend their gratitude to the Dow Chemical Company, the ExxonMobil Chemical Company, and the Equistar Chemical Company for graciously donating their respective PE resins to this study.

4.6 References

Axelson, D.E., G.C. Levy, and L. Mandelkern, *Macromolecules* **12**, 41 (1979).

Berry, G.C. and T.G. Fox, *Adv. Polym. Sci.*, **5**, 261 (1968).

Bin Wadud, S. E. and D. G. Baird, *J. Rheol*. **44**, 1151 (2000).

Bird, R.B., R.C. Armstrong and O. Hassager, *Dynamics of Polymeric Liquids. Volume 1: Fluid Mechanics*, 2nd ed. John Wiley & Sons, New York, 1987.

Brintzinger, H.H., D. Fischer, R. Mu:lhaupt, B. Rieger, and R. Waymouth, *Angew. Chem. Int. Ed. Eng*l. **107**, 1255 (1995).

Bueche, F., *J. Polym. Sci*. **43**, 527 (1960).

Carella, J.M., J.T. Gotro and W.W. Graessley, *Macromolecules* **19**, 659 (1986).

Cox, W.P. and E.H. Merz, *J. Polym. Sci*. **28**, 619 (1958).

Doerpinghaus, P.J., *Flow Behavior of Sparsely Branched Metallocene Catalyzed Polyethylenes*, Ph.D. Dissertation, Virginia Tech, Blacksburg, VA (2002).

Ferry, J. D., *Viscoelastic Properties of Polymers*, 3rd edition, John Wiley & Sons, New York, (1980).

Fetters, L.J. A.D. Kiss, D.S. Pearson, G.F. Quack, F.J. Vitrus, *Macromolecules* **26**, 647 (1993).

Fleissner, M. *Ang. Makromol. Chem*. **94**, 197 (1981).

Flory, P.J., *Principles of Polymer Chemistry*, Cornell University Press, Ithaca, NY (1953).

Gell, C.B., W.W. Graessley, V. Efstratiadis, M. Pitsikalis and N. Hadjichristidis, *J. Polym. Sci. Polym. Phys*. **35**, 1943 (1997).

Graessley, W.W., T. Masuda, J.E.L. Roovers and N. Hadjichristidis, *Macromolecules* **9**, 127 (1976).

Graessley, W. W. and V. R. Raju, *J. Polym. Sci*. **71**, 77 (1984).

Janzen, J. and R. J. Colby, *J. Mol. Struct*. **48**, 569 (1999).

Jordan, E.A., A.M. Donald, L.J. Fetters and J. Klein, *J. ACS Polym. Prepr*. **30**, 63 (1989).

Kim, Y.S., C.I. Chung, S.Y. Lai and K.S. Hyun, *J. Appl. Polym. Sci*. **59**, 125 (1996).

Kiparissides, C., G. Verros, and J.M.S. Rex, *Macromol. Chem. Phys*. **C33**, 437 (1993).

Kraus, G. and J.T. Gruver, *J. Polym. Sci. Part A* **3**, 105 (1965).

Lai, S. Y., J. R. Wilson, G. W. Knight, J. C. Stevens, and P. W. S. Chum, U.S. Patent No. 5,272,236 (1993).

Laun, H.M. and H. Schuch, *J. Rheol*. **33**, 119 (1989).

Lusignan, C. P., *Influence of the linear chain length between branch points on branched polymer structure and rheology*, Ph.D. dissertation, The University of Rochester, 1996.

Lusignan, C. P., T. H. Mourey, J. C. Wilson, and R. H. Colby, *Phys. Rev. E* **60**, 5657 (1999).

Mendelson, R. A., W. A. Bowles, and F. Finger, *J. Polym. Sci*. **8**, 105 (1970).

Munstedt, H. and H.M. Laun, *Rheol. Acta* **20**, 211 (1981).

Raju, V. R., H. Rachapuda, and W. W. Graessley, *J. Polym. Sci. Phys. Ed*. **17**, 1223 (1979a).

Raju, V. R., G. G. Smith, G. Marin, J. Knox, and W. W. Graessley, *J. Polym. Sci. Polym. Phys. Ed*. **17**, 1183 (1979b).

Roovers, J., *Macromolecules* **17**, 1196 (1984).

Roovers, J. and W.W. Graessley, *Macromolecules* **14**, 766 (1981).

Saeda, S., T. Suzuki and K. Yamaguchi, *J. Appl. Polym. Sci*. **15**, 277 (1971).

Shroff, R. N. and H. Mavridis, *Macromolecules* **32**, 8454 (1999).

Sinn, H., W. Kaminsky, H.J. Vollmer, and R. Woldt, *Angew. Chem. Int. Ed. Engl*. **92**, 396 (1980).

Vega, J. F., A. Santamaria, A. Munoz-Escalona, and P. Lafuente, *Macromolecules* **31**, 3639 (1998).

Vinogradov, G. V. and A. Y. Malkin, *Rheology of Polymers: Viscoelasticity and Flow of Polymers*, Springer, New York, (1980).

Wild, L., R. Ranganat, and D. C. Knobeloch, *Polym. Eng. Sci*. **16**, 811 (1976).

Wood-Adams, P. M., *J. Rheol*. **45**, 203 (2001).

Wood-Adams, P. M. and J. M. Dealy, *Macromolecules* **33**, 7481 (2000).

Wood-Adams, P. M., J. M. Dealy, A. W. deGroot, and O. D. Redwine, *Macromolecules* **33**, 7489 (2000).

Zimm, B. H. and W. H. Stockmayer, *J. Am. Chem. Soc*. **17**, 1301 (1949).

5.0 Predicting LCB Structure

Preface

This chapter focuses on the first objective of the research. Specifically, the relationship between extensional strain hardening behavior and long-chain branching is examined. The use of the molecular-theory based pom-pom model provides a method with which to relate molecular structure and rheological response. This chapter is organized as a manuscript for future publication.

Assessing the Branching Architecture of Sparsely Branched Metallocene-Catalyzed Polyethylenes Using the Pom-pom Constitutive Model

Phillip J. Doerpinghaus and Donald G. Baird

Department of Chemical Engineering, Virginia Polytechnic Institute and State University, Blacksburg, VA

(ABSTRACT)

The model parameters for the multi-mode differential pom-pom constitutive equation were determined for densely branched, sparsely branched, and linear polyethylene resins. The versatility and robustness of the pom-pom model is demonstrated through good rheological predictions in both shear and extensional deformations. The model parameters obtained for the sparsely branched materials indicate that the frequency of long-chain branching dominates the degree of strain hardening observed in uniaxial extension. This finding agrees well with the proposed mechanism of long-chain branching using constrained-geometry metallocene catalysts. Although the model parameters agree qualitatively with the long-chain branch content determined from dilute solution measurements, unrealistic values of the number of pom-pom arms at each branch point are also observed from the fitted model parameters.

5.1 Introduction

The recent development of the "pom-pom" constitutive model of McLeish and Larson (1998) has provided new insight into the subtle effects of long-chain branching on the rheological properties of branched polyethylenes. Using a novel molecular structure, McLeish and Larson demonstrate that the constitutive model predictions under shear and extensional deformations resemble the observed rheological response of densely branched polyethylene resins. Most notably, the model correctly predicts strain hardening in both uniaxial and planar extensional flows. Furthermore, the model parameters used to fit available rheological data can be used to construe some idea of the molecular structure as well as the extent of branching. In

the case of the densely branched, low-density polyethylene (LDPE), the pom-pom model seems well suited. However, its application to sparsely branched commercial systems has gone untested. The development of sparsely branched metallocene-catalyzed polyethylene resins using constrained geometry catalysts (CGC) represents a new benchmark with which to test the versatility of the pom-pom model while assessing the architecture of these systems.

The application of the pom-pom model to densely branched materials such as commercial low-density polyethylene (LDPE) was recently undertaken by Inkson *et al*. (1999). Using a series of well-characterized LDPE resins, the authors were able to fit shear and extensional data with considerable accuracy using a multi-mode formulation of the pom-pom differential model. Surprisingly, transient shear viscosity predictions agreed well with experimental measurements using material parameters determined solely from shear dynamic oscillatory and transient extensional data. Subsequent model modifications by Blackwell *et al*. (2000) provided smoother, more accurate predictions to transient and steady extensional viscosity predictions of the same LDPE resins.

The success of the model in predicting the rheological response of LDPE relies upon the idea that segmental tension can be traced from the free ends at the surface of the macromolecule inwards toward the core [Bick and McLeish (1996)]. The maximum accumulated segmental tension is determined by its *priority* [Read and McLeish (2001)], and the rate of relaxation of that stress is determined by its *seniority* [Rubenstein *et al*. (1990)]. In effect, this concept associates the fastest relaxing constitutive modes to the free arms and the slowest relaxing modes to the core segments. This approach is tantamount to deconstructing, or decoupling, the macromolecular superstructure into an ensemble of pom-pom molecules. The results of this

treatment provide strikingly accurate results for densely branched low-density polyethylene [Inkson *et al*. (1999), Blackwell *et al*. (2000)].

The extension of the pom-pom model to sparsely branched systems presents a different challenge. The degree of branching found in sparsely branched metallocene polyethylene is considerably less than that formed from free radical polymerization. The proposed mechanism for branching in metallocene polyethylenes occurs by temperature activated, β-hydride elimination reactions that give rise to vinyl-terminated polymer chains [Woo *et al*. (1994)]. These *macromonomers* can then be re-incorporated into growing chains thereby generating long chain branches. It is believed that sparsely branched metallocene polyethylene resins consist of a mixture of linear, star, and higher branched species [Soares and Haimilec (1995,1997)]. The results of modeling the coordination polymerization of ethylene using CGC catalysts like those developed by the Dow Chemical Company [Lai *et al*. (1993)] suggest that the weight fraction of macromolecules having two or more branch points accounts for a relatively small mass of the whole polymer. As a result, one would expect very few molecular segments capable of being described by a branched pom-pom molecule. This contrasts greatly to the situation observed for highly branched LDPE discussed above.

The accuracy of the pom-pom model predictions and the precision of the model parameters are dependent upon the quality and breadth of the fitted rheological data. This is certainly true when differentiating varying degrees of long-chain branching in LDPE or mPE resins. Prior studies of commercial and model polymer systems have shown that rheological characterization is a sensitive indicator of molecular structure [Schreiber and Bagley (1962), Janzen and Colby (1999), Wood-Adams and Dealy (2000), Graessley and Raju (1984)]. More specifically, studies using model polymer systems have shown that the degree, length, and

structure (i.e. star, comb, random, etc.) of branching have considerable effect on the zero-shear viscosity and the onset of shear-thinning behavior [Graessley *et al*. (1976), Raju *et al*. (1979), Roovers (1984)]. However, various combinations of molecular weight and long-chain branching can lead to similar shear rheological behavior [Doerpinghaus (2002)]. This complication is often observed in commercial materials and requires alternate rheological measurements to differentiate the effects of branching [Meissner (1975), Bin Wadud and Baird (2000)].

In addition to shear deformations, extensional deformations can be used to assess the effects of molecular structure on rheology. In fact, extensional rheological characterization has also been found to be sensitive to long-chain branching [Münstedt and Laun (1979)]. Unlike linear polymers, which exhibit shear and extensional-thinning behavior, long-chain branched polymers often show extensional viscosity growth above the linear viscoelastic (LVE) limit of $3\eta^{+}(t)$. This rise above the LVE envelope is generally referred to as *strain hardening*. Previous studies on linear and branched polyethylenes have shown that the presence and magnitude of strain-hardening behavior are dependent upon the degree and topology of long-chain branching present [Laun and Münstedt (1978), Münstedt and Laun (1981), Khan and Larson (1987), Laun and Schuch (1989)]. More recently, Bin Wadud and Baird (2000) have shown that this is also qualitatively true for sparsely branched metallocene polyethylene resins. In contrast, Kasehagen and Macosko (1998) have argued that extensional strain hardening is simply a result of extremely long relaxation times not readily observed in shearing flows and that the observed rheological response may or may not be attributed to the presence of long-chain branching in randomly branched polybutadienes.

Although extensional measurements of model systems are often difficult to obtain, the results indicate the importance of branch structure over the degree of branching. The extensional

measurements of polymer melts are notoriously difficult to obtain [Dealy and Wissburn (1990)]. The presence of a free surface often leads to nonhomogenous flow and the need for numerous measurements at each extension rate. In the case of model systems, this often prohibits extensional characterization because of the small quantity of material available. However, recent research suggests that more than one branch point per chain is required for extensional strain hardening [Ye and Sridhar (2001), McLeish *et al*. (1999), Lohse *et al*. (2002)]. Ye and Sridhar (2001) measured the extensional viscosity of three-arm polystyrene solutions and found that extensional thinning was observed over a very wide range of extension rates. These observations were found to be qualitatively similar to those of the linear polymer solutions. On the other hand, McLeish *et al*. (1999) and Lohse *et al*. (2002) found that only molecules having multiple branch points exhibit extensional strain hardening behavior. McLeish *et al*. (1999) observed extensional strain hardening in a model, H-shaped polyisoprene (PI), while Lohse *et al*. (2002) observed it for comb-branched hydrogenated polybutadienes (HPB). Furthermore, Lohse *et al*. determined that a very small amount, as little as 5%, of the comb-branched HPB blended with linear polyethylene was required to affect the extensional viscosity. These rather few observations clearly imply that extensional viscosity measurements can be used to assess the degree and possibly the type of long-chain branching that exists in sparsely branched metallocene polyethylenes.

In the present study, a series of five commercially available polyethylene resins is investigated. Three of the five resins are narrow molecular weight distribution, sparsely branched metallocene polyethylenes (mPE) that are the focus of this study. Each of these mPE resins contains a different degree of long-chain branching as determined from dilute solution analysis. In addition to the sparsely branched mPE resins, a linear low-density polyethylene (LLDPE)

resin and a densely branched LDPE is also used. These conventional resins are used to test the versatility of the pom-pom model in the cases of considerable long-chain branching and no long-chain branching. The goal of this study is to determine whether the structure of sparsely branched metallocene polyethylene predicted using the pom-pom molecular constitutive equation is consistent with the proposed mechanism for long-chain branching during polymerization and the level of branching obtained from dilute solution measurements. Using available shear and extensional rheological data, a set of model parameters are fitted for each of the polyethylene resins investigated. From these model parameters, characteristic pom-pom structures are deduced.

5.2 The Pom-pom Constitutive Model

In this section, a brief review of the constitutive model and the basic set of equations used to predict the shear and extensional rheological responses are presented. Although a rigorous derivation of the original model is quite insightful, these details can be found elsewhere [McLeish and Larson (1998)]. The pom-pom molecule is a relatively simple structure consisting of two q-armed stars connected by a single backbone section known as the crossbar (Figure 5.1). Using a generalization of the Doi-Edwards tube model [Doi and Edwards (1986)], the configuration of these pom-pom molecules can be described by two dynamic variables **S** and λ. The tensor **S** describes the average backbone tube orientation and the scalar λ describes the average backbone stretch. Furthermore, the timescales for backbone orientation and stretch are determined by two separate relaxation times, τ_b and τ_s, respectively. The maximum backbone stretch, and thus the maximum accumulated stress, is determined by the number of pom-pom

Figure 5.1: A schematic representation of the simplest pom-pom molecule, the H-polymer (q=2).

Table 5.1: Differential pom-pom constitutive model equation set.

Stress	$\sigma = \sum_i \sigma_i = 3\sum_i g_i \lambda_i^2 \boldsymbol{S}_i$	(5.1)
Orientation	$\boldsymbol{S}_i = \frac{\boldsymbol{A}_i}{\mathrm{tr}\,\boldsymbol{A}_i}$	(5.2a)
	$\frac{D}{Dt}\boldsymbol{A}_i = \boldsymbol{K}\cdot\boldsymbol{A}_i + \boldsymbol{A}_i\cdot\boldsymbol{K}^T - \frac{1}{\tau_{bi}}\left(\boldsymbol{A}_i - \boldsymbol{I}\right)$	(5.2b)
Stretch	$\frac{D}{Dt}\lambda_i = \lambda_i\left(\boldsymbol{K}:\boldsymbol{S}_i\right) - \frac{1}{\tau_{si}}\left(\lambda_i - 1\right)e^{\nu_i^*(\lambda_i - 1)}$	(5.3)

arms, q. For this particular treatment, the effects of arm withdrawal in the original formulation have been neglected [McLeish and Larson (1998)].

The evolution of the dynamic variables **S** and λ are governed by the differential equations appearing in Table 5.1 and the resulting extra stress tensor σ is calculated from these variables. The differential approximation for **S** has been chosen for this study because it provides a similar asymptotic behavior to the full integral form [McLeish and Larson (1998)], but also provides analytical solutions for the orientation tensor components under homogeneous flow conditions. The backbone stretch evolution equation incorporates the concept of drag-strain coupling of the branch point as proposed by Blackwell *et al*. (2000). In this case, the parameter ν^* has been approximated by the suggested value of $2q^{-1}$. A multi-mode formulation has been implemented for this study, and thus each mode will have four unknown parameters: the backbone orientation time τ_{bi}, the individual contribution to the plateau modulus g_i, the number of pom-pom arms q_i, and the backbone stretch orientation time τ_{si}. These unknown parameters are determined from fitting available shear and extensional rheological data.

The recommended procedure by Inkson *et al*. (2000) has been used to determine the model parameters in this study. First, the backbone orientation times (τ_{bi}) and individual plateau moduli (g_i) are determined from linear viscoelastic measurements. This is accomplished using a least squares fit to available data. In this case, the choice of τ_{bi} is arbitrary and one constitutive mode per decade of shear rate was used. Second, the number of pom-pom arms and the stretch orientation time are determined from transient tensile growth measurements. This particular fitting process usually requires a trial-and-error approach. Fortunately, only those modes active at a given extension rate ($\tau_{si}\ \dot{\varepsilon} \sim 1$) are affected. Fitting the slowest extension rate first and proceeding to higher rates generally provides the best results.

5.3 Experimental Section

5.3.1 Materials

The five polyethylene resins employed for this study are commercially available materials. Table 5.2 lists each of the resins considered along with their molecular characteristics as determined by dilute solution measurements. The two Dow Affinity resins are ethylene-octene copolymers produced using the INSITE® catalyst technology. These particular metallocene resins have been investigated in a previous study [Bin Wadud and Baird (2000)]. The ExxonMobil Exact 0201 resin is also an ethylene-octene copolymer produced using the EXXPOL® catalyst technology. The conventional LLDPE (NTX101) is an ethylene-hexene copolymer also manufactured by ExxonMobil using conventional Ziegler-Natta catalysts. The conventional LDPE (NA952) is manufactured by Equistar and is produced using a tubular free-radical polymerization process. None of the resins listed contain any additional additives other than the standard anti-oxidant packages.

The degree of long-chain branching determined from dilute solution measurements are reported in Table 5.2. The sparsely branched mPE resins vary in content from 0.18 to 0.79 LCB/10^4 carbons. This is well over an order of magnitude less than the branching content reported for the conventional LDPE resin (NA952) using C^{13} NMR measurements. Although C^{13} NMR measurements may include some short-chain branches [Axelson (1979)], the breadth of distribution exhibited by NA952 is indicative of a high degree of long-chain branching [Kiparissides *et al*. (1993)]. The NTX101 resin is a linear polyethylene copolymer and was not analyzed for branch content.

Table 5.2: Molecular Weight, MFI, and LCB content of the materials studied.

Resin	**MFI** dg/min	$\mathbf{M_w}$	$\mathbf{M_w/M_n}$	$\mathbf{M_z}$	**LCB** $/10^4$ C
Exact 0201	1.1	88 700	2.14	158 900	0.79
Exact 3132	1.2	111 000	2.04	180 400	--
Affinity PL1840	1.0	87 400	2.43	160 200	0.57
Affinity PL1880	1.0	115 800	2.12	183 700	0.18
NA952	2.0	235 500	17.1	2 619 300	39[a]
NTX101	0.9	122 700	3.44	319 700	--

[a] C^{13} NMR measurement

5.3.2 Shear Rheological Measurements

The shear rheological measurements for each resin were determined using a Rheometrics Mechanical Spectrometer Model 800 (RMS-800). The dynamic oscillatory data were collected over the range of 0.1 – 100 rad s^{-1} using 25 mm parallel plate fixtures. The steady shear rheological measurements were collected over a range of 0.001 – 1.00 s^{-1} using a 25 mm cone and plate fixture. The cone angle used for all steady shear measurements was 0.1 radian. All testing was performed within an inert nitrogen atmosphere to prevent thermo-oxidative degradation. In most cases, the test samples were prepared by compression molding preforms at 170 °C under nominal pressure and allowing them to cool slowly. All steady shear measurements were acquired at test temperature of 150 °C. The dynamic oscillatory shear moduli data were collected over a range of temperatures and shifted to a reference temperature of 150 °C.

The results presented represent an average of at least three runs using different samples each time. The calculated error for the dynamic oscillatory and steady shear measurements was found to be no greater than ±5 and ±10%, respectively.

5.3.3 Extensional Rheological Measurements

Transient uniaxial extensional measurements were obtained using a Rheometrics Extensional Rheometer Model 9000 (RER-9000). This particular extensional rheometer is based upon the rod-pulling design suggested by Münstedt (1979). The transient extensional data were collected over the extension rate range of 0.01 – 1.00 s^{-1}. The maximum Hencky (true) strain achievable with this device is approximately 3.0 using test specimens with initial nominal lengths of 22 mm. The cylindrical test specimens were compression molded from polymer

pellets at 170 °C under nominal pressure and allowed to cool slowly. They were then bonded to test clips using high-temperature UHU® epoxy, mounted to the rheometer, and immersed in a neutrally buoyant silicone oil bath at 150 °C. Once thermal equilibrium was achieved, an applied extension rate deformed the sample and the resulting force was monitored using a leaf spring-LVDT assembly. When non-uniform deformation was visually observed, the acquired sample was discarded and an additional test was performed on a separate specimen.

The results presented for each extension rate represent an average of at least three runs using different samples each time. The calculated error for the extensional viscosity data varies between materials and depends upon the achieved strain. The branched polyethylene resins showed the greatest degree of reproducibility with no more than 10% deviation up to the maximum Hencky strain achievable. The linear resin was much more problematic. The calculated error from ε_H=0 to 2.0 was found to be less than 10%, but above 2.0 strain units homogeneous deformation was difficult to achieve at higher extension rates. In most cases, the extensional rheological data for the NTX101 resin was simply truncated above a $\varepsilon_H = 2.0$.

5.4 Results and Discussion

5.4.1 Linear Viscoelastic Data

The linear viscoelastic data are presented in Figures 5.2-5.4. Figure 5.2 illustrates the observed shear viscosity flow curves for each of the resins over five decades in shear rate. Steady shear measurements were found to overlap well with dynamic oscillatory data in the range of rates investigated here. Figures 5.3 and 5.4 summarize the dynamic storage and loss moduli obtained for each resin at the shifted reference temperature of 150 °C. Together, these data were then used to determine the linear viscoelastic relaxation spectra as described

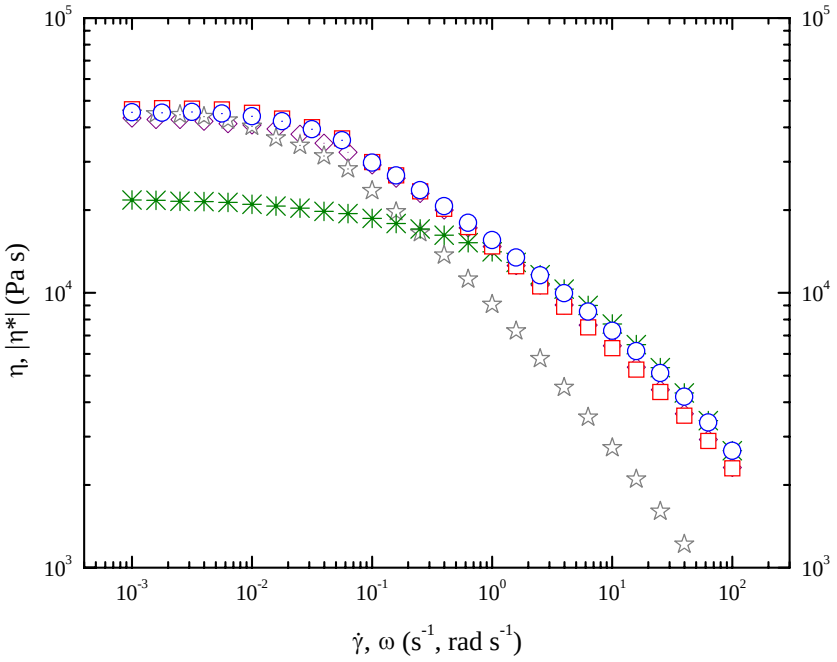

Figure 5.2: Steady shear and complex viscosities at 150 °C. (◇) Exact 0201, (☆) NA952, (✳) NTX101, (□) Affinity PL1840, (○) Affinity PL1880. Dotted symbols represent steady shear measurements; open symbols represent dynamic oscillatory measurements.

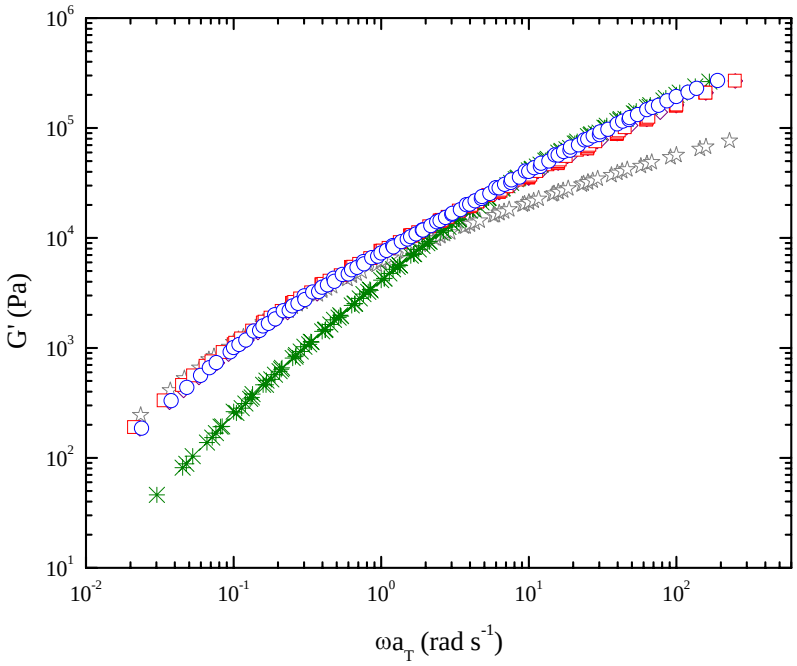

Figure 5.3: Storage moduli at T_{ref} = 150 °C. (◇) Exact 0201, (☆) NA952, (✳) NTX101, (□) Affinity PL1840, (○) Affinity PL1880.

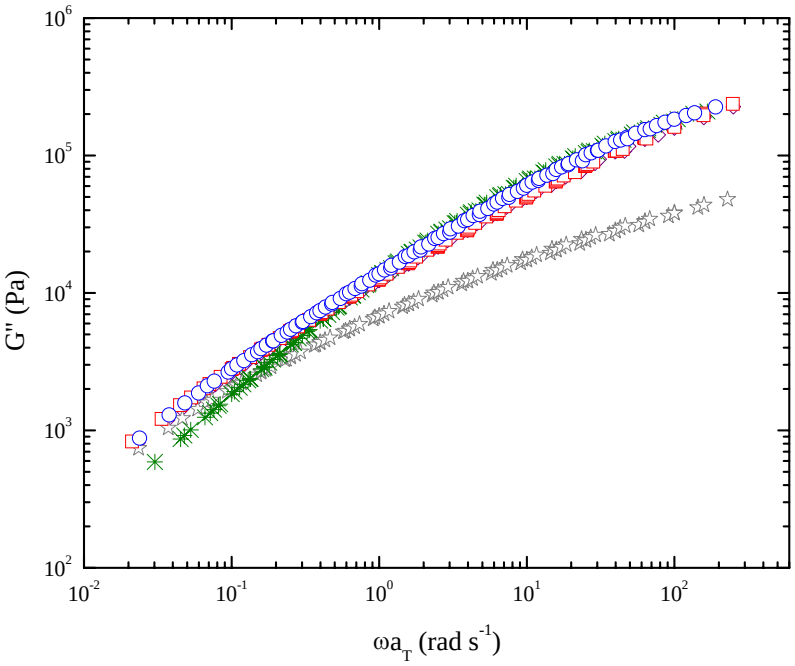

Figure 5.4: Loss moduli at T_{ref} = 150 °C. (◇) Exact 0201, (☆) NA952, (✳) NTX101, (□) Affinity PL1840, (○) Affinity PL1880.

previously. The arbitrarily chosen values for τ_{bi}, and the fitted values of g_i obtained from a numerical error-minimizing routine, can be found in Tables 5.3-5.8.

One of the greatest limitations observed during parameter fitting of τ_{bi} and g_i parameters was the lack of adequate low frequency data. This was certainly true for the branched materials that exhibited shear-thinning behavior at rates less than 0.01 s^{-1}. As a result, steady shear data was often used in combination with the dynamic data to fit the model parameters over the five decades of deformation rates. Despite this approach, it was later determined that an additional mode corresponding to $\tau_{bi} = 10^3$ s was required to accurately fit the lowest extension rate data for the densely branched NA952 resin. Surprisingly, this extremely long relaxation mode is not readily observed during shearing flows, which is in partial agreement with the findings of Kasehagen and Macosko (1998).

5.4.2 Densely Branched Structures

In order to establish the consistency of the technique used in this study with those used in prior studies by Inkson *et al*. (1999) and Blackwell *et al*. (2000), a densely branched LDPE resin is examined first. The experimental and predicted transient extensional and shear growth curves for NA952 are featured in Figure 5.5. The corresponding values of the q_i and τ_{bi}/τ_{si} obtained from fitting the extensional curves at extensional rates of 0.01, 0.1 and 1.0 s^{-1} are shown in Table 5.3. The predicted transient extensional viscosities found in Figure 5.5 (a) agree quite well with measured values. The onset and degree of strain hardening are captured quite well for all three of the rates presented. The only uncertainties from this treatment are the values of q_i. Because steady state extensional viscosities were not obtained up to the maximum Hencky strain of 3.0, the actual value of q_i for each mode could not be established. Therefore, the minimum values of

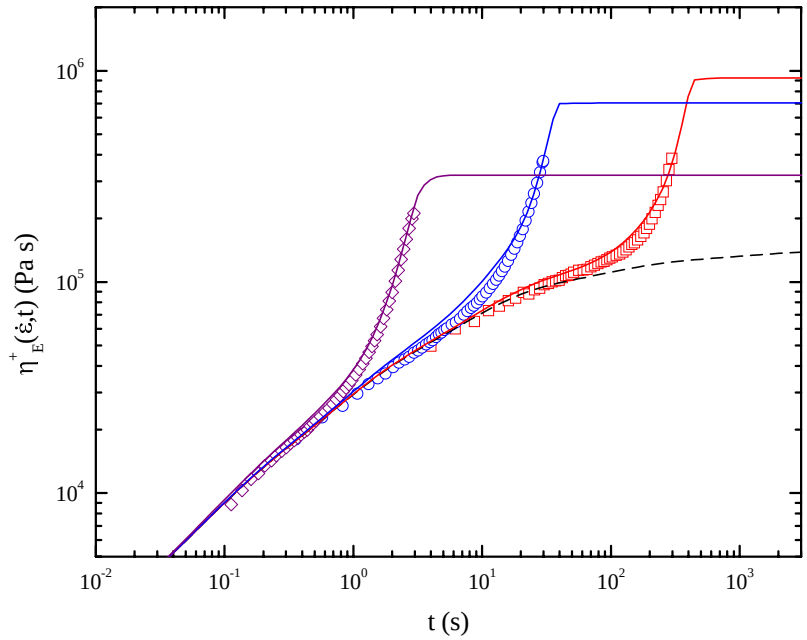

(a)

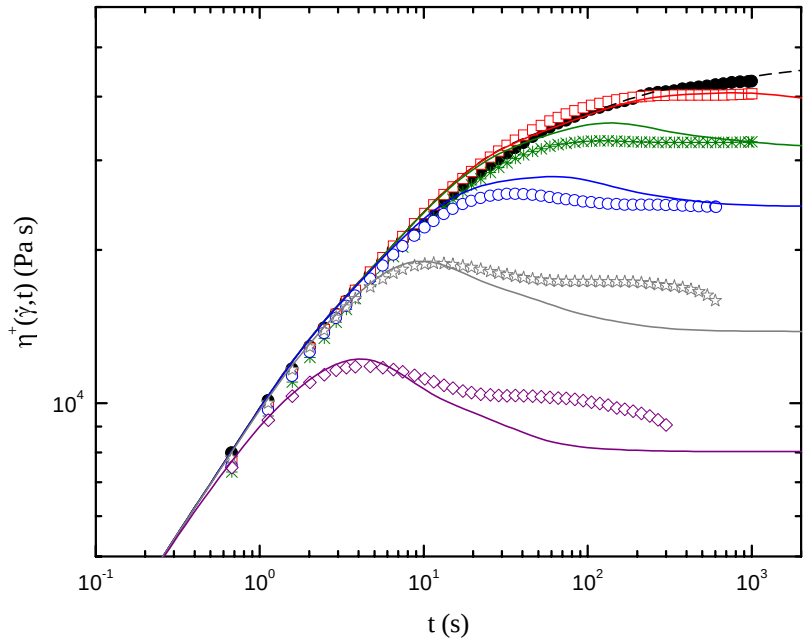

(b)

Figure 5.5: Transient (a) extensional and (b) shear viscosity growth curves for NA952. (●) $\dot{\varepsilon},\dot{\gamma}$ = 0.001 s^{-1}, (□) $\dot{\varepsilon},\dot{\gamma}$ = 0.01 s^{-1}, (✳) $\dot{\varepsilon},\dot{\gamma}$ = 0.0316 s^{-1}, (○) $\dot{\varepsilon},\dot{\gamma}$ = 0.1 s^{-1}, (☆) $\dot{\varepsilon},\dot{\gamma}$ = 0.316 s^{-1}, (◇) $\dot{\varepsilon},\dot{\gamma}$ = 1.0 s^{-1}. Solid lines represent model predictions. Dashed line represent LVE growth curves.

Table 5.3: Pom-pom model parameters for NA952.

τ_{bi}	g_i	q_i	τ_{bi}/τ_{si}
10^{-2}	6.07×10^{4}	1	3.0
10^{-1}	2.28×10^{4}	1	3.0
10^{0}	7.90×10^{3}	1	3.0
10^{1}	1.88×10^{3}	7	2.5
10^{2}	1.10×10^{2}	12	1.3
10^{3}	5.20×10^{0}	20	1.0

q_i that provide acceptable fits to the rheological data have been reported here. The true values of q_i may in fact be higher.

The predicted transient shear viscosities are found in Figure 5.5 (b). The level of agreement is quite good considering the model parameters have been optimized for uniaxial extensional data. The predicted steady state viscosities agree well with experimental data in the low shear rate range from 0.001 – 0.1 $s^{-1}$and begin to deviate by as much as 20% at the higher rates. On the other hand, the departure from the LVE limiting curve and the observed magnitude of the stress overshoot appear to be more accurate at higher rates.

The results obtained for the densely branched polyethylene used in this study are consistent with the trends observed by Inkson *et al*. (1999) and Blackwell *et al* (2000) in similar LDPE resins. The model parameters determined from extension are descriptive of a highly branched low density-polyethylene resins. Surprisingly, the overall fits for transient extensional and shear rheological data are quite good despite the use of fewer pom-pom modes than either Inkson *et al*. or Blackwell *et al* used in their studies. The maximum number of modes used in this study was six modes for the LDPE with the remaining four resins being modeled by only five modes. Although this may lead to a greater degree of response averaging across the modes, this treatment best reflects the amount of rheological data available for these systems.

5.4.3 Sparsely Branched Structures

Having analyzed a densely long-chain branched system, it now seems logical to turn our attention to sparsely branched resins. As stated before, the sparsely branched resins are believed to represent a collection of discrete linear, star and pom-pom shaped molecules. As such, the degree of strain hardening is expected to be less and the number of branched pom-pom modes is

expected to be few. In this subsection, the pom-pom model predictions for the three sparsely branched metallocene resins listed in Table 5.2 will be presented.

Based on dilute solution measurements, the Exact 0201 material features the greatest degree of branching of the metallocene resins at 0.79 LCB/10^4 carbons. As noted earlier, this is more than an order of magnitude less that the branching content observed in the densely branched LDPE system. The experimental and predicted transient extensional and shear viscosity growth curves are presented in Figure 5.6. The corresponding values of the q_i and τ_{bi}/τ_{si} are tabulated in Table 5.4. The transient extensional viscosity predictions agree quite well with the experimental data. The constitutive model accurately captures the onset and magnitude of strain-hardening behavior. Furthermore, the transient shear predictions are surprisingly accurate. Once again, the model parameters have been optimized for the extensional measurements. The fitted parameters clearly indicate that only one branched pom-pom mode is present and that its effects are evident at $\dot{\varepsilon}$=1.0 s^{-1}. In fact, the magnitude of q_i for the longest relaxing mode was accurately determined from the maximum in the extensional viscosity data at $\dot{\varepsilon}$ = 1.0 s^{-1}. On the other hand, the relaxation time ratio τ_{bi}/τ_{si} was determined from the transient extensional viscosity data at $\dot{\varepsilon}$ = 0.1 s^{-1}. Both of which led to excellent predictions at the smallest extension rate of $\dot{\varepsilon}$ = 0.01 s^{-1}.

The predicted transient growth curves for Affinity PL1840 are illustrated in Figure 5.7. The transient extensional predictions are not as accurate at low extension rates, predicting more strain hardening than observed experimentally. Furthermore, at the highest extension rate the observed onset of strain hardening occurs sooner than predicted. This, of course, may be a consequence of having a single branched pom-pom mode active or two decades in extension rate. The model parameters appearing in Table 5.5 were again determined from the maximum

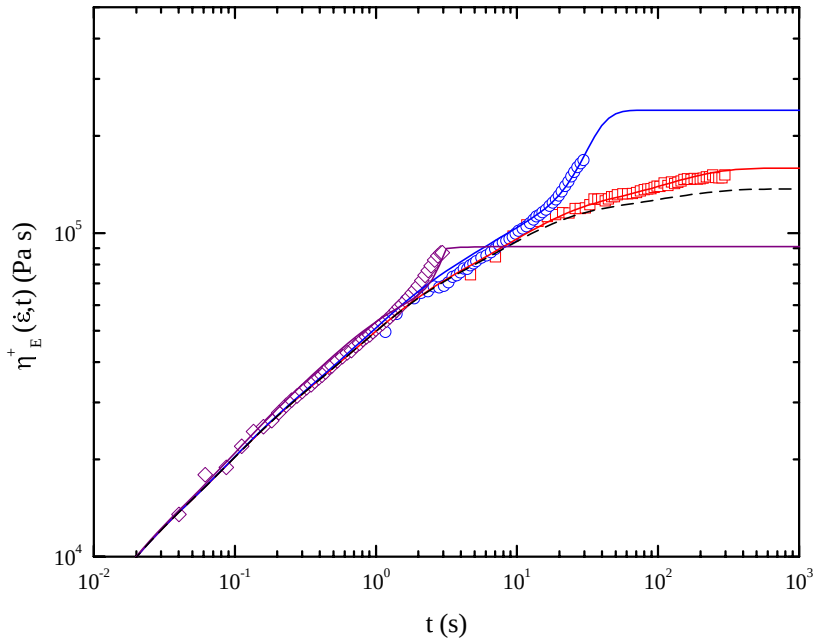

(a)

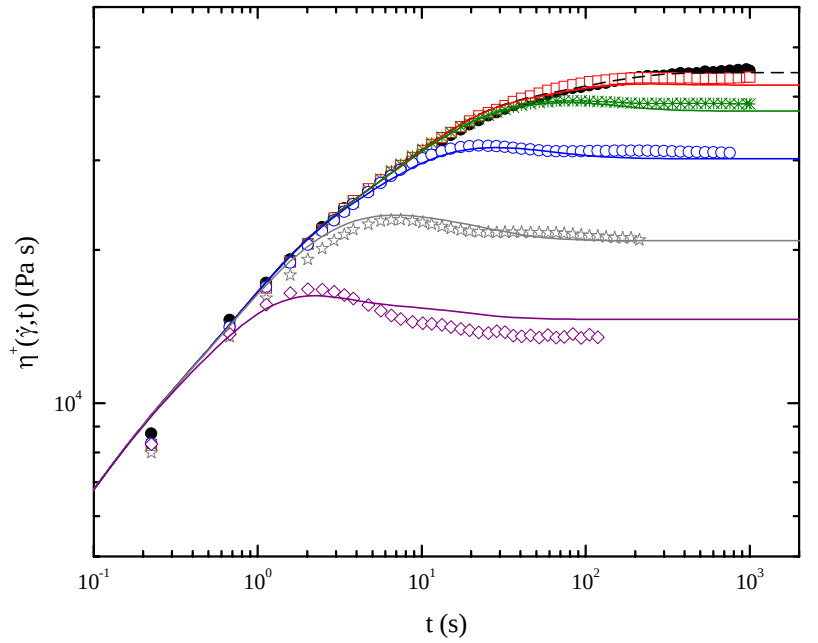

(b)

Figure 5.6: Transient (a) extensional and (b) shear viscosity growth curves for Exact 0201. (●) $\dot{\varepsilon},\dot{\gamma}$ = 0.001 s^{-1}, (□) $\dot{\varepsilon},\dot{\gamma}$ = 0.01 s^{-1}, (✳) $\dot{\varepsilon},\dot{\gamma}$ = 0.0316 s^{-1}, (○) $\dot{\varepsilon},\dot{\gamma}$ = 0.1 s^{-1}, (☆) $\dot{\varepsilon},\dot{\gamma}$ = 0.316 s^{-1}, (◇) $\dot{\varepsilon},\dot{\gamma}$ = 1.0 s^{-1}. Solid lines represent model predictions. Dashed line represent LVE growth curves.

Table 5.4: Pom-pom model parameters for Exact 0201

τ_{bi}	g_i	q_i	τ_{bi}/τ_{si}
10^{-2}	2.56×10^{5}	1	10
10^{-1}	4.55×10^{4}	1	10
10^{0}	1.21×10^{4}	1	10
10^{1}	1.82×10^{3}	1	10
10^{2}	7.23×10^{1}	11	3.5

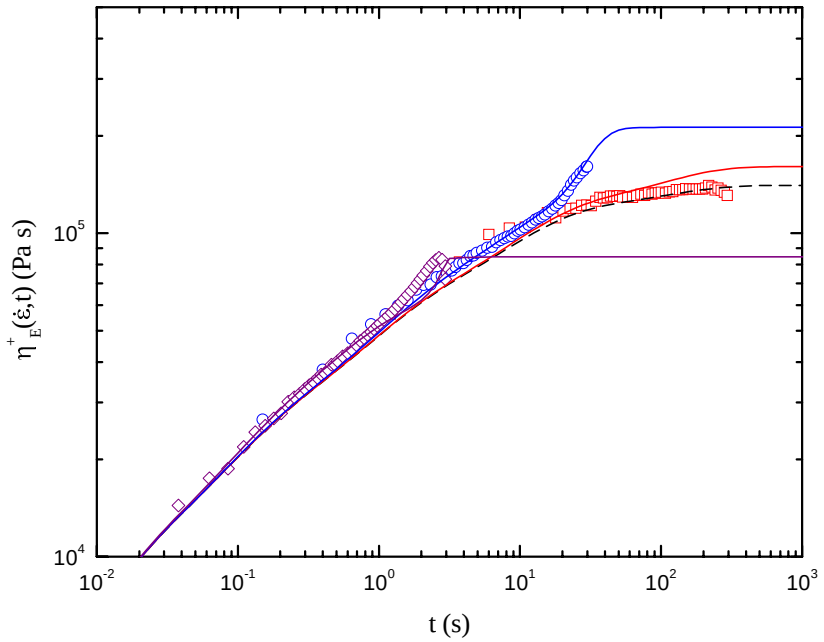

(a)

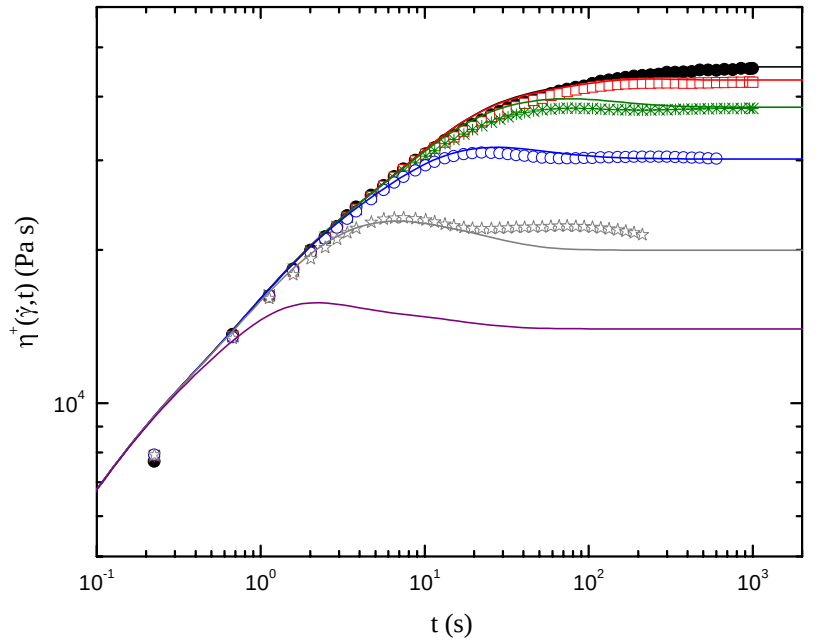

(b)

Figure 5.7: Transient (a) extensional and (b) shear viscosity growth curves for Affinity PL1840. (●) $\dot{\varepsilon},\dot{\gamma}$ = 0.001 s^{-1}, (□) $\dot{\varepsilon},\dot{\gamma}$ = 0.01 s^{-1}, (✳) $\dot{\varepsilon},\dot{\gamma}$ = 0.0316 s^{-1}, (○) $\dot{\varepsilon},\dot{\gamma}$ = 0.1 s^{-1}, (☆) $\dot{\varepsilon},\dot{\gamma}$ = 0.316 s^{-1}, (◇) $\dot{\varepsilon},\dot{\gamma}$ = 1.0 s^{-1}. Solid lines represent model predictions. Dashed line represent LVE growth curves.

Table 5.5: Pom-pom model parameters for Affinity PL1840

τ_{bi}	g_i	q_i	τ_{bi}/τ_{si}
10^{-2}	2.46×10^{5}	1	10
10^{-1}	4.90×10^{4}	1	10
10^{0}	1.06×10^{4}	1	10
10^{1}	2.02×10^{3}	1	10
10^{2}	7.61×10^{1}	10	4.0

viscosity observed at $\dot{\varepsilon} = 1.0\ s^{-1}$ and the transient growth form at $\dot{\varepsilon} = 0.1\ s^{-1}$. Surprisingly, the number of pom-pom arms determined for the slowest relaxing mode is essentially the same as that for the Exact 0201 resin. This occurs despite differences in the dilute solution measurements of long-chain branching content and the noticeably reduced degree of strain-hardening behavior at an extension rate of $0.01\ s^{-1}$. Regardless, the transient shear viscosity curves are reasonably accurate over the range covered.

The Affinity PL1880 resin contains the least amount of long-chain branching according to dilute solution measurements and consequently does not exhibit a substantial degree of strain-hardening behavior. This reduced response makes it difficult to accurately gage the effectiveness of the pom-pom model's fitting ability to the data presented in Figure 5.8. In fact, the material response at $\dot{\varepsilon} = 0.01\ s^{-1}$ appears to be strain softening with respect to $3\eta^{+}(t)$. Despite concern regarding the sensitivity of the pom-pom model to fit the response exhibited by the Affinity PL1880, the same method employed for the previous two materials was used. The model parameters obtained from fitting the four linear and one branched pom-pom modes are summarized in Table 5.6. Again one observes that the number of pom-pom arms is still relatively large at a value of seven, but the relaxation time ratio has increased to a value of 8. This is at least a factor of two greater than those reported for either Exact 0201 or PL1840. Clearly, the separation in timescales appears to be the dominating factor for predicting strain-hardening behavior in sparsely branched mPE resins.

The model predictions obtained for sparsely branched metallocene resins agree qualitatively well with both transient extensional and shear viscosity measurements. The observed strain-hardening behavior that arises from as few as 0.18 LCB/10^4 carbons is modeled well using a set of linear and branched pom-pom structures. The fitted model parameters

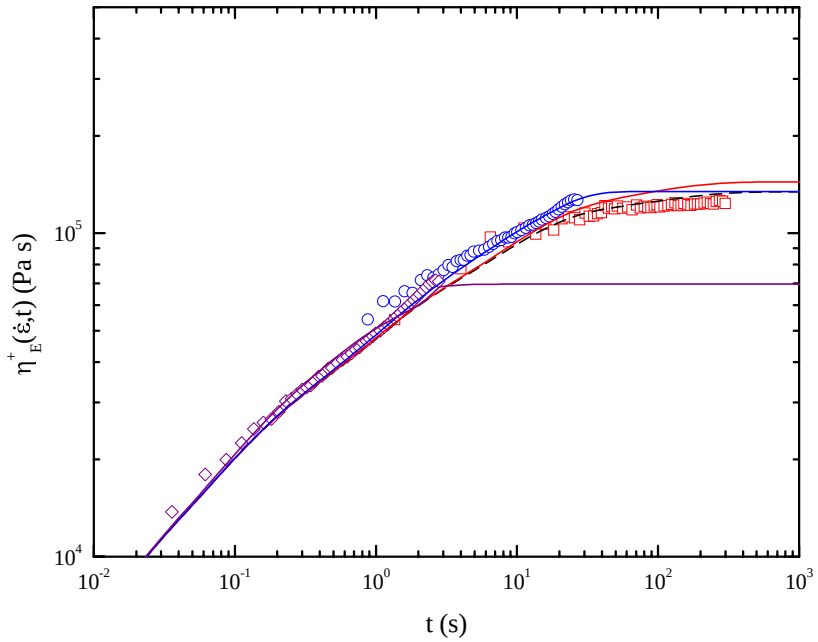

(a)

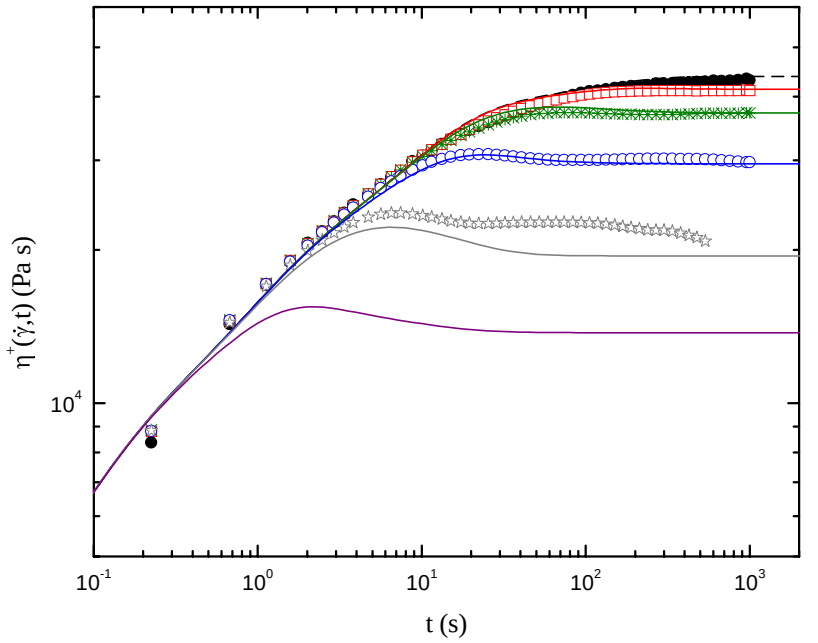

(b)

Figure 5.8: Transient (a) extensional and (b) shear viscosity growth curves for Affinity PL1880. (●) $\dot{\varepsilon},\dot{\gamma}$ = 0.001 s^{-1}, (□) $\dot{\varepsilon},\dot{\gamma}$ = 0.01 s^{-1}, (✳) $\dot{\varepsilon},\dot{\gamma}$ = 0.0316 s^{-1}, (○) $\dot{\varepsilon},\dot{\gamma}$ = 0.1 s^{-1}, (☆) $\dot{\varepsilon},\dot{\gamma}$ = 0.316 s^{-1}, (◇) $\dot{\varepsilon},\dot{\gamma}$ = 1.0 s^{-1}. Solid lines represent model predictions. Dashed lines represent LVE growth curves.

Table 5.6: Pom-pom model parameters for Affinity PL1880

τ_{bi}	g_i	q_i	τ_{bi}/τ_{si}
10^{-2}	2.08×10^{5}	1	10
10^{-1}	5.50×10^{4}	1	10
10^{0}	9.88×10^{3}	1	10
10^{1}	2.01×10^{3}	1	10
10^{2}	6.35×10^{1}	7	8.0

appearing in Tables 5.4-5.6 show that only one branched pom-pom mode exists in each of parameter sets and that this mode is represented by the longest relaxation time. Furthermore, the fitted parameters imply that the separation in orientation and stretch timescales is equally, if not more, important in describing the observed extensional strain-hardening behavior as is the number of pom-pom arms, q_i. The implications arising from these model parameters are discussed in a later section.

5.4.4 Linear Structures

Although the pom-pom constitutive model has been specifically designed to address the rheological effects of long-chain branching, the linear case may be equally important. This can of course be accomplished by setting the number of pom-pom arms equal to one (Table 5.7). However, in the light of the results obtained from the sparsely branched systems, one could also increase the separation in orientation and stretch timescales to an infinite extent thereby decreasing or negating the predicted degree of extensional strain hardening. Therefore, one would assume that accurate modeling of linear materials is important as the degree of long-chain branching becomes very small.

In order to test the versatility of the pom-pom model, a conventional linear low-density has been considered. The molecular characteristics of the linear NTX101 resin can be found in Table 5.2. The rheological data and corresponding pom-pom model predictions can be found in Figure 5.9. Knowing that this Ziegler-Natta polymerized resin has no long-chain branches, the choice of nonlinear parameters becomes trivial. The value of q_i is set to one for all modes and the relaxation timescale ratios become inconsequential (or approach infinity). Beginning with the transient shear predications in Figure 5.9 (b), the predicted results are quantitatively good.

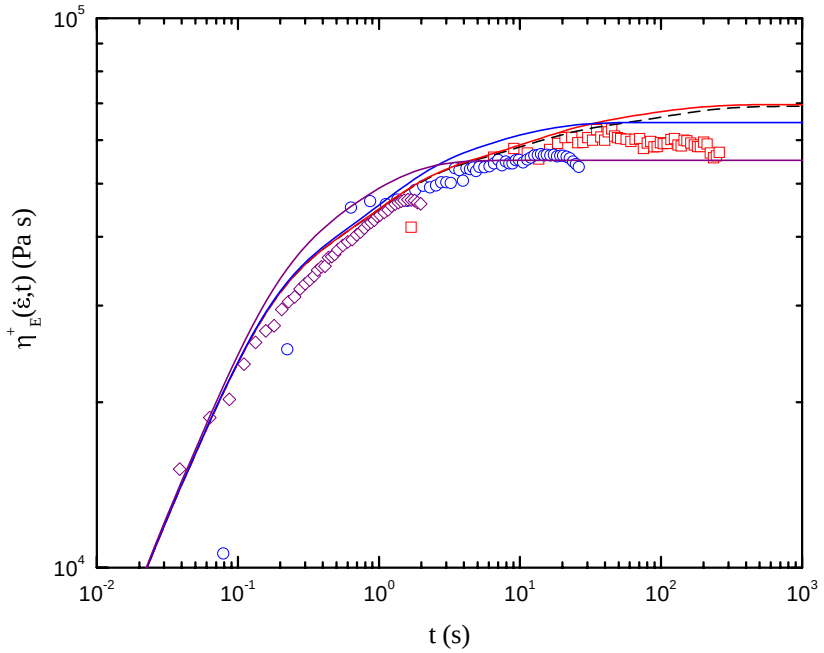

(a)

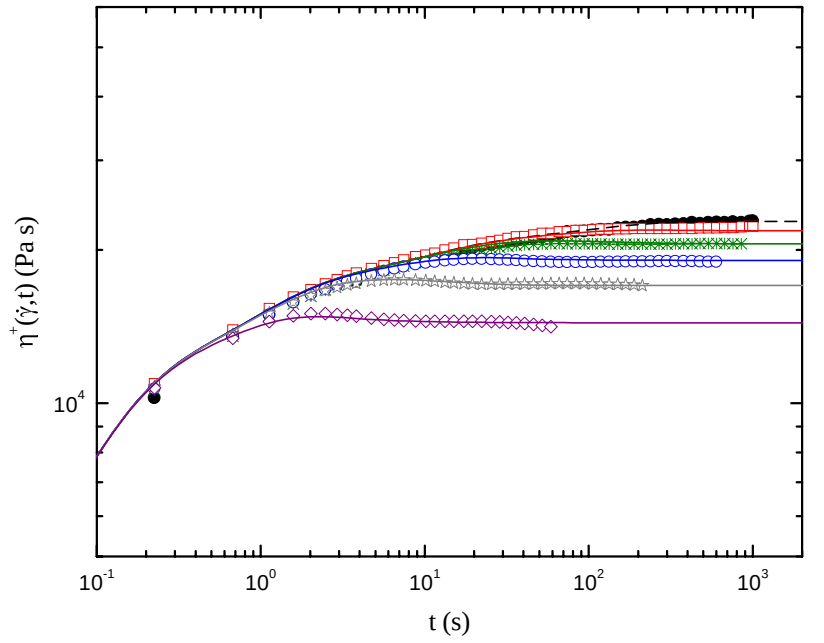

(b)

Figure 5.9: Transient (a) extensional and (b) shear viscosity growth curves for NTX101. (●) $\dot{\varepsilon},\dot{\gamma}$ = 0.001 s^{-1}, (□) $\dot{\varepsilon},\dot{\gamma}$ = 0.01 s^{-1}, (✳) $\dot{\varepsilon},\dot{\gamma}$ = 0.0316 s^{-1}, (○) $\dot{\varepsilon},\dot{\gamma}$ = 0.1 s^{-1}, (☆) $\dot{\varepsilon},\dot{\gamma}$ = 0.316 s^{-1}, (◇) $\dot{\varepsilon},\dot{\gamma}$ = 1.0 s^{-1}. Solid lines represent model predictions. Dashed lines represent LVE growth curves.

Table 5.7: Pom-pom model parameters for NTX101

τ_{bi}	g_i	q_i	τ_{bi}/τ_{si}
10^{-2}	1.49×10^{5}	1	10
10^{-1}	9.05×10^{4}	1	10
10^{0}	6.43×10^{3}	1	10
10^{1}	3.53×10^{2}	1	10
10^{2}	2.25×10^{1}	1	10

The onset of thinning behavior, magnitude of the viscosity overshoot, and steady-state viscosity are well predicted. On the other hand, the extensional viscosity prediction exhibits some anomalous behavior. Clearly, the experimental data plotted in Figure 5.9 (a) grows with $3\eta^+(t)$ and deviates negatively at some critical value of the applied Hencky strain. The predictions, on the other hand, clearly indicate an initial degree of strain hardening before reaching steady state. This numerical artifact has been attributed to the approximating form of the differential pom-pom constitutive model [Bishko *et al*. (1999)]. The full integral form of the pom-pom model does not suffer from this anomaly.

The pom-pom predictions for linear polyethylene melts are very accurate in shear flows. This is not surprising because of the greater dependence upon chain orientation rather than stretch. As a result, the transient shear and extensional characteristics can be determined solely from linear viscoelastic data. Unfortunately, the differential form of the pom-pom model gives rise to physically unrealistic predictions in extensional deformations. This artifact will have very little effect on the predictions of highly branched systems, but may become important when dealing with predominantly linear systems or systems in which the branched species do not contribute to strain hardening behavior (i.e. star-branched polymers).

5.4.5 Interpretation of Suggested Pom-Pom Structures

The model parameters obtained for the sparsely branched metallocene polyethylenes suggest that the observed degree of extensional strain hardening is more sensitive to the separation in orientation and stretch timescales as evidenced by τ_{bi}/τ_{si} than the number of pom-pom arms, q_i. A decrease in the reported long-chain branch content from 0.79 to 0.18 LCB/10^4 carbons for Exact 0201 and Affinity PL1880 results in a 36% decrease in q_i and a 128% increase

in τ_{bi}/τ_{si}. This observation indicates that the molecular dependence of τ_{bi}/τ_{si} is the dominating factor for assessing an average branched structure.

According to the original derivations by McLeish and Larson (1998), the relaxation timescale ratio is directly proportional to the product of the normalized crossbar molecular weight and the fraction of the total molecular weight contained within the crossbar,

$$\frac{\tau_{bi}}{\tau_{si}} \propto s_b \phi_b \tag{5.4}$$

Thus, an increase in the effective distance between branch points will increase the timescale separation. This premise appears to be consistent with the long-chain branching mechanism described earlier. That is, the frequency of β-hydride elimination reactions during polymerization will determine the frequency of, or molecular weight between, long-chain branches. Therefore, the greater the number of branch points for a given molecular weight, the lower the molecular weight between branch points and the smaller the relaxation timescale ratio. Surprisingly, this trend agrees qualitatively with the dilute solution measurements of the degree of branching obtained for the metallocene polyethylenes.

One peculiar result taken from the same model parameters was the large value of q_i determined for the longest relaxing mode. The observed magnitudes of q_5 ranged from 11 for the Exact 0201 resin to 7 for the Affinity PL1880. Although the reduction in value of q agrees qualitatively with dilute solution measurements, the magnitudes appear physically unrealistic. Knowing that synthetic chemistry limits the number of carbon bonds to four, the maximum number of arms q for a "true" pom-pom molecule would be three. Clearly this is significantly less than the reported values for q_5. If the pom-pom ensemble approach used for LDPE is extended to sparsely branched metallocene resins, then several inconsistencies still remain. First, one would expect faster relaxing pom-pom modes with less branching to also appear in the

parameter set. A single, highly branched mode appears to violate the priority constraint and leads to an intangible structure. Second, if one assumes a statistical structure derived from the reaction kinetics of metallocene catalysts [Soares and Hamielec (1997), Read and McLeish (2001)], the number of branch points per molecule (or 10^4 carbons) associated with a priority of order 10 is considerably higher than the dilute solution measurements.

Ultimately, a wide range of shear and extensional rheological data is required for complete characterization of the model parameters and assessment of the implied molecular structure. Although the fitted model parameters appear to agree with the proposed reaction mechanism for long-chain branching and the dilute solution measurements, they may not be unique. One major consequence of discretizing the relaxation spectrum into a finite set of pom-pom modes is the loss of uniqueness. Furthermore, the range and quality of rheological data will determine the number and precision of those modes, respectively. In this case, the unusually high number of pom-pom arms associated with the longest relaxation time could be a result of too few relaxation modes in the range of 10 – 1000 s. Additional data at longer times or lower frequencies may be required.

5.5 Conclusions

The exceptional ability of the multi-mode differential pom-pom constitutive model to describe the rheological behavior of various polyethylene structures has been demonstrated. Most notably, the ability to describe the extensional strain-hardening behavior of sparsely branched polyethylenes produced from metallocene catalysts. This represents a unique extension of the pom-pom constitutive model to sparse, randomly branched materials having an *average* number of branch points per chain less than two. Assuming that a minimum of two branch points

is required for strain hardening behavior, the rheological contributions from a relatively small fraction of the whole polymer is remarkable.

The model parameters obtained for the sparsely branched polyethylene systems indicate that the separation in the relaxation timescales determines the observed degree of strain hardening. This suggests that the frequency of branch points and not the number of branches, q, at a branch point dominate the extensional rheological response. Not surprisingly, this agrees quite well with the believed mechanism for long-chain branching using constrained-geometry metallocene catalysts. Using the model parameters for the relaxation timescale ratio, the implied degree of long-chain branching for each mPE resin agrees qualitatively with dilute solution measurements. On the other hand, the number of pom-pom arms associated with the branched pom-pom modes is unrealistically large. The apparent scaling of q_i with the observed extensional strain-hardening behavior does not agree with the believed long-chain branching mechanism.

5.6 Acknowledgement

The authors would like to thank A. Willem deGroot and David Gillespie at the Dow Chemical Company for providing the LCB and MWD data for all resins presented in this study. The authors would also like to thank T.C.B. McLeish, R.S. Graham, and P. Wapperom for useful discussions regarding the pom-pom constitutive model.

5.7 References

Axelson, D.E., G.C. Levy and L. Mankelkern, *Macromolecules* **12**, 41 (1979).

Bick, D.K. and T.C.B. McLeish, *Phys. Rev. Lett*. **76**, 2587 (1996).

Bin Wadud, S. E. and D. G. Baird, *J. Rheol*. **44**, 1151 (2000).

Bishko, G.B., O.G. Harlen, T.C.B. McLeish, and T.M. Nicholson, *J. Non-Newt. Fluid Mech*. **82**, 255 (1999).

Blackwell, R.B., T.C.B. McLeish, and O.G. Harlen, *J. Rheol*. **44**, 121 (2000).

Dealy, J.M. and K.F. Wissbrun, *Melt Rheology and Its Role in Plastics Processing: Theory and Applications*, Van Nostrand Reinhold, New York, 1990.

Doi, M. and S.F. Edwards, *The Theory of Polymer Dynamics*, Oxford University Press, Oxford, U.K., 1986.

Doerpinghaus, P.J., *Flow Behavior of Sparsely Branched Metallocene Catalyzed Polyethylenes*, Ph.D. Dissertation, Virginia Tech, Blacksburg, VA (2002).

Graessley, W.W., T. Masuda, J.E.L. Roovers and N. Hadjichristidis, *Macromolecules* **9**, 127 (1976).

Graessley, W.W. and V.R. Raju, *J. Polym. Sci.: Polym. Symp*. **71**, 77 (1984).

Inkson, N.J., T.C.B. McLeish, O.G. Harlen, D.J. Groves, *J. Rheol*. **43**, 873 (1999).

Janzen, J. and R. J. Colby, *J. Mol. Struct*. **48**, 569 (1999).

Kasehagen, L.J. and C.W. Macosko, *J. Rheol*., **42**, 1303 (1998).

Khan, S.A. and R.G. Larson, *J. Rheol*. **31**, 207 (1987).

Kiparissides, C., G. Verros and J.M.S. Rex, *Macromol. Chem. Phys*., **C33**, 437 (1993).

Lai, S. Y., J. R. Wilson, G. W. Knight, J. C. Stevens, and P. W. S. Chum, U.S. Patent No. 5,272,236 (1993).

Laun, H.M. and H. Münstedt, *Rheol. Acta* **17**, 415 (1978).

Laun, H.M. and H. Schuch, *J. Rheol*. **33**, 119 (1989).

Lohse, D.J., S.T. Milner, L.J. Fetters, M. Xenidou, N. Hadjichristidis, R.A. Mendelson, C.A. Garcia-Franco, and M.K. Lyon, *Macromolecules* **35**, 3066 (2002).

McLeish, T.C.B. and R.G. Larson, *J. Rheol*. **42**, 82 (1998).

McLeish, T.C.B., J. Allgaier, D.K. Bick, G. Bishko, P. Biswas, R. Blackwell, B. Blottiere, N. Clarke, B.Gibbs, D.J. Groves, A. Hakiki, R.K. Heenan, J.M. Johnson, R. Kant, D.J. Read, and R.N. Young, *Macromolecules* **32**, 6734 (1999).

Meissner, J., *Pure Appl. Chem*. **42**, 553 (1975).

Münstedt, H., *J. Rheol*. **23**, 421 (1979).

Münstedt, H. and H.M. Laun, *Rheol. Acta* **18**, 492 (1979).

Münstedt, H. and H.M. Laun, *Rheol. Acta* **20**, 211 (1981).

Raju, V. R., H. Rachapuda, and W. W. Graessley, *J. Polym. Sci. Phys. Ed*. **17**, 1223 (1979).

Read, D.J. and T.C.B. McLeish, *Macromolecules* **34**, 1928 (2001).

Roovers, J., *Macromolecules* **17**, 1196 (1984).

Rubenstein, M., S. Zurek, T.C.B. McLeish, and R.C. Ball, *J. Physc. (France)* **51**, 757 (1990).

Schreiber, H.P. and E.B. Bagley, *J. Polym. Sci*. **58**, 29 (1962).

Soares, J.B.P. and A.E. Hamielec, *Macromol. Theory Simul*. **4**, 1085 (1995).

Soares, J.B.P. and A.E. Hamielec, *Macromol Theory Simul*. **6**, 591 (1997).

Woo, T.K., L. Fan, and T. Ziegler, *Organometallics* **13**, 2252 (1994).

Wood-Adams, P. M., J. M. Dealy, A. W. deGroot, O. D. Redwine, *Macromolecules* **33**, 7489 (2000).

Ye, X. and T. Sridhar, *Macromolecules*, **34**, 8270 (2001).

6.0 Melt Fracture Behavior

Preface

This chapter addresses the third objective of the research. Specifically, the influence that long-chain branching and narrow molecular weight distribution ultimately have on the melt fracture behavior of commercial polyethylenes is investigated. This chapter is organized as a manuscript for future publication.

Comparison of the melt fracture behavior of metallocene and conventional polyethylenes.

Phillip J. Doerpinghaus and Donald G. Baird

Department of Chemical Engineering, Virginia Polytechnic Institute and State University, Blacksburg, VA 24061

(ABSTRACT)

The influence of sparse long-chain branching and molecular weight distribution on the melt fracture behavior of polyethylene melts was investigated. Four commercial polyethylene resins were employed for this study: a conventional low-density polyethylene, a conventional linear low-density polyethylene, a linear metallocene polyethylene, and a sparsely branched metallocene polyethylene. Rheological measurements were obtained for both shear and extensional deformations, and melt fracture experiments were carried out using a controlled rate capillary rheometer. A single capillary geometry was used to focus on the effects of material properties rather than geometric factors. For the linear polyethylenes, surface melt fracture, slip-stick fracture and gross melt fracture were all observed. Conversely, the branched PE resins did not exhibit a slip-stick regime and the degree of gross fracture was observed to be much more severe than the linear resins. These variations can be explained by the effects that long-chain branching has on the onset of shear-thinning behavior (slip-stick fracture) and the degree of extensional strain hardening (gross melt fracture). Although there is some indication that the breadth of molecular weight distribution indirectly influences surface melt fracture, the results remain inconclusive.

6.1 Introduction

The term *melt fracture* is loosely applied to describe any type of extrudate distortion that results in a variation in shape along the length of the extrudate. Melt fracture is generally classified into three separate types: surface fracture, slip-stick fracture, and gross fracture. Surface melt fracture (SMF) is characterized by high frequency, fine scale surface irregularities, with variations in the extrudate diameter of less than 10%. Slip-stick fracture is described by oscillating pressure gradients and extrusion rates. These measured oscillations represent a discontinuity in the rheological flow curve. Finally, gross fracture is characterized by severe extrudate distortion, typically on the order of the extrudate diameter itself. This particular form of melt fracture occurs at the highest extrusion rates and may or may not be preceded by surface melt fracture and slip-stick fracture. Several comprehensive reviews discussing the origin and mechanism of melt fracture have been published previously [Petrie and Denn (1976), Larson (1992), Piau *et al*.(1994)].

Surprisingly, the type and severity of melt fracture manifested has been found to depend on the material extruded. For example, low-density polyethylene (LDPE) does not exhibit all three types of melt fracture. Rather, LDPE is observed to transition from a smooth extrudate directly to a grossly deformed one above an apparent critical wall shear stress, τ_c. τ_c is of the order of 10^5 Pa, but the exact value may be mildly influenced by die geometry, polymer molecular weight, or extrusion temperature [Tordella (1969)]. Conversely, linear polyethylenes like high-density polyethylene (HDPE) and linear low-density polyethylene (LLDPE) can exhibit all three types of melt fracture [Tordella (1963), Uhland (1979), Kalika and Denn (1987)]. In general, SMF is observed at a $\tau_c \sim 0.1$-0.16 MPa, slip-stick fracture follows at a higher wall shear stress of ~ 0.2-0.4 MPa, and gross fracture can occur at even higher values. In some cases,

typical gross melt fracture behavior is preceded by a relatively smooth region of flow without significant distortion [Uhland (1979)]. This dependence on the type of resin extruded appears to a function of the rheological properties stemming from molecular structure.

Melt fracture phenomena are influenced by the effects that weight average molecular weight (M_w), molecular weight distribution (MWD), and long-chain branching (LCB) have on the melt flow behavior. One of the most comprehensive studies of the effects of molecular structure on melt fracture behavior was performed by Blyler and Hart (1970). In their study, M_w was found to increase the magnitude of the flow curve discontinuity (or pressure oscillations) in the stick-slip fracture regime, but did not significantly affect the onset of slip-stick fracture in linear polyethylenes. Studies by Lim and Schowalter (1989) and Vinogradov *et al*. (1984) using linear polybutadiene melts yielded similar results. Blyler and Hart (1970) also investigated the effects of MWD on melt fracture behavior. By mixing small amounts of low molecular weight PE wax (M_w ~ 1600 g/mol) into high molecular weight polymer, they observed a noticeable reduction in the degree of slip-stick fracture. At the highest concentration of PE wax, the flow curve discontinuity disappeared altogether. Goyal *et al*. (1997) investigated the slip-stick fracture behavior of LLDPE and observed a nonlinear relationship between the onset of slip-stick fracture and the MWD. They claimed that a proper balance between melt viscosity and elasticity is required to maximize the critical wall shear stress. Surprisingly, these observations did not agree with those of Blyler and Hart.

When considering the melt fracture behavior of LDPE and linear polyethylenes, it is tempting to attribute these differences in behavior to the effects that long-chain branching has on melt rheology. While similar distinctions hold for some materials, it does not for others [den Otter (1970, 1971)]. Neither polypropylene [Vinogradov *et al*. (1970)] nor linear silicones

[Benbow and Lamb (1963)] exhibit the characteristic flow curve discontinuity of linear PE resins. As a result, the direct correlation of melt fracture behavior to the presence of long-chain branching must be treated with appropriate caution.

Blyler and Hart (1970) concluded their study on linear and branched polyethylenes by blending LDPE with high molecular weight HDPE. They observed that the magnitude of the flow curve discontinuity decreased with LDPE content, while the critical wall shear stress at the onset of fracture increased. Blyler and Hart reasoned that although LDPE fractions undergo gross melt fracture at a similar wall shear stress, the inlet-type mechanism proposed for LDPE provides strain relief to the remaining linear material that typically undergoes slip-stick fracture. Additionally, Venet and Vergnes (1997) found that the presence of sparse long-chain branching in γ-irradiated LLDPE significantly reduced the severity of SMF observed. Venet and Vergnes concluded that the reduced severity of sharkskin in the sparsely branched LLDPE is due to its extensional strain-hardening behavior arising from LCB. Therefore, the presence of long-chain branching appears to mitigate the magnitude of melt fracture through its influence on the rheological properties.

Much of the prior work reviewed above was performed using conventional LDPE and LLDPE resins. More recently, the development of metallocene catalysts has led to a new class of polyethylenes with narrow molecular weight distribution. Although narrow molecular weight distribution linear PE resins exhibit better physical and mechanical properties, they also suffer from poor melt processability and are more susceptible to melt fracture at low flow rates [Lai *et al*. (1993)]. This behavior can limit their application in film blowing and blow molding applications where LLDPE resins are typically used. In an effort to alleviate these problems, the incorporation of sparse long-chain branching using constrained geometry catalysts has been used

to enhance shear thinning behavior and delay the onset of melt fracture to higher shear rates [Lai *et al*. (1993)].

Although very few melt fracture studies of metallocene polyethylenes exist, those that do present very peculiar results. Initial studies by Vega *et al*. (1996) reported that linear metallocene-catalyzed HDPE resins exhibited both surface and slip-stick melt fracture at critical wall shear stresses of 0.18 MPa and 0.25 MPa, respectively. Interestingly, beyond the slip-stick regime, the measured flow curves were found to be independent of temperature, which is consistent with plug-flow behavior. Hatzikirakos and coworkers (1997) investigated the flow behavior of sparsely branched mPE resins made using Dow Chemical Company's INSITE technology and observed several idiosyncrasies not previously observed in conventional linear polyethylenes. The first was a long induction period prior to steady state flow. During this induction period, the driving pressure was found to pass through a maximum and then decrease to a lower steady state pressure over a period of as much as 80 minutes. Most surprisingly, SMF was initially observed during the transient study, but disappeared prior to steady state. The authors concluded that the anomalous extrusion behavior was due to physico-chemical changes at the die surface leading to slip and atypical melt fracture. More recently, Fernandez *et al*. (2001) observed a striking melt fracture phenomenon in high molecular weight linear mPE resins. Studying the capillary flow of highly elastic linear mPE resins, a hydrodynamic instability was identified by which the emerging polymer melt splits into two symmetric, helical extrudates. This flow-splitting phenomenon was correlated to a crack propagation mechanism that occurs above a critical wall shear stress of 0.28 MPa ($\dot{\gamma}_a$=3.6 s^{-1}).

With only a few, and rather disparate, observations of melt fracture behavior in mPE resins, the subtle effects that narrow molecular weight distribution and degrees of sparse long-

chain branching have on the melt fracture phenomena remain unclear. In the current study, a set of conventional and metallocene polyethylene resins are investigated. The conventional resins consist of a free radical polymerized LDPE and a Ziegler-Natta polymerized LLDPE. The metallocene resins consist of linear and sparsely branched mPE resins having narrow molecular weight distribution. The objective of this study is to better understand the effects that MWD and LCB ultimately have on the observed melt fracture phenomena for polyethylene melts. Simple shear and uniaxial extensional measurements, extrudate imaging, and shear stress/shear rate flow curves are used to assess these effects.

6.2 Material and Methods

6.2.1 Materials

A series of four commercial grade polyethylenes was investigated for this study: a conventional low-density polyethylene (LDPE), a conventional linear low-density polyethylene (LLDPE), a metallocene linear low-density polyethylene (mLLDPE), and a metallocene branched low-density polyethylene (mBLDPE). The conventional LDPE is produced by Equistar Chemical under the product name NA952. NA952 is a tubular, free-radical polymerized ethylene homopolymer. The conventional LLDPE is produced by ExxonMobil under the product name NTX101. This resin is an ethylene-hexene copolymer polymerized using Ziegler-Natta catalysts. The remaining metallocene polyethylenes are both produced by ExxonMobil using EXXPOL® catalyst technology. The mLLDPE resin is an ethylene-hexene copolymer marketed under the product name Exact 3132 and the mBLDPE resin is an ethylene-octene copolymer marketed under the product name Exact 0201. The Exact 0201 resin contains sparse long-chain branching

in its molecular structure. According to the manufactures, none of these resins contain slip or anti-block agents that might obscure their intrinsic flow behavior.

The relevant physical and molecular properties of these resins are tabulated in Table 6.1. The NA952 resin has a very large weight average molecular weight of 235,500 g/mol and a broad molecular weight distribution of 17.1. These values are characteristic of highly branched polyethylenes. The degree of long-chain branching obtained from C^{13} NMR analysis confirms this idea. The NTX101 resin has a more modest M_w of 112,800 g/mol and a relatively narrow molecular weight distribution of 3.41. No long-chain branches are present in the structure of the NTX101 resin. The Exact 3132 resin has an M_w of 111,000 g/mol and a narrow molecular weight distribution of 2.04. Again, no long-chain branches are present in the structure of the Exact 3132 resin. Finally, the Exact 0201 resin has a relatively low M_w of 88,400 g/mol and a breadth of distribution of 2.10. The degree of long-chain branching, as determined from dilution solution low-angle laser light scattering (LALLS) measurements, is estimated to be 0.79 LCB/10^4 carbons. This degree of sparse long-chain branching represents approximately one LCB per two molecules.

6.2.2 Rheological Characterization

Initial rheological characterization of these materials was carried out using a Rheometrics Mechanical Spectrometer Model 800 (RMS-800). Dynamic oscillatory data were collected over the range of 0.1 – 100 rad s^{-1} using 25 mm parallel plate fixtures. Steady shear rheological measurements were collected over a range of 0.001 – 1.0 s^{-1} using a 25 mm cone and plate fixture. The cone angle used was 0.1 radians. All testing was performed within an inert nitrogen atmosphere to prevent thermo-oxidative degradation. In most cases, the test samples were

Table 6.1: Molecular Weight, MFI, and LCB content of the materials studied.

Resin	**MFI** dg/min	$\mathbf{M_w}$	$\mathbf{M_w/M_n}$	$\mathbf{M_z}$	**LCB** $/10^4$ C
Exact 0201	1.1	88 700	2.14	158 900	0.79
Exact 3132	1.2	111 000	2.04	180 400	--
NA952	2.0	235 500	17.1	2 619 300	39[a]
NTX101	0.9	122 700	3.44	319 700	--

[a] C^{13} NMR measurement

prepared by compression molding preforms at 170 °C under nominal pressure and allowing them to cool slowly. All steady shear and dynamic oscillatory measurements were acquired at a test temperature of 150 °C. The results presented represent an average of at least three runs using different samples each time. The calculated error for the dynamic oscillatory and steady shear measurements was found to be no greater than ±5 and ±10%, respectively.

Transient uniaxial extensional measurements were obtained using a Rheometrics Extensional Rheometer Model 9000 (RER-9000). This particular extensional rheometer is based upon the design of Munstedt (1979). Transient extensional data was collected at the highest attainable extension rate of 1.0 s^{-1}. The maximum Hencky (true) strain achievable with this device is approximately 3.0 using test specimens with initial nominal lengths of 22 mm. The cylindrical test specimens were compression molded from polymer pellets at 170 °C under nominal pressure and allowed to cool slowly. They were then bonded to test clips using high-temperature UHU® epoxy, mounted to the rheometer, and immersed in a neutrally buoyant silicone oil bath at 150 °C. Once thermal equilibrium was achieved, an applied extension rate deformed the sample and the resulting force was monitored using a leaf spring-LVDT assembly. The results presented for each extension rate represent an average of at least three runs using different samples. The calculated error for the extensional viscosity data was found to be less than ±10%.

6.2.3 Capillary experiments

Capillary extrusion experiments were carried out using a Goettfert Rheograph 2001 capillary rheometer operating at 150 °C. A single capillary die made from tungsten carbide steel and having a diameter of 1.0 mm and a length of 20 mm was used throughout this study. The

entrance angle for the die was 180° (flat) and the contraction ratio between the reservoir and capillary die was measured to be 15. The driving pressure required for flow was measured using a Dynisco melt transducer (0-500 bar) mounted at the bottom of a deep pressure hole and positioned 15 mm upstream of the capillary die entrance. The resulting pressure traces were captured using a high-speed 12-bit A/D data acquisition system and stored on a personal computer.

6.2.4 Specimen imaging

The polymer extrudate collected from the capillary extrusion experiments was imaged using a Leo 1550 field-emission scanning electron microscope (FE-SEM). This device was chosen because it provides better contrast at low magnifications than standard optical microscopy. The fracture samples were first cut and mounted to sample stages, and then a 10nm thick coating of elemental gold was sputter coated onto the surface. Once coated, the samples were then mounted in the FE-SEM and imaged under high vacuum ($< 1.5x10^{-5}$ Torr) using an accelerating voltage (tension) of 10kV. The working distance was maintained at 20 mm and the magnification at 20x. All micrographs presented represent a 2.0 x 4.5 mm (W x L) area.

6.3 Results

6.3.1 Preliminary Rheological Characterization

The shear rheological measurements for each of the polymers examined in this study are presented in Figures 6.1 and 6.2. The steady and complex shear viscosities found in Figure 6.1 illustrate the effects that molecular weight distribution and long-chain branching have on shear rheology. The highly long-chain branched NA952 resin transitions to non-Newtonian flow

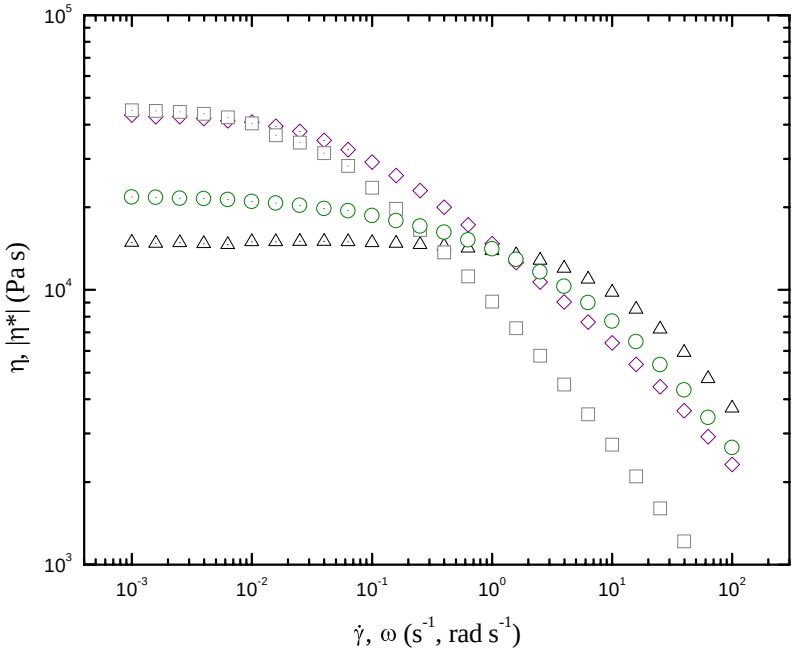

Figure 6.1: Steady and complex shear viscosities at T=150 °C. (□) NA952, (◇) Exact 0201, (○) NTX101, (△) Exact 3132. Dotted symbols represent steady shear measurements; open symbols represent dynamic oscillatory measurements.

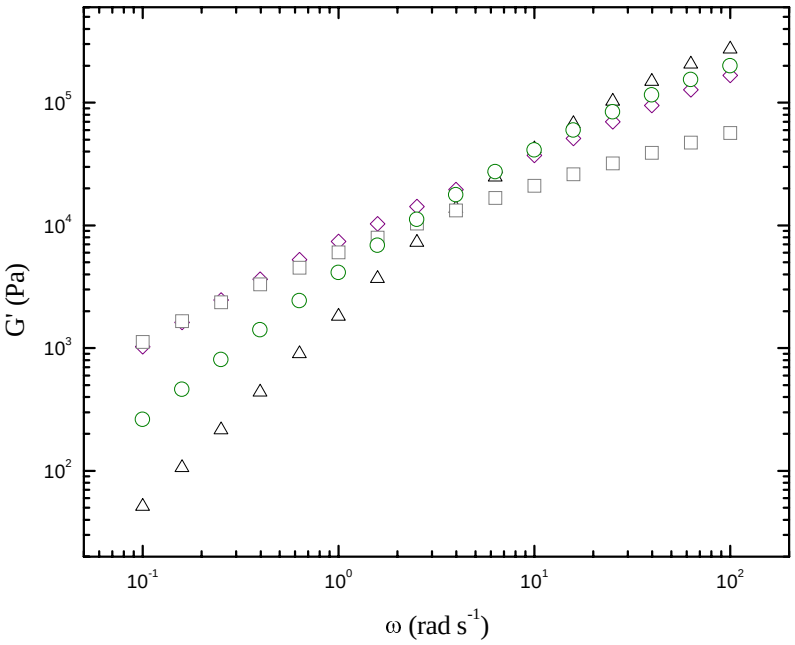

Figure 6.2: Dynamic storage moduli obtained at T=150 °C. (□) NA952, (◇) Exact 0201, (○) NTX101, (△) Exact 3132.

behavior at low shear rates and exhibits the greatest degree of shear-thinning behavior. The Exact 0201 resin, having a sparse degree of long-chain branching, also shows considerable shear-thinning behavior. On the other hand, the linear resins exhibit much less sensitivity to shear rate and the reduction in shear viscosity is much less over the range of rates investigated. Figure 6.2 shows the dynamic storage moduli for each resin. At low frequencies there are observable differences between the resins, but at higher frequencies (rates), where melt fracture occurs, the narrow molecular weight resins converge while the broad MWD NA952 remains consistently lower. Similar trends were observed for the primary normal stress difference, N_1 [Doerpinghaus (2002)].

The transient extensional measurements are shown in Figure 6.3. The transient extensional growth curves obtained at $\dot{\varepsilon}=1.0\ s^{-1}$ show the very different flow behaviors found in commercial PE resins. The NA952 exhibits a substantial degree of extensional strain-hardening behavior. This is evidenced by the marked increase in η_E^+ above the linear viscoelastic envelope of $3\eta^+(t)$. Exact 0201 also shows some extensional strain-hardening behavior, but at a much reduced magnitude. Conversely, the linear polyethylenes show signs of extensional strain softening. In fact, it was very difficult to obtain homogenous deformation of the linear materials because of a necking instability often associated with strain softening materials [Dealy and Wissbrun (1990)].

The preliminary rheological measurements presented in this section indicate that long-chain branching and molecular weight distribution have a significant influence on the flow behavior of commercial polyethylenes. Long-chain branching increases the degree of shear thinning while also increasing the degree of extensional strain hardening. Certainly, a high degree of shear thinning is desired during processing to delay the onset of melt fracture (either

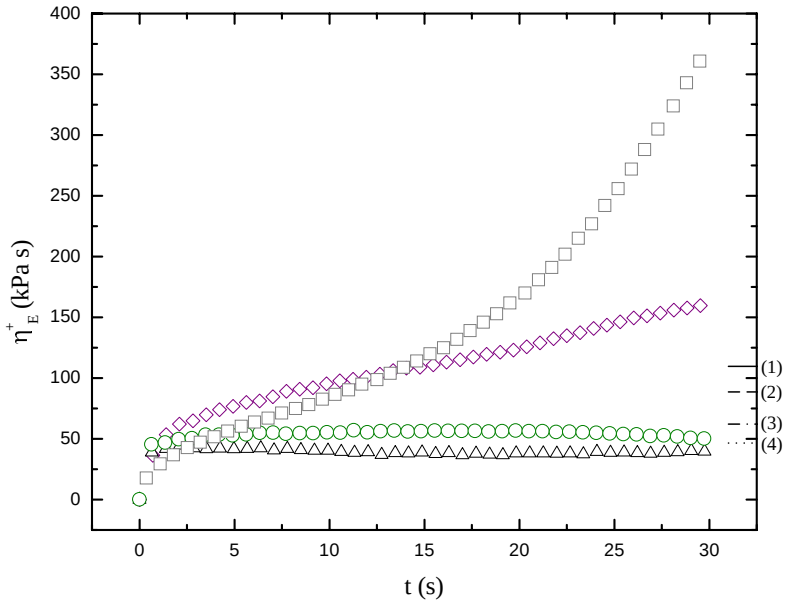

Figure 6.3: Transient extensional viscosities obtained at T=150 °C. (□) NA952, (◇) Exact 0201, (○) NTX101, (△) Exact 3132. Values of $3\eta^+(t)$ at t=30s for (1) Exact 0201, (2) NA952, (3) NTX101, (4) Exact 3132.

surface or gross) to higher flow rates, but a high degree of extensional strain hardening can also mitigate the severity of melt fracture when present [Venet and Vergnes (1997)]. Although much of the rheological data presented here reflects flow behavior at relatively low deformation rates, it is the low shear and extension rate range that probes the long relaxation times. These long relaxation times appear to play a larger role in the flow behavior of polymer melts than the short relaxation times.

6.3.2 Extrusion Studies

In the following section, the flow curves obtained for each resin will be presented in terms of the apparent wall shear stress τ_w versus the apparent wall shear rate $\dot{\gamma}_a$. Due to the presence of melt fracture, viscometric measurements cannot be obtained nor can appropriate corrections be applied (i.e. Bagley end correction, Rabinowitch correction) without adding uncertainty to the measured quantities. Therefore, the apparent quantities, assuming Newtonian behavior, are utilized. τ_w for flow through a capillary is defined as,

$$\tau_w = \frac{R}{2}\frac{\Delta P}{L} = \frac{\Delta P}{80} \tag{6.1}$$

Here, R is the capillary radius, ΔP is the measured pressure drop across the capillary, and L is the capillary length. The appropriate substitutions for R and L yield the greatly simplified relationship used in this study. Additionally, the apparent wall shear rate $\dot{\gamma}_a$ is defined by,

$$\dot{\gamma} = \frac{4Q}{\pi R^3} \tag{6.2}$$

where Q is the imposed flow rate. Again, it should be recognized that $\dot{\gamma}_a$ is not truly a measure of the wall shear rate, because corrections for wall slippage and the non-parabolic velocity profile

have not been applied. Therefore, $\dot{\gamma}_a$ is most representative of the imposed flow rate as determined by the capillary rheometer than the true wall shear rate.

Low-density polyethylene (LDPE)

The flow curve obtained for NA952 at a temperature of 150 °C is plotted in Figure 6.4. The flow curve is a smooth function of shear rate across the entire flow rate range probed and exhibits a mild decrease in the slope of the stress-shear rate curve. The only indication of melt fracture is denoted by the critical wall shear rate for gross melt fracture, $\dot{\gamma}_{gmf}$. $\dot{\gamma}_{gmf}$ was observed at an apparent shear rate of 63 s^{-1}, which corresponds to a wall shear stress of 0.09 MPa. The micrographs shown in Figure 6.5 illustrate the evolution of melt fracture in this highly branched LDPE resin. Beyond $\dot{\gamma}_{gmf}$, the degree of distortion continued to increase with no noticeable variation in the type of fracture. Throughout the examination, the surface of the extrudate remained relatively smooth.

The results obtained for NA952 are similar to the melt fracture behavior reported for LDPE resins. The direct transition form smooth, stable flow to gross distortion has been documented in previous studies by Tordella (1957) and Bagley and Schrieber (1964). The occurrence of gross fracture in LDPE is generally associated with the entrance region of the extrusion die [Tordella (1957), Bagley and Schreiber (1964), White (1973)]. At high flow rates, recirculating vortices present in the entry region become unstable, leading to random oscillations and chaotic flow throughout the extrusion die [see for example Tordella (1969)]. The work of White and Baird (1986) has shown that extensional strain hardening is one of the requirements for vortex formation and supports the idea that gross melt fracture in NA952 is an extensional deformation driven instability.

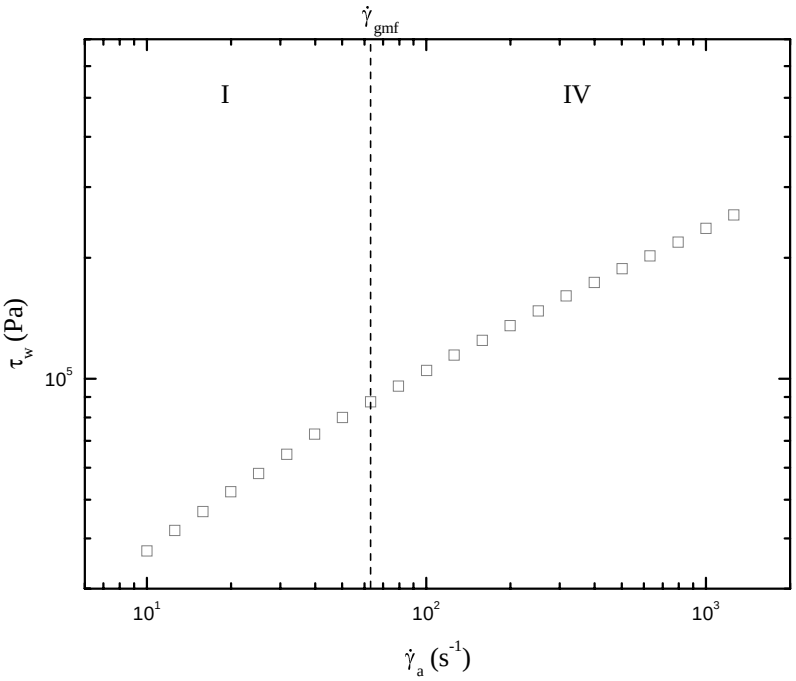

Figure 6.4: Melt fracture flow curve for NA952 obtained at T=150 °C. $\dot{\gamma}_{gmf}$ denotes the onset of gross melt fracture. (I: stable flow regime, IV: gross melt fracture regime)

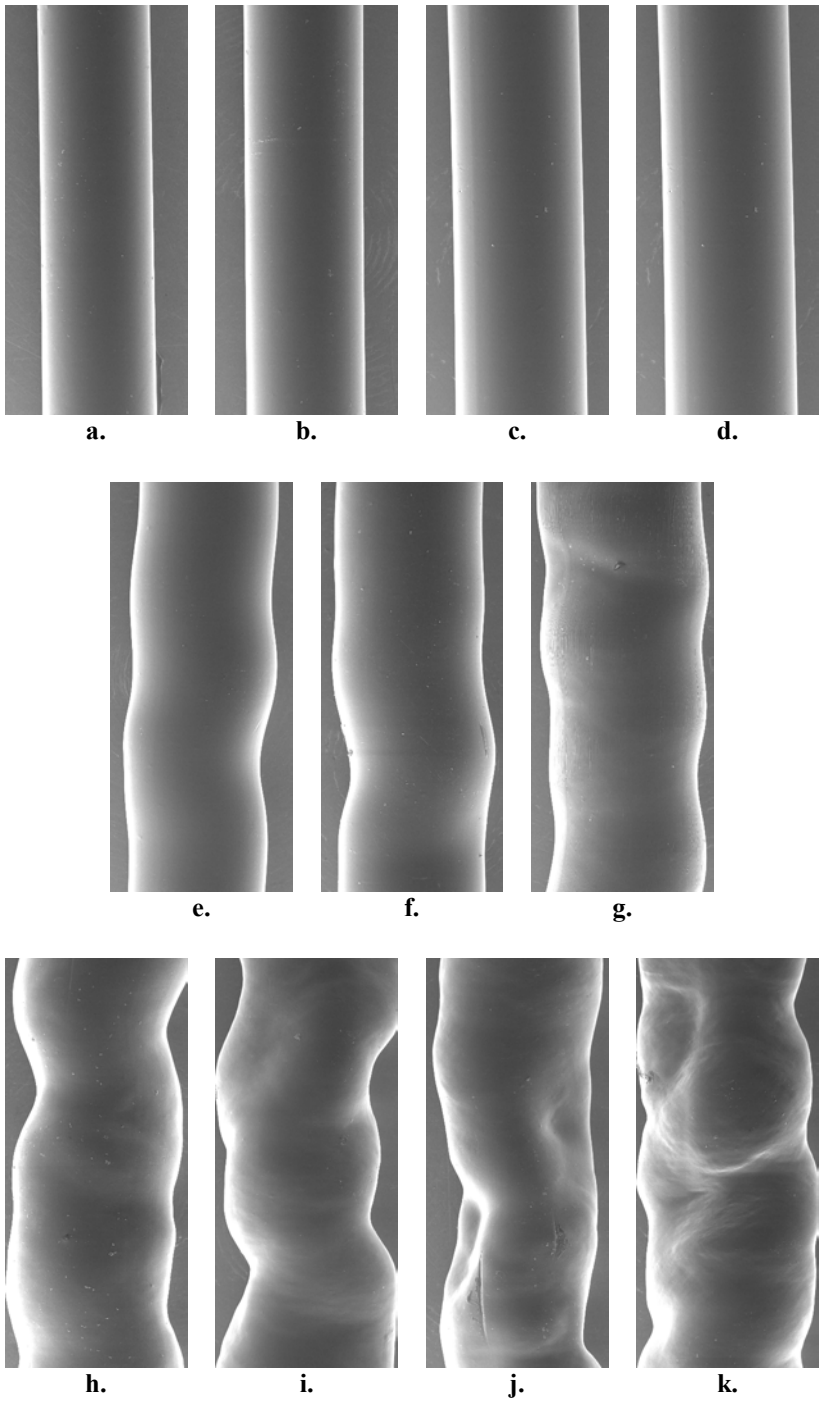

Figure 6.5: FESEM micrographs obtained for NA952. Apparent wall shear rates(stresses) are **a**. 10 s^{-1} (0.037 MPa), **b**. 15.8 s^{-1} (0.047 MPa), **c**. 25.1 s^{-1} (0.058 MPa), **d**. 39.8 s^{-1} (0.073 MPa), **e**. 63.1 s^{-1} (0.088 MPa), **f**. 100 s^{-1} (0.105 MPa), **g**. 158 s^{-1} (0.125 MPa), **h**. 251 s^{-1} (0.148 MPa), **i**. 398 s^{-1} (0.174 MPa), **j**. 631 s^{-1} (0.202 MPa), and **k**. 1000 s^{-1} (0.237 MPa).

Linear low-density polyethylene (LLDPE)

The melt fracture flow curve obtained for the NTX101 resin is plotted in Figure 6.6. One can clearly observe noticeable differences in the flow behavior of this conventional linear PE resin to that of the conventional LDPE resin above. The most obvious difference is that flow curve is divided into four discrete regions representing different states of flow. The first region represents stable flow. The micrographs found in Figure 6.6 clearly show smooth extrudates at shear rates corresponding to $\dot{\gamma}_a$=10 and 15.8 s^{-1}. However, beyond $\dot{\gamma}_a$ = 25.1 s^{-1} surface distortions were observed.

The second region of the flow curve is denoted by the critical wall shear rate for surface melt fracture $\dot{\gamma}_{smf}$. Surface melt fracture is first observed at $\dot{\gamma}_a$ = 25.1 s^{-1} (τ_w = 0.16 MPa). The corresponding micrograph in Figure 6.7 gives some indication of this by a slight matting of the extrudate surface. Further increases in the flow rate led to noticeable increases in the severity of surface melt fracture as evidenced by micrographs obtained at $\dot{\gamma}_a$ = 39.8, 63.1 and 100 s^{-1}. Throughout this second region, pressure traces were observed to be steady.

Beyond $\dot{\gamma}_a$ = 100s^{-1}, the observed extrudate began to periodically spurt from the capillary die. This spurt was associated with the onset of slip-stick fracture and resulted in the characteristic discontinuity in the calculated flow curve. The critical wall shear stress was measured to be 0.32 MPa. This transition from stable to oscillatory driving pressures is demonstrated in Figure 6.8. Most interestingly, further increases in the flow rate first led to a narrow region of stable flow free of pressure oscillations or surface distortions, but was then followed by a high frequency, slip-stick fracture regime. This behavior is easily observed from the micrographs appearing in Figure 6.6. Furthermore, the pressure traces in this second slip-

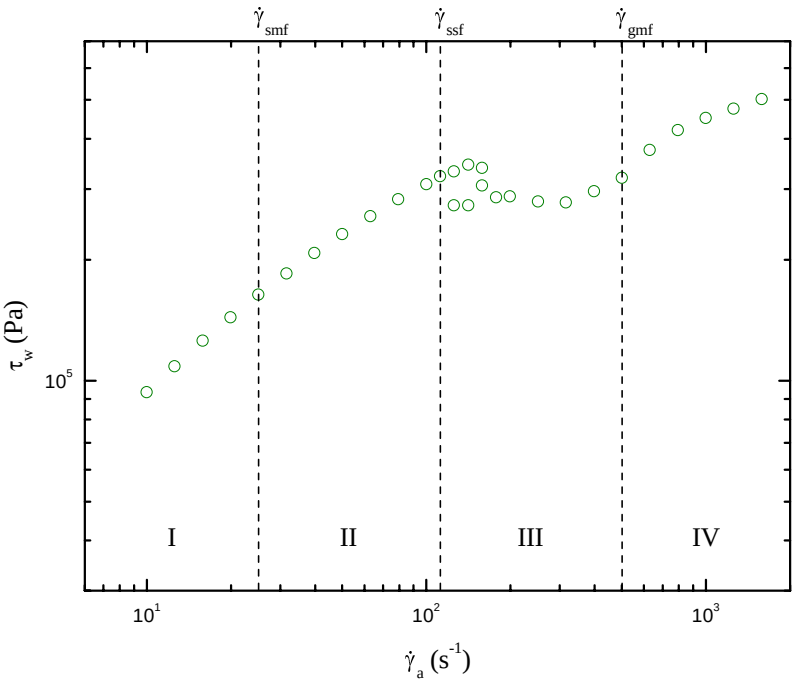

Figure 6.6: Melt fracture flow curve for NTX101 obtained at T=150 °C. $\dot{\gamma}_{smf}$ denotes the onset of surface melt fracture, $\dot{\gamma}_{ssf}$ denotes the onset of slip-stick fracture, and $\dot{\gamma}_{gmf}$ denotes the onset of gross melt fracture. (I: stable flow regime, II: surface melt fracture regime, III: slip-stick fracture regime, IV: gross melt fracture regime)

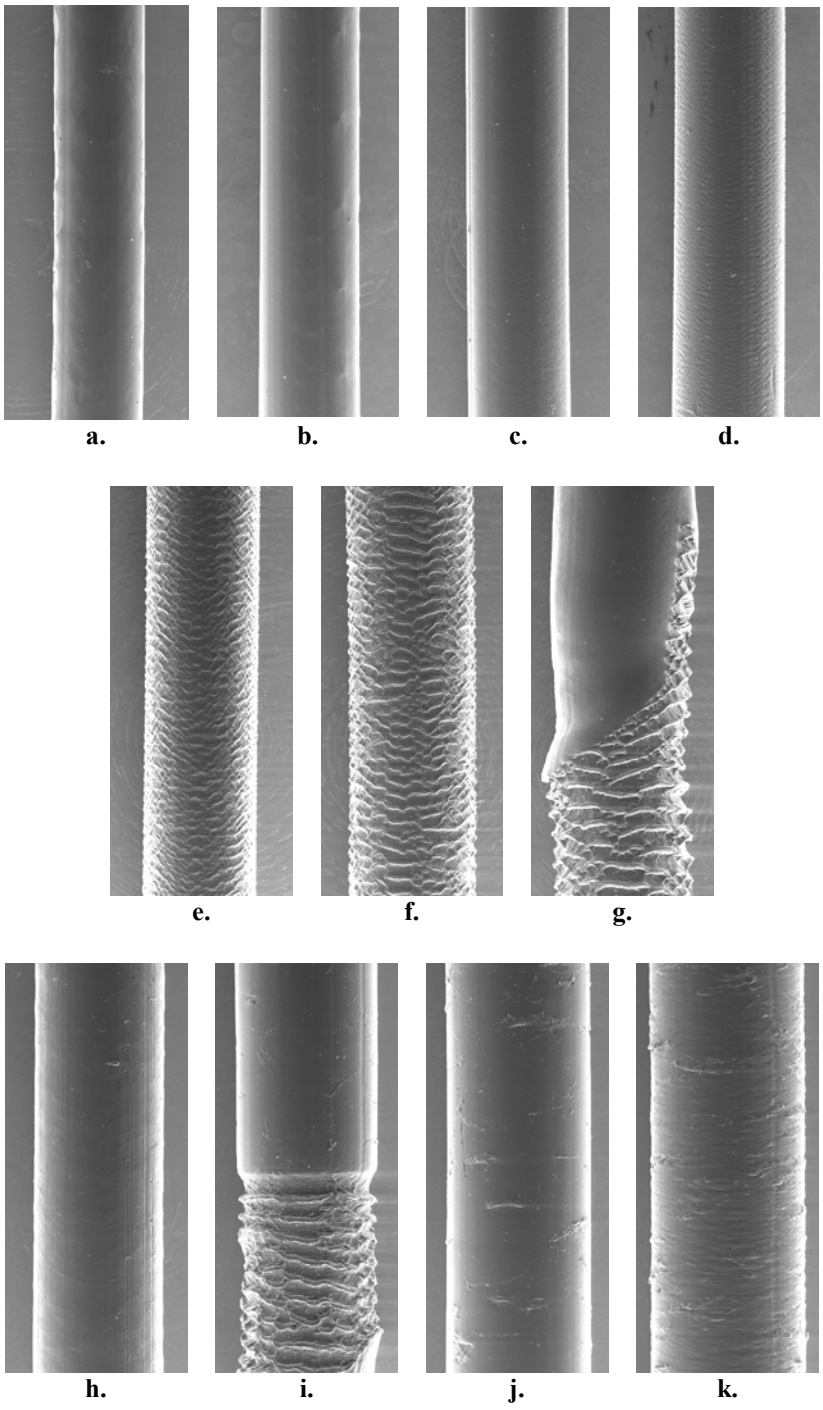

Figure 6.7: FESEM micrographs obtained for NTX101. Apparent wall shear rates(stresses) are **a**. 10 s^{-1} (0.094 MPa), **b**. 15.8 s^{-1} (0.126 MPa), **c**. 25.1 s^{-1} (0.164 MPa), **d**. 39.8 s^{-1} (0.208 MPa), **e**. 63.1 s^{-1} (0.257 MPa), **f**. 100 s^{-1} (0.308 MPa), **g**. 158 s^{-1} (0.322 MPa), **h**. 251 s^{-1} (0.279 MPa), **i**. 398 s^{-1} (0.296 MPa), **j**. 631 s^{-1} (0.375 MPa), and **k**. 1000 s^{-1} (0.451 MPa).

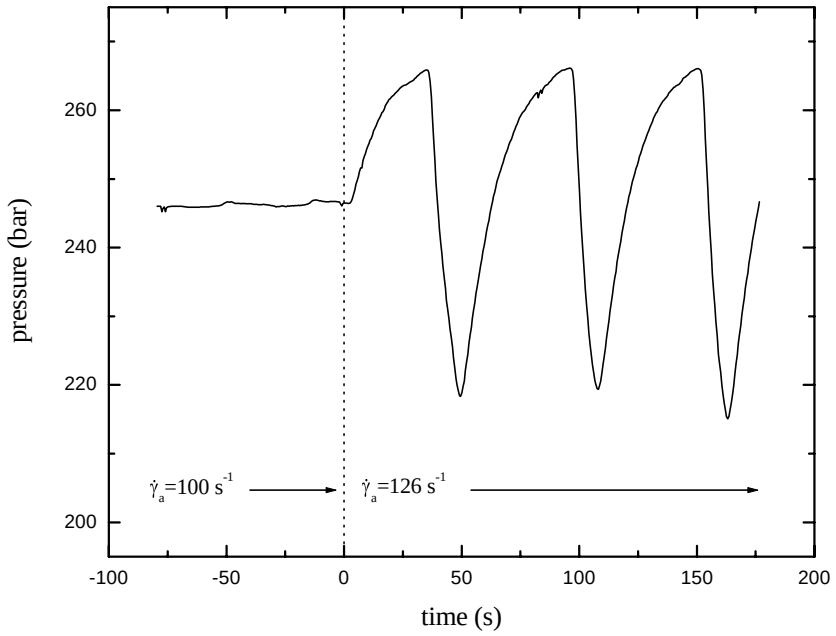

Figure 6.8: Transition from stable flow at $\dot{\gamma}^a$ = 100 s^{-1} to unsteady, oscillating flow at $\dot{\gamma}_a$ = 126 s^{-1} for NTX101.

stick regime were found to be relatively stable, owing to the high frequency, and mostly independent of flow rate.

The fourth region of the flow curve is denoted by $\dot{\gamma}_{gmf}$ and occurs at $\dot{\gamma}_a$ = 500 s^{-1}. Although this region is difficult to discern from the flow curve itself, it is marked by a combination of stable pressure measurements and relatively smooth extrudate surfaces. Furthermore, τ_w associated with gross melt fracture has decreased to a value of 0.31 MPa. This behavior is indicative of continuous slipping through the die. Gross distortion of the extrudate was not observed in the shear rate range probed for this study.

The observed melt fracture behavior of NTX101 agrees in part with previous studies of LLDPE resins. The onset of surface fracture at τ_w = 0.16 MPa agrees well with the studies by Moynihan *et al*. (1990) and Ramamurthy (1986), but is 30% lower than that observed by Kalika and Denn (1987). On the other hand, the onset of slip-stick fracture at τ_w = 0.32 MPa is more than 25% less than the value of 0.43 MPa observed by both Ramamurthy and Kalika and Denn. These variations may be explained by the differences in the materials of construction [Ramamurthy (1986)] of the extrusion dies or variations in die geometry, specifically L/D [Moynihan *et al*. (1990)]. Surprisingly, the curious flow behavior observed within the slip-stick fracture regime has been previously documented by Pudjijanto and Denn (1994). From their work with similar LLDPE materials, Pudjijanto and Denn observed that a stable "island" of flow existed within the slip-stick fracture regime for processing temperatures from 139-146 °C and apparent wall shear rates from 185-260 s^{-1}. Unfortunately, no clear explanation was provided for this phenomenon.

Linear metallocene polyethylene (mLLDPE)

The linear metallocene polyethylene Exact 3132 represents a system in which the molecular weight distribution is quite narrow. The flow curve calculated for Exact 3132 is presented in Figure 6.9. Again one observes the four-region flow curve denoted by: stable flow, surface melt fracture, slip-stick fracture, and gross fracture. The transition from the stable flow to surface melt fracture occurs at a relatively low apparent wall shear rate. Smooth extrudates are observed up to $\dot{\gamma}_a = 15.8\ s^{-1}$, after which surface distortions are observed. This is clearly a side effect of the delayed onset and reduced degree of shear thinning observed in the rheological results presented in Figure 6.1. The micrographs in Figure 6.10 indicate a matted texture at $\dot{\gamma}_{smf}$ and corresponds to $\tau_w = 0.16$ MPa. Further increases in flow rate lead to dramatic increases in the severity and form of surface melt fracture. The micrographs obtained at $\dot{\gamma}_a = 63.1$ and $100\ s^{-1}$ represent a transition from disordered sharkskin fracture to screw thread-like distortions. Interestingly, the pitch of the thread-like distortion appears to decrease with increasing apparent shear rate.

Exact 3132 also exhibits slip-stick fracture much like the conventional LLDPE before. In this case, $\dot{\gamma}_{ssf}$ occurs at $100\ s^{-1}$ and corresponds to a critical wall shear stress of 0.41 MPa. The transition from smooth to oscillating pressure traces is demonstrated in Figure 6.11. Several differences in slip-stick fracture behavior are noticed between the Exact 3132 and NTX101 resins. First, no peculiar "island" of stability is witnessed for the Exact 3132 resin. Slip-stick fracture is consistent throughout the regime. Second, the initial magnitudes of the pressure oscillations appear to be smaller than those initially observed in the NTX101 resin. The amplitudes of oscillation for the first three slip-stick fracture points in each flow curve range between 0.016-0.021 MPa for Exact 3132 as compared to 0.033-0.072 MPa for NTX101.

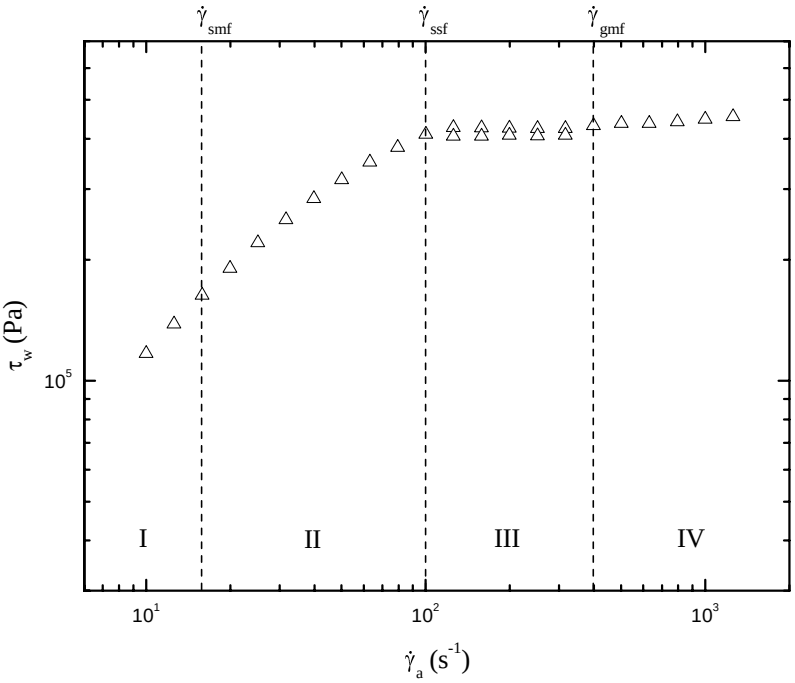

Figure 6.9: Melt fracture flow curve for Exact 3132 obtained at T=150 °C. $\dot{\gamma}_{smf}$ denotes the onset of surface melt fracture, $\dot{\gamma}_{ssf}$ denotes the onset of slip-stick fracture, and $\dot{\gamma}_{gmf}$ denotes the onset of gross melt fracture. (I: stable flow regime, II: surface melt fracture regime, III: slip-stick fracture regime, IV: gross melt fracture regime)

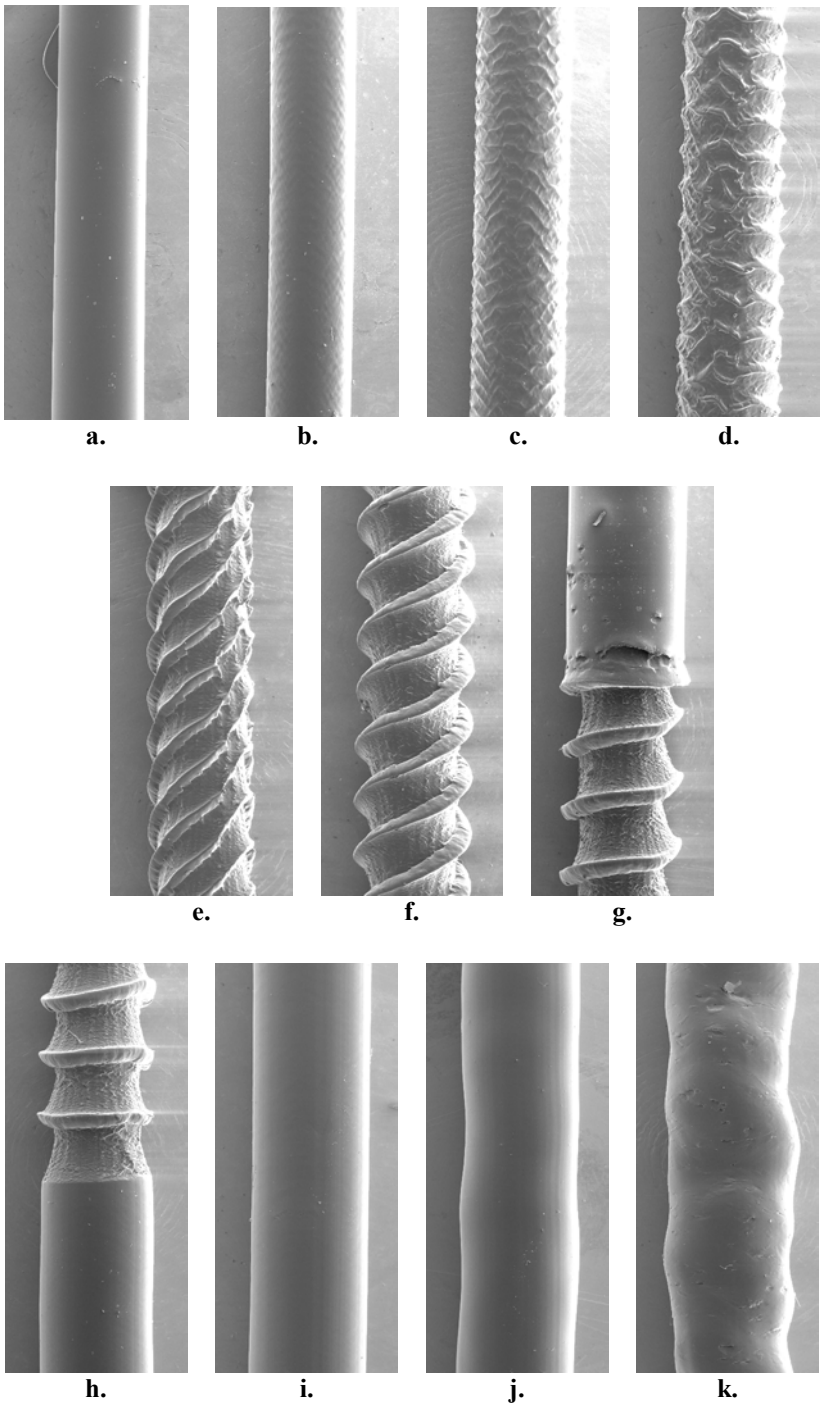

Figure 6.10: FESEM micrographs obtained for Exact 3132. Apparent wall shear rates(stresses) are **a**. 10 s^{-1} (0.117 MPa), **b**. 15.8 s^{-1} (0.163 MPa), **c**. 25.1 s^{-1} (0.220 MPa), **d**. 39.8 s^{-1} (0.284 MPa), **e**. 63.1 s^{-1} (0.350 MPa), **f**. 100 s^{-1} (0.411 MPa), **g**. 158 s^{-1} (0.416 MPa), **h**. 251 s^{-1} (0.415 MPa), **i**. 398 s^{-1} (0.431 MPa), **j**. 631 s^{-1} (0.437 MPa), and **k**. 1000 s^{-1} (0.448 MPa).

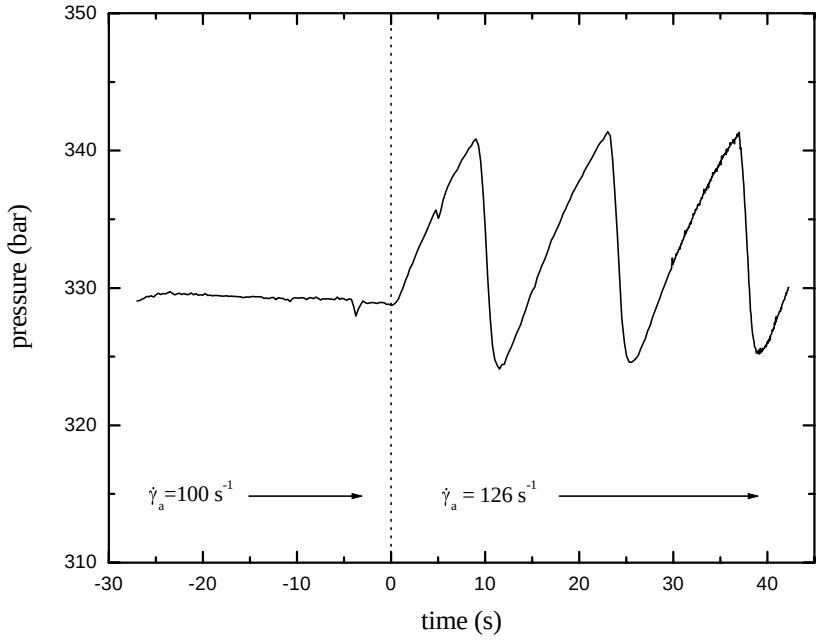

Figure 6.11: Transition from stable flow at $\dot{\gamma}^a$ = 100 s^{-1} to unsteady, oscillating flow at $\dot{\gamma}_a$ = 126 s^{-1} for Exact 3132.

Finally, the range of apparent shear rates over which slip-stick fracture is observed is somewhat narrower for the Exact 3132 resin than the NTX101 resin.

The gross melt fracture regime is first observed at $\dot{\gamma}_a$ = 398 s^{-1}. Once again, steady pressure traces and smooth extrudate surfaces mark the beginning of this flow regime. The extrudate surfaces are observed to be very smooth, much like those of LDPE resins, and wavy distortion becomes more evident at $\dot{\gamma}_a$ = 631 and 1000 s^{-1}. Furthermore, a large slip velocity is assumed to be present due to the apparent insensitivity of the apparent wall shear stress to increases in $\dot{\gamma}_a$.

The melt fracture results obtained for the linear metallocene polyethylene Exact 3132 are consistent with observations obtained for other linear polyethylene systems. Primarily, the presence of all three melt fracture forms, including the characteristic discontinuity in the stress-strain rate flow curve, is indicative of linear PE resins. The critical wall shear stress for surface melt fracture at 0.16 MPa agrees with previous work by Vega *et al*. (1996) on linear metallocene polyethylenes, and the onset of slip-stick fracture at 0.41 MPa agrees with the results obtained by Perez-Gonzalez *et al*. (2000) on the same material.

Sparsely branched metallocene polyethylene (mBLDPE)

The flow curve for the Exact 0201 resin is found in Figure 6.12. The stable flow region of the flow curve extends to higher shear rates and the onset of surface melt fracture is delayed until $\dot{\gamma}_a$=40 s^{-1}, which corresponds to an apparent wall shear stress of 0.17 MPa. Micrographs presented in Figure 6.13 clearly show that increasing the flow rate also increases the severity and form of surface melt fracture manifested. Over the shear rate range of 40-251 s^{-1}, the surface distortions gradually order from sharkskin to screw thread-like distortions. Furthermore, the

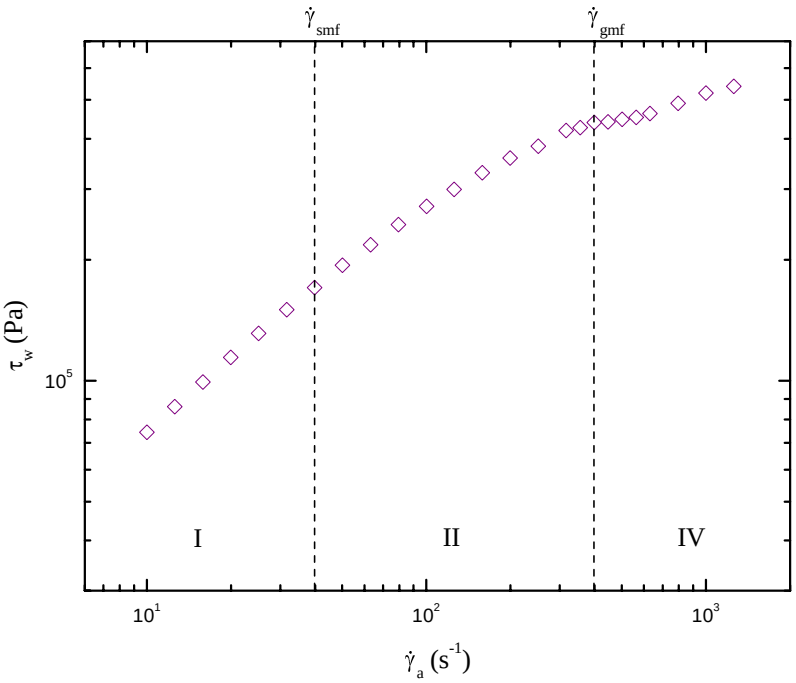

Figure 6.12: Melt fracture flow curve for Exact 0201 obtained at T=150 °C. $\dot{\gamma}_{smf}$ denotes the onset of surface melt fracture and $\dot{\gamma}_{gmf}$ denotes the onset of gross melt fracture. (I: stable flow regime, II: surface melt fracture regime, IV: gross melt fracture regime)

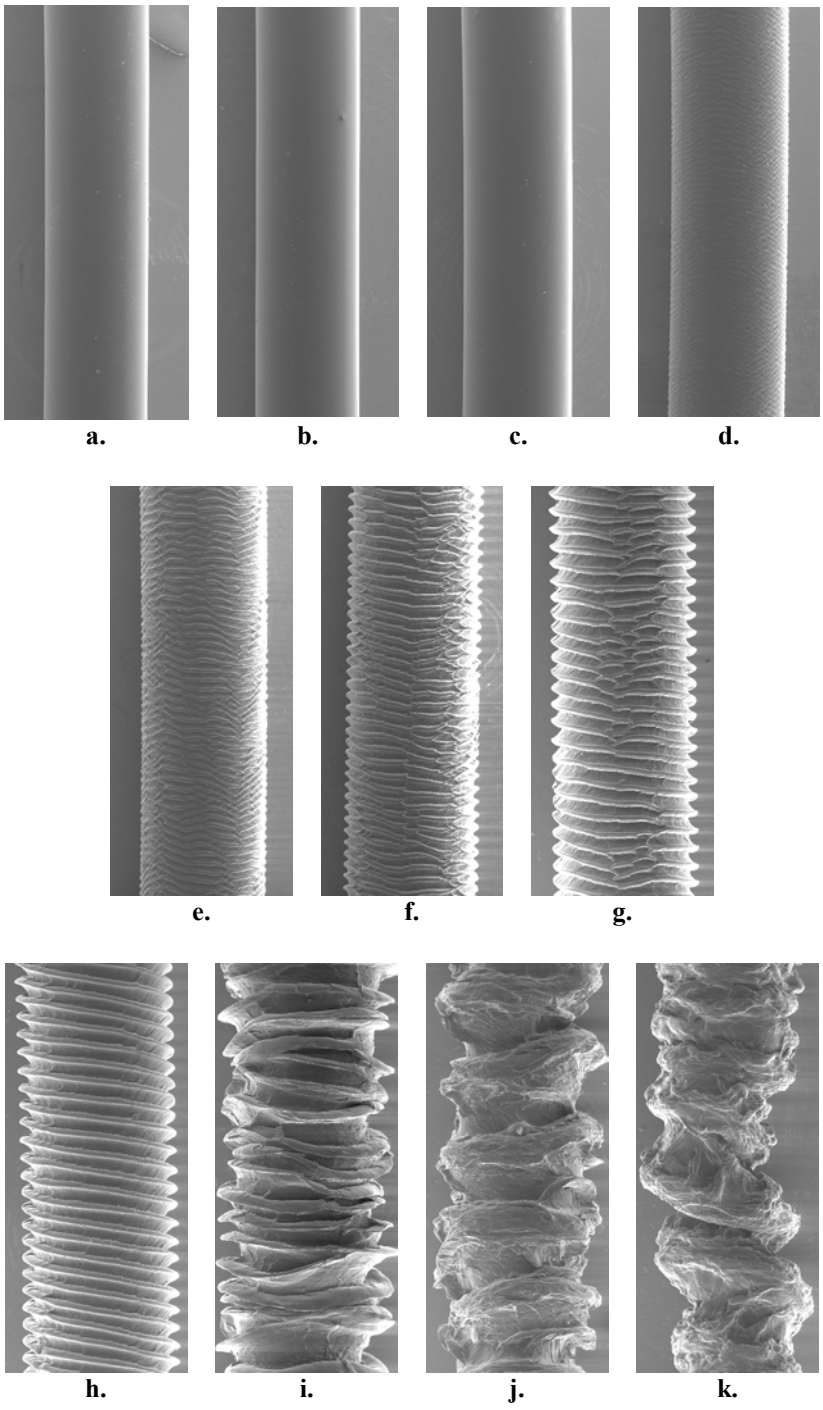

Figure 6.13: FESEM micrographs obtained for Exact 0201. Apparent wall shear rates(stresses) are **a**. 10 s^{-1} (0.074 MPa), **b**. 15.8 s^{-1} (0.099 MPa), **c**. 25.1 s^{-1} (0.131 MPa), **d**. 39.8 s^{-1} (0.171 MPa), **e**. 63.1 s^{-1} (0.218 MPa), **f**. 100 s^{-1} (0.271 MPa), **g**. 158 s^{-1} (0.329 MPa), **h**. 251 s^{-1} (0.384 MPa), **i**. 398 s^{-1} (0.439 MPa), **j**. 631 s^{-1} (0.462 MPa), and **k**. 1000 s^{-1} (0.520 MPa).

severity of fracture also increases as evidenced by the deepening of the grooves in the extrudate. The pitch of thread-like distortions is also small when compared to similar micrographs for the Exact 3132 resin. Surprsingly, these observations directly contradict those of Hatzikirakos *et al*. (1997). In their studies, SMF was found to be a transient phenomenon that disappeared under steady-state flow conditions.

Most surprisingly, no clear evidence of slip-stick fracture was observed for Exact 0201. Despite further refinement of measurements in the apparent shear rate range of 300-600 s^{-1}, no discontinuity in the flow curve associated with pressure oscillations was measured. The micrograph obtained at $\dot{\gamma}_a$ = 398 s^{-1} may indicate a very high frequency slip-stick fracture (f~115 Hz), but this fact remains inconclusive. The only other indication of possible slip-stick fracture behavior is the inflection point in the flow curve at 400 s^{-1}. The plateau-like behavior of stress with shear rate in that vicinity of the flow curve suggests melt fracture mechanics consistent with the linear resins reviewed thus far, rather than the highly branched NA952 resin.

Assuming that no slip-stick region is present, or that its range is very narrow, the next melt fracture regime observed was gross melt fracture. Beyond $\dot{\gamma}_{gmf}$ at 400 s^{-1}, the extrudate showed significant distortion as seen in Figure 6.13. At the highest $\dot{\gamma}_a$ observed, the extrudate was grossly distorted and showed signs of spiraling. Furthermore, the flow curve shows increased sensitivity to flow rate as evidenced by the increase in slope. This is consistent with observations of the gross melt fracture regime observed in previous three PE resins. Coincidentally, the critical wall shear stress for the onset of gross fracture was found to be 0.44 MPa, which is very similar to the τ_w for the onset of slip-stick fracture in Exact 3132.

6.4 Discussion

The results presented in the previous section clearly indicate that the shear and extensional rheological characteristics of the investigated polyethylene resins vary considerably between resins. Furthermore, these variations in rheological properties appear to have a significant effect on the melt fracture behavior at higher flow rates. With metallocene polyethylenes, the specific effects that narrow molecular weight distribution and the presence of long-chain branching in small concentrations can now be realized. Previous studies using conventional PE resins were limited by the extremes in molecular structure and rheological behavior exhibited by those resins. In the following section, the observed melt fracture phenomena for the four resins investigated in this study will be discussed in relation to the effects of narrow molecular weight distribution and long-chain branching.

6.4.1 Surface melt fracture

The onset of surface melt fracture was found to vary between 0.16 and 0.17 MPa. These results compare well with those obtained by Ramamurthy (1986) for similar LLDPE materials, but are as much as 25% less than those presented by Kalika and Denn (1987). Again, this may be explained by the slight dependence on the extrusion die geometry [Ballenger *et al*. (1971), Moynihan et al. (1990), Piau et al. (1990)] or the material of construction of the extrusion die [Ramamurthy (1986)]. Although the critical wall shear rates were found to vary between 15.8 and 39.8 s^{-1}, these differences are largely related to the degree of shear thinning observed in Figure 6.1. In the case of Exact 3132, the relative insensitivity of the shear viscosity to deformation rate results in the earliest onset of surface melt fracture (critical shear rate).

From observations of the extruded materials, the presence of surface melt fracture appears to be mostly dependent on the molecular weight distribution of the polymers. The LDPE resin, having the broadest molecular weight distribution of 17.1, does not exhibit surface melt fracture. On the other hand, the two linear and one sparsely branched PE resins, having much narrower MWD ranging from 2.04 to 3.41, do exhibit surface melt fracture. Unfortunately, previous work by Sukhadia (1997) suggests that broad MWD does not alleviate sharkskin melt fracture in linear polyethylenes. In his study, Sukhadia argued that the severity of SMF increased with the characteristic relaxation time of the polymer melt. However, in this case, the LDPE resin exhibits the longest characteristic relaxation time (based on the onset of shear-thining behavior), yet does not exhibit SMF. Therefore, the exact nature of SMF cannot be directly ascribed to the effects of breadth of molecular weight distribution, other than narrow MWD systems are more prone to it.

6.4.2 Slip-stick fracture

The observable discontinuity in the stress-strain rate flow curve is related to the presence of slip-stick fracture. Surprisingly, only two of the four resins investigated in this study experienced slip-stick fracture. The NTX101 and Exact 3132 resins both manifested oscillating pressure gradients above a critical wall shear stress. The critical wall shear stresses for the onset of slip stick fracture were determined to be 0.32 MPa for NTX101 and 0.41 MPa for Exact 3132.

As noted earlier, the characteristics of fracture varied considerably between the two resins. The intermediate region of stability within the slip-stick regime observed for NTX101 contrasted with the uniform and consistent slip-stick fracture observed for Exact 3132. The only significant difference in molecular structure is a slight broadening in the MWD, which is not

expected to significantly affect the onset or consistency of spurt flow [Blyler and Hart (1970)]. In this case, the differences in the manufacturing process of these resins may be to blame. Ziegler-Natta polymerized PE resins generally have a significant concentration of calcium stearate in their formulation to act as acid scavengers for catalysts residues [Grossman (2001a)]. Conversely, metallocene catalysts are more active than their Ziegler-Natta counterparts and have less catalyst residues and require less calcium stearate as a result [Klender *et al*. (1998)]. The fact that calcium stearate has a melting point in the range of 145-160 °C and is often used as a lubricant for polyolefins [Grossman (2001b)] may cause it to function as a processing aid at low temperatures. Therefore, the aberrant flow behavior observed in this study may be due to additive effects rather than those associated with molecular structure. Investigations at higher temperatures may resolve this problem.

Barring the effects of additives, the presence of slip-stick fracture is most dependent upon the presence of long-chain branching. Neither of the branched resins investigated exhibited a discernable slip-stick fracture regime. This mitigation of spurt flow was accomplished with as little as 0.79 LCB/10^4 carbons. Although slip-stick fracture is often associated with adhesive failure at the melt/die interface, a recent molecular theory proposed by Yang *et al*. (1998) suggest that the sharp slip-stick discontinuity occurs through a chain-chain entanglement/disentanglement process arising from a coil-stretch transition [Wang and Drda (1996)]. Therefore, one would expect that long-chain branching could greatly dampen this entanglement/disentanglement process and thus reduce the severity of slip-stick fracture via additional entanglement restraints.

6.4.3 Gross melt fracture

The onset of gross melt fracture was found to vary substantially between resins. NA952 exhibited gross melt fracture at very low shear rates corresponding to $\dot{\gamma}_a = 63.1 \ \ s^{-1}$. In fact, this instability that first occurred at $\tau_w = 0.09$ MPa was the only form of melt fracture observed. Further increases in flow rate simply increased the severity of fracture. In contrast, the linear PE resins only exhibited gross melt fracture following slip-stick fracture. The onset of gross fracture was observed to occur at much higher shear rates of $\dot{\gamma}_a = 501.1$ ($\tau_w = 0.31$ MPa) and 398.1 s^{-1} ($\tau_w = 0.41$ MPa) for the NTX101 and Exact 3132 resins, respectively. The sparsely branched resin also underwent gross melt fracture, but this was not preceded by slip-stick fracture but rather severe surface melt fracture. For Exact 0201, the onset of gross fracture occurred at an apparent wall shear stress of 0.44 MPa and $\dot{\gamma}_a = 398\ s^{-1}$.

As reported earlier, the extensional viscosity measurements indicate that the degree of long-chain branching heavily influences the strain-hardening behavior of the PE resins. NA952 exhibits the greatest degree of extensional strain-hardening behavior, while the linear PE resins appear to strain soften in uniaxial extension. The sparsely branched mPE resin demonstrates a modest degree of extensional strain-hardening behavior. In light of the observations by Tordella (1957) for gross melt fracture and White and Baird (1986) for entry flow characteristics, gross fracture is expected to occur at much lower flow rates for NA952 and much higher rates for the remaining resins. The results outlined above agree with this hypothesis. Furthermore, the gross distortion exhibited by the sparsely branched Exact 0201 is arguably more severe than those exhibited by the linear PE resins at the shear rates investigated. Again, this supports the belief

that the entry region is the site of instability, and that the extensional viscosity of the material, as affected by long-chain branching, contributes to the presence and severity of fracture.

6.5 Conclusions

The melt fracture behavior of commercial polyethylenes varies considerably according to the molecular structure of the material and the resulting shear and extensional properties. The effects of molecular weight distribution and long-chain branching were investigated using a combination of conventional and metallocene polyethylene resins. The effects of narrow molecular weight distribution appeared to be most prevalent on the surface melt fracture behavior of the linear and sparsely branched PE resins. These resins exhibited SMF at critical wall shear stress of 0.16 and 0.17 MPa. On the other hand, low-density polyethylene (LDPE), represented by a broad molecular weight distribution and high degree of long-chain branching, did not exhibit surface melt fracture. However, prior studies indicate that broad MWD does not always alleviate the effects of SMF, thus the effects of molecular structure on surface distortions are not yet fully understood.

The effects of long-chain branching on melt fracture behavior are much more obvious. Using the results obtained from the highly branched LDPE material and the sparsely branched mPE resin, two noticeable effects on melt fracture behavior were observed. First, the occurrence of slip-stick fracture is eradicated or greatly mitigated in resins possessing long-chain branching. The conventional LDPE material did not exhibit the characteristic discontinuity in the stress-strain rate flow curve commonly seen in linear materials nor was there any indication of the spurt flow. Furthermore, as little as 0.79 LCB/10^4 carbons was required to mitigate the pressure oscillations observed during slip-stick flow for the sparsely branched mPE resin. Owing to the

fact that both of these materials exhibit early onsets of shear-thinning behavior (Figure 6.1) demonstrates how shear rheology directly affects slip-stick fracture. Second, the occurrence of gross melt fracture and its severity is also governed by the presence of long-chain branching. In this case, extensional strain-hardening behavior arising from LCB leads to more severe gross melt fracture. This indirect relation is formed from knowledge of vortex instabilities in the die entry region that occur at relatively high flow rates. The highly branched LDPE resin undergoes gross fracture at low apparent wall shear stresses, while the linear and sparsely branched resins undergo gross fracture at higher stresses. With respect to the sparsely branched mPE resin, gross fracture is more pronounced than that of the linear materials over the range of flow rates investigated. Using these observations, it appears that sparse long-chain branching can be used to alter the melt fracture behavior of commercial polyethylenes.

6.6 Acknowledgements

The authors would like to thank D. Godshall and S. McCartney for their assistance with FESEM microscopy. The authors would also like to extend their gratitude to the ExxonMobil Chemical Company and the Equistar Chemical Company for graciously donating their respective PE resins to this study.

6.7 References

Bagley, E.B. and H.P. Schreiber, *Trans. Soc. Rheol*. **5**, 341 (1964).

Ballenger, T., I.-J. Chen, J.W. Crowder, G.E. Hagler, D.C. Bogue, and J.L. White, *Trans. Soc. Rheol*. **15**, 195 (1971).

Benbow, J.J. and P. Lamb, *S.P.E. Trans*. **3**, 7 (1963).

Blyler, Jr., L.L. and A.C. Hart, Jr., *Polym. Eng. Sci*. **10**, 193 (1970).

Dealy, J.M. and K.F. Wissbrun, *Melt Rheology and Its Role in Plastics Processing: Theory and Applications*, Van Nostrand Reinhold, New York, 1990.

den Otter, J.L., *Plastics Polym*. **38**, 155 (1970).

den Otter, J.L., *Rheo. Acta* **10**, 200 (1971).

Fernandez, M., A. Santamaria, A. Munoz-Escalona, and L. Mendez, *J. Rheol*. **45**, 595 (2001).

Goyal, S.K., I.B. Kazatchkov, N. Bohnet, and S.G. Hatzikiriakos, SPE ANTEC Tech. Paper, no. 167 (1997).

Grossman, R.F., "Antioxidants," in *Polymer Modifiers and Additives*, ed. J.T. Lutz, Jr. and R.F. Grossman, Marcel Dekker, New York, 2001a.

Grossman, R.F., "Lubricants," in *Polymer Modifiers and Additives*, ed. J.T. Lutz, Jr. and R.F. Grossman, Marcel Dekker, New York, 2001b.

Hatzikirakos, S., I.B. Kazatchkov, and D. Vlassopoulos, *J. Rheol*. **41**, 1299 (1997).

Kalika, D.S. and M.M. Denn, *J. Rheol*. **31**, 815 (1987).

Klender, G.J., R.A. Hendriks, J. Semen, and K.P. Becnel, "The Performance of Primary and Secondary Antioxidants in Polyolefins Produced with Metallocene Catalysts," in *Metallocene-Catalyzed Polymers*, eds. G.M. Benedikt and B.L. Goodall, Plastics Design Library, Norwich, 1998.

Lai, S. Y., J. R. Wilson, G. W. Knight, J. C. Stevens, and P. W. S. Chum, U.S. Patent No. 5,272,236 (1993).

Larson, R.G., *Rheol. Acta* **31**, 213 (1992).

Lim, F.J. and W.R. Schowalter, *J. Rheol*. **33**, 1359 (1989).

Moynihan, R., D.G. Baird, and R. Ramanathan, *J. Non-Newt. Fluid Mech*. **36**, 255 (1990).

Münstedt, H., *J. Rheol*. **23**, 421 (1979).

Perez-Gonzalez, J., L. de Vargas, V. Pavlinek, B. Hausnerova, and P. Saha, *J. Rheol*. **44**, 441-451 (2000).

Petrie, C.S.J. and M.M. Denn, *AIChE. J*. **22**, 209 (1976).

Piau, J.M., N. El Kissi, F. Toussaint, and A. Mezghani, *Rheol. Acta* **34**, 40 (1995).

Piau, J.M., N. El Kissi, B. Tremblay, *J. Non-Newt. Fluid Mech*. **34**, 145 (1990).

Pudjijanto, S. and M.M. Denn, *J. Rheol*. **38**, 1735 (1994).

Ramamurthy, A.V., *J. Rheol*. **30**, 337 (1986).

Sukhadia, A.M., *SPE ANTEC* Tech. Paper, no. 49 (1997).

Tordella, J.P., "Unstable flow of molten polymers," Rheology: Theory and Applications, Ed. Frederick R. Eirich, Academic Press, New York (1969).

Tordella, J.P., *Trans. Soc. Rheol*. **1**, 203 (1957).

Tordella, J.P., *J. Appl. Polym. Sci*. **7**, 215 (1963).

Uhland, E., *Rheol. Acta* **18**, 1 (1979).

Vega, J.F., A. Munoz-Escalona, A. Santamaria, M.E. Munoz, and P. Lafuente, *Macromolecules*, **29**, 960 (1996).

Venet, C. and B. Vergnes, *J. Rheol*. **41**, 873 (1997).

Vinogradov, G.V., V.P. Protasov, and V.E. Dreval, *Rheo. Acta* **23**, 46 (1984).

Vinogradov, G.V., M.L. Friedman, B.V. Yarlykov, and A.Y. Malkin, *Rheol. Acta* **9**, 323 (1970).

Wang, S.-Q., P.A. Drda, *Macromolecules* **29**, 4115 (1996).

White, J.L., *Appl. Polym. Symp*. **20**, 155 (1973).

White, S.A. and D.G. Baird, *J. Non-Newt. Fluid Mech*. **20**, 93 (1986).

Yang, X., H. Ishida, and S.-Q. Wang, *J. Rheol*. **42**, 63 (1998).

7.0 Numerical Simulations

Preface

This chapter is focused on the third objective of the research. Specifically, the ability to predict the pressure profiles along the benchmark abrupt 4:1 planar contraction using finite element method (FEM) simulations is examined. Two polyethylene melts representing the extrema of rheological response are investigated. This chapter is organized as a manuscript for future publication.

Pressure Profiles Along a Abrupt 4:1 Planar Contraction

P.J. Doerpinghaus and D.G. Baird

Department of Chemical Engineering, Virginia Polytechnic Institute and State University, Blacksburg, VA

(ABSTRACT)

The ability to accurately predict the pressure profile along an abrupt 4:1 planar contraction is investigated. Predicted pressure profiles obtained using the Phan-Thien and Tanner (PTT) and Generalized Newtonian Fluid (GNF) models are compared to experimental measurements for LDPE and LLDPE polymer melts. The results obtained for the extensional strain hardening LDPE resin show that numerical predictions are consistently less than the experimental values by 10-15%. Furthermore, no significant difference between the PTT and GNF predictions were observed over the range of convergent solutions. On the other hand, the numerical predictions for the LLDPE melt were within 1.5-7% of the experimental values over the entire range of stable flow rates investigated. Again, the differences in accuracy of the PTT and GNF models were small. In fact, the GNF model was generally more accurate than the PTT model for the case of LLDPE. Closer investigation of the predicted streamlines patterns near the contraction clearly shows larger, more intense vortices for the extensional strain hardening LDPE than for the LLDPE melt, which is in agreement with experimental observations. However, analysis of the plane of symmetry shows that the magnitude of the planar extensional stress is mitigated by the fluid relaxation behavior as the melt briefly passes through the contraction region. Although it appears that a viscoelastic constitutive equation is not necessary for predicting the pressure profile along an abrupt 4:1 planar contraction, this is a fortuitous result of the small extensional deformations observed in the contraction region over the limited range of convergent solutions.

7.1 Introduction

The presence of an abrupt contraction during pressure driven flow of molten polymers gives rise to an additional pressure drop associated with the stretching of fluid elements in the vicinity of the contraction. This additional pressure drop is manifested under creeping flow conditions (Re ~ 0) and is often referred to as the *entrance pressure drop* (ΔP_{ent}). In Figure 7.1, a schematic representation of the pressure profile along a contraction is presented. The magnitude of ΔP_{ent}, and the resulting increase in the driving pressure, are expected to depend upon the contraction geometry (i.e. contraction ratio, contraction angle, etc.), but also appears to be sensitive to the extensional rheological properties of the material investigated [Laun and Schuch (1989)].

Surprisingly, most experimental and numerical investigations of contraction flow behavior have focused on the subtleties of the flow kinematics in the contraction region [Boger (1987), White *et al*. (1987)]. Much of the interest in contraction flows has centered on the velocity fields, streamline patterns, and principal stress fields in relation to numerical predictions [see for example Luo and Mitsoulis (1990), Park *et al*. (1992), Martyn *et al*. (2000)]. Unfortunately, these past studies did not investigate macroscopic measurements of the hydrodynamic pressure, which may be the most significant factor in the design of extrusion dies. Although detailed studies of the flow kinematics are important in assessing the accuracy of a numerical technique, the question of whether the pressure profile can be accurately predicted has been largely ignored.

Historically, the abrupt 4:1 contraction has been the contraction geometry of choice for analyzing the influence of viscoelastic properties on polymeric flow phenomena [see for example Tanner and Walters (1998)]. This flow geometry is quite simple, yet manifests mixed flow

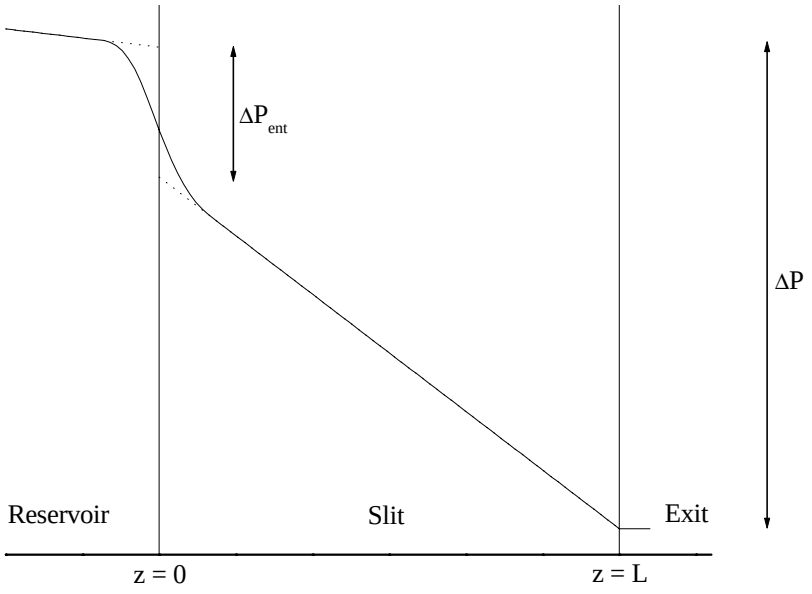

Figure 7.1: A schematic representation of the hydrodynamic pressure profile along an abrupt planar contraction. The magnitude of ΔP_{ent} has been exaggerated for effect.

kinematics. In particular, simple shear flow dominates the regions well upstream and downstream of the contraction, while the contraction region is greatly influenced by extensional deformations. One of the most unique flow characteristics arising from contraction flow is the presence of recirculating vortices in the re-entrant corner regions. During stable flow conditions, natural tapering of the bulk flow into the contraction leads to "dead" regions where vortices are manifested. This natural tapering effectively reduces the cross-sectional area of flow upstream of the contraction and contributes to the observed entrance pressure drop. Studies by Ballenger and White (1970), den Otter (1970), and White and Baird (1986), to name a few, have found that not all polymer melts exhibit vortex formation. Specifically, Ballenger and White found that highly long-chain branched low-density polyethylene (LDPE) exhibited substantial vortex growth, while linear high-density polyethylene (HDPE) did not. Similar results were observed by den Otter for branched and linear polydimethylsiloxane (PDMS) resins. White and Baird (1986) investigated the streamlines of LDPE and polystyrene (PS) and found that flow tapering was related to the degree of extensional strain hardening and the intensity of the vortices was determined by the shear thinning behavior. Highly branched LDPE, exhibiting considerable extensional strain hardening and shear thinning behavior, showed significant tapering and intense vortices. These observations indicate that flow tapering, recirculating vortices, and possibly the magnitude of ΔP_{ent}, are strongly influenced by the melt rheological properties.

The extensional flow characteristics of long-chain branched polymers, such as LDPE, are substantially different from linear polymers [Münstedt (1981)]. Highly branched polymers exhibit extensional strain-hardening behavior, which contrasts to the strain-softening behavior often observed in linear polymers. Strain hardening refers to the rise in extensional viscosity above the linear viscoelastic limit of $3\eta^+(t)$. Previous studies have shown that the magnitude of

strain hardening in randomly branched LDPE resins is influenced by the degree of branching [White (1978), Münstedt and Laun (1981), Minoshima and White (1986)]. Interestingly, linear resins having broad molecular weight distributions or the presence of very high molecular weight species can also exhibit some degree of extensional strain hardening [Münstedt (1980), Frank and Meissner (1984)]. Therefore, accurate modeling of the extensional behavior of the polymer melt would seem important when trying to predict the presence of tapered flow and its effect on the pressure profile.

The question, however, is whether one needs to use a highly viscoelastic constitutive equation to model the pressure drop across a 4:1 contraction or whether a purely viscous constitutive equation is accurate enough. The simplest rheological constitutive equation used to describe polymer melts is the inelastic Generalized Newtonian Fluid (GNF) model. Although capable of describing the shear-thinning nature of polymer melts, the GNF model does not capture viscoelastic phenomena such as fluid memory, normal stress differences, and extensional strain-hardening behavior. On the other hand, viscoelastic constitutive equations such as the Phan-Thien/Tanner (PTT) and factorized K-BKZ models are known to accurately describe nonlinear rheological phenomena [Phan-Thien and Tanner (1977), Kaye (1962), Bernstein *et al*. (1964)]. Both the PTT and K-BKZ models can accurately describe shear thinning, normal stress differences, and extensional strain-hardening behavior in uniaxial extension. This is especially important when predicting free surface flows, such as die swell. The major weakness of using the K-BKZ model is that it cannot accurately predict simultaneously both shear thinning and planar extensional strain hardening [Samurkas *et al*. (1989), Ahmed and Mackley (1995)]. As a result, its use in planar contraction geometries is severely limited. More recently, McLeish and Larson (1998) have developed the pom-pom constitutive model that specifically addresses the effects of

long-chain branching on extensional viscosity. The pom-pom model is capable of predicting extensional strain hardening in both uniaxial and planar extension. Unfortunately, the large number of model parameters and the arbitrary nature by which they are chosen may limit its implementation in numerical simulations at present.

Recently, numerical simulations using a variety of constitutive equations have been reported concerned with prediction of the entrance pressure drop across axisymmetric contraction geometries. Hatzikirakos and Mitsoulis (1996) studied the Bagley end correction of linear low-density polyethylene (LLDPE) both experimentally and numerically using the K-BKZ constitutive equation. They found that the numerical simulations significantly underestimated the experimental observations. Similar results were reported by Mitsoulis and coworkers (1998) and by Barakos and Mitsoulis (1995) for LLDPE and LDPE resins, respectively. Beraudo *et al*. (1996) investigated the Bagley end correction for LLPDE using the multi-mode PTT constitutive model and found that numerical simulations under predicted the experimentally measured ΔP_{ent} by a factor of two at low rates and by a factor of four at high rates. Interestingly, Mitsoulis *et al*. (1998) found that the entrance pressure drop loss predicted by the K-BKZ model was insensitive to the extensional characteristics over the range of rates and model parameters used in their study. In fact, an inelastic GNF constitutive model was found to provide similar results for ΔP_{ent} to the more complex viscoelastic constitutive equation. This observation indicates that the use of a viscoelastic constitutive equation may not be required under certain flow conditions.

Although measurements of ΔP_{ent} are useful and are believed to provide an indication of the extensional character of the fluid [Cogswell (1972), Binding (1988)], the method used to calculate these quantities often leads to significant uncertainty. The most common method for determining ΔP_{ent} is by applying the Bagley end correction [Bagley (1957)]. This method

involves extrapolating the measured pressure drop across multiple capillaries of same diameter and differing length to a L/D of zero. This extrapolated quantity then represents ΔP_{ent} for the given contraction ratio. The effects of pressure, viscous heating, and wall slip can also contribute to substantial error in the value of ΔP_{ent}. Although the use of a very short die (L/D ~0) mitigates these effects, the relatively small measurable pressure drop can also lead to significant uncertainty. In order to avoid uncertainties associated with explicitly calculating ΔP_{ent}, measurement of the hydrodynamic pressure along the contraction geometry should provide more accurate results. This approach addresses the effects of ΔP_{ent} on the upstream pressure measurements while reducing uncertainty associated with extrapolating experimental measurements. This technique also simplifies the application of numerical predictions by eliminating the need to extrapolate predicted pressure profiles to the contraction entrance.

The objective of the current study is to determine the role that viscoelasticity and more importantly extensional strain hardening has on the flow behavior of polymer melts through an abrupt contraction. This is accomplished by comparing experimentally measured pressure profiles along a 4:1 contraction die to predictions obtained from finite element method (FEM) numerical simulations. Two well-characterized polyethylene resins having different shear and extensional flow characteristics will be investigated in this study. A multi-mode PTT model and an inelastic GNF model will be used to model the rheological characteristics of each polyethylene and predict the pressure profiles along the chosen 4:1 contraction geometry. Comparing the PTT and GNF predictions will isolate the specific role of fluid memory and extensional strain hardening on the pressure profile predictions. Predicted streamline patterns and the planar extensional strain rates and stresses along the plane of symmetry will be used to further compare the influence of viscoelasticity and extensional strain hardening.

7.2 Constitutive Equations

The viscoelastic and inelastic constitutive equations used in this study are briefly outlined in this section. The reader should note that the following equations have been formulated using the convention described by Bird *et al*. (1987), in which a tensile stress is taken to be negative.

7.2.1 Phan Thien and Tanner (PTT) Model

The Phan Thien and Tanner (PTT) model was chosen to describe the viscoelastic properties of the polyethylene resins utilized in this study. The PTT model is a differential constitutive model based on network theory of concentrated polymer solutions and melts [Phan-Thien and Tanner (1977), Phan-Thien (1978)]. A multi-mode formulation using the exponential coefficient appears as,

$$\boldsymbol{\tau} = \sum_i \boldsymbol{\tau}_i \tag{7.1}$$

$$\exp\left(-\frac{\varepsilon\lambda_i}{\eta_i} tr\,\boldsymbol{\tau}_i\right)\tau_i + \lambda_i \boldsymbol{\tau}_{i(1)} + \xi\lambda_i\left(\dot{\boldsymbol{\gamma}}\cdot\boldsymbol{\tau}_i + \boldsymbol{\tau}_i\cdot\dot{\boldsymbol{\gamma}}\right) = -\eta_i\dot{\boldsymbol{\gamma}} \tag{7.2}$$

where $\dot{\boldsymbol{\gamma}}$ is the rate of deformation tensor and $\tau_{i(1)}$ is the upper-convected derivative of stress for the i-th mode and are defined by,

$$\dot{\boldsymbol{\gamma}} = \nabla\boldsymbol{v} + (\nabla\boldsymbol{v})^{\dagger} \tag{7.3}$$

$$\boldsymbol{\tau}_{i(1)} = \frac{\partial\boldsymbol{\tau}_i}{\partial t} + \boldsymbol{v}\cdot\nabla\boldsymbol{\tau}_i - \left(\dot{\boldsymbol{\gamma}}\cdot\boldsymbol{\tau}_i + \boldsymbol{\tau}_i\cdot\dot{\boldsymbol{\gamma}}\right) \tag{7.4}$$

The extra stress τ is calculated from the sum of the individual extra stresses for each mode, τ_i. λ_i and η_i correspond to the relaxation time and strength for the i-th mode, respectively. In addition to the usual linear viscoelastic constants, two nonlinear parameters are also used. ε characterizes

the rate of destruction of entanglement "crosslinks" in the network model and ξ the rate of non-affine deformation. In this study, single values of ε and ξ common to all modes have been used.

7.2.2 Generalized Newtonian Fluid (GNF) Model

In addition to a viscoelastic constitutive model, a generalized Newtonian fluid (GNF) model was also used. The GNF model predicts the shear viscosity according to a specified viscosity model, and predicts an extensional viscosity that is three times that of the shear viscosity. An inelastic, purely viscous constitutive model was chosen to contrast the effects of memory and nonlinear extensional properties. The viscosity model chosen to best describe the shear-thinning nature of both polymer fluids was the Carreau-Yasuda (C-Y) model [Carreau (1968), Yasuda *et al*. (1981)]. The GNF constitutive equation and the Carreau-Yasuda viscosity model can be expressed as,

$$\boldsymbol{\tau} = -\eta(\dot{\gamma})\dot{\boldsymbol{\gamma}} \tag{7.5}$$

$$\eta(\dot{\gamma}) = (\eta_0 - \eta_\infty)\left[1 + (\lambda\dot{\gamma})^a\right]^{\frac{n-1}{a}} + \eta_\infty \tag{7.6}$$

where η_0 and η_∞ are the zero-shear and infinite-shear viscosities, respectively, λ is a time constant, n is the power law index, and a is a dimensionless parameter that describes the transition region between the zero-shear and power-law regions. The scalar quantity $\dot{\gamma}$ represents the magnitude of the rate of deformation tensor $\dot{\boldsymbol{\gamma}}$ and is defined by:

$$\dot{\gamma} = \sqrt{\tfrac{1}{2}\dot{\boldsymbol{\gamma}} : \dot{\boldsymbol{\gamma}}} \tag{7.7}$$

7.3 Experimental Methods

7.3.1 Materials

Two commercial grade polyethylenes were investigated in this study. A low-density polyethylene (LDPE) produced by Equistar Chemical under the product name NA952 and a linear low-density polyethylene (LLDPE) produced by ExxonMobil under the product name NTX101. The LDPE is a tubular, free radical polymerized polyethylene having a high degree of short and long-chain branches. The LLDPE is an ethylene-hexene copolymer produced using conventional Ziegler-Natta catalysts. Neither of the resins investigated contain slip or anti-block agents that might obscure their flow properties.

The relevant physical and molecular properties are tabulated in Table 7.1. The LDPE resin has a very large weight average molecular weight of 235,500 g/mol and a broad molecular weight distribution of 17.1. These values are characteristic of highly branched polyethylenes. The degree of long-chain branching obtained from C^{13} NMR analysis was estimated to be 3.9 long-chain branches per 1000 carbons. The LLDPE has a more modest M_w of 112,800 g/mol and a relatively narrow molecular weight distribution of 3.41. No long-chain branches are present in the structure of the NTX101 resin.

7.3.2 Rheological Testing

The shear rheological measurements for each resin were determined using a Rheometrics Mechanical Spectrometer Model 800 (RMS-800). The shear viscosity curves for each PE resin are presented in Figure 7.2. The dynamic oscillatory data were collected over the frequency range of 0.1 – 100 rad s^{-1} using 25 mm parallel plate fixtures. The steady shear rheological measurements were collected over the shear rate range of 0.001 – 1.0 s^{-1} using a 25 mm cone and

Table 7.1: Molecular Weight, MFI, and LCB content of the materials studied.

Resin	ρ g/cm^3	**MFI** dg/min	$\mathbf{M_w}$	$\mathbf{M_w/M_n}$	$\mathbf{M_z}$	**LCB** /10^4 C
NA952	0.918	2.0	235 500	17.1	2 619 300	39[a]
NTX101	0.917	0.9	122 700	3.44	319 700	--

[a] C^{13} NMR measurement

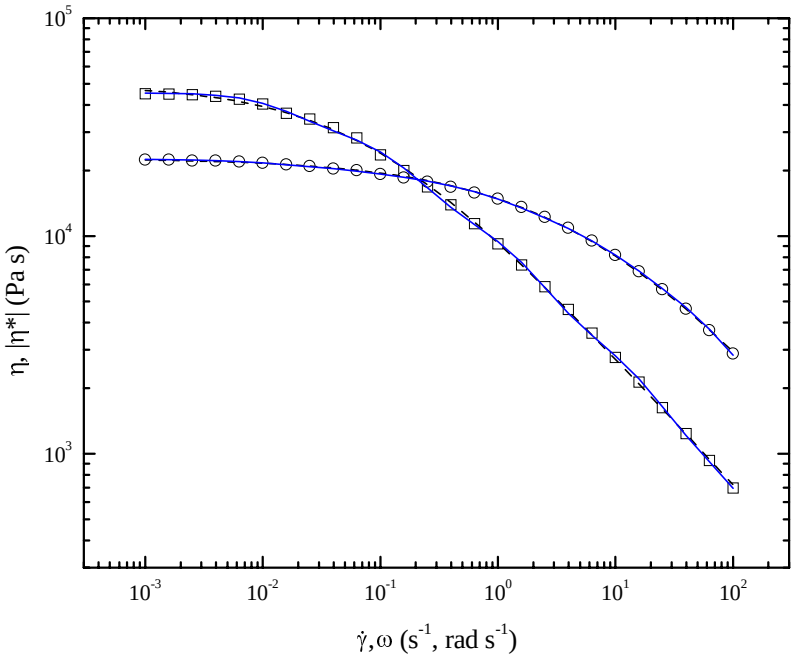

Figure 7.2: Steady and dynamic oscillatory viscosity measurements obtained at T=150 °C. Experimental measurements: (□) LDPE, (○) LLDPE; Numerical Predictions: (——) PTT, (– – –) GNF.

plate fixture. The cone angle used for all steady shear measurements was 0.1 radian. All testing was performed within an inert nitrogen atmosphere to prevent thermo-oxidative degradation. In most cases, the test samples were prepared by compression molding preforms at 170 °C under nominal pressure and allowing them to cool slowly. All steady shear and dynamic oscillatory measurements were acquired at a test temperature of 150 °C. The results presented represent an average of at least three runs using different samples each time. The calculated error for the dynamic oscillatory and steady shear measurements was found to be no greater than ±5 and ±10%, respectively.

High shear rate viscosity data were collected using a Goettfert Rheograph 2001 (RG2001) capillary rheometer. The high shear rate rheological measurements were collected over the range of 10 – 100 s^{-1}. Three capillaries with a diameter of 1.0 mm and L/D ratios of 10, 20, and 30 were used for measurements performed at temperatures of 150 °C. Using the Rabinowitsch correction to calculate the true wall shear rate and the Bagley end correction to calculate the true wall shear stress, the shear viscosity as a function of shear rate was calculated from the imposed volumetric flowrate and the resulting pressure drop. This data was used exclusively to determine the PTT constitutive model parameter ξ and can be found presented elsewhere [Doerpinghaus (2002)].

Uniaxial extensional stress growth measurements were obtained using a Rheometrics Extensional Rheometer Model 9000 (RER-9000). This particular extensional rheometer is based upon the design of Münstedt (1979). The transient extensional data were collected over the extension rate range of 0.01 – 1.00 s^{-1}. Extensional viscosity measurements obtained at $\dot{\varepsilon} = 1.0$ s^{-1} are presented in Figure 7.3. The maximum Hencky (true) strain achievable with this device is approximately 3.0 using test specimens with initial nominal lengths of 22 mm. The cylindrical

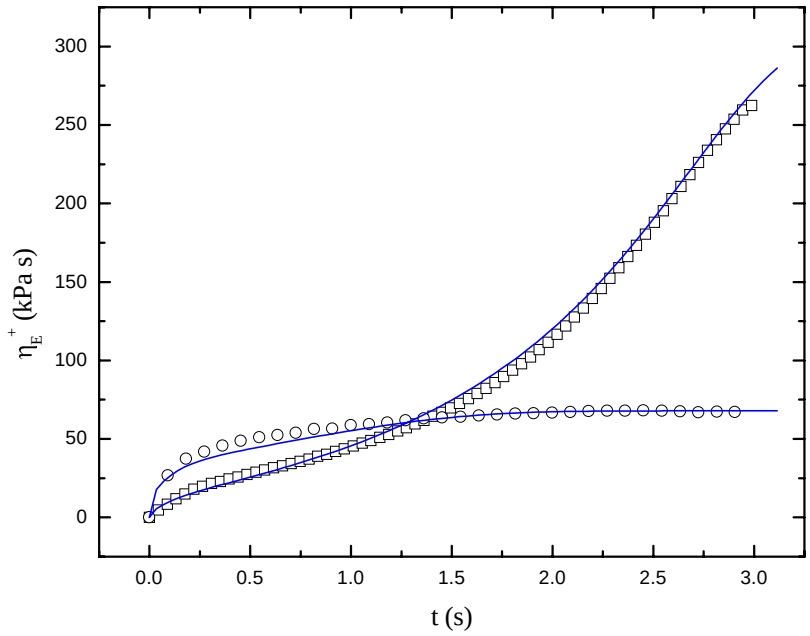

Figure 7.3: Transient extensional viscosity measurements at T=150 °C. Experimental measurements: (□) LDPE, (○) LLDPE; Numerical predictions: (——) PTT model.

test specimens are compression molded from polymer pellets at 170 °C under nominal pressure and allowed to cool slowly. They were then bonded to test clips using high-temperature UHU® epoxy, mounted to the rheometer, and immersed in a neutrally buoyant silicone oil bath at 150 °C. Once thermal equilibrium was achieved, an applied extension rate deformed the sample and the resulting force was monitored using a leaf spring-LVDT assembly. The results presented for each extension rate represent an average of at least three runs using different samples. The calculated error for the extensional viscosity data was found to be less than ±10%.

7.3.3 Flow System

The abrupt planar contraction die utilized in this study consists of two halves machined from 440C stainless steel. When bolted together, the desired flow channel is formed. Figure 7.4 shows a schematic representation of the contraction die. The flow channel is 12.7 mm wide and is divided into two regions. The upstream region is 108 mm long and 5.08 mm high. The downstream region is 25.4 mm long and 1.27 mm high. The ratio of the die heights results in a 4:1 contraction ratio.

Six pressure transducer ports were machined along the flow channel of the die (Figure 7.2). The four upstream transducer ports were machined flush with the channel wall, while the two downstream transducer ports were machined at the bottom of deep pressure holes. Although the use of pressure holes can lead to error in the measurement of the hydrodynamic pressure, a previous study using similar polymer melts showed that the magnitude of the error does not exceed ±5% of the absolute pressure [Chang (1986)]. During operation, Dynisco melt pressure transducers ranging from 3.45 to 10.3 MPa (500 – 1500 psig) were used to monitor the

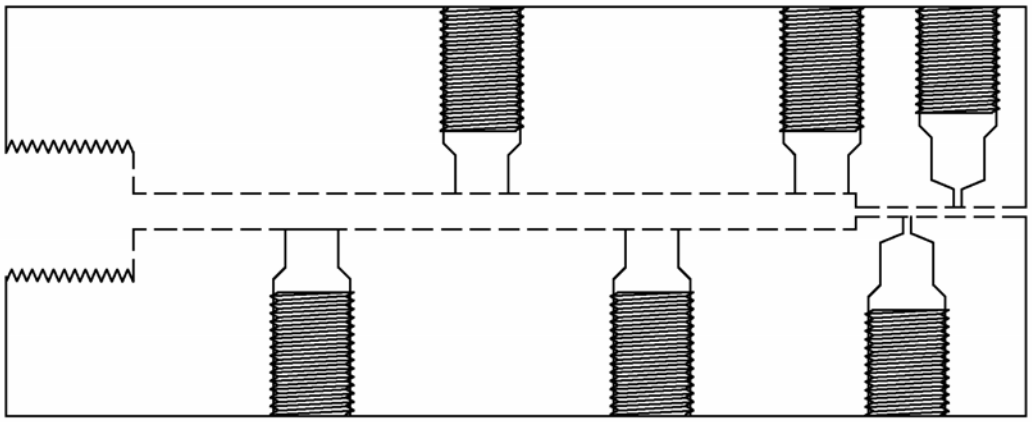

Figure 7.4: Schematic of the abrupt 4:1 planar contraction die used in this study.

hydrodynamic pressure. The calculated error for the experimental pressure measurements was found to be ±2% at the nominal apparent shear rate cited.

The polymer melt was supplied to the planar contraction die using an extruder-gear pump assembly. The polymer was first plasticated using a 25.4 mm Killion laboratory extruder and then fed to a Zenith (HPB-5556) gear pump operating at 150 °C. A 1/4 hp US Motors Varidrive AC motor coupled to a Reynold Ltd. 21.4:1 gear reduction unit was used to drive the gear pump. This arrangement provides precise, pulseless flow of polymer over the volumetric flowrate range of 15.0 – 150 mm^3/s.

7.4 Numerical Methods

7.4.1 Model Parameter Fitting

The Phan-Thien and Tanner (PTT) model parameters were determined from shear and extensional viscosity data. Table 7.2 summarizes the PTT model parameters obtained for the LDPE and LLPDE resins. The discrete relaxation spectra (λ_i, η_i) were obtained from nonlinear regression of the steady shear viscosity and dynamic oscillatory measurements. Arbitrary values of λ_i were chosen over the range of data available. The nonlinear parameter ξ was determined from shifting the dynamic viscosity (η') to overlay the steady shear viscosity (η) in the non-Newtonian flow regime. Finally, the ε parameter was determined from transient extensional data at the highest extension rate of 1.0 s^{-1} using a least squares optimization technique [Doerpinghaus (2002)]. The corresponding fits to rheological data are found in Figures 7.2 and 7.3.

The Carreau-Yasuda (C-Y) viscosity model parameters were determined from shear viscosity data alone. The C-Y parameters for each resin are tabulated in Table 7.3. The value of

Table 7.2: PTT Model Parameters

λ_i	η_i (LDPE)	η_i (LLDPE)
10^{-2}	8.50×10^2	3.83×10^3
10^{-1}	2.38×10^3	6.36×10^3
10^{0}	7.78×10^3	7.37×10^3
10^{1}	1.78×10^4	2.89×10^3
10^{2}	1.67×10^4	2.09×10^3
ξ	0.191	0.179
ε	0.034	0.239

Table 7.3: GNF Model Parameters

	LDPE	LLDPE
η_0	49430	22740
η_∞	0	0
λ	12.5	0.130
n	0.409	0.336
a	0.625	0.487

η_0 was empirically determined from available rheological data and η_∞ was assumed to be approximately zero. The choice of η_∞ had little influence on the other parameters. The remaining parameters were determined from nonlinear regression of available data. The corresponding fit to the shear viscosity data is found in Figure 7.2.

7.4.2 Finite Element Method

The finite element method was employed to solve simultaneously the governing equations for isothermal, inertialess flow of incompressible viscoelastic fluids. The equations of continuity and motion for incompressible, creeping flow can be written in the following forms, respectively,

$$\nabla \cdot \boldsymbol{v} = 0 \tag{7.8}$$

$$\nabla \cdot \boldsymbol{\tau} + \nabla P = 0 \tag{7.9}$$

where ∇ is the gradient operator, $\boldsymbol{v}$ is velocity field, τ is the extra stress tensor, and P is the modified pressure ($P = p - \rho \mathbf{g} \cdot \mathbf{x}$). Equations 7.8 and 7.9 represent four (4) independent scalar equations containing as many as 10 unknown quantities. In order to close the equation set, one of the two rheological constitutive equations described earlier must also be used.

The commercial finite element method package Polyflow (Fluent/Polyflow s.a., version 3.8) was used to perform all numerical simulations on a dedicated SGI Origin 200 server. The viscoelastic predictions were determined using the elastic viscous split stress (EVSS) technique [Rajagopolan *et al*. (1990)] coupled with inconsistent streamline upwinding (SU) [Marchal and Crochet (1987)]. This particular approach reduces the computational expense and enhances the range of convergence for multi-mode viscoelastic simulations. On the other hand, the Generalized Newtonian Fluid (GNF) predictions were determined using Newton iterations upon

the locally calculated viscosities. For both fluid descriptions, quadratic, continuous (P^2-C^0) interpolation of the velocity field and linear, continuous (P^1-C^0) interpolation of the pressure field are utilized. Here, the superscripts refer to the order the polynomial P used to interpolate the solution and the piecewise continuity C between elements. Linear, continuous (P^1-C^0) interpolation of the stress field was also used in the viscoelastic predictions.

Because the governing equations for viscoelastic fluid result in a set of highly nonlinear equations, a convergent solution cannot be obtained in a single step. The parameters leading to non-linearity must be incremented gradually, or evolved. For this study, the volumetric flow rate (Q_{2D}) has been chosen as the evolution parameter. The initial flow rate is chosen such that the fluid is Newtonian in nature. Once a solution is obtained the flow rate is gradually increased using the previous solution as an initial guess for the next evolutive step. This process gradually builds the elastic contribution into the predictions. Furthermore, each intermediate solution has physical significance because the fluid properties have not been changed, merely the volumetric flow rate. Once a convergent solution is obtained ($\varepsilon < 10^{-4}$) for the flow rate of interest, the simulation is concluded.

7.4.3 Computational Mesh

The finite element mesh used to describe the abrupt contraction geometry is found in Figure 7.5. This mesh contains 992 elements and 1113 nodes. The influence of mesh refinement on the convergence of the solution has been investigated [Doerpinghaus (2002)] but is not shown here for clarity. The finite element mesh used in this study was found to be essentially independent of element size and provided convergent solutions with the least computational expense.

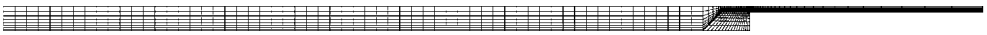

(a)

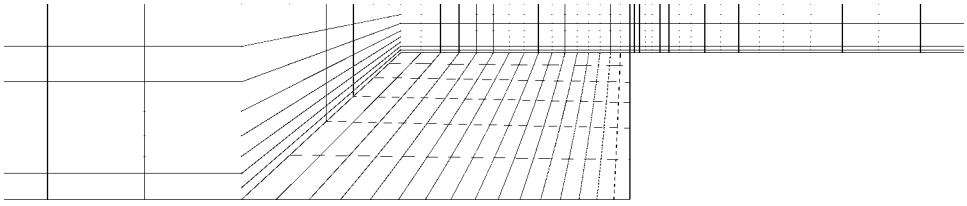

(b)

Figure 7.5: Computational finite element mesh; (a) full mesh domain, (b) expanded view of entry region.

The boundary conditions applied to the finite element mesh were as follows: fully developed flow ($v_2 = 0$, flow rate Q) at inflow, no slip ($v_1 = v_2 = 0$) along the wall, fully developed flow ($v_2 = 0$, flow rate Q) at outflow, and planar symmetry ($f_1 = 0$, $v_2 = 0$) along the centerline. Here, v is defined as the velocity and f as the force. The subscripts 1 and 2 refer to the flow direction and normal direction, respectively.

7.5 Results and Discussion

In this section, the pressure profiles, streamline patterns, and centerline predictions obtained from numerical simulations will be presented and discussed. The imposed volumetric flow rate will be identified by the apparent wall shear rate defined as,

$$\dot{\gamma}_a = \frac{6Q}{WH^2} \tag{7.10}$$

where Q is the imposed volumetric flowrate, W is the channel width, and H is the downstream channel height. Furthermore, at each simulated flow rate the relative elastic contribution will be determined from the dimensionless Weissenberg number, We. Because multi-mode constitutive model formulations complicate the determination of the fluid characteristic relaxation time, the following definition has been used,

$$We = \frac{N_1}{2\tau_w} \tag{7.11}$$

where N_1 is the primary normal stress difference (τ_{11}-τ_{22}) evaluated at the wall in the downstream section and τ_w is the wall shear stress (τ_{12}) evaluated at the same location. The exact location is determined by the onset of fully developed flow. This quantity is often referred to as the stress ratio and is used as a measure for the level of numerical convergence. In light of

various physical flow instabilities that occur at high flow rates (i.e. melt fracture), the range of convergence will be monitored against the apparent wall shear stress, τ_w.

7.5.1 Pressure Profiles

The experimental and predicted pressure profiles for LDPE at $\dot{\gamma}_a = 8.55\ s^{-1}$ are depicted in Figure 7.6. The experimental pressure measurements obtained from each of the six pressure transducers mounted along the flow channel are compared to the predicted pressure profiles obtained from both the PTT and GNF constitutive models. A number of interesting features can be addressed. First, the upstream pressure profile shows that the experimental values are generally higher than either of the predicted curves. The numerical predictions are consistently 12-14% less than the experimental values, which exceed the observed experimental error in the pressure measurements. Second, the difference between the viscoelastic and inelastic models is small at the imposed flow rate. The PTT model predicts less than a 5% increase over the GNF model predictions. This minimal increase in the observed hydrostatic pressure occurs despite We = 1.61, a substantial value for We. In addition to the Weissenberg number, the downstream wall shear stress τ_w is also presented. With a value of only 0.03 MPa, the possible effects of melt fracture that arise at $\tau_w > 0.1$ MPa are not a significant concern [Petrie and Denn (1976)].

Figure 7.7 shows the pressure profiles for LLDPE at $\dot{\gamma}_a = 8.55\ s^{-1}$. First, in can be seen that the model predictions are much more accurate for the LLDPE resin than they are for the LDPE resin. Both the PTT and GNF model predictions are within 5.0% of the experimentally measured pressures. Second, the GNF model appears to do a better job of predicting the pressure profile than the PTT model. The GNF predictions are in very good agreement with the measured profile having an average error of only 1.4%. This overall better agreement is most likely due to

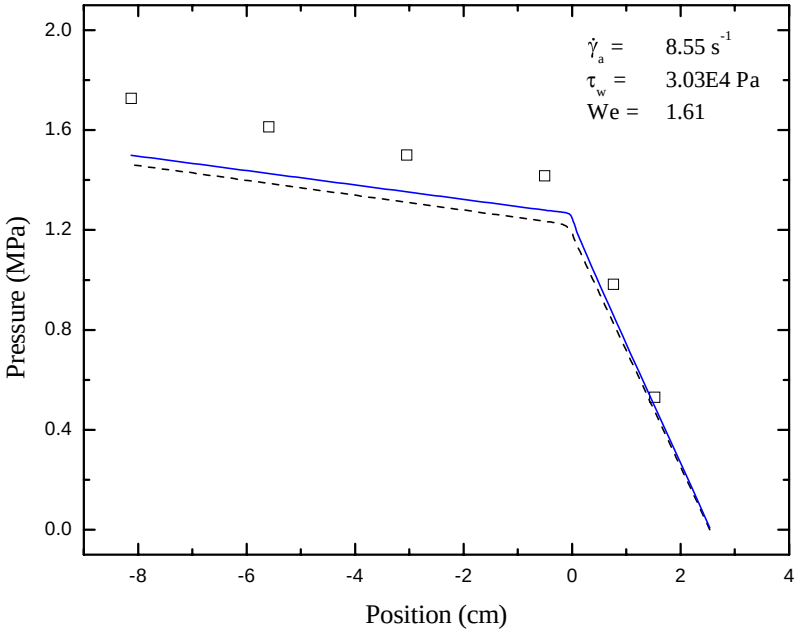

Figure 7.6: Pressure profile for LDPE at $\dot{\gamma}_a$ = 8.55 s^{-1}. Experimental measurements (□), PTT predictions (——), GNF predictions (– – –).

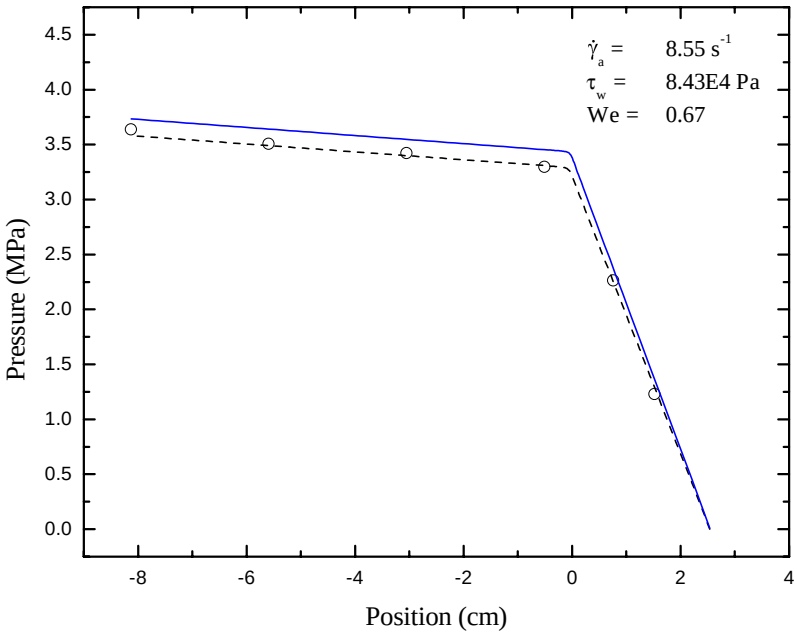

Figure 7.7: Pressure profile for LLDPE at $\dot{\gamma}_a$ = 8.55 s^{-1}. Experimental measurements (○), PTT predictions (——), GNF predictions (– – –).

the lack of significant nonlinear behavior for LLDPE. The delayed onset of shear thinning, short relaxation times, and the lack of extensional strain hardening are much more Newtonian like than the behavior exhibited by the LDPE melt. As a result, the GNF model does as good of job at describing the pressure drop through the contraction die as the PTT model. The value of We is also much smaller at 0.67, but τ_w is noticeably higher at 0.08 MPa. The reduced degree of shear thinning in LLDPE contributes to this higher value of the wall shear stress.

Further increases in the imposed flow rate resulted in a loss of convergence in the numerical solutions for the PTT predictions of LDPE. Table 7.4 summarizes the range of flow rates investigated and the average error between experimental and numerical profiles for each fluid description. Surprisingly, the PTT predictions for LLDPE did not suffer from this limitation. PTT predictions for the LLDPE resin were obtained up to the maximum apparent shear rate investigated of 37.0 s^{-1}. The experimental measurements of the pressure profile and the *obtainable* numerical predictions at the highest apparent shear rate are presented in Figure 7.8 and 7.9. Figure 7.8 compares the experimental values for LDPE at $\dot{\gamma}_a$ = 37.0 s^{-1} to the GNF model predictions. Once again, considerable under prediction is observed, with an average error of 12%. This is most likely due to poorly captured extensional characteristics that are important in the entrance region. On the other hand, Figure 7.9 exhibits the opposite trend for LLDPE. Now the model predictions consistently over predict the measured pressure profiles. This reversal may at first seem inconsistent, but the calculated wall shear stress is in excess of 0.21 MPa and surface melt fracture was observed experimentally. In this case, the presence of a finite slip velocity at the die wall associated with melt fracture may justify this decrease in the observed profile values, but experimental slip velocity measurements were not performed to confirm this.

Table 7.4: Model Prediction Errors

	LDPE		**LLDPE**	
$\dot{\gamma}_a$	PTT % Error	GNF % Error	PTT % Error	GNF % Error
4.36	11	12	2.8	1.9
8.55	12	14	5.1	1.4
13.6	–	14	6.0	1.5
19.3	–	14	7.1	2.5
25.1	–	13	7.2	4
30.9	–	13	11	5.3
37.0	–	12	13	6.7

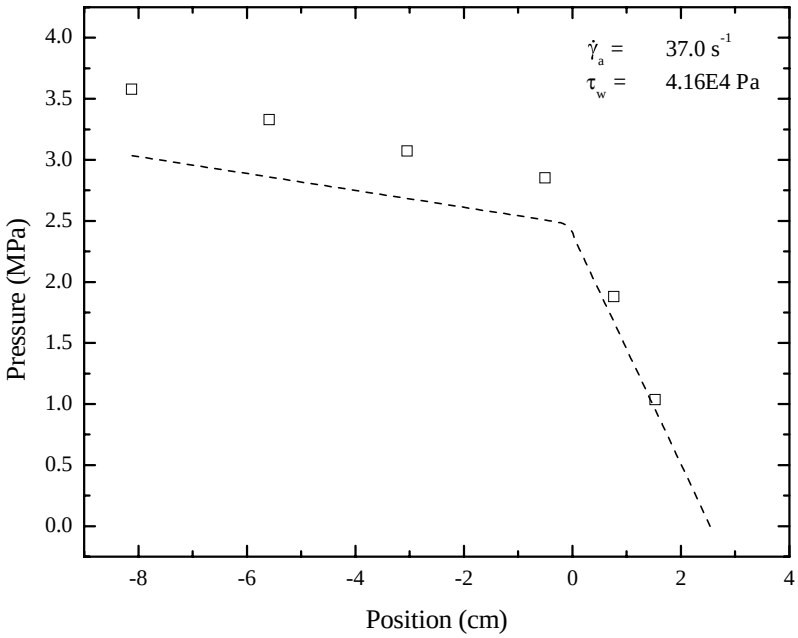

Figure 7.8: Pressure profile for LDPE at $\dot{\gamma}_a = 37.0\ s^{-1}$. Experimental measurements (□), GNF predictions (– – –).

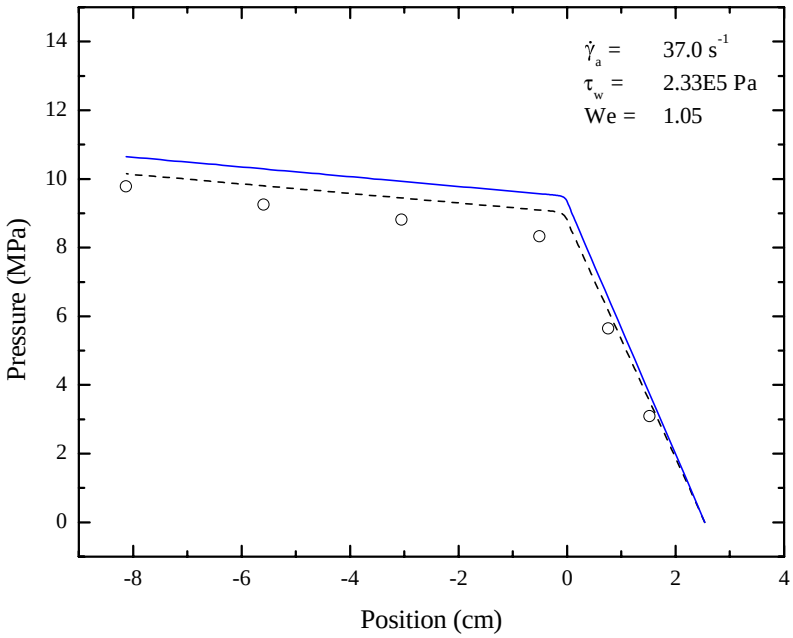

Figure 7.9: Pressure profile for LLDPE at $\dot{\gamma}_a$ = 37.0 s^{-1}. Experimental measurements (○), PTT predictions (——), GNF predictions (– – –).

The results obtained from the measured and calculated pressure profiles clearly indicate that model predictions for the LLDPE resin are generally more accurate than those for the LDPE resin. The consistent under prediction of the hydrodynamic pressure along the contraction die for LDPE implies that the calculated magnitude of ΔP_{ent} is less than observed. This agrees in general with the observations of Barakos and Mitsoulis (1995) and Mitsoulis *et al*. (2000). Conversely, the results obtained for LLDPE would appear to be very accurate, at least to within the accuracy of the experimental pressure measurements of ±2%. Therefore, from the standpoint of die design and processing operations, the predictions for LLDPE are accurate, while the predictions for LDPE are subject to more uncertainty.

Surprisingly, comparing the predictions obtained from the PTT and GNF models indicate that the use of a viscoelastic model may not be necessary for the 4:1 contraction geometry at least with respect to pressure measurements. Within the range of convergent solutions, the differences between the predicted pressure profiles for the PTT and GNF models were found to be small in comparison to the error between predicted and experimental quantities. This trend was observed for both LDPE and LLDPE. This suggests that the shear viscosity determines the measured hydrodynamic pressure and that use of a computationally expensive, viscoelastic constitutive equation may not be necessary. Of course, this assessment only applies to the shear rate ranges (and Weissenberg numbers) covered *numerically*.

The loss of convergence continues to be a problem for numerical simulations at high Weissenberg numbers. The highly strain hardening LDPE was limited to a maximum apparent shear rate of 8.55 s^{-1}, corresponding to a Weissenberg number of 1.61 and a wall shear stress of only 0.03 MPa. The exact cause for loss of convergence is not entirely clear, but the high degree of strain hardening in planar extension combined with the presence of a corner singularity in the

flow domain may have contributed. Conversely, the convergence range for the LLDPE simulations extended over the entire range of experimental flow rates investigated. In fact, numerical predictions were obtained at flow rates and wall shear stresses beyond the observed onset of surface melt fracture.

7.5.2 Predicted Streamline Patterns

Streamline patterns were obtained in the entrance region to better understand the influence that viscoelasticity and extensional strain hardening have on the flow kinematics. Figure 7.10 shows the predicted streamlines obtained from PTT and GNF simulations for both LDPE and LLDPE at $\dot{\gamma}_a = 8.55\ s^{-1}$. This apparent shear rate was chosen because it represents the maximum rate for which convergent PTT predictions are available for both LDPE and LLDPE. Figure 7.10 (a) presents the predictions for LDPE. Clearly, the PTT model predicts sizeable re-circulating vortices in the re-entrant corners and pronounced tapering of the flow into the contraction. This tapering becomes more apparent when the GNF predictions, which do not exhibit vortices, are also plotted. The streamline along the plane of symmetry as predicted by the PTT model represents $\Psi_{max} = 1.0$ and the minimum value found at the center of the vortex is $\Psi_{min} = -0.0053$. Conversely, LLDPE does not show a considerable degree of tapering into the contraction. Figure 7.10 (b) shows that the predictions for the PTT and GNF model for LLDPE are very similar with only slight deviations near the contraction. Although a small vortex is predicted in the PTT simulated streamlines, the minimum value of the streamline function is $\Psi_{min} = -0.0016$, which is more than three times smaller than that calculated for LDPE. This reduced intensity of the vortex has been observed for polymer melts exhibiting less shear-thinning behavior [White and Baird (1986)].

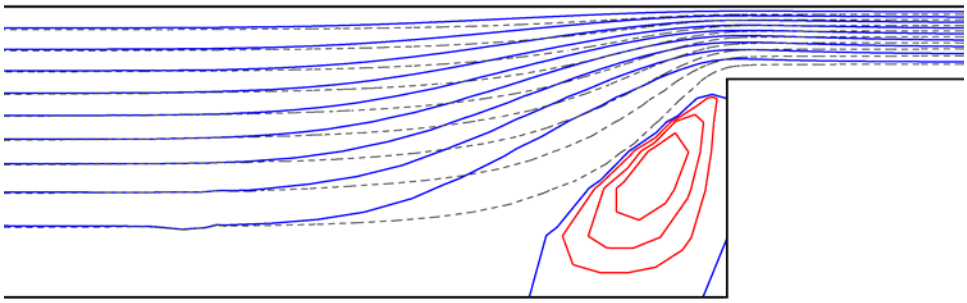

(a) LDPE

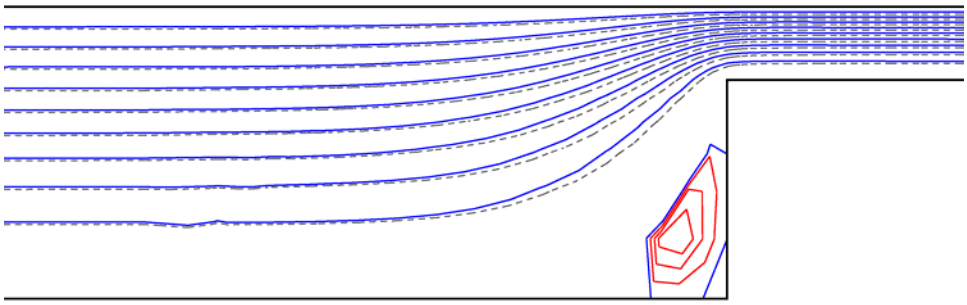

(b) LLDPE

Figure 7.10: Streamline patterns for LDPE and LLDPE at $\dot{\gamma}_a$ = 8.55 s^{-1}. Solid lines represent PTT predictions and dashed lines represent GNF predictions at same values of Ψ.

The predicted degree of flow tapering as well as the intensity of the re-circulating vortices is dependent upon the constitutive model and the model parameters used. The streamline predictions of the PTT model for LDPE show significant vortex growth and flow tapering into the contraction. On the other hand, less tapering and diminished vortices are predicted for the LLDPE melt. These results agree qualitatively with prior experimental observations and numerical simulations of linear and branched polyethylene melts [White and Kondo (1977), Dupont and Crochet (1988), Ahmed *et al*. (1995)]. However, one begins to realize that capturing the correct flow kinematics does not necessarily imply accurate prediction of the hydrodynamic pressures. A better assessment of the effects of viscoelasticity and extensional strain hardening may lie in the extra stress predictions.

7.5.3 Plane of Symmetry Analysis

The plane of symmetry represents the region of pure planar extensional deformation within the contraction die. Well upstream and downstream of the contraction the planar extension rate approaches zero, while at the contraction the extension rate becomes significant. In this section, the predicted extension rates and the calculated net planar stresses σ_1 (= τ_{11}-τ_{22}) will be analyzed.

Figure 7.11 presents the predicted extensional characteristics of LDPE in the vicinity of the abrupt contraction. The planar extension rate and the unsteady planar stress σ_1^+ are plotted as a function of position for both the PTT and GNF model predictions. The planar extension rates are first observed to increase at a location upstream of approximately 0.45 cm. As a fluid element approaches the contraction it then begins to stretch more rapidly before passing through a maximum extension rate of $\dot{\varepsilon}$=1.36 s^{-1} for the PTT predictions and $\dot{\varepsilon}$=1.31 s^{-1} for the GNF

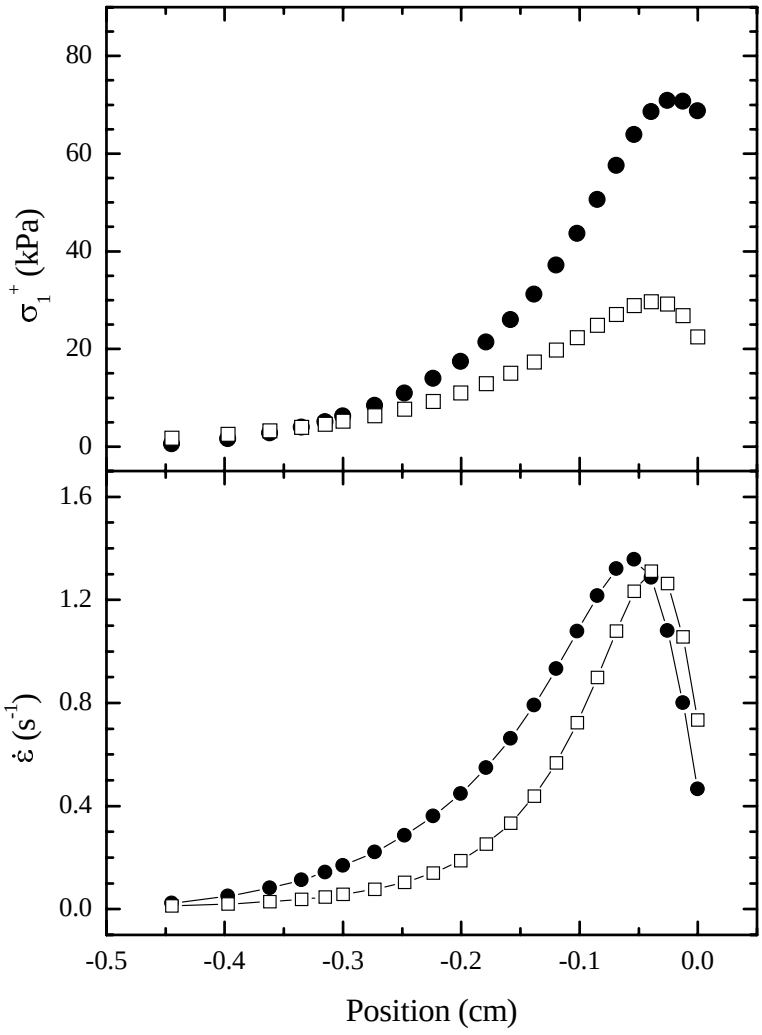

Figure 7.11: Predicted extension rates and extensional stresses along the plane of symmetry for LDPE at $\dot{\gamma}_a = 8.55\ s^{-1}$. (●) PTT predictions, (□) GNF predictions. Lines have been drawn to aid eye.

predictions. Further comparisons between the two models shows that the increase in extension rate is more acute for the GNF model than the PTT model. This observation is best explained by the tapered streamlines first shown in Figure 7.10 (a). The flow tapering leads to a gradual increase in the extension rate as the fluid element passes through the contraction rather than a sharp increase. Although the planar stresses show similar trends, the magnitudes of the net stress are substantially different. The PTT model predicted planar stress for the LDPE resin is 130% greater than that of the GNF predictions at their peak extension rates near y = -0.5 cm. This difference is due to the strain-hardening behavior predicted by the PTT constitutive model.

The model predictions for LLDPE are illustrated in Figure 7.12. In this case, one clearly notices the strong similarity between the PTT and GNF model predictions. The predicted planar extension rates are in good agreement. The increase, maximum, and decrease in $\dot{\varepsilon}$ as a function of position are almost equivalent. This is markedly different from the predictions observed for LDPE. These similarities in the extension rates concur with the streamline patterns previously witnessed in Figure 7.10 (b). Although there is considerably less disparity in the predicted planar stresses for LLPDE compared to those of LDPE, they do exhibit some differences at the peak extension rate near y = -0.025 cm. The PTT predictions are approximately 25% greater than the GNF predictions. This can be attributed to the slight differences in the extensional characteristics of the two constitutive models. This may also explain the 5% difference in the pressure profiles presented in Figure 7.7.

The planar stresses presented in Figure 7.11 and 7.12 represent non-steady values of σ_1. Because fluid memory slows the growth to steady state, the influence of strain hardening is not readily apparent. Figure 7.13 presents the normalized values of the planar stresses (σ_1^+/σ_1) as a function of position. The steady state predictions of σ_1 were calculated for homogenous planar

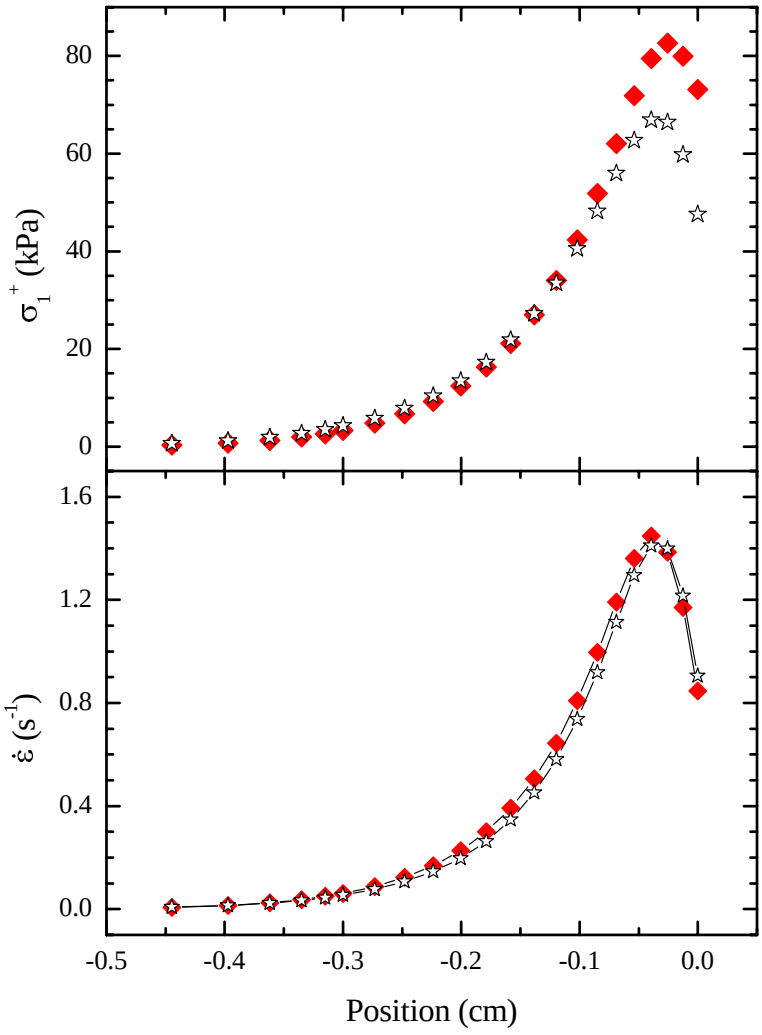

Figure 7.12: Predicted extension rates and extensional stresses along the plane of symmetry for LLDPE at $\dot{\gamma}_a = 8.55\ s^{-1}$. (◆) PTT predictions, (△) GNF predictions. Lines have been drawn to aid eye.

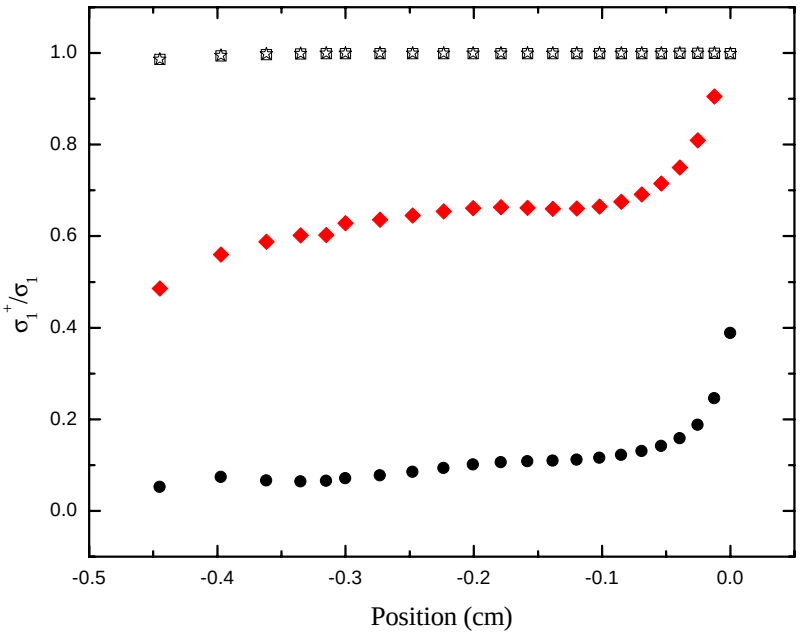

Figure 7.13: Normalized planar extensional stresses along the plane of symmetry at $\dot{\gamma}_a = 8.55\ s^{-1}$. LDPE: (●) PTT predictions, (□) GNF predictions; LLDPE: (◆) PTT predictions, (△) GNF predictions.

extension using the predicted extension rates appearing in Figures 7.11 and 7.12. First, it is readily observed from Figure 7.13 that the unsteady planar stresses predicted by the PTT model for LDPE are considerably less than the steady-state planar stresses. On average, σ_1^+ is less than 10% of the steady-state value. On the other hand, the PTT model predictions for LLDPE are much closer to steady state with σ_1^+ approaching 60% of its steady-state value. The sudden upturn in normalized stresses near the contraction is a result of the decrease in extension rate observed in Figures 7.11 and 7.12 combined with the relaxation behavior of each fluid. Finally, the GNF model predictions attain steady state almost instantly. This behavior is expected from an inelastic constitutive model with instantaneous fluid response. Therefore, one clearly observes from Figure 7.13 the influence that fluid memory can also have on the predicted stresses along the plane of symmetry.

The results obtained from analyzing the plane of symmetry suggest that the extensional characteristics of the polymer liquid are important, but may obscured by the melt relaxation behavior in the case of a 4:1 contraction. In light of the fact that the predicted pressure profiles for LDPE were consistently lower than the measured quantities, one concern was that the PTT model parameters were not accurately predicting the extensional properties of LDPE. More specifically, in this study it was chosen to use a single value of ε common to all modes and then to fit that parameter using uniaxial extensional data obtained at 1.0 s^{-1}. Although this approach may lead to poor predictions at lower extension rates, it was determined that fitting to the highest available extension rate was most relevant to predicting the pressure profiles at the higher flow rates used here. In order to confirm this idea, model fitting of the ε parameter was performed using extensional data obtained at $\dot{\varepsilon}$=0.01, 0.1 and 1.0 s^{-1}. The corresponding values of ε were determined to be 10^{-6}, 0.021, and 0.034, respectively. From those parameters, the transient planar

extensional viscosities were calculated as function of strain at a planar extension rate of 1.0 s^{-1}. The calculated results are presented in Figure 7.14. One notices that the observed extensional viscosities increase with decreasing values of ε. Again, it should be noted that ε=0.034 refers to data obtained at 1.0 s^{-1}. Therefore, at high strains variations in the extensional viscosities are observed, and these variations *could* give rise to different pressure profile predictions. However, a fluid element passing through a 4:1 contraction will experimence a maximum, accumulated strain of only 1.39 strain units along the plane of symmetry. This can be calculated by the simple relation, $\varepsilon_H = \ln \beta$, where β is the planar contraction ratio. From Figure 7.14, the differences in the planar extensional viscosities associated with ε_H=1.39 are found to be less than 9%. This relative insensitivity to ε was also observed for the calculated extensional viscosities at $\dot{\varepsilon}$=0.01 and 0.1 s^{-1} and the corresponding pressure profiles and streamline patterns predicted from simulations (not shown for brevity) [Doerpinghaus (2002)]. Therefore, the influence of parameter fitting and the accuracy of the extensional viscosity predictions at high strains, or even steady state, are not as important as at small strains. Of course, this fortuitous result may not apply at larger contraction ratios in which the total strain is larger.

7.6 Conclusions

Experiments and numerical simulations have been performed for the planar contraction flow of two polyethylene melts. The influence of fluid properties, primarily extensional strain-hardening behavior, on the measured and predicted pressure profiles along a 4:1 abrupt planar contraction has been investigated. Of particular interest was whether numerical predictions could accurately predict a macroscopic quantity such as the hydrodynamic pressure along the

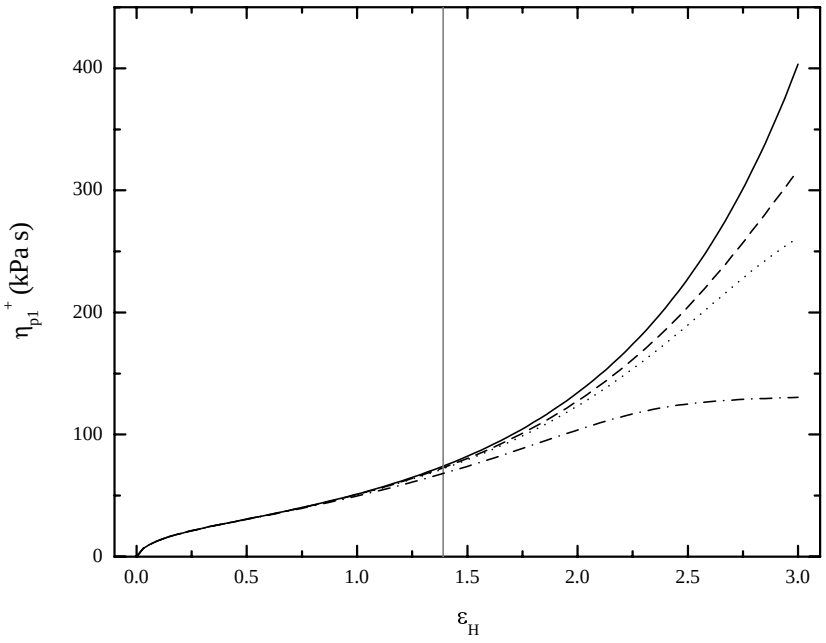

Figure 7.14: Calculated planar extensional viscosities (η_{p1}^{+}) at an extension rate of $\dot{\varepsilon}$=1.0 s^{-1} for different values of the ε parameter. $\varepsilon = 1.28 \cdot 10^{-6}$ (——), 0.021 (– – –), 0.034 (· · ·), and an arbitrary value of 0.100 (—·—).

contraction die. This ability is fundamental to die design and necessary during extrusion operations.

The accuracy of the predicted pressure profiles was found to depend on the fluid characteristics. Numerical predictions for the LDPE resin were consistently lower than the experimental values. At the highest convergent (viscoelastic) apparent shear rate of $\dot{\gamma}_a = 8.55\ s^{-1}$, both the PTT and GNF models under predicted the pressure profiles by more than 12%. Although the PTT model predictions were somewhat greater than the GNF predictions, the effects of extensional strain hardening were not readily apparent. On the other hand, the numerical predictions for the LLDPE resin were much more accurate. The PTT and GNF model predictions were within 5% of the experimental values at $\dot{\gamma}_a = 8.55\ s^{-1}$. In fact, the GNF predictions were arguably more accurate than the PTT model predictions. At higher rates, the possible effects of melt fracture and wall slip led to over prediction of the upstream pressure values by both constitutive models. In the case of LLDPE, the onset of melt fracture corresponded well with a predicted wall shear stress, τ_w, in excess of 0.1 MPa. Thus making τ_w a good numerical indicator for the presence of physical instabilities at high flow rates.

The predicted streamline patterns and the extensional properties along the plane of symmetry clearly indicate that fluid relaxation behavior and extensional strain hardening influence the flow kinematics in the entry region. Pronounced tapering of the flow into the abrupt contraction with the presence of sizeable re-circulating corner vortices are predicted for the LDPE material. Conversely, streamlines for the LLDPE material are very similar to the GNF predictions and the size and magnitude of the corner vortex is substantially smaller. The extensional deformation along the plane of symmetry suggests that the fluid relaxation behavior negates the effects of extensional strain-hardening behavior in the contraction region. LDPE,

exhibiting a long characteristic relaxation time and high degree of extensional strain hardening, attains only 10% of the steady state planar extensional stress as it passes through the contraction region. LLDPE, which exhibits a shorter relaxation time and extensional strain-softening behavior, attains 60% of its steady state stress. Thus the relaxation behavior of the polymer melt limits the magnitude of the planar extensional stress developed through a 4:1 contraction.

The relatively small extensional strains encountered along the plane of symmetry for an abrupt 4:1 planar contraction do not give rise to a significant extensional response. This is confirmed by the relative insensitivity of the predicted values to variations in nonlinear extensional parameter ε for the PTT model. This fortuitous response may also explain the similarities exhibited by the PTT and GNF model predictions despite variations in the predicted flow kinematics. Additional studies investigating larger contraction ratios or other flow geometries that give rise to large extensional strains should be performed to assess the significance of extensional strain hardening on pressure profile predictions. In the case of the 4:1 planar contraction studied here, the under predicted pressure profiles for LDPE are not completely understood but could be elucidated further using full-field flow birefringence and velocimetry measurements of the contraction region.

7.7 Acknowledgments

The authors would like to thank A. Willem deGroot at the Dow Chemical Company for providing the LCB and MWD data. The authors would also like to extend their gratitude to the ExxonMobil Chemical Company and the Equistar Chemical Company for graciously donating their respective PE resins to this study.

7.8 References

Ahmed, R. and M.R. Mackley, *J. Non-Newt. Fluid Mech*. **56**, 127 (1995).

Ahmed, R., R.F. Liang, and M.R. Mackley, *J. Non-Newt. Fluid Mech*. **59**, 129 (1995).

Bagley, E.B., *J. Appl. Phys*. **28**, 624 (1957).

Ballenger, T.F. and J.L. White, *Chem. Eng. Sci*. **25**, 1191 (1970).

Barakous, G. and E. Mitsoulis, *J. Rheol*. **39**, 193 (1995).

Beraudo, C., T. Coupez, A. Fortin, Y. Demay, B. Vergnes, J.F. Agassant, *Proc. XIIth Int. Congr. Rheology*, Quebec City, 417 (1996).

Bernstein, B., E. Kearsely, and L. Zapas, *Trans. Soc. Rheol*. **7**, 391 (1963).

Binding, D.M., *J. Non-Newt. Fluid Mech*. **27**, 173 (1988).

Bird, R.B., R.C. Armstrong and O. Hassager, *Dynamics of Polymeric Liquids. Volume 1: Fluid Mechanics*, 2nd ed. John Wiley & Sons, New York, 1987.

Boger, D.V., *Ann. Rev. Fluid Mech*. **19**, 157 (1987).

Carreau, P.J., *Shear Flow Properties of Concentrated Solutions of Linear and Star Branched Polystyrenes*, Ph.D. dissertation, University of Wisconsin, Madison (1968).

Chang, S.-Y., *Use of hole pressure data to obtain N1 at high shear rates for polymer melts*, Masters Thesis, Virginia Tech, Blacksburg, VA (1986).

Cogswell, F.N., *Trans. Soc. Rheol*. 16, 383 (1972).

den Otter, J.L., *Plastics Polym*. **38**, 1555 (1970).

Doerpinghaus, P.J., *Flow behavior of sparsely branched metallocene-catalyzed polyethylenes*, Ph.D. dissertation, Virginia Tech, Blacksburg, VA (2002).

Dupont, S. and M.J. Crochet, *J. Non-Newt. Fluid Mech*. **29**, 81 (1988).

Franck, A. and J. Meissner, *Rheol. Acta* **23**, 117 (1984).

Hatzikiriakos, S.G. and E. Mitsoulis, *Rheol. Acta* **36**, 545 (1996).

Kaye, A., College of Aeronautics, Cranfield, Note No. 134 (1962).

Laun, H.M. and H. Schuch, *J. Rheol*. **33**, 119 (1989).

Luo, X.-L. and E. Mitsoulis, *J. Rheol*. **34**, 309 (1990).

Marchal, J.M. and M.J. Crochet, *J. Non-Newt. Fluid Mech*. **26**, 177 (1987).

Martyn, M.T., C, Nakason, and P.D. Coates, *J. Non-Newt. Fluid Mech*. **91**, 109 (2000).

McLeish, T.C.B. and R.G. Larson, *J. Rheol*. **42**, 82 (1998).

Minoshima, W. and J.L. White, *J. Non-Newt. Fluid Mech*. **19**, 251 (1986).

Mitsoulis, E., S.G. Hatzikiriakos, K. Christodoulou, D. Vlassopoulous, *Rheol. Acta* **37**, 438 (1998).

Münstedt, H., *J. Rheol*. **23**, 421 (1979).

Münstedt, H., *J. Rheol*. **24**, 847 (1980).

Münstedt, H., *Rheo. Acta* **20**, 211 (1981).

Münstedt, H. and H.M. Laun, *Rheol. Acta* **20**, 211 (1981).

Park, H.J., D.G. Kiriakidis, E. Mitsoulis, and K.-J. Lee, *J. Rheol*. **36**, 1563 (1992).

Petrie, C.J.S. and M.M. Denn, *AIChE J*. **22**, 209 (1976).

Phan Thien, N., *J. Rheol*. **22**, 259 (1978).

Phan Thien, N. and R.I. Tanner, *J. Non-Newt. Fluid Mech*. **2**, 353 (1977).

Rajagopolan, D., R.C. Armstrong, and R.A. Brown, *J. Non-Newt. Fluid Mech*. **36**, 135 (1990).

Samurkas, T., R.G. Larson, and J.M. Dealy, *J. Rheol*. **33**, 559 (1989).

Tanner, R.I. and K. Walters, *Rheology: An historical perspective*, Elsevier, Amsterdam, 1998.

White, J.L., *Appl. Polym. Symp*. **33**, 31 (1978).

White, J.L. and A. Kondo, *J. Non-Newt. Fluid Mech*. **3**, 41 (1977).

White, S.A. and D.G. Baird, *J. Non-Newt. Fluid Mech*. **20**, 93 (1986).

White, S.A., A.D. Gotsis, and D.G. Baird, *J. Non-Newt. Fluid Mech*. **24**, 121 (1987).

Yasuda, K., R.C. Armstrong, and R.E. Cohen, *Rheol. Acta* **20**, 163 (1981).

8.0 Recommendations

8.0 Recommendations

Material Considerations

1) The zero-shear viscosity enhancement observed in this study and the observations of Janzen and Colby for peroxide-treated PE resins demonstrate a non-monotonic relationship between η_0 and LCB content. However, the degree of enhancement/ reduction predicted by the Janzen-Colby viscosity relation using dilute solution measurements was much greater than observed. A closer investigation of this behavior using a series of mPE resins that definitively spans the maximum in the η_0-LCB curve would be useful.
2) The relative insensitivity of the rheological properties to increases in LCB content from 0.57 to 0.79 LCB/10^4 carbons implies poor precision of GPC-LALLS techniques or the possibility of variations in the average molecular topology of resins produced by different manufacturers (Dow vs. ExxonMobil). A comprehensive study of the rheological properties of sparsely branched polyethylenes produced from different methods (i.e. metallocene catalysts, peroxide-induced, γ-irradiation) in relation to their dilute solution characterization may be useful.
3) The McLeish-Larson pom-pom model suggests that two or branch points per molecule is required for the manifestation of extensional strain hardening in PE resins. Synthesis of model materials (in sufficient quantities) with one (star), two (H polymer), and more (comb) LCB per molecule may help elucidate this theory regarding the origin of extensional strain-hardening behavior.

Experimental Considerations

1) The additional enhancement in the onset of shear thinning and the primary normal stress difference coefficient suggests that the equilibrium compliance J_e^0 may also be affected by LCB content. Therefore, creep experiments followed by constrained recoil should be performed to quantify the influence of LCB on J_e^0 in sparsely and densely branched PE resins. Furthermore, the same experiments can be used to probe the extremely long relaxation times exhibited by the highly branched LDPE resin.
2) From the melt fracture studies, the effects of molecular architecture were evident from the melt fracture forms. However, die geometry and temperature can also affect the melt fracture forms. Geometric variables may mitigate or amplify the observations witnessed from the current study. With respect to temperature, the peculiar slip-stick behavior may not exist at higher temperatures.
3) From the profiling studies, it was apparent that adequate resolution of the pressure profile near the abrupt contraction was limited by the small geometries implemented. The use of an axisymmetric pressure-profiling die may provide additional spatial resolution of the contraction region via small pressure holes and radial arrangement of pressure taps. With additional resolution, the nonlinear nature of the pressure profile near the contraction should become more evident and may assist in differentiating the flow behavior of PE resins.

Numerical Considerations

1) The 4:1 planar contraction geometry was found not to generate a substantial extensional response. Therefore the influence that viscoelastic constitutive equations have on the numerical predictions of the hydrodynamic pressure were not manifested or were minimal. Using planar contractions with larger contraction ratios or geometries that give rise to sustained extensional flow (i.e. semi-hyperbolic dies) should impart more extensional dependency upon predicted quantities. As a result, greater disparity between the viscoelastic and inelastic predictions should be observed.
2) With greater extensional contributions to flow properties, the need for a viscoelastic constitutive equation capable of accurately predicting the extensional behavior is greater. For resins with long-chain branching, it becomes important to accurately describe the degree of extensional strain hardening manifested. Therefore, a better understanding of the structural dependencies of constitutive model parameters and their sensitivity to long-chain branch content may be useful.

Appendix A. Steady & Dynamic Rheological Data

A.1. Equistar Petrothene NA952-000 (LDPE)

Dynamic Oscillatory T=150 °C

ω	G′	G′′	tan δ	|η*|
0.10000	1126.8	2012.3	1.7859	23063
0.15849	1659.8	2647.5	1.5950	19716
0.25119	2367.2	3413.2	1.4419	16536
0.39811	3309.3	4338.7	1.3111	13706
0.63097	4519.8	5441.8	1.2040	11211
1.0000	6044.3	6767.6	1.1197	9073.5
1.5850	7958.8	8309.4	1.0441	7259.5
2.5120	10357	10102	0.97541	5759.5
3.9813	13238	12220	0.92308	4525.0
6.3101	16764	14652	0.87399	3528.5
10.001	21000	17462	0.83152	2731.0
15.850	26065	20662	0.79272	2098.5
25.121	32075	24329	0.75851	1602.6
39.813	39136	28513	0.72856	1216.2
63.101	47335	33220	0.70181	916.45
100.00	56755	38416	0.67687	685.34

Steady Shear T=150 °C

$\dot{\gamma}$	η	Ψ_1
0.00100	45040	
0.00159	44800	
0.00251	44500	
0.00398	43800	
0.00631	42500	
0.01000	40360	
0.01585	36590	
0.02512	34390	
0.03160		638920
0.03981	31470	
0.06310	28260	
0.10000		377300
0.31620		132073
1.00000		33240

A.1. Equistar Petrothene NA952-000 (LDPE)

Dynamic Oscillatory T=170 °C

ω	G′	G′′	tan δ	|η*|
0.10000	554.08	1281.1	2.3121	13958
0.15849	874.38	1744.1	1.9947	12310
0.25119	1320.8	2320.5	1.7569	10630
0.39811	1934.1	3035.6	1.5695	9041.2
0.63097	2746.0	3903.7	1.4216	7564.3
1.0000	3818.1	4947.5	1.2958	6249.2
1.5850	5180.7	6207.3	1.1982	5101.2
2.5120	6931.4	7722.9	1.1142	4131.0
3.9813	9084.0	9450.7	1.0404	3292.5
6.3101	11769	11533	0.97994	2611.4
10.001	15066	13849	0.91924	2046.3
15.850	19012	16598	0.87305	1592.3
25.121	23768	19812	0.83358	1231.8
39.813	29481	23508	0.79741	947.06
63.101	36188	27648	0.76401	721.71
100.00	43969	32284	0.73425	545.49

Dynamic Oscillatory T=190 °C

ω	G′	G′′	tan δ	|η*|
0.10000	267.32	810.42	3.0316	8533.6
0.15849	449.68	1138.9	2.5326	7725.5
0.25119	721.77	1564.0	2.1669	6857.4
0.39811	1114.4	2104.5	1.8884	5981.8
0.63097	1655.5	2773.0	1.6751	5118.5
1.0000	2389.2	3598.1	1.5060	4319.0
1.5850	3361.8	4602.5	1.3691	3596.0
2.5120	4635.3	5787.7	1.2486	2951.8
3.9813	6220.5	7259.0	1.1669	2401.1
6.3101	8245.6	8955.8	1.0861	1929.2
10.001	10795	10971	1.0162	1539.0
15.850	13893	13338	0.96004	1215.1
25.121	17657	16052	0.90913	949.94
39.813	22301	19223	0.86201	739.51
63.101	27715	22852	0.82452	569.27
100.00	34150	26919	0.78826	434.84

A.2. ExxonMobil NTX101 (LLDPE)

Dynamic Oscillatory T=150 °C

ω	G′	G′′	tan δ	|η*|
0.10000	262.79	1836.8	6.9897	18555
0.15849	462.73	2794.4	6.0389	17871
0.25119	809.61	4215.3	5.2066	17088
0.39811	1413.4	6296.2	4.4547	16209
0.63097	2436.3	9286.2	3.8116	15215
1.0000	4140.4	13490	3.2581	14110
1.5850	6893.2	19268	2.7952	12911
2.5120	11234	26994	2.4029	11639
3.9813	17770	37043	2.0847	10319
6.3101	27433	49715	1.8122	8998.5
10.001	41118	65190	1.5855	7706.9
15.850	59816	83432	1.3948	6476.9
25.121	84471	104200	1.2336	5339.7
39.813	115970	127130	1.0962	4322.1
63.101	154570	151470	0.97994	3429.7
100.00	200020	176310	0.88145	2666.3

Steady Shear T=150 °C

$\dot{\gamma}$	η	Ψ_1
0.00100	21770	
0.00159	21730	
0.00251	21540	
0.00398	21500	
0.00631	21340	
0.01000	21000	
0.01585	20700	
0.02512	20330	
0.03981	19790	
0.06310	19420	
0.10000		59800
0.17780		40237
0.31620		24994
0.56230		16174
1.00000		9775
1.77800		6028

A.2. ExxonMobil NTX101 (LLDPE)

Dynamic Oscillatory T=170 °C

ω	G′	G′′	tan δ	|η*|
0.10000	144.19	1304.8	9.0493	13128
0.15849	268.17	2006.4	7.4819	12772
0.25119	484.63	3045.0	6.2831	12275
0.39811	871.60	4579.8	5.2545	11710
0.63097	1521.1	6826.7	4.4880	11085
1.0000	2647.0	10033	3.7904	10376
1.5850	4491.1	14535	3.2364	9598.4
2.5120	7512.3	20718	2.7579	8773.0
3.9813	12133	28953	2.3863	7885.0
6.3101	19211	39571	2.0598	6971.1
10.001	29460	52978	1.7983	6061.4
15.850	44024	69616	1.5813	5196.7
25.121	63876	88929	1.3922	4358.6
39.813	90033	111120	1.2342	3592.1
63.101	123010	135520	1.1017	2900.4
100.00	163150	161030	0.98703	2292.3

Dynamic Oscillatory T=190 °C

ω	G′	G′′	tan δ	|η*|
0.10000	89.101	946.56	10.623	9507.4
0.15849	167.32	1462.8	8.7426	9289.9
0.25119	310.08	2238.7	7.2199	8997.6
0.39811	566.07	3399.1	6.0047	8655.7
0.63097	1014.5	5107.4	5.0342	8252.7
1.0000	1786.5	7580.9	4.2433	7788.3
1.5850	3084.5	11105	3.6002	7271.6
2.5120	5214.8	15994	3.0670	6696.8
3.9813	8608.8	22654	2.6315	6087.1
6.3101	13787	31678	2.2976	5475.1
10.001	21644	43059	1.9894	4818.9
15.850	33016	57259	1.7343	4170.0
25.121	48812	74442	1.5251	3543.6
39.813	70254	94872	1.3504	2965.1
63.101	97842	117730	1.2032	2425.9
100.00	132480	142290	1.0741	1944.2

A.3. ExxonMobil Exact 0201 (mBLDPE)

Dynamic Oscillatory T=150 °C

ω	G′	G′′	tan δ	|η*|
0.10000	1026.9	2733.6	2.6619	29202
0.15849	1622.7	3808.6	2.3471	26121
0.25119	2467.8	5225.4	2.1174	23006
0.39811	3644.4	7085.0	1.9441	20013
0.63097	5255.6	9532.0	1.8137	17251
1.0000	7406.6	12749	1.7213	14744
1.5850	10324	17030	1.6496	12565
2.5120	14261	22679	1.5903	10665
3.9813	19628	30141	1.5356	9034.2
6.3101	27005	39860	1.4760	7630.1
10.001	37202	52308	1.4061	6418.3
15.850	51150	67955	1.3285	5366.2
25.121	70096	86783	1.2381	4440.8
39.813	95180	108850	1.1436	3631.8
63.101	127370	133600	1.0489	2925.4
100.00	167090	160080	0.95805	2314.0

Steady Shear T=150 °C

$\dot{\gamma}$	η	Ψ_1
0.00100	43290	
0.00159	42750	
0.00251	42770	
0.00398	42100	
0.00631	41290	
0.01000	40840	
0.01585	39480	
0.02512	37800	
0.03160		490706
0.03981	35070	
0.06310	32460	
0.10000		317200
0.31620		75633
1.00000		15743

A.3. ExxonMobil Exact 0201 (mBLDPE)

Dynamic Oscillatory T=170 °C

ω	G′	G′′	tan δ	|η*|
0.10000	520.54	1810.6	3.4782	18839
0.15849	867.10	2590.1	2.9870	17234
0.25119	1399.1	3641.0	2.6023	15528
0.39811	2174.3	5051.8	2.3235	13815
0.63097	3277.5	6926.6	2.1134	12145
1.0000	4782.1	9398.0	1.9652	10544
1.5850	6865.8	12690	1.8482	9103.0
2.5120	9716.1	17093	1.7592	7826.8
3.9813	13568	22847	1.6839	6674.3
6.3101	18926	30493	1.6112	5687.5
10.001	26419	40566	1.5355	4840.7
15.850	36651	53444	1.4582	4088.5
25.121	50855	69375	1.3642	3424.2
39.813	69947	88719	1.2684	2837.6
63.101	95227	111400	1.1699	2322.6
100.00	127540	136570	1.0708	1868.6

Dynamic Oscillatory T=190 °C

ω	G′	G′′	tan δ	|η*|
0.10000	264.26	1167.8	4.4190	11973
0.15849	461.05	1713.3	3.7161	11195
0.25119	776.51	2462.9	3.1718	10281
0.39811	1265.9	3490.1	2.7571	9325.5
0.63097	1988.2	4873.1	2.4510	8341.2
1.0000	3025.6	6726.6	2.2232	7375.5
1.5850	4477.5	9178.7	2.0500	6443.4
2.5120	6465.2	12452	1.9260	5585.2
3.9813	9245.4	16843	1.8218	4826.0
6.3101	13065	22621	1.7315	4139.9
10.001	18355	30240	1.6475	3537.2
15.850	25724	40220	1.5635	3012.1
25.121	35981	52893	1.4700	2546.6
39.813	50017	68710	1.3737	2134.6
63.101	68960	87659	1.2712	1767.5
100.00	94050	109710	1.1666	1445.1

A.4. ExxonMobil Exact 3132 (mLLDPE)

Dynamic Oscillatory T=150 °C

ω	G′	G′′	tan δ	|η*|
0.10000	56.667	1581.7	27.913	15827
0.15849	115.58	2486.7	21.516	15707
0.25119	237.06	3891.2	16.414	15520
0.39811	479.36	6076.0	12.675	15310
0.63097	989.05	9439.3	9.5438	15042
1.0000	2017.2	14530	7.2029	14668
1.5850	4067.8	22065	5.4243	14156
2.5120	7966.0	32870	4.1264	13464
3.9813	14939	47728	3.1949	12561
6.3101	26603	67213	2.5265	11456
10.001	44891	91414	2.0364	10183
15.850	71568	119810	1.6741	8805.1
25.121	108180	152590	1.4106	7445.9
39.813	155960	186500	1.1958	6106.4
63.101	214150	220410	1.0292	4870.2
100.00	281640	253180	0.89896	3787.1

Steady Shear T=150 °C

$\dot{\gamma}$	η	Ψ_1
0.00100	14881	
0.00158	14775	
0.00251	14855	
0.00398	14727	
0.00631	14625	
0.01000	14956	
0.01585	14979	
0.02512	15019	
0.03981	15025	
0.06310	14974	
0.10000		10200
0.17780		7813
0.31620		7151
0.56230		5800
1.00000		4038
1.77800		3069

A.4. ExxonMobil Exact 3132 (mLLDPE)

Dynamic Oscillatory T=170 °C

ω	G′	G′′	tan δ	|η*|
0.10000	20.966	992.02	47.316	9922.3
0.15849	45.078	1566.2	34.744	9886.2
0.25119	99.687	2462.4	24.701	9810.9
0.39811	205.63	3869.1	18.816	9732.3
0.63097	445.12	6050.2	13.592	9614.8
1.0000	932.40	9399.6	10.081	9445.4
1.5850	1933.8	14490	7.4930	9223.5
2.5120	3990.6	22044	5.5239	8917.9
3.9813	7757.0	32790	4.2272	8463.3
6.3101	14641	47721	3.2593	7910.6
10.001	26240	67151	2.5592	7209.0
15.850	44510	91968	2.0663	6446.2
25.121	71036	120590	1.6976	5571.6
39.813	107470	152820	1.4219	4692.5
63.101	154650	187040	1.2094	3846.1
100.00	211940	221160	1.0435	3063.2

Dynamic Oscillatory T=190 °C

ω	G′	G′′	tan δ	|η*|
0.10000	11.373	676.39	59.471	6764.9
0.15849	25.243	1072.2	42.473	6766.7
0.25119	56.957	1690.1	29.674	6732.3
0.39811	119.99	2658.7	22.158	6685.1
0.63097	250.08	4171.6	16.681	6623.4
1.0000	499.98	6545.0	13.090	6563.9
1.5850	1050.6	10149	9.6607	6437.7
2.5120	2186.7	15617	7.1420	6277.6
3.9813	4499.5	23684	5.2638	6055.2
6.3101	8722.7	35096	4.0235	5731.1
10.001	16305	50858	3.1193	5340.4
15.850	28973	71373	2.4634	4859.9
25.121	48250	96573	2.0015	4297.5
39.813	76350	126150	1.6523	3703.7
63.101	114300	158820	1.3895	3101.0
100.00	162480	192720	1.1861	2520.8

A.5. Dow Affinity PL1840 (mBLDPE)

Dynamic Oscillatory T=150 °C

ω	G′	G′′	tan δ	|η*|
0.10000	1082.4	2789.3	2.5770	29919
0.15849	1704.3	3884.6	2.2793	26766
0.25119	2578.7	5285.4	2.0496	23412
0.39811	3779.7	7113.3	1.8820	20233
0.63097	5424.2	9514.6	1.7541	17358
1.0000	7605.2	12652	1.6636	14762
1.5850	10527	16793	1.5953	12505
2.5120	14409	22267	1.5453	10558
3.9813	19673	29479	1.4985	8901.8
6.3101	26810	38945	1.4526	7492.9
10.001	36602	51164	1.3979	6290.4
15.850	50012	66693	1.3335	5259.4
25.121	68279	85621	1.2540	4359.5
39.813	92613	108130	1.1676	3575.9
63.101	124170	133800	1.0775	2892.8
100.00	163550	161630	0.98826	2299.4

Steady Shear T=150 °C

$\dot{\gamma}$	η	Ψ_1
0.00100	46600	
0.00178	47000	
0.00316	46800	
0.00562	46500	
0.01000	45200	
0.01780	43100	
0.03160	40100	349503
0.05620	36500	
0.10000		293500
0.31620		79934
1.00000		16182

A.5. Dow Affinity PL1840 (mBLDPE)

Dynamic Oscillatory T=170 °C

ω	G′	G′′	tan δ	|η*|
0.10000	573.52	1903.9	3.3197	19884
0.15849	942.04	2708.0	2.8747	18091
0.25119	1524.0	3795.5	2.4904	16283
0.39811	2348.6	5234.4	2.2287	14411
0.63097	3514.8	7112.3	2.0236	12573
1.0000	5105.0	9589.5	1.8784	10863
1.5850	7255.4	12851	1.7712	9310.9
2.5120	10142	17198	1.6958	7948.0
3.9813	14079	22892	1.6259	6750.2
6.3101	19432	30451	1.5671	5724.7
10.001	26774	40312	1.5056	4838.9
15.850	36868	53209	1.4432	4084.1
25.121	50700	69358	1.3680	3420.0
39.813	69436	89124	1.2835	2837.7
63.101	94458	112620	1.1922	2329.4
100.00	126590	139050	1.0984	1880.5

Dynamic Oscillatory T=190 °C

ω	G′	G′′	tan δ	|η*|
0.10000	283.90	1235.6	4.3523	12678
0.15849	496.23	1805.5	3.6383	11814
0.25119	836.89	2583.9	3.0875	10813
0.39811	1368.6	3655.0	2.6707	9803.4
0.63097	2140.9	5079.1	2.3724	8735.6
1.0000	3236.5	6979.9	2.1566	7693.5
1.5850	4768.1	9481.8	1.9886	6696.2
2.5120	6835.3	12791	1.8713	5773.3
3.9813	9766.6	17179	1.7589	4963.4
6.3101	13662	23013	1.6844	4241.3
10.001	19042	30706	1.6125	3612.8
15.850	26404	40759	1.5437	3064.0
25.121	36597	53664	1.4663	2585.7
39.813	50559	69920	1.3829	2167.2
63.101	69549	89754	1.2905	1799.5
100.00	94372	112650	1.1937	1469.6

A.6. Dow Affinity PL1880 (mBLDPE)

Dynamic Oscillatory T=150 °C

ω	G′	G′′	tan δ	|η*|
0.10000	1004.2	2803.3	2.7916	29777
0.15849	1580.4	3928.3	2.4856	26717
0.25119	2403.3	5423.8	2.2568	23617
0.39811	3550.5	7422.6	2.0906	20668
0.63097	5129.6	10113	1.9715	17972
1.0000	7280.7	13745	1.8879	15554
1.5850	10252	18663	1.8205	13434
2.5120	14390	25293	1.7577	11584
3.9813	20230	34132	1.6872	9965.8
6.3101	28518	45711	1.6029	8538.3
10.001	40248	60532	1.5040	7268.6
15.850	56603	79033	1.3963	6133.2
25.121	79045	101030	1.2781	5106.5
39.813	108780	126360	1.1616	4187.9
63.101	146750	154100	1.0501	3372.4
100.00	193070	183080	0.94827	2660.7

Steady Shear T=150 °C

$\dot{\gamma}$	η	Ψ_1
0.00100	45400	
0.00178	45200	
0.00316	45500	
0.00562	44900	
0.01000	43900	
0.01780	42100	
0.03160	39400	319460
0.05620	35900	
0.10000		254200
0.31620		73773
1.00000		15598

A.6. Dow Affinity PL1880 (mBLDPE)

Dynamic Oscillatory T=170 °C

ω	G′	G′′	tan δ	|η*|
0.10000	514.23	1864.0	3.6248	19336
0.15849	863.70	2679.2	3.1020	17761
0.25119	1388.0	3784.2	2.7263	16046
0.39811	2154.7	5273.0	2.4472	14308
0.63097	3236.5	7292.1	2.2531	12644
1.0000	4744.2	10024	2.1128	11089
1.5850	6832.4	13710	2.0066	9664.6
2.5120	9745.2	18662	1.9149	8380.8
3.9813	13827	25451	1.8406	7275.0
6.3101	19680	34439	1.7499	6286.1
10.001	27949	46265	1.6554	5404.8
15.850	39706	61295	1.5437	4607.7
25.121	56173	80062	1.4253	3893.3
39.813	78707	102450	1.3017	3245.0
63.101	108460	128200	1.1820	2661.2
100.00	145980	155800	1.0673	2135.1

Dynamic Oscillatory T=190 °C

ω	G′	G′′	tan δ	|η*|
0.10000	266.00	1255.8	4.7213	12837
0.15849	473.16	1851.3	3.9126	12056
0.25119	803.58	2673.6	3.3271	11114
0.39811	1313.6	3798.8	2.8918	10097
0.63097	2059.4	5335.1	2.5906	9063.5
1.0000	3133.8	7416.8	2.3667	8051.4
1.5850	4644.6	10241	2.2050	7094.9
2.5120	6710.9	14087	2.0992	6211.7
3.9813	9736.5	19268	1.9790	5422.4
6.3101	13941	26307	1.8871	4718.3
10.001	20012	35602	1.7791	4083.8
15.850	28659	47899	1.6714	3521.6
25.121	40883	63314	1.5487	3000.2
39.813	57936	82505	1.4241	2532.2
63.101	81150	105270	1.2972	2106.4
100.00	111340	130720	1.1741	1717.1

Appendix B. Transient Extensional Rheological Data

B.1. Equistar Petrothene NA952-000 (LDPE)

Transient Uniaxial Extension ($\dot{\varepsilon}$=0.01 s^{-1}) T=150 °C

ε_H	$\tau_{11}-\tau_{22}$	error
0	0	0
0.0136	340.8	57
0.0401	605.3	65
0.0617	732.1	62
0.0870	793.6	44
0.1117	892.1	31
0.1358	937.6	72
0.1593	994.6	41
0.1823	1023	52
0.2085	1088	28
0.2304	1071	50
0.2553	1119	19
0.2797	1139	13
0.3035	1183	28
0.3267	1202	57
0.3494	1222	30
0.3716	1236	43
0.3963	1243	60
0.4205	1277	47
0.4441	1304	72
0.4672	1310	62
0.4897	1327	34
0.5145	1355	52
0.5386	1369	59
0.5622	1390	59
0.5853	1394	96
0.6078	1391	61
0.6298	1383	81
0.6514	1387	70
0.6748	1421	25
0.6977	1458	69
0.7223	1438	55
0.7441	1452	64
0.7697	1502	47
0.7926	1471	76
0.817	1506	60
0.8388	1515	58
0.8641	1532	58
0.8849	1521	88
0.909	1529	68
0.9326	1543	55
0.9573	1591	59
0.9797	1574	61

ε_H	$\tau_{11}-\tau_{22}$	error
1.003	1580	65
1.028	1613	69
1.051	1613	70
1.074	1621	57
1.099	1641	70
1.121	1631	73
1.145	1619	106
1.167	1658	76
1.193	1681	88
1.214	1670	67
1.238	1704	62
1.262	1699	65
1.286	1708	68
1.31	1730	60
1.333	1759	66
1.356	1775	66
1.38	1780	51
1.403	1810	59
1.426	1819	56
1.45	1837	69
1.474	1848	78
1.497	1856	58
1.521	1875	69
1.545	1873	66
1.568	1907	101
1.591	1909	75
1.615	1927	69
1.638	1929	93
1.662	1980	97
1.686	1976	65
1.709	2000	60
1.733	2039	52
1.756	2044	41
1.78	2040	64
1.803	2085	49
1.827	2110	29
1.85	2144	49
1.873	2170	32
1.896	2187	36
1.92	2205	67
1.943	2218	35
1.967	2279	56
1.99	2300	58

ε_H	$\tau_{11}-\tau_{22}$	error
2.014	2313	46
2.037	2338	42
2.061	2420	7
2.084	2420	93
2.108	2486	61
2.132	2504	86
2.155	2544	75
2.178	2562	71
2.202	2591	122
2.226	2632	107
2.249	2676	122
2.272	2684	137
2.296	2818	108
2.319	2816	108
2.343	2851	127
2.366	2898	136
2.39	2954	130
2.413	2897	202
2.436	3033	230
2.46	3034	280
2.483	3080	292
2.507	3145	274
2.53	3187	342
2.553	3221	263
2.577	3321	287
2.6	3426	299
2.624	3510	253
2.648	3549	311
2.671	3596	314
2.694	3699	362
2.718	3702	290
2.741	3813	349
2.765	3875	331
2.788	3971	387
2.812	4016	432
2.831	4107	382
2.859	4249	446
2.882	4369	540
2.906	4468	303
2.929	4565	383
2.952	4591	392
2.976	4704	479

B.1. Equistar Petrothene NA952-000 (LDPE)

Transient Uniaxial Extension ($\dot{\varepsilon}$=0.10 s^{-1}) T=150 °C

ε_H	$\tau_{11}-\tau_{22}$	error
0	0	0
0.0045	1241	242
0.0357	2189	125
0.0574	2780	133
0.0828	3152	184
0.1076	3600	99
0.1318	3993	107
0.1554	4266	32
0.1785	4492	51
0.2048	4809	59
0.2268	5048	25
0.2518	5226	60
0.2728	5373	60
0.2967	5623	38
0.3201	5760	53
0.3429	5951	64
0.3684	6166	67
0.3933	6314	37
0.4145	6443	73
0.4412	6690	96
0.4643	6888	133
0.4869	7021	84
0.5117	7210	77
0.5360	7349	54
0.5596	7527	93
0.5827	7649	51
0.6053	7783	60
0.6274	7897	93
0.6466	7876	32
0.6771	8181	51
0.7022	8403	63
0.7245	8507	60
0.7484	8692	60
0.7718	8850	104
0.7967	9048	72
0.8210	9158	60
0.8447	9318	118
0.8679	9388	82
0.8905	9533	48
0.9145	9642	56
0.9379	9927	101
0.9625	10065	118
0.9848	10250	149

ε_H	$\tau_{11}-\tau_{22}$	error
1.010	10377	57
1.033	10563	83
1.057	10663	110
1.080	10827	76
1.103	11007	100
1.127	11200	70
1.152	11370	122
1.174	11577	131
1.198	11740	70
1.222	11933	71
1.245	12043	99
1.270	12260	130
1.292	12470	72
1.317	12663	87
1.340	12867	117
1.363	13033	117
1.387	13280	151
1.411	13447	159
1.435	13747	274
1.459	13940	252
1.482	14153	261
1.506	14423	294
1.530	14603	293
1.553	14843	266
1.576	15100	312
1.600	15217	146
1.624	15593	284
1.647	15837	315
1.671	16110	320
1.694	16283	210
1.718	16593	164
1.742	16917	232
1.766	17207	214
1.789	17530	282
1.813	17800	243
1.837	18117	257
1.860	18423	293
1.884	18700	295
1.907	19053	275
1.931	19417	298
1.954	19730	327
1.978	20097	323
2.001	20487	352

ε_H	$\tau_{11}-\tau_{22}$	error
2.025	20793	345
2.048	21250	350
2.072	21597	402
2.096	22033	434
2.120	22483	458
2.143	22900	459
2.167	23343	482
2.191	23757	499
2.214	24203	556
2.238	24593	544
2.261	25193	613
2.285	25733	615
2.309	26187	673
2.333	26677	769
2.356	27193	759
2.380	27733	863
2.402	28123	786
2.427	28907	980
2.451	29470	991
2.474	30037	1071
2.498	30633	1138
2.521	31187	1219
2.545	31873	1240
2.568	32483	1311
2.592	33180	1481
2.616	33857	1531
2.640	34493	1593
2.663	35167	1649
2.687	35800	1841
2.710	36513	1988
2.734	37223	2032
2.757	37897	2183
2.781	38693	2271
2.805	39517	2408
2.828	40267	2589
2.852	41033	2784
2.876	41773	2883
2.899	42537	3026
2.923	43167	3052
2.947	44060	3283
2.970	44823	3438
2.994	45507	3629

B.1. Equistar Petrothene NA952-000 (LDPE)

Transient Uniaxial Extension ($\dot{\varepsilon}$=1.00 s^{-1}) T=150 °C

ε_H	$\tau_{11}-\tau_{22}$	error
0	0	0
0.0136	1487	604
0.0403	5567	103
0.0620	7678	1581
0.0874	8269	1787
0.1122	10913	524
0.1364	12708	1093
0.1600	14368	675
0.1831	15293	136
0.2056	16653	801
0.2313	17583	433
0.2528	18598	345
0.2774	19520	484
0.3013	20303	430
0.3247	21228	400
0.3475	21943	553
0.3698	22565	717
0.3917	23350	639
0.4161	24038	702
0.4399	24553	775
0.4631	25638	783
0.4859	26338	793
0.5108	27115	848
0.5325	27810	839
0.5563	28483	860
0.5796	29178	892
0.6024	29890	890
0.6246	30498	902
0.6488	31225	962
0.6677	31708	904
0.6931	32243	1008
0.7180	33700	1176
0.7400	34205	909
0.7637	34695	1019
0.7868	35818	1167
0.8114	36648	1126
0.8335	37393	1086
0.8570	37993	1093
0.8800	38778	1192
0.9025	39560	1138
0.9263	40288	1180
0.9495	41213	1277
0.9740	42215	1282

ε_H	$\tau_{11}-\tau_{22}$	error
0.9961	43005	1263
1.019	43898	1302
1.044	44868	1309
1.066	45785	1454
1.089	46605	1466
1.112	47523	1534
1.136	48653	1562
1.159	49605	1553
1.183	50653	1610
1.205	51603	1615
1.228	52648	1659
1.252	53775	1716
1.275	54958	1750
1.299	56085	1763
1.323	57313	1853
1.346	58543	1847
1.369	59808	1883
1.392	61075	1941
1.414	62300	1969
1.439	63700	2050
1.462	65173	2078
1.485	66523	2082
1.509	67910	2163
1.532	69485	2225
1.555	71000	2251
1.578	72525	2305
1.601	74175	2373
1.625	75865	2427
1.648	77638	2488
1.671	79378	2547
1.694	81215	2605
1.718	83160	2645
1.740	85008	2695
1.764	87155	2836
1.787	89215	2844
1.811	91295	2950
1.834	93465	3026
1.857	95708	3049
1.880	97913	3097
1.903	100200	3197
1.927	102593	3303
1.950	105200	3371
1.973	107625	3329

ε_H	$\tau_{11}-\tau_{22}$	error
1.996	110200	3534
2.019	112975	3610
2.043	115625	3654
2.066	118450	3781
2.089	121325	3857
2.113	124250	3977
2.136	127450	4058
2.159	130450	4093
2.182	133625	4176
2.206	136850	4302
2.229	140075	4418
2.252	143400	4418
2.275	146900	4580
2.298	150350	4657
2.322	153950	4779
2.345	157675	4901
2.368	161375	4982
2.392	165050	5063
2.415	168875	5144
2.438	172600	5267
2.461	176625	5432
2.485	180600	5436
2.508	184575	5607
2.531	188475	5729
2.554	192650	5778
2.578	196675	5956
2.601	200875	6085
2.624	205100	6185
2.648	209200	6297
2.671	213200	6430
2.694	217475	6584
2.717	221575	6748
2.740	225850	7027
2.763	229800	7088
2.787	233775	7295
2.810	238100	7555
2.833	242050	7845
2.856	245850	8053
2.880	249725	8401
2.903	253625	8628
2.926	257175	8954
2.949	260925	9405

B.2. ExxonMobil NTX101 (LLDPE)

Transient Uniaxial Extension ($\dot{\varepsilon}$=0.01 s^{-1}) T=150 °C

ε_H	$\tau_{11}-\tau_{22}$	error
0	0	0
0.0169	507.9	95
0.0401	650.8	43
0.0649	681.9	51
0.0901	707.0	48
0.1127	693.1	35
0.1358	676.2	33
0.1622	703.9	49
0.1852	721.9	22
0.2085	740.1	50
0.2331	740.5	47
0.2571	723.6	33
0.2797	724.6	53
0.3026	739.3	36
0.3259	731.6	43
0.3502	764.2	58
0.3739	741.1	11
0.3986	731.7	18
0.4220	758.1	37
0.4463	766.3	41
0.4693	744.6	25
0.4918	739.2	34
0.5165	736.1	10
0.5406	738.3	26
0.5642	751.2	26
0.5872	714.0	29
0.6103	736.6	61
0.6340	733.8	27
0.6555	721.9	11
0.6794	747.1	35
0.7039	744.9	35
0.7278	718.9	23
0.7500	704.7	9
0.7728	697.3	21
0.7982	743.5	14
0.8220	727.6	25
0.8447	743.2	22
0.8688	712.5	22
0.8919	702.1	8
0.9154	718.0	33
0.9392	705.5	15
0.9629	714.7	13
0.9865	731.1	15

ε_H	$\tau_{11}-\tau_{22}$	error
1.010	725.6	28
1.034	702.7	18
1.057	734.6	20
1.080	718.8	9
1.104	735.9	34
1.128	710.4	6
1.151	734.4	19
1.174	721.6	15
1.198	744.5	29
1.222	741.7	22
1.245	734.2	33
1.268	733.3	39
1.292	717.8	24
1.316	720.9	15
1.339	713.4	9
1.362	734.4	46
1.386	711.0	23
1.410	697.5	26
1.433	723.4	9
1.457	742.7	27
1.480	728.2	11
1.504	738.1	13
1.528	714.4	35
1.551	737.6	8
1.575	712.3	18
1.598	731.3	15
1.622	723.1	13
1.646	728.5	13
1.669	721.4	17
1.692	716.8	19
1.716	704.8	25
1.740	729.8	27
1.763	711.6	17
1.787	702.2	24
1.810	721.2	25
1.834	712.1	37
1.857	713.1	48
1.881	710.4	26
1.904	702.4	55
1.928	721.5	41
1.951	713.0	53
1.975	721.4	47
1.999	711.8	52

ε_H	$\tau_{11}-\tau_{22}$	error
2.022	732.5	54
2.046	747.9	47
2.069	734.5	71
2.093	709.6	48
2.116	713.7	51
2.140	711.8	43
2.164	728.7	40
2.187	712.1	49
2.211	718.5	28
2.234	675.3	59
2.257	686.9	50
2.281	672.9	47
2.304	664.3	32
2.328	671.8	60
2.351	675.7	52
2.375	696.3	46
2.398	688.8	41
2.422	673.4	34
2.445	670.7	57
2.469	705.7	43
2.493	683.9	57
2.516	690.0	63
2.540	710.6	50
2.563	670.9	97
2.587	690.4	102
2.610	702.7	97
2.634	701.6	97
2.657	749.8	81
2.681	732.2	108
2.704	708.7	91
2.728	745.3	46
2.751	690.3	56
2.775	689.2	43
2.799	712.0	71
2.822	736.9	10
2.846	697.1	41
2.869	756.2	77
2.893	745.8	41
2.916	745.4	26
2.940	754.6	42
2.963	756.4	40
2.987	764.4	27

B.2. ExxonMobil NTX101 (LLDPE)

Transient Uniaxial Extension ($\dot{\varepsilon}$=0.10 s^{-1}) T=150 °C

ε_H	$\tau_{11}-\tau_{22}$	error
0	0	0
0.0079	1294	1486
0.0225	3044	2190
0.0638	5510	191
0.0869	5665	393
0.1126	5598	207
0.1357	5704	293
0.1592	5671	216
0.1821	5934	41
0.2074	6039	66
0.2311	6001	126
0.2551	6047	94
0.2777	6129	155
0.3015	6133	204
0.3247	6116	122
0.3482	6503	316
0.3728	6449	94
0.3960	6173	153
0.4201	6499	292
0.4452	6475	108
0.4682	6516	124
0.4913	6421	58
0.5154	6538	83
0.5395	6551	123
0.5630	6510	232
0.5867	6526	240
0.6097	6466	255
0.6341	6657	136
0.6556	6467	277
0.6783	6770	299
0.7033	6693	110
0.7272	6731	164
0.7489	6427	185
0.7728	6594	270
0.7981	6781	183
0.8218	6689	175
0.8450	6653	179
0.8691	6571	45
0.8917	6685	152
0.9152	6648	243
0.9394	6762	70
0.9635	6756	156
0.9875	6741	67
1.011	6708	159
1.034	6552	282
1.058	6693	135
1.081	6739	223
1.105	6727	211
1.129	6935	102
1.152	6563	149
1.176	6790	232
1.200	6731	170
1.224	6879	134
1.247	6906	173
1.271	6867	144
1.295	6796	75
1.319	6941	152
1.342	6909	140
1.366	6764	135
1.389	6911	200
1.413	6830	137
1.437	6961	74
1.460	6874	183
1.484	6859	216
1.508	6860	223
1.532	6907	60
1.555	6898	152
1.579	6827	82
1.602	6819	72
1.626	6896	119
1.650	6811	188
1.674	6870	177
1.697	6893	135
1.721	6874	101
1.745	6870	184
1.768	6891	122
1.792	6847	135
1.816	6877	185
1.839	6825	143
1.863	6840	106
1.886	6767	129
1.910	6859	180
1.934	6854	140
1.957	6859	107
1.981	6916	145
2.004	6864	160
2.028	6802	182
2.051	6840	112
2.075	6842	156
2.099	6848	178
2.123	6847	218
2.146	6789	176
2.170	6851	181
2.194	6764	84
2.217	6823	146
2.241	6771	189
2.265	6777	235
2.288	6774	182
2.312	6740	284
2.335	6731	186
2.359	6660	218
2.383	6690	128
2.406	6685	250
2.430	6692	179
2.454	6682	186
2.477	6616	217
2.501	6643	161
2.524	6591	165
2.548	6565	127
2.572	6618	154
2.596	6604	127
2.619	6505	160
2.643	6550	151
2.667	6427	167
2.690	6377	115
2.714	6401	102
2.737	6376	138
2.761	6415	127
2.785	6425	56
2.808	6434	118
2.832	6300	100
2.856	6233	120
2.879	6289	104
2.903	6153	174
2.927	6150	162
2.950	6173	273
2.974	6111	216
2.995	5998	226

B.2. ExxonMobil NTX101 (LLDPE)

Transient Uniaxial Extension ($\dot{\varepsilon}$=1.00 s^{-1}) T=150 °C

ε_H	$\tau_{11}-\tau_{22}$	error
0	0	0
0.0165	4676	393
0.0386	18433	161
0.0631	22860	215
0.0870	24690	715
0.1103	28633	398
0.1332	31327	502
0.1580	32880	590
0.1811	33607	900
0.2048	35993	464
0.2280	37183	378
0.2518	37920	461
0.2763	39197	365
0.3001	40080	165
0.3223	40697	355
0.3462	41440	489
0.3684	42430	227
0.3912	43000	234
0.4155	43103	154
0.4383	44720	121
0.4624	44910	456
0.4850	45357	301
0.5099	46170	317
0.5324	46813	165
0.5553	46860	104
0.5785	47493	497
0.6020	47677	158
0.6258	48027	90
0.6474	48260	252
0.6702	48303	114
0.6939	48943	114
0.7178	50363	307
0.7398	49440	214
0.7634	49563	400
0.7871	50827	83
0.8096	51420	62
0.8336	51337	101
0.8570	51587	226
0.8799	52063	205
0.9023	51817	85
0.9259	52143	178
0.9491	53053	270
0.9734	53333	133

ε_H	$\tau_{11}-\tau_{22}$	error
0.9961	53103	49
1.020	53630	185
1.043	53573	110
1.065	53497	236
1.089	53950	131
1.113	54553	129
1.136	54547	100
1.159	54747	256
1.182	54460	122
1.205	54867	142
1.229	55887	261
1.252	55790	105
1.275	55493	188
1.299	56243	247
1.322	56190	110
1.345	56050	184
1.368	56397	285
1.392	56423	280
1.415	56610	313
1.438	56737	81
1.461	56630	257
1.485	56700	269
1.508	56890	182
1.532	57060	296
1.555	56957	359
1.578	57040	291
1.601	56870	231
1.624	56980	380
1.647	57133	425
1.671	56897	346
1.694	56963	300
1.718	56800	440
1.741	56900	382
1.764	56997	418
1.787	56853	499
1.811	56580	497
1.834	56737	526
1.857	56430	582
1.880	56187	613
1.904	56050	633
1.927	56347	462
1.950	56213	716
1.973	55940	772

ε_H	$\tau_{11}-\tau_{22}$	error
1.997	55903	857
2.020	55697	918
2.043	55377	940
2.066	55233	997
2.089	54900	1083
2.113	54667	1210
2.136	54563	1267
2.159	54057	1347
2.183	53727	1452
2.206	53437	1551
2.229	52877	1634
2.252	52663	1734
2.276	52230	1771
2.299	51783	1971
2.322	51310	2051
2.346	50897	2196
2.369	50363	2286
2.392	49763	2469
2.415	49110	2557
2.439	48550	2664
2.462	48060	2811
2.485	47443	2955
2.508	46707	3129
2.531	45913	3181
2.555	45453	3312
2.578	44693	3455
2.601	43933	3691
2.625	43270	3871
2.648	42387	3985
2.671	41527	4300
2.694	40693	4370
2.718	39867	4550
2.741	39003	4770
2.764	37977	4781
2.787	36977	5063
2.810	36030	5110
2.834	35083	5135
2.857	34100	5292
2.880	33143	5395
2.904	31980	5610
2.927	31130	5609
2.950	30097	5702

B.3. ExxonMobil Exact 0201 (mBLDPE)

Transient Uniaxial Extension ($\dot{\varepsilon}$=0.01 s^{-1}) T=150 °C

ε_H	$\tau_{11}-\tau_{22}$	error
0	0	0
0.0234	208.2	90
0.0469	708.6	102
0.0703	806.0	91
0.0938	933.4	36
0.1172	1011	23
0.1406	1037	30
0.1641	1072	23
0.1875	1089	20
0.2109	1104	26
0.2344	1101	42
0.2578	1136	39
0.2813	1137	20
0.3047	1141	49
0.3281	1167	12
0.3516	1217	17
0.3750	1213	27
0.3984	1216	62
0.4219	1199	37
0.4453	1215	19
0.4688	1235	13
0.4922	1235	11
0.5156	1253	17
0.5391	1272	17
0.5625	1262	49
0.5859	1247	26
0.6094	1278	42
0.6328	1258	12
0.6563	1268	53
0.6797	1266	20
0.7031	1272	32
0.7266	1279	11
0.7500	1287	12
0.7734	1297	33
0.7969	1305	57
0.8203	1293	40
0.8438	1298	38
0.8672	1326	66
0.8906	1299	46
0.9141	1297	50
0.9375	1330	55
0.9610	1334	66
0.9844	1342	53

ε_H	$\tau_{11}-\tau_{22}$	error
1.008	1323	48
1.031	1328	38
1.055	1338	70
1.078	1360	49
1.102	1366	66
1.125	1363	53
1.149	1348	31
1.172	1323	66
1.195	1346	95
1.219	1374	20
1.242	1374	68
1.266	1368	61
1.289	1358	56
1.313	1350	64
1.336	1364	58
1.359	1369	66
1.383	1371	66
1.406	1368	63
1.43	1381	63
1.453	1386	49
1.477	1376	63
1.5	1385	71
1.524	1394	80
1.547	1411	87
1.57	1421	86
1.594	1401	61
1.617	1416	93
1.641	1401	83
1.664	1385	82
1.688	1408	74
1.711	1394	112
1.734	1398	71
1.758	1409	97
1.781	1407	79
1.805	1400	56
1.828	1422	82
1.852	1401	58
1.875	1394	73
1.899	1396	62
1.922	1412	58
1.945	1408	54
1.969	1403	61
1.992	1398	67

ε_H	$\tau_{11}-\tau_{22}$	error
2.016	1405	51
2.039	1411	29
2.063	1382	64
2.086	1431	51
2.109	1415	53
2.133	1409	69
2.156	1426	92
2.18	1429	58
2.203	1433	51
2.227	1408	69
2.25	1423	56
2.274	1417	14
2.297	1431	64
2.32	1425	72
2.344	1432	43
2.367	1420	63
2.391	1438	54
2.414	1433	39
2.438	1445	34
2.461	1451	58
2.484	1441	61
2.508	1415	71
2.531	1405	84
2.555	1448	73
2.578	1408	32
2.602	1401	32
2.625	1428	38
2.648	1446	40
2.672	1407	61
2.695	1395	42
2.719	1410	35
2.742	1383	40
2.766	1423	66
2.789	1422	77
2.813	1453	56
2.836	1402	64
2.859	1387	85
2.883	1416	57
2.906	1403	48
2.930	1449	43
2.953	1447	79
2.977	1442	19

B.3. ExxonMobil Exact 0201 (mBLDPE)

Transient Uniaxial Extension ($\dot{\varepsilon}$=0.10 s^{-1}) T=150 °C

ε_H	$\tau_{11}-\tau_{22}$	error
0	0	0
0.0234	1741	615
0.0469	2723	447
0.0703	3637	554
0.0938	4689	882
0.1172	4716	621
0.1406	5355	888
0.1641	5903	932
0.1875	5995	1099
0.2109	6222	742
0.2344	6295	746
0.2578	6513	921
0.2813	6476	791
0.3047	6550	833
0.3281	6717	872
0.3516	6983	1033
0.3750	7052	1038
0.3984	7202	1153
0.4219	7406	1054
0.4453	7378	930
0.4688	7580	970
0.4922	7670	936
0.5156	7794	929
0.5391	7878	948
0.5625	7987	1025
0.5859	8112	908
0.6094	8143	992
0.6328	8128	886
0.6563	8331	880
0.6797	8499	1058
0.7031	8462	1064
0.7266	8568	888
0.7500	8785	889
0.7734	8914	921
0.7969	8969	881
0.8203	8887	953
0.8438	9091	923
0.8672	9116	790
0.8906	9152	909
0.9141	9198	820
0.9375	9287	981
0.9610	9324	884
0.9844	9538	848

ε_H	$\tau_{11}-\tau_{22}$	error
1.008	9617	801
1.031	9634	860
1.055	9779	794
1.078	9752	833
1.102	9869	753
1.125	9891	756
1.149	9990	668
1.172	9946	787
1.195	10067	686
1.219	10160	734
1.242	10241	635
1.266	10305	756
1.289	10446	796
1.313	10419	800
1.336	10610	745
1.359	10691	764
1.383	10715	784
1.406	10815	741
1.430	10830	735
1.453	10815	669
1.477	10890	695
1.500	11005	550
1.524	11048	549
1.547	11095	518
1.570	11138	574
1.594	11188	614
1.617	11320	573
1.641	11313	545
1.664	11358	657
1.688	11515	611
1.711	11543	661
1.734	11663	552
1.758	11738	640
1.781	11775	560
1.805	11853	627
1.828	11945	554
1.852	11918	646
1.875	12070	609
1.899	12135	552
1.922	12158	513
1.945	12288	526
1.969	12293	560
1.992	12515	493

ε_H	$\tau_{11}-\tau_{22}$	error
2.016	12563	613
2.039	12583	554
2.063	12745	555
2.086	12793	575
2.109	12893	590
2.133	13133	536
2.156	13193	592
2.180	13248	577
2.203	13373	447
2.227	13403	652
2.250	13478	610
2.274	13645	551
2.297	13625	488
2.320	13738	460
2.344	13835	501
2.367	13890	482
2.391	14090	660
2.414	14190	443
2.438	14288	507
2.461	14350	530
2.484	14430	407
2.508	14485	505
2.531	14628	423
2.555	14695	388
2.578	14803	365
2.602	14948	378
2.625	14983	373
2.649	15118	383
2.672	15128	328
2.695	15215	226
2.719	15410	303
2.742	15350	207
2.766	15415	119
2.789	15490	121
2.813	15595	131
2.836	15678	152
2.860	15745	208
2.883	15770	132
2.906	15865	258
2.930	15925	288
2.953	15955	428
2.977	16030	612

B.3. ExxonMobil Exact 0201 (mBLDPE)

Transient Uniaxial Extension ($\dot{\varepsilon}$=1.00 s^{-1}) T=150 °C

ε_H	$\tau_{11}-\tau_{22}$	error
0	0	0
0.0180	3780	214
0.0401	15688	1665
0.0617	20825	1598
0.0870	21940	1145
0.1117	25518	804
0.1358	28283	990
0.1593	29295	792
0.1823	30593	1370
0.2048	32415	1368
0.2304	34103	1558
0.2518	35375	898
0.2763	36470	862
0.3001	37653	992
0.3234	38725	953
0.3462	39495	1014
0.3684	40478	862
0.3933	41485	1039
0.4145	42235	865
0.4383	43220	680
0.4643	44710	841
0.4869	45143	753
0.5090	46015	818
0.5333	46903	709
0.5570	47718	710
0.5802	48295	768
0.6028	48755	689
0.6250	49525	1053
0.6466	50308	1173
0.6702	49743	1451
0.6954	51173	946
0.7178	53060	1088
0.7398	52270	1290
0.7634	52665	771
0.7864	54175	809
0.8109	54558	813
0.8329	55050	535
0.8583	55535	604
0.8792	55958	518
0.9035	56220	578
0.9271	56930	478
0.9503	57605	485
0.9728	58188	490

ε_H	$\tau_{11}-\tau_{22}$	error
0.9966	58713	559
1.020	59145	526
1.044	59903	436
1.066	60215	421
1.089	60360	441
1.114	61048	544
1.137	61868	398
1.160	62090	445
1.183	62500	427
1.206	62943	494
1.229	63410	366
1.253	64070	509
1.276	64563	358
1.300	64873	504
1.323	65493	332
1.346	65983	471
1.369	66588	307
1.392	66925	136
1.415	67710	505
1.439	68348	488
1.462	68678	330
1.486	69015	338
1.509	69438	398
1.532	70003	309
1.555	70388	447
1.578	70830	407
1.601	71325	347
1.625	71810	389
1.648	72360	300
1.671	72845	406
1.695	73390	311
1.718	73873	282
1.741	74313	280
1.765	75050	188
1.788	75575	299
1.811	75860	276
1.835	76333	281
1.858	77003	228
1.881	77253	297
1.904	77693	287
1.928	78388	188
1.950	78943	253
1.974	79283	335

ε_H	$\tau_{11}-\tau_{22}$	error
1.997	79885	184
2.020	80500	332
2.044	81235	346
2.067	81805	262
2.090	82430	608
2.114	82940	127
2.137	83760	170
2.160	84310	594
2.183	84770	184
2.206	85365	290
2.230	85905	346
2.253	86590	311
2.276	87450	85
2.299	87780	396
2.323	88315	205
2.346	89135	163
2.369	89670	396
2.393	90590	170
2.416	91165	813
2.439	91290	368
2.462	92675	163
2.486	92945	757
2.509	93040	396
2.532	93705	502
2.555	94985	445
2.578	95095	205
2.602	95950	240
2.625	97120	806
2.648	97420	1061
2.672	97470	467
2.695	98295	799
2.718	98840	1032
2.741	99040	721
2.765	99330	665
2.788	99635	516
2.811	99915	64
2.834	99950	71
2.858	100800	566
2.881	101000	849
2.904	100600	283
2.927	101150	212
2.951	101200	141

B.4. ExxonMobil Exact 3132 (mLLDPE)

Transient Uniaxial Extension ($\dot{\varepsilon}$=0.0316 s^{-1}) T=150 °C

ε_H	$\tau_{11}-\tau_{22}$	error
0	0	0
0.0135	422.1	490
0.0401	667.7	718
0.0617	1393	498
0.0870	1493	194
0.1117	1551	97
0.1358	1622	151
0.1593	1515	175
0.1823	1692	232
0.2085	1560	205
0.2304	1579	136
0.2553	1677	66
0.2797	1667	119
0.3035	1598	175
0.3267	1613	173
0.3494	1630	80
0.3716	1437	215
0.3963	1695	221
0.4205	1646	149
0.4470	1681	77
0.4700	1656	172
0.4925	1587	119
0.5172	1590	99
0.5413	1620	112
0.5648	1589	105
0.5878	1563	80
0.6127	1616	63
0.6347	1544	110
0.6395	1656	449
0.6886	1582	475
0.7134	1547	90
0.7354	1528	161
0.7591	1579	142
0.7843	1588	44
0.8069	1609	117
0.8309	1519	173
0.8544	1587	143
0.8792	1568	69
0.9016	1573	206
0.9253	1563	168
0.9503	1574	109
0.9728	1543	146
0.9966	1570	127
1.021	1562	66
1.044	1593	113
1.068	1543	117
1.093	1604	140
1.115	1578	102
1.140	1506	134
1.163	1520	133
1.187	1575	75
1.210	1539	58
1.234	1514	83
1.258	1515	109
1.282	1587	125
1.306	1670	186
1.329	1581	101
1.353	1482	143
1.376	1525	92
1.400	1571	116
1.424	1580	137
1.448	1613	99
1.471	1528	78
1.495	1524	119
1.519	1527	105
1.543	1559	69
1.567	1565	142
1.590	1561	78
1.614	1593	124
1.637	1522	101
1.661	1539	81
1.685	1568	96
1.708	1534	126
1.732	1559	140
1.756	1586	103
1.780	1580	101
1.804	1516	121
1.827	1551	122
1.851	1550	115
1.875	1525	137
1.898	1523	141
1.922	1551	119
1.945	1549	110
1.968	1533	114
1.992	1536	157
2.016	1595	132
2.039	1536	155
2.063	1534	113
2.087	1588	149
2.111	1623	141
2.135	1542	109
2.158	1546	115
2.182	1544	96
2.206	1544	117
2.229	1607	184
2.253	1518	188
2.276	1537	91
2.300	1566	116
2.324	1613	125
2.347	1561	140
2.371	1575	168
2.395	1564	107
2.417	1596	153
2.441	1628	172
2.465	1576	124
2.488	1593	153
2.511	1562	112
2.535	1607	146
2.559	1622	159
2.583	1635	162
2.607	1591	121
2.631	1583	141
2.654	1606	127
2.678	1585	106
2.701	1585	160
2.725	1586	121
2.748	1594	127
2.772	1645	138
2.796	1659	161
2.819	1647	108
2.843	1655	133
2.867	1629	125
2.891	1646	151
2.913	1735	93
2.937	1833	221
2.960	1816	191
2.984	1794	221
3.002	1896	213

B.4. ExxonMobil Exact 3132 (mLLDPE)

Transient Uniaxial Extension ($\dot{\varepsilon}$=0.10 s^{-1}) T=150 °C

ε_H	$\tau_{11}-\tau_{22}$	error
0	0	0
0.0136	3319	651
0.0403	4168	294
0.0663	4734	358
0.0916	4933	438
0.1163	5037	204
0.1404	5106	165
0.1639	5405	196
0.1869	5211	501
0.2130	5442	134
0.2349	5180	242
0.2599	5290	216
0.2843	5167	288
0.3080	5054	260
0.3312	5083	134
0.3539	5071	344
0.3792	5214	302
0.4009	4992	156
0.4251	5134	109
0.4487	5132	178
0.4717	5177	69
0.4970	5064	201
0.5217	5094	121
0.5432	4991	197
0.5668	5106	121
0.5923	4946	100
0.6148	5037	58
0.6392	5173	102
0.6607	5235	83
0.6840	4798	316
0.7090	4952	196
0.7312	4852	213
0.7551	5119	191
0.7784	5095	40
0.8033	4874	396
0.8255	4984	134
0.8493	4974	41
0.8743	4875	72
0.8969	4738	29
0.9208	4918	159
0.9442	4840	218
0.9688	5113	64
0.9927	4935	125

ε_H	$\tau_{11}-\tau_{22}$	error
1.016	4910	164
1.039	4846	150
1.063	4809	53
1.086	4839	102
1.111	4978	113
1.133	4695	295
1.158	4934	113
1.180	4806	126
1.204	4777	182
1.228	4743	229
1.251	4654	99
1.275	4499	113
1.299	4689	132
1.323	4595	193
1.347	4683	227
1.370	4932	121
1.394	4768	179
1.417	4643	214
1.441	4700	67
1.465	4598	192
1.488	4752	230
1.513	4724	167
1.536	4585	104
1.560	4593	178
1.584	4515	242
1.607	4690	165
1.630	4673	219
1.654	4598	90
1.677	4607	184
1.701	4474	106
1.724	4617	227
1.748	4758	134
1.773	4628	211
1.796	4574	188
1.820	4678	199
1.843	4535	154
1.867	4562	208
1.890	4485	269
1.914	4475	194
1.937	4651	122
1.961	4543	222
1.984	4662	70
2.008	4592	227

ε_H	$\tau_{11}-\tau_{22}$	error
2.032	4640	140
2.055	4636	173
2.079	4661	101
2.103	4726	209
2.126	4646	55
2.150	4622	64
2.174	4579	131
2.197	4622	237
2.220	4519	309
2.244	4552	19
2.267	4635	171
2.291	4661	253
2.315	4642	187
2.338	4565	28
2.362	4603	193
2.385	4654	284
2.409	4790	288
2.433	4720	126
2.456	4725	232
2.480	4704	269
2.503	4746	317
2.527	4706	79
2.551	4725	122
2.574	4828	195
2.598	4812	175
2.622	4664	34
2.646	4694	259
2.669	4753	174
2.692	4624	200
2.716	4748	205
2.740	4713	160
2.763	4716	157
2.787	4856	47
2.811	4870	278
2.834	4758	42
2.858	4722	94
2.881	4744	218
2.905	4881	251
2.929	4825	56
2.953	4851	54
2.976	4818	196
3.000	4781	72

B.4. ExxonMobil Exact 3132 (mLLDPE)

Transient Uniaxial Extension ($\dot{\varepsilon}$=1.00 s^{-1}) T=150 °C

ε_H	$\tau_{11}-\tau_{22}$	error
0	0	0
0.0165	6012	1822
0.0408	19724	10154
0.0645	27333	2054
0.0877	30123	1391
0.1103	35258	439
0.1361	37080	1148
0.1577	39615	1728
0.1823	39740	260
0.2063	40568	377
0.2298	41815	437
0.2527	42425	502
0.2751	42685	267
0.2970	43523	237
0.3215	43465	400
0.3424	43375	688
0.3687	45115	331
0.3915	44943	353
0.4138	45058	547
0.4383	45625	209
0.4622	45533	332
0.4855	45400	345
0.5083	45495	371
0.5306	45333	281
0.5524	45493	314
0.5738	44233	800
0.5970	44640	1470
0.6219	46958	476
0.6462	45825	1017
0.6678	44708	840
0.6911	45993	630
0.7158	46193	485
0.7380	45985	350
0.7616	45813	424
0.7847	46268	418
0.8072	45468	600
0.8311	45578	478
0.8544	45913	391
0.8772	45970	550
0.9012	45930	398
0.9246	45668	410
0.9475	46015	429
0.9714	46153	559

ε_H	$\tau_{11}-\tau_{22}$	error
0.9933	45575	556
1.018	45623	592
1.040	46045	524
1.063	45605	626
1.087	45585	548
1.110	45333	648
1.133	45133	633
1.157	45388	566
1.180	45700	570
1.203	44900	816
1.226	45200	699
1.249	45273	656
1.273	44955	742
1.296	44745	680
1.320	44715	681
1.343	44678	755
1.366	44673	719
1.389	44480	775
1.412	43998	813
1.436	44273	722
1.459	44083	752
1.483	43783	796
1.505	43755	756
1.529	43480	796
1.552	43408	861
1.576	43508	661
1.599	43420	791
1.622	43198	869
1.645	42850	995
1.668	42828	811
1.692	43015	878
1.715	42485	975
1.738	42130	895
1.761	42268	908
1.784	41748	956
1.808	41415	971
1.831	41473	931
1.854	41228	1032
1.878	40765	1030
1.900	40565	997
1.924	40413	1020
1.947	40078	1028
1.970	39800	1077

ε_H	$\tau_{11}-\tau_{22}$	error
1.993	39555	1095
2.017	39298	1091
2.040	39180	1118
2.063	38815	1144
2.087	38390	1102
2.110	38193	1152
2.133	37655	1178
2.156	37038	1052
2.179	37268	1213
2.203	36818	1283
2.226	36330	1135
2.249	36203	1192
2.273	35810	1193
2.296	35388	1314
2.319	35030	1375
2.342	34478	1369
2.365	34213	1345
2.389	33825	1392
2.412	33323	1425
2.435	33098	1565
2.458	32373	1441
2.481	32010	1456
2.505	31518	1517
2.528	31050	1519
2.551	30618	1568
2.575	30093	1564
2.598	29638	1593
2.621	29063	1694
2.644	28653	1667
2.667	28205	1597
2.690	27653	1693
2.714	27225	1597
2.737	26708	1748
2.760	26268	1733
2.783	25728	1744
2.807	25175	1831
2.830	24550	1831
2.853	24080	1861
2.876	23583	1768
2.900	23193	1912
2.923	22675	1896
2.946	21990	1891

B.5. Dow Affinity PL1840 (mBLDPE)

Transient Uniaxial Extension ($\dot{\varepsilon}$=0.01 s^{-1}) T=150 °C

ε_H	$\tau_{11}-\tau_{22}$	error
0	0	0
0.0120	581.6	101
0.0371	841.8	40
0.0602	1026	94
0.0841	1072	120
0.1088	1079	107
0.1330	1138	87
0.1565	1196	92
0.1795	1154	104
0.2020	1211	105
0.2265	1235	85
0.2491	1236	77
0.2736	1260	59
0.2975	1263	43
0.3197	1259	46
0.3436	1299	49
0.3680	1335	78
0.3907	1330	85
0.4150	1333	65
0.4387	1346	36
0.4618	1346	60
0.4863	1344	30
0.5093	1351	50
0.5336	1339	47
0.5572	1351	54
0.5804	1335	41
0.6030	1327	40
0.6275	1354	57
0.6467	1325	55
0.6725	1359	53
0.6977	1375	34
0.7200	1376	31
0.7426	1345	56
0.7661	1340	57
0.7904	1373	48
0.8148	1383	52
0.8373	1376	65
0.8612	1376	27
0.8846	1350	64
0.9075	1379	30
0.9310	1393	46
0.9557	1365	32
0.9782	1381	13

ε_H	$\tau_{11}-\tau_{22}$	error
1.002	1407	29
1.025	1368	27
1.049	1384	27
1.072	1373	56
1.096	1369	44
1.120	1381	38
1.143	1373	33
1.166	1411	15
1.190	1387	23
1.213	1402	41
1.237	1386	68
1.260	1395	26
1.284	1411	34
1.308	1423	20
1.331	1412	24
1.355	1408	40
1.378	1408	40
1.402	1419	55
1.425	1413	23
1.449	1396	36
1.472	1403	29
1.496	1436	45
1.519	1416	18
1.543	1426	32
1.566	1399	40
1.590	1427	45
1.613	1415	22
1.637	1424	22
1.661	1425	31
1.684	1400	24
1.707	1419	26
1.731	1416	35
1.755	1419	22
1.778	1416	32
1.802	1423	36
1.825	1414	28
1.849	1408	47
1.872	1420	16
1.896	1429	21
1.919	1405	36
1.943	1409	52
1.966	1420	21
1.990	1419	34

ε_H	$\tau_{11}-\tau_{22}$	error
2.013	1424	44
2.037	1423	56
2.060	1426	28
2.083	1424	39
2.107	1440	19
2.131	1443	30
2.154	1448	36
2.178	1440	13
2.201	1446	20
2.224	1481	22
2.247	1482	31
2.270	1428	30
2.292	1425	32
2.315	1425	19
2.339	1424	54
2.362	1410	34
2.386	1405	23
2.409	1399	26
2.433	1402	41
2.456	1426	65
2.480	1439	51
2.503	1420	32
2.527	1428	43
2.551	1429	48
2.574	1412	51
2.597	1402	29
2.621	1409	27
2.644	1402	49
2.668	1445	37
2.691	1403	53
2.715	1390	55
2.738	1388	55
2.762	1394	78
2.785	1362	81
2.809	1380	59
2.832	1365	87
2.856	1407	116
2.879	1389	45
2.902	1330	74
2.926	1373	99
2.949	1355	169
2.973	1358	103

B.5. Dow Affinity PL1840 (mBLDPE)

Transient Uniaxial Extension ($\dot{\varepsilon}$=0.10 s^{-1}) T=150 °C

ε_H	$\tau_{11}-\tau_{22}$	error
0	0	0
0.0150	2812	442
0.0401	4013	391
0.0645	5003	305
0.0884	5547	114
0.1117	5953	462
0.1371	6334	298
0.1606	6582	525
0.1848	7098	354
0.2085	7342	278
0.2340	7362	306
0.2577	7750	223
0.2797	7811	269
0.3035	8021	267
0.3289	8131	226
0.3515	8330	173
0.3747	8564	209
0.3984	8560	184
0.4225	8764	309
0.4470	9007	328
0.4700	9047	309
0.4953	9226	192
0.5172	9261	351
0.5413	9331	237
0.5648	9503	318
0.5895	9584	346
0.6127	9577	293
0.6355	9612	338
0.6545	9673	70
0.6810	10128	159
0.7052	9992	356
0.7281	10009	352
0.7513	10282	259
0.7746	10129	391
0.7994	10320	255
0.8230	10420	239
0.8460	10347	112
0.8698	10323	156
0.8936	10533	214
0.9175	10587	182
0.9408	10630	115
0.9654	10840	173
0.9888	10900	249

ε_H	$\tau_{11}-\tau_{22}$	error
1.012	10823	107
1.036	10940	165
1.059	10990	217
1.083	11077	132
1.107	11083	75
1.131	11247	248
1.154	11203	137
1.177	11313	235
1.201	11237	165
1.225	11420	200
1.249	11673	379
1.272	11657	247
1.296	11683	189
1.320	11670	259
1.343	11743	281
1.367	11823	217
1.391	11837	172
1.414	11850	167
1.438	11997	206
1.461	11997	159
1.485	11983	145
1.509	12150	225
1.533	12167	255
1.557	12283	242
1.580	12417	257
1.604	12353	199
1.627	12447	172
1.651	12530	192
1.675	12530	199
1.698	12550	191
1.722	12767	170
1.746	12723	142
1.770	12853	233
1.793	12927	199
1.817	12973	176
1.840	13013	174
1.864	13023	214
1.887	13127	273
1.911	13347	161
1.935	13280	219
1.958	13320	160
1.982	13400	182
2.005	13517	167

ε_H	$\tau_{11}-\tau_{22}$	error
2.029	13660	150
2.052	13710	185
2.076	13863	180
2.100	14083	216
2.124	14073	182
2.147	14197	152
2.171	14243	193
2.195	14273	215
2.216	14383	311
2.241	14577	180
2.264	14747	206
2.288	14990	176
2.312	14933	215
2.336	15050	173
2.359	15090	185
2.383	15187	217
2.406	15293	300
2.430	15457	163
2.454	15537	163
2.477	15640	147
2.501	15633	169
2.524	15697	163
2.548	15757	127
2.572	15870	191
2.595	16000	155
2.619	16040	191
2.643	16110	166
2.666	16197	211
2.690	16197	255
2.713	16297	96
2.737	16370	207
2.760	16447	190
2.784	16480	201
2.808	16550	325
2.832	16597	255
2.855	16657	358
2.879	16643	386
2.902	16790	338
2.926	16903	512
2.950	17057	381
2.974	17017	438
2.997	17033	613

B.5. Dow Affinity PL1840 (mBLDPE)

Transient Uniaxial Extension ($\dot{\varepsilon}$=1.00 s^{-1}) T=150 °C

ε_H	$\tau_{11}-\tau_{22}$	error
0	0	0
0.0147	4189	508
0.0379	15970	430
0.0628	19368	1137
0.0849	20750	1313
0.1097	24248	655
0.1328	26885	1086
0.1564	28148	1177
0.1795	29698	1398
0.2029	30798	573
0.2277	33423	1437
0.2509	34508	1472
0.2745	35378	1216
0.2976	36558	1339
0.3209	37613	1380
0.3438	38430	1350
0.3676	39520	1334
0.3902	40510	1354
0.4123	40860	1593
0.4368	41888	884
0.4607	43510	1379
0.4834	43650	1265
0.5070	44583	1185
0.5300	45588	1517
0.5538	46055	1378
0.5770	46723	1188
0.5991	47293	1366
0.6225	47663	1287
0.6454	48635	1248
0.6667	48368	855
0.6914	49735	579
0.7151	51733	1440
0.7381	51288	918
0.7602	51365	378
0.7838	52800	1230
0.8079	53320	1321
0.8314	53828	1243
0.8544	54235	1193
0.8778	55085	1291
0.9003	55223	1330
0.9235	55793	1122
0.9472	56863	1246
0.9707	57470	1237

ε_H	$\tau_{11}-\tau_{22}$	error
0.9937	57598	1209
1.017	58263	1205
1.041	59035	1223
1.064	59373	1253
1.086	59610	1237
1.110	60485	1173
1.134	61153	1222
1.157	61550	1224
1.180	61918	1248
1.203	62338	1248
1.226	62910	1266
1.250	63450	1319
1.273	64063	1281
1.296	64453	1326
1.320	65190	1344
1.343	65533	1378
1.366	66118	1114
1.389	66645	1159
1.412	67120	1171
1.436	67923	1407
1.459	68570	1389
1.482	68965	1379
1.506	69375	1486
1.529	70130	1456
1.552	70418	1469
1.575	70955	1488
1.599	71468	1497
1.622	72060	1560
1.645	72475	1536
1.669	72995	1624
1.692	73558	1606
1.715	73903	1581
1.738	74395	1615
1.762	75165	1647
1.785	75733	1652
1.808	76068	1694
1.832	76693	1736
1.855	77285	1748
1.878	77538	1746
1.901	78148	1812
1.924	78873	1830
1.948	79348	1845
1.971	79790	1883

ε_H	$\tau_{11}-\tau_{22}$	error
1.994	80448	1888
2.017	81003	1935
2.040	81498	1993
2.064	82060	2001
2.087	82640	1980
2.110	83290	2108
2.134	83920	2165
2.157	84348	2135
2.180	84920	2270
2.203	85435	2294
2.226	85810	2246
2.250	86438	2397
2.273	87080	2538
2.296	87350	2538
2.319	88033	2492
2.343	88563	2550
2.366	88973	2670
2.390	89565	2500
2.413	89740	2761
2.436	90428	2898
2.459	90610	2984
2.482	90980	3037
2.506	91235	3101
2.529	91630	3052
2.552	92085	2897
2.575	92410	3073
2.599	92760	3480
2.622	93083	3723
2.645	93193	3835
2.668	93145	3907
2.692	93160	4144
2.715	93088	4354
2.738	93073	4425
2.761	92643	4625
2.785	92370	4796
2.808	92180	5035
2.831	91643	5205
2.854	91040	5454
2.878	90530	5661
2.901	89710	5914
2.924	88763	6205
2.947	87830	6449

B.6. Dow Affinity PL1880 (mBLDPE)

Transient Uniaxial Extension ($\dot{\varepsilon}$=0.01 s^{-1}) T=150 °C

ε_H	$\tau_{11}-\tau_{22}$	error
0	0	0
0.0135	608.6	37
0.0401	873.2	24
0.0645	1094	75
0.0870	1058	30
0.1117	1168	80
0.1358	1118	6
0.1593	1200	44
0.1823	1150	85
0.2085	1246	57
0.2316	1265	53
0.2553	1256	26
0.2785	1238	38
0.3035	1299	49
0.3256	1271	47
0.3494	1274	99
0.3726	1294	11
0.3963	1302	7
0.4205	1367	38
0.4451	1344	37
0.4681	1359	19
0.4916	1338	27
0.5154	1365	17
0.5395	1344	22
0.5631	1351	51
0.5861	1337	11
0.6086	1382	16
0.6330	1350	10
0.6545	1260	26
0.6779	1374	39
0.7029	1378	48
0.7267	1370	61
0.7491	1320	13
0.7725	1348	12
0.7974	1376	12
0.8210	1360	31
0.8434	1352	34
0.8679	1343	25
0.8911	1355	29
0.9139	1354	34
0.9379	1361	13
0.9619	1381	18
0.9854	1376	40

ε_H	$\tau_{11}-\tau_{22}$	error
1.009	1380	28
1.032	1335	21
1.056	1349	12
1.079	1358	25
1.103	1381	24
1.126	1356	18
1.150	1369	16
1.173	1362	24
1.197	1371	74
1.220	1379	14
1.244	1370	21
1.267	1397	32
1.291	1396	25
1.315	1410	18
1.338	1385	14
1.362	1380	13
1.385	1351	27
1.409	1374	39
1.432	1376	20
1.456	1383	8
1.479	1367	17
1.503	1386	25
1.527	1389	28
1.550	1393	33
1.574	1366	36
1.597	1381	26
1.621	1386	45
1.645	1388	26
1.668	1375	14
1.691	1353	21
1.715	1373	35
1.739	1390	33
1.762	1374	14
1.786	1393	34
1.809	1394	55
1.833	1386	33
1.857	1375	60
1.880	1395	26
1.903	1382	71
1.927	1382	21
1.950	1385	36
1.974	1362	20
1.997	1377	46

ε_H	$\tau_{11}-\tau_{22}$	error
2.021	1402	19
2.045	1391	55
2.068	1370	31
2.091	1409	42
2.115	1412	51
2.139	1384	58
2.162	1400	42
2.186	1392	38
2.209	1402	53
2.233	1409	63
2.256	1411	62
2.280	1405	9
2.303	1409	74
2.327	1381	87
2.351	1378	77
2.374	1390	110
2.398	1398	62
2.421	1385	97
2.445	1382	60
2.468	1381	61
2.492	1385	67
2.515	1383	85
2.539	1417	63
2.562	1386	70
2.586	1414	96
2.610	1407	57
2.633	1422	71
2.657	1394	64
2.680	1406	115
2.704	1397	58
2.727	1443	118
2.750	1418	131
2.774	1430	97
2.798	1443	118
2.821	1406	105
2.845	1421	135
2.868	1412	154
2.892	1420	168
2.915	1361	176
2.939	1390	182
2.962	1421	176
2.986	1389	185

B.6. Dow Affinity PL1880 (mBLDPE)

Transient Uniaxial Extension ($\dot{\varepsilon}$=0.10 s^{-1}) T=150 °C

ε_H	$\tau_{11}-\tau_{22}$	error
0	0	0
0.0135	3444	412
0.0313	4651	318
0.0638	5092	513
0.0881	5840	542
0.1127	6652	342
0.1368	6627	285
0.1603	7133	299
0.1833	7058	337
0.2085	7729	307
0.2322	7994	59
0.2562	7876	153
0.2806	8043	175
0.3043	8285	186
0.3275	8594	251
0.3510	8477	144
0.3755	8837	226
0.3986	8912	252
0.4212	8915	203
0.4463	9189	68
0.4700	9230	92
0.4946	9460	62
0.5172	9350	139
0.5413	9618	93
0.5648	9640	107
0.5878	9598	201
0.6121	9549	16
0.6359	9949	180
0.6590	9872	94
0.6817	9806	198
0.7061	10343	184
0.7300	10203	66
0.7522	10063	74
0.7770	10280	129
0.8003	10508	140
0.8245	10503	172
0.8476	10410	112
0.8717	10450	68
0.8952	10495	226
0.9186	10408	82
0.9423	10655	47
0.9664	10888	26
0.9899	10778	90
1.014	11025	61
1.037	10850	27
1.060	10905	62
1.084	11118	110
1.108	11078	114
1.131	11125	190
1.156	11255	47
1.178	11233	73
1.202	11325	118
1.226	11415	37
1.250	11485	168
1.273	11425	104
1.297	11490	141
1.321	11495	86
1.345	11575	95
1.369	11548	62
1.392	11638	114
1.416	11658	85
1.440	11773	154
1.463	11723	85
1.487	11848	108
1.510	11888	71
1.534	11910	136
1.558	11973	136
1.581	11885	177
1.605	12048	173
1.629	12125	170
1.652	12138	171
1.676	12105	170
1.699	12188	168
1.723	12173	178
1.747	12183	189
1.771	12378	231
1.795	12473	159
1.818	12465	237
1.842	12463	235
1.865	12445	233
1.889	12538	192
1.913	12680	246
1.936	12595	244
1.960	12688	226
1.983	12823	245
2.007	12895	307
2.031	12920	289
2.054	12973	309
2.078	13040	336
2.101	13073	286
2.125	13175	345
2.149	13170	374
2.173	13245	374
2.196	13263	392
2.220	13298	464
2.243	13253	402
2.267	13395	408
2.291	13428	402
2.314	13368	335
2.338	13495	375
2.361	13500	374
2.385	13565	464
2.409	13583	529
2.432	13640	497
2.456	13665	451
2.480	13605	535
2.503	13720	531
2.527	13668	612
2.551	13715	564
2.574	13768	534
2.598	13715	584
2.622	13708	627
2.645	13698	622
2.669	13643	762
2.693	13665	648
2.716	13710	728
2.739	13560	660
2.763	13585	735
2.787	13550	735
2.810	13558	890
2.834	13425	982
2.858	13348	973
2.882	13318	989
2.904	14080	2884
2.929	13150	1229
2.953	12998	1209
2.976	12865	1357
3.000	12625	1415

B.6. Dow Affinity PL1880 (mBLDPE)

Transient Uniaxial Extension ($\dot{\varepsilon}$=1.00 s^{-1}) T=150 °C

ε_H	$\tau_{11}-\tau_{22}$	error
0	0	0
0.0135	4967	141
0.0357	17120	520
0.0617	22347	631
0.0870	24823	567
0.1117	27920	252
0.1358	30917	393
0.1593	32337	445
0.1823	33110	713
0.2048	34927	240
0.2304	37620	367
0.2518	38357	492
0.2763	39600	236
0.3001	40877	301
0.3234	41527	335
0.3462	42083	253
0.3684	43413	146
0.3933	44907	395
0.4145	45053	196
0.4383	46260	221
0.4614	47543	258
0.4869	47780	443
0.5090	48460	233
0.5333	49697	283
0.5544	49997	178
0.5776	50547	206
0.6003	51120	236
0.6250	51457	311
0.6490	52410	262
0.6702	53010	275
0.6931	53213	208
0.7178	54630	105
0.7398	55023	267
0.7634	54467	266
0.7864	56047	231
0.8109	57107	326
0.8329	57490	217
0.8563	57313	227
0.8792	58563	313
0.9035	58690	304
0.9253	58823	232
0.9485	59853	146
0.9728	60827	284

ε_H	$\tau_{11}-\tau_{22}$	error
0.9966	60877	361
1.020	61243	342
1.043	62017	333
1.066	61953	332
1.088	62507	320
1.112	63357	284
1.136	63867	301
1.159	64213	346
1.181	64483	323
1.205	64510	340
1.228	65613	310
1.251	66243	280
1.275	66090	324
1.298	66987	467
1.322	67490	274
1.345	67593	367
1.368	68067	335
1.391	68443	323
1.414	68910	376
1.438	69730	235
1.461	70307	275
1.485	70613	343
1.508	71137	455
1.531	71803	327
1.554	71983	316
1.578	72400	490
1.601	72853	387
1.624	73163	451
1.648	73723	427
1.670	73963	429
1.694	74437	457
1.717	74640	469
1.740	75273	469
1.764	75970	475
1.787	76220	472
1.811	76487	474
1.834	77073	548
1.857	77437	526
1.880	77653	576
1.903	78150	544
1.926	78610	544
1.950	78967	565
1.973	79287	591

ε_H	$\tau_{11}-\tau_{22}$	error
1.996	79890	602
2.019	80237	618
2.042	80637	594
2.066	81077	621
2.089	81533	674
2.112	81940	656
2.136	82523	746
2.159	82887	676
2.182	83210	704
2.205	83600	756
2.229	83900	779
2.252	84363	820
2.275	84793	809
2.298	85147	830
2.321	85480	863
2.345	85927	866
2.369	86540	575
2.392	86780	579
2.415	86770	889
2.438	87173	584
2.461	88043	987
2.485	87587	1008
2.508	87970	589
2.531	88533	1061
2.554	88783	1060
2.577	89020	1073
2.601	88983	1116
2.624	89143	1092
2.647	89240	1065
2.671	89090	1070
2.694	89150	1097
2.717	89010	1064
2.740	88857	1123
2.763	88623	1076
2.787	88187	1089
2.810	88033	1175
2.833	87617	1181
2.856	87127	1187
2.880	86687	1308
2.903	86053	1429
2.926	85340	1412
2.949	84517	1649

Appendix C. Capillary Rheometry Data

C.1 Equistar Petrothene NA952-000 (LDPE); T=150 °C; D=1mm

$\dot{\gamma}$	τ	η	ΔP_{ent}
12.65	31311	2476	4.28
16.92	34736	2053	5.17
21.33	37975	1780	6.38
25.86	42133	1630	7.36
33.03	46886	1420	8.37
42.77	51661	1208	9.92
54.39	56775	1044	11.7
68.46	62269	909.6	13.1
87.57	68433	781.5	14.6
113.5	74589	657.4	16.0
138.9	81094	583.7	17.7
173.4	89286	514.9	19.0
223.1	97394	436.6	20.5
284.9	106381	373.4	22.4
374.3	115392	308.3	24.5

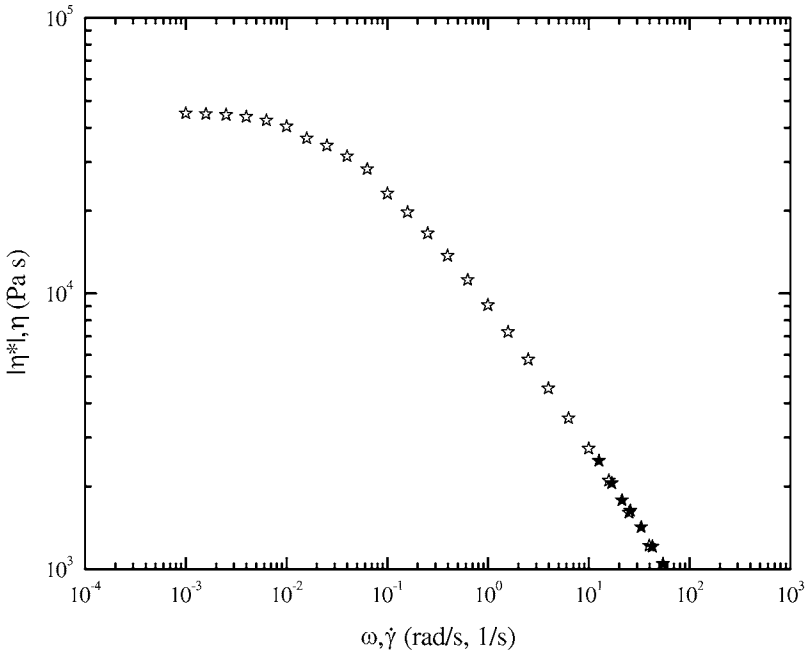

Figure C.1: Overlay of torsional & capillary rheometry data for NA952.

C.2 ExxonMobil NTX101 (LLDPE); T=150 °C; D=1mm

$\dot{\gamma}$	τ	η	ΔP_{ent}
11.37	90631	7968	2.02
14.32	105058	7336	2.18
18.20	121810	6694	2.01
23.38	140225	5998	2.00
30.13	160008	5311	2.05
38.57	181188	4697	2.01
49.93	204508	4096	2.07
65.28	227658	3487	2.44
85.46	251842	2947	3.02
114.1	275433	2413	4.41

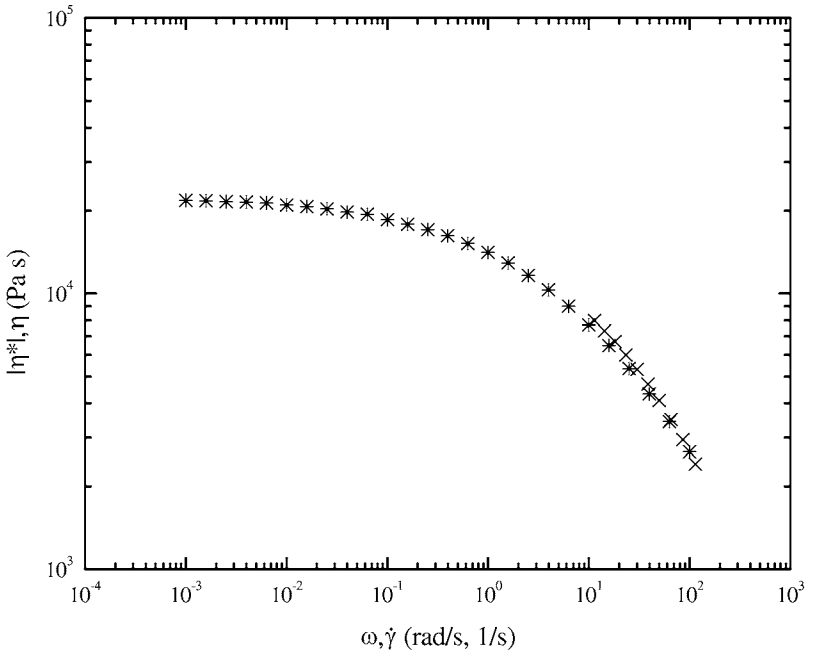

Figure C.2: Overlay of torsional & capillary rheometry data for NTX101

C.3 ExxonMobil Exact 0201 (mBLDPE); T=150 °C; D=1mm

$\dot{\gamma}$	τ	η	ΔP_{ent}
11.04	68865	6238	4.16
14.06	80730	5744	4.34
17.97	94144	5239	4.63
22.87	108920	4762	4.78
28.76	125857	4375	5.00
36.55	145767	3989	4.76
47.31	167223	3535	4.58
60.49	189543	3133	4.97
77.53	215089	2774	4.49
100.7	241083	2394	4.82
131.4	268696	2045	4.87
174.5	295640	1695	5.56
236.7	321934	1360	6.86
349.0	345208	989.0	9.76
629.7	361158	573.5	15.8

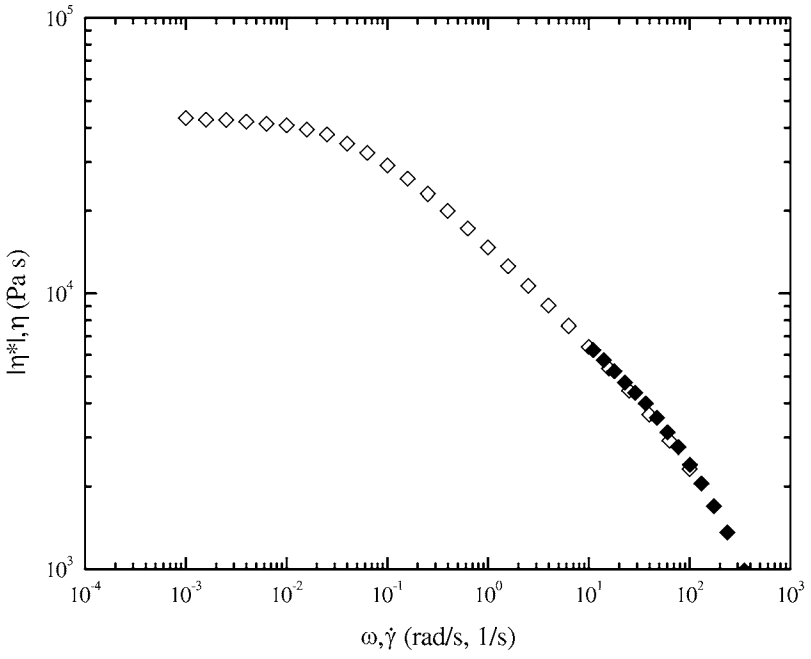

Figure C.3: Overlay of torsional & capillary rheometry data for Exact 0201

C.4 ExxonMobil Exact 3132 (mLLDPE); T=150 °C; D=1mm

$\dot{\gamma}$	τ	η	ΔP_{ent}
10.38	115351	11108	-0.17
13.54	139102	10275	-1.02
17.55	164014	9347	-1.17
22.35	191926	8585	-1.56
28.51	223747	7849	-2.60
37.37	258866	6927	-4.28
49.14	292247	5948	-4.62
64.98	328325	5053	-5.89
96.83	360713	3725	-5.55
202.9	380213	1874	-0.24

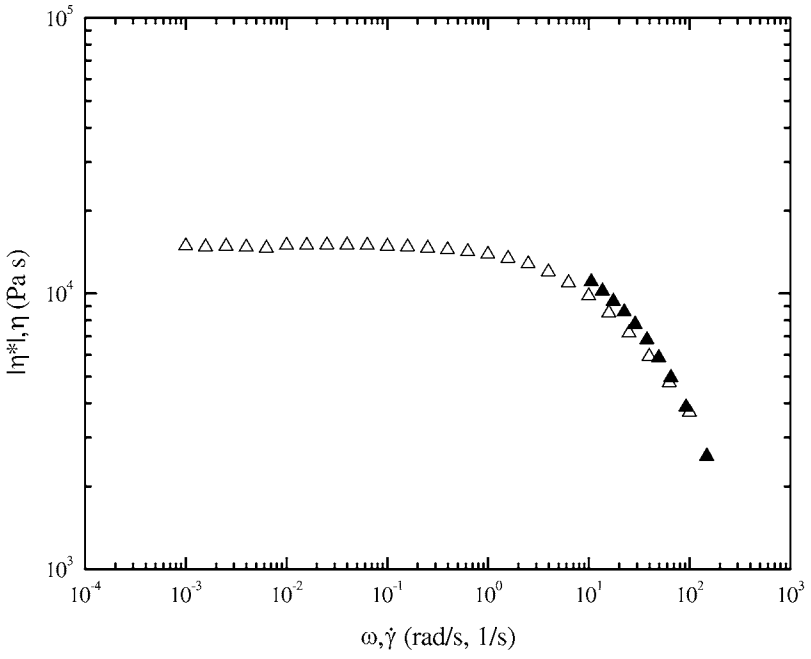

Figure C.4 Overlay of torsional & capillary rheometry data for Exact 3132

C.5 Dow Affinity PL1840 (mBLDPE); T=150 °C; D=1mm

$\dot{\gamma}$	τ	η	ΔP_{ent}
10.99	71051	6465	-3.94
14.20	83195	5859	-6.37
18.74	96216	5134	-8.64
25.28	108529	4293	-10.2
35.21	120201	3414	-11.0
51.29	129505	2525	-10.2
67.70	137195	2027	-8.15
77.54	146176	1885	-5.85
89.31	158498	1775	-3.43
104.6	173789	1661	-1.08
121.3	194187	1601	1.01
146.9	222822	1516	0.82
186.4	255773	1372	-0.34
238.3	291932	1225	-1.70
305.7	331239	1084	-2.52

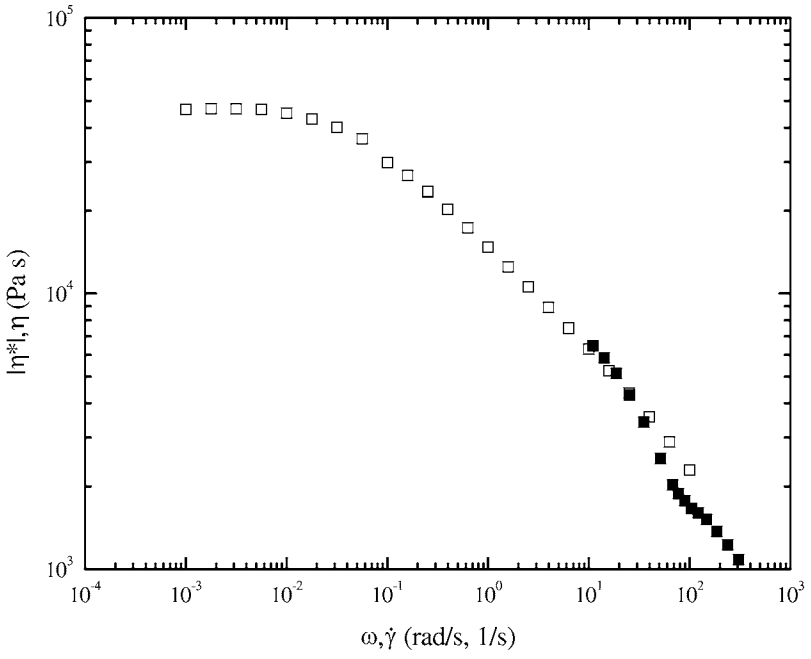

Figure C.5: Overlay of torsional & capillary rheometry data for PL1840

C.6 Dow Affinity PL1880 (mBLDPE); T=150 °C; D=1mm

$\dot{\gamma}$	τ	η	ΔP_{ent}
12.83	69719	5433	-1.21
15.99	77722	4860	-2.01
21.10	86903	4119	-3.07
31.77	94728	2981	-2.85
38.65	99625	2577	-1.00
38.48	109628	2849	-0.49
45.57	127526	2799	-2.06
59.81	146767	2454	-3.27
76.76	165303	2154	-2.77
94.42	187854	1990	-2.63
118.1	214940	1819	-2.89
149.4	245254	1642	-2.60
191.7	279664	1459	-2.02
253.4	315090	1243	-0.90
344.4	348796	1013	2.00

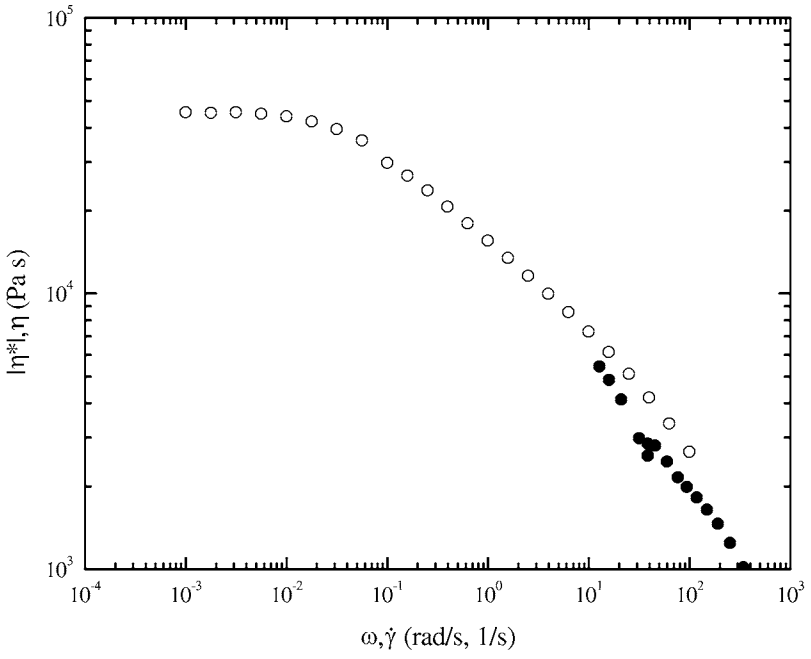

Figure C.6: Overlay of torsional & capillary rheometry data for PL1880

C.7 Capillary Rheometry Corrections

Rabinowitch Correction (non-parabolic profile)

$$\dot{\gamma} = \frac{\dot{\gamma}_a}{4}\left(3 + \frac{d\ln\dot{\gamma}_a}{d\ln\tau}\right) \qquad \text{C.1}$$

Bagley End Correction (entrance pressure drop)

$$\tau = \frac{\Delta P - \Delta P_{ends}}{2(L/R)} \qquad \text{C.2}$$

$$\Delta P_{ends} = \lim_{L/R \to 0} \Delta P \qquad \text{C.3}$$

Appendix D. Rheological Constitutive Model Parameter Fitting Subroutines

D.1 Generalized Newtonian Fluid (GNF) model parameter fitting application

```
module global_defs
	integer :: nobs, choice
	real(kind(1D0)), allocatable :: xdata(:), ydata(:)
	real(kind(1D0)) :: critical
end module global_defs

!-------------------------------------------------------------------------------

program gnf
	use global_defs

	implicit none

	integer :: i, j, ierr, ideriv, irank, ldr, nparm, funit=10, iparam(6), flag=1, counter=0
	real(kind(1D0)) :: dfe, sse, rparam(7), psse, ptheta(2), gc, delta
	real(kind(1D0)), allocatable :: R(:,:), theta(:), scale(:), iwk(:), wk(:)
	character(len=12) :: fname

	external drnlin, error

!  Read experimental data

	write (*,fmt='("Enter the data file name: ")',advance='NO')
	read (*,*) fname
	open(unit=funit, file=fname,status='old')

	read (funit,*) nobs

	allocate(xdata(1:nobs), stat=ierr)
	if (ierr.ne.0) stop 'Unable to allocate array(1)'
	allocate(ydata(1:nobs), stat=ierr)
	if (ierr.ne.0) stop 'Unable to allocate array(2)'

	do i=1,nobs
		read(funit,*) xdata(i), ydata(i)
	end do

	close(funit)

!  Identify desired model and assign dynamic arrays

	do while (flag.eq.1)
	flag = 0

	write (*,*)
	write (*,fmt='("Which GNF model would like to use?")')
	write (*,fmt='(" (1) Power Law Fluid")')
	write (*,fmt='(" (2) Cross/Ellis Model")')
	write (*,fmt='(" (3) Bird-Carreau")')
	write (*,fmt='(" (4) Carreau-Yasuda")')
	write (*,fmt='(" (5) Bingham")')
	write (*,fmt='(" (6) Herschel-Bulkley")')
	write (*,fmt='("Choice: ")', advance='NO')
	read (*,*) choice

	select case (choice)
		case (1)
			nparm = 2
		case (2)
			nparm = 3
		case (3)
			nparm = 3
		case (4)
			nparm = 4
		case (5)
			nparm = 2
		case (6)
```

```
                    nparm = 3
                case default
                    write (*,*)
                    write (*,fmt='("Error... Please make an appropriate choice.")')
                    flag = 1
        end select

        end do

        allocate(theta(nparm), stat=ierr)
        if (ierr.ne.0) stop 'Unable to allocate array(3)'
        allocate(R(nparm,nparm), stat=ierr)
        if (ierr.ne.0) stop 'Unable to allocate array(4)'
        allocate(scale(nparm), stat=ierr)
        if (ierr.ne.0) stop 'Unable to allocate array(5)'
        allocate(wk(11*(nparm+1)+4), stat=ierr)
        if (ierr.ne.0) stop 'Unable to allocate array(6)'
        allocate(iwk(nparm), stat=ierr)
        if (ierr.ne.0) stop 'Unable to allocate array(7)'

        write (*,*)
        write (*,fmt='("Computing ...")', advance = 'NO')

!  Assign initial values (conservative approach)

        select case (choice)
            case (1)
                theta(1) = ydata(1)
                theta(2) = 0.5D0
            case (2)
                theta(1) = ydata(1)
                theta(2) = 0.5D0
                theta(3) = 0.5D0
            case (3)
                theta(1) = ydata(1)
                theta(2) = 0.5D0
                theta(3) = 0.5D0
            case (4)
                theta(1) = ydata(1)
                theta(2) = 0.5D0
                theta(3) = 0.5D0
                theta(4) = 2.0D0
            case (5)
                theta(1) = ydata(nobs)
                theta(2) = ydata(1)*xdata(1)
            case (6)
                theta(1) = ydata(nobs)
                theta(2) = 0.5D0
                theta(3) = ydata(1)*xdata(1)
        end select

!  Call DRNLIN subroutine

        ideriv = 0
        ldr = nparm

        if (choice.eq.1) then

            psse = 1.0D+99
            delta = -1.0D0
            critical = 0.0D0

            do while (delta.lt.0.0D0)

                call dr8lin (iparam, rparam)
                iparam(3)=9999
                iparam(4)=9999
                rparam(3)=1.0D-20

                call dr2lin (error, nparm, ideriv, theta, R, ldr, irank, dfe, sse, iparam, rparam, scale, iwk, wk)
```

```
                        delta = sse - psse

                        if (delta.lt.0.0D0) then
                                ptheta = theta
                                psse = sse
                                counter = counter + 1
                        end if

                        critical = xdata(counter)

                end do
                critical = xdata(counter-1)
                theta = ptheta
                sse = psse

        else

                call dr8lin (iparam, rparam)
                iparam(3)=9999
                iparam(4)=9999
                rparam(3)=1.0D-20

                call dr2lin (error, nparm, ideriv, theta, R, ldr, irank, dfe, sse, iparam, rparam, scale, iwk, wk)

        end if

        write (*,fmt='(" Done")')
        write (*,*)

! Output regressed values and SSE

        select case (choice)
                case (1)
                        write (*,fmt='("m = ", ES12.4)') ptheta(1)
                        write (*,fmt='("n = ", ES12.4)') ptheta(2)
                        write (*,fmt='("c = ", ES12.4)') critical
                case (2)
                        write (*,fmt='(2x, "eta0 = ", ES12.4)') theta(1)
                        write (*,fmt='("lambda = ", ES12.4)') theta(2)
                        write (*,fmt='(5x, "n = ", ES12.4)') theta(3)
                case (3)
                        write (*,fmt='(2x, "eta0 = ", ES12.4)') theta(1)
                        write (*,fmt='("lambda = ", ES12.4)') theta(2)
                        write (*,fmt='(5x, "n = ", ES12.4)') theta(3)
                case (4)
                        write (*,fmt='(2x, "eta0 = ", ES12.4)') theta(1)
                        write (*,fmt='("lambda = ", ES12.4)') theta(2)
                        write (*,fmt='(5x, "n = ", ES12.4)') theta(3)
                        write (*,fmt='(5x, "a = ", ES12.4)') theta(4)
                case (5)
                        write (*,fmt='(2x, "mu = ", ES12.4)') theta(1)
                        write (*,fmt='("tau0 = ", ES12.4)') theta(2)
                case (6)
                        write (*,fmt='(3x, "m = ", ES12.4)') theta(1)
                        write (*,fmt='(3x, "n = ", ES12.4)') theta(2)
                        write (*,fmt='("tau0 = ", ES12.4)') theta(3)
        end select

        write (*,*)
        write (*,fmt='("SSE = ", ES10.4, " (log-log)")') sse

! Deallocate dynamic arrays

        if (allocated(xdata)) deallocate(xdata)
        if (allocated(ydata)) deallocate(ydata)
        if (allocated(theta)) deallocate(theta)
        if (allocated(R)) deallocate(R)
        if (allocated(scale)) deallocate(scale)
        if (allocated(wk)) deallocate(wk)
```

```
        if (allocated(iwk)) deallocate(iwk)

        write (*,*)
        write (*,fmt='("Press any key to continue...")')
        pause

end program gnf

!-------------------------------------------------------------------------------

subroutine error (nparm, theta, iopt, iobs, frq, wt, E, DE, iend)
        use global_defs

        implicit none

        integer :: nparm, iopt, iobs, iend
        real(kind(1D0)) :: theta(nparm), wt, frq, E, DE(nparm)
        real(kind(1D0)) :: rate, ymodel, plf, cross, b_c, c_y, bingham, h_b

        external plf, cross, b_c, c_y, bingham, h_b

   if (iobs .le. nobs) then
        wt = 1.0D0
        frq = 1.0D0
        iend = 0

        rate = xdata(iobs)

                select case (choice)
                case (1)
                        ymodel = plf (rate, theta)
                case (2)
                        ymodel = cross (rate, theta)
                case (3)
                        ymodel = b_c (rate, theta)
                case (4)
                        ymodel = c_y (rate, theta)
                case (5)
                        ymodel = bingham (rate, theta)
                case (6)
                        ymodel = h_b (rate, theta)
                end select

        if (minval(theta).lt.0.0D0) then
                E = 1.0D99
        else
                E = log10(ydata(iobs)) - log10(ymodel)
        end if

   else
        iend = 1
   end if

        return
end subroutine error

!-------------------------------------------------------------------------------

function plf (rate, theta)
        use global_defs
        implicit none

        real(kind(1D0)) :: rate, theta(2), plf

        if (rate.le.critical) then
                plf = ydata(1)
        else
                plf = theta(1)*rate**(theta(2)-1.0D0)
        end if
```

```
        return
end function plf

function cross (rate, theta)
        implicit none

        real(kind(1D0)) :: rate, theta(3), cross

        cross = theta(1)/(1.0D0+(theta(2)*rate)**theta(3))

        return
end function cross

function b_c (rate, theta)
        implicit none

        real(kind(1D0)) :: rate, theta(3), b_c

        b_c = theta(1)*(1.0D0 + (theta(2)*rate)**2)**((theta(3)-1.0D0)/2.0D0)

        return
end function b_c

function c_y (rate, theta)
        implicit none

        real(kind(1D0)) :: rate, theta(4), c_y

        c_y = theta(1)*(1.0D0+(theta(2)*rate)**theta(4))**((theta(3)-1.0D0)/theta(4))

        return
end function c_y

function bingham (rate, theta)
        implicit none

        real(kind(1D0)) :: rate, theta(2), bingham

        bingham = theta(1) + theta(2)/rate

        return
end function bingham

function h_b (rate, theta)
        implicit none

        real(kind(1D0)) :: rate, theta(3), h_b

        h_b = theta(1)*rate**(theta(2)-1.0D0) + theta(3)/rate

        return
end function h_b
```

D.2 Phan-Thien/Tanner (PTT) model parameter fitting application

```
module material_defs
        real(kind(1D0)), allocatable :: rt(:), ratio(:)
        real(kind(1D0)) :: xi, eps
end module material_defs

module exp_data
        integer :: nobs1, nobs2
        real(kind(1D0)), allocatable :: xdata(:), ydata(:), udata(:), vdata(:), wdata(:)
end module exp_data

module temp
        integer :: mode
        real(kind(1D0)), allocatable :: temp_rs(:)
        real(kind(1D0)) :: rate, erate
end module temp

!-----------------------------------------------------------------------------------------

program ptt_fit

        use material_defs
        use exp_data
        use temp

        implicit none

        integer :: i, j, k, rtimes, ierr, funit=10, counter

        real(kind(1D0)) :: sse1, sse2, error, t_eps
        real(kind(1D0)), allocatable :: rs(:), t_rs(:)

        character(len=12) :: fname1, fname2

!  Open resource file

        open(unit=funit, file='resource.txt', status='old')

        read(funit,*) fname1
        read(funit,*) fname2
        read(funit,*) rtimes

!  Initialize primary arrays based upon # of relax. times
        allocate(rt(1:rtimes), stat=ierr)
        if (ierr.ne.0) stop 'Unable to allocate array(1)'
        allocate(rs(1:rtimes), stat=ierr)
        if (ierr.ne.0) stop 'Unable to allocate array(2)'
        allocate(ratio(1:rtimes), stat=ierr)
        if (ierr.ne.0) stop 'Unable to allocate array(3)'

        do mode=1,rtimes
                read(funit,*) rt(mode), ratio(mode)
        end do

        read(funit,*) xi
        read(funit,*) eps

        close(funit)

!  Read experimental data from specified files

        open(unit=funit+1, file=fname1, status='old')
        read (funit+1,*) nobs1

        allocate(xdata(1:nobs1), stat=ierr)
        if (ierr.ne.0) stop 'Unable to allocate array(4)'
        allocate(ydata(1:nobs1), stat=ierr)
        if (ierr.ne.0) stop 'Unable to allocate array(5)'
```

```
        do i=1,nobs1
                read(funit+1,*) xdata(i), ydata(i)
        end do

        close(funit+1)

        open(unit=funit+2, file=fname2, status='old')
        read (funit+2,*) nobs2

        allocate(udata(1:nobs2), stat=ierr)
        if (ierr.ne.0) stop 'Unable to allocate array(6)'
        allocate(vdata(1:nobs2), stat=ierr)
        if (ierr.ne.0) stop 'Unable to allocate array(7)'
        allocate(wdata(1:nobs2), stat=ierr)
        if (ierr.ne.0) stop 'Unable to allocate array(8)'

        do i=1,nobs2
                read(funit+2,*) udata(i), vdata(i), wdata(i)
        end do

        erate = wdata(nobs2)/udata(nobs2)

        close(funit+2)

!  Initialize temporary array(s)

        allocate(temp_rs(1:rtimes), stat=ierr)
        if (ierr.ne.0) stop 'Unable to allocate array(9)'
        allocate(t_rs(1:rtimes), stat=ierr)
        if (ierr.ne.0) stop 'Unable to allocate array(0)'

!  Master DO Loop

        rs = 1.0D+03

        error = 1.0D+00
        counter = 0

        write (*,100,advance='NO')
100     format('Iteration ')

        do while (error.gt.1.0D-4)

                counter = counter + 1

                write (*,101,advance='NO') counter
101             format(I1' ... ')

                t_rs(:) = rs(:)
                t_eps = eps

                call shear_fit (rtimes, rs, sse1)

                call ext_fit (rtimes, rs, sse2)

                error = 0.0D0
                do mode = 1,rtimes
                        error = error + ((rs(mode)-t_rs(mode))/rs(mode))**2
                end do
                error = error + ((eps-t_eps)/eps)**2

        end do

        write (*,102)
102     format('DONE.')

        print *
        write (*,fmt='(ES9.3, 4x, ES9.3, 4x)') sse1, sse2
```

```
! Output parameter info

        open(unit=funit+3,file='ptt-params.txt',status='replace')

        write (funit+3,fmt='(I1)') rtimes
        do mode=1,rtimes
                write (funit+3, fmt='(ES9.3, 4x, ES9.3, 4x, ES9.3)') rt(mode), rs(mode)/(1.0D0-ratio(mode)), ratio(mode)
        end do
        write (funit+3,fmt='(ES9.3)') xi
        write (funit+3,fmt='(ES9.3)') eps

        close (funit+3)

! Deallocate dynamic arrays

        if (allocated(t_rs)) deallocate(t_rs)
        if (allocated(temp_rs)) deallocate(temp_rs)
        if (allocated(wdata)) deallocate(wdata)
        if (allocated(vdata)) deallocate(vdata)
        if (allocated(udata)) deallocate(udata)
        if (allocated(ydata)) deallocate(ydata)
        if (allocated(xdata)) deallocate(xdata)
        if (allocated(ratio)) deallocate(ratio)
        if (allocated(rs)) deallocate(rs)
        if (allocated(rt)) deallocate(rt)

end program ptt_fit

!-----------------------------------------------------------------------------------------------

subroutine shear_fit (rtimes, rs, sse)

        use material_defs
        use exp_data
        use temp

        implicit none

        integer :: rtimes, ideriv, ldr, irank, iparam(6)
        real(kind(1D0)) :: rs(rtimes), R(rtimes,rtimes), dfe, sse
        real(kind(1D0)) :: rparam(7), scale(rtimes), iwk(rtimes), wk(11*(rtimes+1)+4)

        external dr8lin, dr2lin, error

        ldr = rtimes

        ideriv = 0

        call dr8lin (iparam, rparam)
        iparam(3)=9999
        iparam(4)=9999
        rparam(3)=1.0D-15
        call dr2lin (error, rtimes, ideriv, rs, R, ldr, irank, dfe, sse, iparam, rparam, scale, iwk, wk)

        return
end subroutine shear_fit

subroutine error (rtimes, rs, iopt, iobs, frq, wt, E, DE, iend)

        use material_defs
        use exp_data
        use temp

        implicit none

        integer :: rtimes, iopt, iobs, iend, itmax
        real(kind(1D0)) :: rs(rtimes), frq, wt, E, DE(rtimes)
        real(kind(1D0)) :: errrel, xguess(4), X(4), fnorm
        real(kind(1D0)) :: eta, tau_s(4), tau_n
```

```
        external steady, dneqnj, fcn, fcnj

        temp_rs(:) = rs(:)

        errrel = 1.0D-10
        itmax = 1000

        if (iobs .le. nobs1) then

        wt     = 1.0D0
    frq    = 1.0D0
    iend   = 0

    rate = xdata(iobs)

    tau_s = 0.0D0
    tau_n = 0.0D0

            do mode = 1,rtimes
                call steady (rtimes,rs,xguess)
                        xguess = -xguess
                call dneqnj (fcn,fcnj,errrel,4,itmax,Xguess,X,fnorm)
                tau_s(:) = tau_s(:) + X(:)
                tau_n = tau_n - rs(mode)*ratio(mode)/(1.0D0-ratio(mode))*rate
                end do

                eta = - tau_s(1)/rate - tau_n/rate

                if (minval(rs).lt.0.0D0) then
                        E = 1.0D10
                else
                        E = (eta/ydata(iobs)-1.0D0)**2
                end if

        else

    iend = 1

        end if

        return
end subroutine error

subroutine steady (rtimes,rs,xguess)
        use material_defs
        use temp

        implicit none

        integer :: rtimes
        real(kind(1D0)) :: rs(rtimes), xguess(4), D

        D = 1.0D0 + xi*(2.0D0-xi)*(rt(mode)*rate)**2

        xguess(1) = rs(mode)/D*rate
        xguess(2) = (1.0D0-xi/2.0D0)*2.0D0*rs(mode)*rt(mode)/D*rate**2.0D0
        xguess(3) =      (-xi/2.0D0)*2.0D0*rs(mode)*rt(mode)/D*rate**2.0D0
        xguess(4) = 0.0D0

        return
end subroutine steady

subroutine fcn (X, F, N)
        use material_defs
        use temp

        implicit none

        integer :: N
        real(kind(1D0)) :: X(N), F(N), Z, rs(size(temp_rs))
```

```
        rs(:) = temp_rs(:) ! use the contents of temp_rs in local array rs

        Z = exp(-eps*rt(mode)/rs(mode)*(X(1)+X(2)+X(3)))

        F(1) = Z*X(1) - rt(mode)*X(3)*rate + rt(mode)*xi/2.0D0*(X(2)+X(3))*rate + rs(mode)*rate
        F(2) = Z*X(2) - rt(mode)*X(1)*rate*2.0D0 + rt(mode)*xi*X(1)*rate
        F(3) = Z*X(3) + rt(mode)*xi*X(1)*rate
        F(4) = Z*X(4)

        return
end subroutine fcn

subroutine fcnj (N, X, FJAC)
        use material_defs
        use temp

        implicit none

        integer :: N
        real(kind(1D0)) :: X(N), FJAC(N,N), Z, dZ, rs(size(temp_rs))

        rs(:) = temp_rs(:) ! use the contents of temp_rs in local array rs

        Z = exp(-eps*rt(mode)/rs(mode)*(X(1)+X(2)+X(3)))
        dZ = -eps*rt(mode)/rs(mode)*Z

        FJAC(1,1) = Z
        FJAC(1,2) = dZ*X(1) + rt(mode)*xi/2.0D0*rate
        FJAC(1,3) = dZ*X(1) - rt(mode)*rate + rt(mode)*xi/2.0D0*rate
        FJAC(1,4) = dZ*X(1)
        FJAC(2,1) = -rt(mode)*rate*2.0D0 + rt(mode)*xi*rate
        FJAC(2,2) = Z + dZ*X(2)
        FJAC(2,3) = dZ*X(2)
        FJAC(2,4) = dZ*X(2)
        FJAC(3,1) = rt(mode)*xi*rate
        FJAC(3,2) = dZ*X(3)
        FJAC(3,3) = Z + dZ*X(3)
        FJAC(3,4) = dZ*X(3)
        FJAC(4,1) = 0.0D0
        FJAC(4,2) = dZ*X(4)
        FJAC(4,3) = dZ*X(4)
        FJAC(4,4) = Z + dZ*X(4)

        return
end subroutine fcnj

!-----------------------------------------------------------------------------------------------

subroutine ext_fit (rtimes, rs, sse)

        use exp_data
        use material_defs
        use temp

        implicit none

        integer :: cont, counter, k, N=3, rtimes, iobs, ido
        real(kind(1D0)) :: A(1,1), T, tend, tol, Y(3), param(50)
        real(kind(1D0)) :: sse, minn, msse, begn, step, visc, stress_n, stress(nobs2,3), time(nobs2), rs(rtimes)

        external dfunc, dfuncj, divpag

        temp_rs(:) = rs(:)

!  IMSL parameters

        call sset (50, 0.0D0, param, 1)
        param(4) = 1.0D+08
        tol = 1.0D-09
```

```
! Looping structures ...

        cont = 1

        minn = 1.0D+00
        msse = 1.0D+99

        begn = 1.0D+00
        step = 2.0D-02

        counter = 0

        do while (cont.eq.1)

                do k = 1,50
                        eps = begn - step*dble(k-1)
                        stress = 0.0D0
                        stress_n = 0.0D0
                        do mode=1,rtimes
                                ido = 1
                                T = 0.0D0
                                Y(:) = 0.0D0
                                do iobs=2,nobs2
                                tend = udata(iobs)
                                call divpag (ido, N, dfunc, dfuncj, A, T, tend, tol, param, Y)
                                stress(iobs,:) = stress(iobs,:) + Y(:)
                                time(iobs) = tend
                                end do
                                stress_n = stress_n + 3.0D0*rs(mode)*ratio(mode)/(1.0D0-ratio(mode))*erate
                                ido = 3
                                call divpag (ido, N, dfunc, dfuncj, A, T, tend, tol, param, Y)
                        end do
                        sse = 0.0D0
                        do iobs=1,nobs2
                                sse = sse + (vdata(iobs)-stress(iobs,1)+stress(iobs,3)-stress_n)**2
                        end do
                        if (sse.lt.msse) then
                                minn = eps
                                msse = sse
                        end if
                end do

                begn = minn + step
                step = 4.0D-02*step

                counter = counter + 1
                if (counter.eq.4) then
                        cont = 0
                end if

        end do

end subroutine ext_fit

subroutine dfunc(N, T, Y, YP)
        use material_defs
        use temp

        integer :: N
        real(kind(1D0)) :: T, Y(N), YP(N)
        real(kind(1D0)) :: Z, rs(size(temp_rs))

        rs(:) = temp_rs(:)

        Z = exp(-eps*rt(mode)/rs(mode)*(Y(1)+Y(2)+Y(3)))

        YP(1) = (-Z*Y(1) - rt(mode)*(1.0D0-xi)*erate*Y(1) + rs(mode)*erate)/rt(mode)
        YP(2) = (-Z*Y(2) - rt(mode)*(1.0D0-xi)*erate*Y(2) + rs(mode)*erate)/rt(mode)
        YP(3) = (-Z*Y(3) + 2.0D0*rt(mode)*(1.0D0-xi)*erate*Y(3) - 2.0D0*rs(mode)*erate)/rt(mode)
```

```
        return
end subroutine dfunc

subroutine dfuncj (N, T, Y, dypdy)
        integer :: N
        real(kind(1D0)) :: T, Y(:), dypdy(:)

        return
end subroutine dfuncj
```

D.3 McLeish-Larson Pom-Pom model prediction subroutines

D.3.1 Dynamic Link Library subroutines

```
stdcall subroutine orientS(t,k,r,tb,S1,S2,S3,S4)
	implicit none

	integer :: k, flag
	real(kind(1D0)) :: t, r, tb, S1, S2, S3, S4
	real(kind(1D0)) :: A(4), trace

	flag = 0

! prelim checking
	if (t.lt.0.0D0) flag = -1
	if (k.lt.1.or.k.gt.3) flag = -2
	if (r.lt.0.0D0) flag = -3
	if (tb.lt.0.0D0) flag = -4

! if everything okay then calculate, otherwise assign value of flag to S2
	if (flag.eq.0) then
		call orientA(t,k,r,tb,A)
		trace = A(2)+A(3)+A(4)
		S1 = A(1)/trace
		S2 = A(2)/trace
		S3 = A(3)/trace
		S4 = A(4)/trace
	else
		S1 = 0.0D0
		S2 = dble(flag)
		S3 = 0.0D0
		S4 = 0.0D0
	end if

	return
end subroutine orientS

stdcall subroutine orient2(p0,p1,p2,p3,S1,S2,S3,S4)
	implicit none

	integer :: p1, k, flag, rule, irule
	real(kind(1D0)) :: p0, t, p2, r, p3, tb
	real(kind(1D0)) :: S1a, S2a, S3a, S4a, S1b, S2b, S3b, S4b
	real(kind(1D0)) :: S1, S2, S3, S4
	real(kind(1D0)) :: errabs, errrel, errest

	external DQDAG, DQDAGI, F1, F2, F3, F4

	common /integral/rule,t,k,r,tb

	t =  p0
	k =  p1
	r =  p2
	tb = p3

	flag = 0

! prelim checking
	if (t.lt.0.0D0) flag = -1
	if (k.lt.1.or.k.gt.3) flag = -2
	if (r.lt.0.0D0) flag = -3
	if (tb.lt.0.0D0) flag = -4

! reduce time if excessive
	if (p0/p3.gt.1.0D5) t=1.0D5*p3

! if everything okay then calculate, otherwise assign value of flag to S2
	if (flag.eq.0) then
```

```
                call integrate(p0,p1,p2,p3,S1,S2,S3,S4)

        else
                S1 = 0.0D0
                S2 = dble(flag)
                S3 = 0.0D0
                S4 = 0.0D0
        end if

        return
end subroutine orient2

stdcall subroutine Lambda(ti,tf,Li,Lf,p0,p1,p2,p3,p4)
        implicit none

        integer :: ido,p0,k,flag

        real(kind(1D0)) :: ti,tf,Li,Lf,p1,p2,p3,p4
        real(kind(1D0)) :: rate,tb,q,ts
        real(kind(1D0)) :: param(50),tol,Z(1,1),L(1)

        common /diff/k,rate,tb,q,ts

        external DIVPAG, SSET, fcn, fcnj

        k = p0
        rate = p1
        tb = p2
        q = p3
        ts = p4

        flag = 0

! prelim checking
        if (ti.lt.0.0D0.or.tf.lt.0.0D0) flag = -1
        if (ti.ge.tf) flag = -2
        if (Li.lt.1.0D0.or.Li.gt.q) flag = -3
        if (k.lt.1.or.k.gt.3) flag = -4
        if (rate.lt.0.0D0) flag = -5
        if (tb.lt.0.0D0) flag = -6
        if (q.lt.1.0D0) flag = -7
        if (ts.lt.0.0D0) flag = -8

! perform calculations if flag = 0, otherwise print value of flag
        if (flag.eq.0) then
                call SSET (50, 0.0D0, param, 1)
                tol = 1.0D-09
                param(4) = 1.0D+08

                L(1) = Li

                if (q.gt.1.0D0) then
                        ido = 1
                        call DIVPAG (ido, 1, fcn, fcnj, Z, ti, tf, tol, param, L)
                        ido = 3
                        call DIVPAG (ido, 1, fcn, fcnj, Z, ti, tf, tol, param, L)
                else
                        L(1) = 1.0D0
                end if

                if (L(1).lt.1.0D0) L(1)=1.0D0
                if (L(1).gt.q) L(1)=q

                Lf = L(1)
        else
                Lf = dble(flag)
        end if

        return
```

```
end subroutine Lambda

stdcall subroutine Lambda2(ti,tf,Li,Lf,p0,p1,p2,p3,p4)
	implicit none

	integer :: ido,p0,k,flag

	real(kind(1D0)) :: ti,tf,Li,Lf,p1,p2,p3,p4
	real(kind(1D0)) :: rate,tb,q,ts
	real(kind(1D0)) :: param(50),tol,Z(1,1),L(1)

	common /diff/k,rate,tb,q,ts

	external DIVPAG, SSET, fcn, fcnj

	k = p0
	rate = p1
	tb = p2
	q = p3
	ts = p4

	flag = 0

! prelim checking
	if (ti.lt.0.0D0.or.tf.lt.0.0D0) flag = -1
	if (ti.ge.tf) flag = -2
	if (Li.lt.1.0D0.or.Li.gt.q) flag = -3
	if (k.lt.1.or.k.gt.3) flag = -4
	if (rate.lt.0.0D0) flag = -5
	if (tb.lt.0.0D0) flag = -6
	if (q.lt.1.0D0) flag = -7
	if (ts.lt.0.0D0) flag = -8

! perform calculations if flag = 0, othewise print value of flag
	if (flag.eq.0) then
		call SSET (50, 0.0D0, param, 1)
		tol = 1.0D-09
		param(4) = 1.0D+08

		L(1) = Li

		if (q.gt.1.0D0) then
			ido = 1
			call DIVPAG (ido, 1, fcn, fcnj, Z, ti, tf, tol, param, L)
			ido = 3
			call DIVPAG (ido, 1, fcn, fcnj, Z, ti, tf, tol, param, L)
		else
			L(1) = 1.0D0
		end if

		if (L(1).lt.1.0D0) L(1)=1.0D0
		if (L(1).gt.q) L(1)=q

		Lf = L(1)
	else
		Lf = dble(flag)
	end if

	return

end subroutine Lambda2

!---------------------------------------------------------------------------------------

subroutine fcn(N, X, Y, Yprime)
	implicit none

	integer :: N, k
	real(kind(1D0)) :: X, Y(N), Yprime(N)
```

```
	real(kind(1D0)) :: A(4), S(4), nu, KS, r, tb, q, ts, trace

	common /diff/k,r,tb,q,ts

	nu = 1.0D0/q

	call orientA(X,k,r,tb,A)

	trace = A(2)+A(3)+A(4)

	S(:) = A(:)/trace

	select case (k)
		case (1)
			KS = r*S(1)
		case (2)
			KS = r*S(2) - r*S(3)/2.0D0 - r*S(4)/2.0D0
	end select

	Yprime(1) = Y(1)*KS - (Y(1)-1.0D0)/ts*exp(nu*(Y(1)-1.0D0))

	if (Y(1).ge.q.and.Yprime(1).gt.0.0D0) then
		Yprime(1) = 0.0D0
	end if

	return
end

subroutine fcnj (N, X, Y, dypdy)
	implicit none

	integer :: N
	real(kind(1D0)) :: X, Y(N), dypdy(N)

	return
end

subroutine orientA(t,k,r,tb,A)
	implicit none

	integer :: k
	real(kind(1D0)) :: A(4), p
	real(kind(1D0)) :: t, r, tb

	p = 0.0D0

	select case (k)
		case (1) ! shear
			A(1) = r*tb*(1.0D0-exp(-t/tb))
			A(2) = 1.0D0 + 2.0D0*r**2*tb**2*(1.0D0-exp(-t/tb)-t/tb*exp(-t/tb))
			A(3) = 1.0D0
			A(4) = A(3)
		case (2) ! uniaxial
			A(1) = 0.0D0
			if (r.eq.(0.5D0/tb)) then
				p = r/1.0D3
			end if
			if (t*(2.0D0*(r+p)-1.0D0/tb).lt.4.4D1) then
				A(2) = 1.0D0/(1.0D0-2.0D0*(r+p)*tb)*(1-exp(t*(2.0D0*(r+p)-1.0D0/tb))) + &
					exp(t*(2.0D0*(r+p)-1.0D0/tb))
			else
				A(2) = 1.0D0/(2.0D0*(r+p)*tb-1.0D0)*1.285D+19 + 1.285D+19
			endif
			A(3) = 1.0D0/(1.0D0+r*tb)*(1.0D0-exp(-t*(r+1.0D0/tb))) + exp(-t*(r+1.0D0/tb))
			A(4) = A(3)
		case (3) ! planar
			A(:) = 1.0D0
	end select

	return
```

```
end

!-------------------------------------------------------------------------------
subroutine integrate(t,r,tb,k,S1,S2,S3,S4)

	integer :: rule

	real(kind(1D0)) :: t, S1a, S2a, S3a, S4a, S1b, S2b, S3b, S4b, S1, S2, S3, S4
	real(kind(1D0)) :: errabs, errrel, errest

	common /integral/rule,t,k,r,tb

	errabs = 0.0D+00
	errrel = 1.0D-09

	rule = 1
	call DQDAG (F1, 0.0D0, t, errabs, errrel, 2, S1a, errest)
	call DQDAG (F2, 0.0D0, t, errabs, errrel, 2, S2a, errest)
	call DQDAG (F3, 0.0D0, t, errabs, errrel, 2, S3a, errest)
	call DQDAG (F4, 0.0D0, t, errabs, errrel, 2, S4a, errest)

	rule = 2
	call DQDAGI (F1, t, 1, errabs, errrel, S1b, errest)
	call DQDAGI (F2, t, 1, errabs, errrel, S2b, errest)
	call DQDAGI (F3, t, 1, errabs, errrel, S3b, errest)
	call DQDAGI (F4, t, 1, errabs, errrel, S4b, errest)

	S1 = dble(S1a + S1b)
	S2 = dble(S2a + S2b)
	S3 = dble(S3a + S3b)
	S4 = dble(S4a + S4b)

	return
end subroutine integrate

double precision function F1 (X)
	implicit none

	integer :: rule, k

	real(kind(1D0)) :: X
	real(kind(1D0)) :: M, strain, I1, I2, J, T1, T2, B, C, t, rate, tb

	common /integral/rule,t,k,rate,tb

	if (X/tb.gt.6.90D2) then
		M = 0.0D0
	else
		M = exp(-X/tb)/tb
	end if

	if (rule.eq.1) then
		strain = rate*X
	else
		strain = rate*t
	end if

	I1 = 3.0D0 + strain**2
	I2 = I1

	J = I1+2.0D0*dsqrt(I2+13.0D0/4.0D0)

	T1 = 5.0/(J-1.0D0)
	T2 = -5.0/(J-1.0D0)/dsqrt(I2+13.0D0/4.0D0)

	B = strain
	C = -strain

	F1 = M*(T1*B+T2*C)
```

```
	return
end function F1

double precision function F2 (X)
	implicit none

	integer :: rule, k

	real(kind(1D0)) :: X
	real(kind(1D0)) :: M, strain, I1, I2, J, T1, T2, B, C, t, rate, tb

	common /integral/rule,t,k,rate,tb

	if (X/tb.gt.6.90D2) then
		M = 0.0D0
	else
		M = exp(-X/tb)/tb
	end if

	if (rule.eq.1) then
		strain = rate*X
	else
		strain = rate*t
	end if

	I1 = 3.0D0 + strain**2
	I2 = I1

	J = I1+2.0D0*dsqrt(I2+13.0D0/4.0D0)

	T1 = 5.0/(J-1.0D0)
	T2 = -5.0/(J-1.0D0)/dsqrt(I2+13.0D0/4.0D0)

	B = 1.0D0 + strain**2
	C = 1.0D0

	F2 = M*(T1*B+T2*C)

	return
end function F2

double precision function F3 (X)
	implicit none

	integer :: rule, k

	real(kind(1D0)) :: X
	real(kind(1D0)) :: M, strain, I1, I2, J, T1, T2, B, C, t, rate ,tb

	common /integral/rule,t,k,rate,tb

	if (X/tb.gt.6.90D2) then
		M = 0.0D0
	else
		M = exp(-X/tb)/tb
	end if

	if (rule.eq.1) then
		strain = rate*X
	else
		strain = rate*t
	end if

	I1 = 3.0D0 + strain**2
	I2 = I1

	J = I1+2.0D0*dsqrt(I2+13.0D0/4.0D0)

	T1 = 5.0/(J-1.0D0)
	T2 = -5.0/(J-1.0D0)/dsqrt(I2+13.0D0/4.0D0)
```

```
        B = 1.0D0
        C = 1.0D0 + strain**2

        F3 = M*(T1*B+T2*C)

        return
end function F3

double precision function F4 (X)
        implicit none

        integer :: rule, k

        real(kind(1D0)) :: X
        real(kind(1D0)) :: M, strain, I1, I2, J, T1, T2, B, C, t, rate, tb

        common /integral/rule,t,k,rate,tb

        if (X/tb.gt.6.90D2) then
                M = 0.0D0
        else
                M = exp(-X/tb)/tb
        end if

        if (rule.eq.1) then
                strain = rate*X
        else
                strain = rate*t
        end if

        I1 = 3.0D0 + strain**2
        I2 = I1

        J = I1+2.0D0*dsqrt(I2+13.0D0/4.0D0)

        T1 = 5.0/(J-1.0D0)
        T2 = -5.0/(J-1.0D0)/dsqrt(I2+13.0D0/4.0D0)

        B = 1.0D0
        C = 1.0D0

        F4 = M*(T1*B+T2*C)

        return
end function F4
```

D.3.2 Microsoft Excel Visual Basic interface subroutines

```
Declare Sub orientS Lib "d:\temp\pompom.dll" (t As Double, k As Integer, r As Double, tb As Double, S1 As Double, S2 As Double,  S3 As Double, S4 As Double)
Declare Sub Lambda Lib "d:\temp\pompom.dll" (ti As Double, tf As Double, Li As Double, Lf As Double, k As Integer, rate As Double, tb As Double, q As Double, ts As Double)

Function SS(t As Double, r As Double, tb As Double)

   Dim k As Integer
   Dim S(1 To 3) As Double
   Dim S1 As Double
   Dim S2 As Double
   Dim S3 As Double
   Dim S4 As Double

   k = 1
   Call orientS(t, k, r, tb, S1, S2, S3, S4)
```

```
    S(1) = S1
    S(2) = S2
    S(3) = S3

    SS = Array(S)
End Function

Function ES(t As Double, r As Double, tb As Double)

    Dim k As Integer
    Dim S(1 To 2) As Double
    Dim S1 As Double
    Dim S2 As Double
    Dim S3 As Double
    Dim S4 As Double

    k = 2
    Call orientS(t, k, r, tb, S1, S2, S3, S4)

    S(1) = S2
    S(2) = S3

    ES = Array(S)
End Function

Function sL(ti As Double, tf As Double, Li As Double, rate As Double, tb As Double, q As Double, ts As Double)

    Dim k As Integer

    k = 1
    Call Lambda(ti, tf, Li, Lf, k, rate, tb, q, ts)

    sL = Lf
End Function

Function eL(ti As Double, tf As Double, Li As Double, rate As Double, tb As Double, q As Double, ts As Double)

    Dim k As Integer

    k = 2
    Call Lambda(ti, tf, Li, Lf, k, rate, tb, q, ts)

    eL = Lf
End Function
```

Appendix E. Additional Numerical Simulation Data

E.1 Various mesh geometries investigated

Mesh: s1.msh Nodes: 309 Elements: 248

(full view)

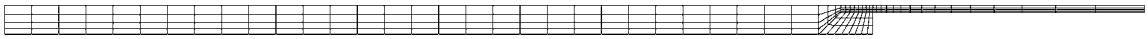

(10x view)

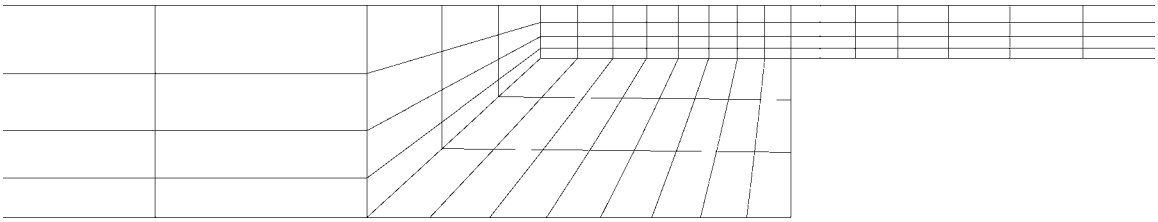

Mesh: s2.msh Nodes: 1113 Elements: 992

(full view)

(10x view)

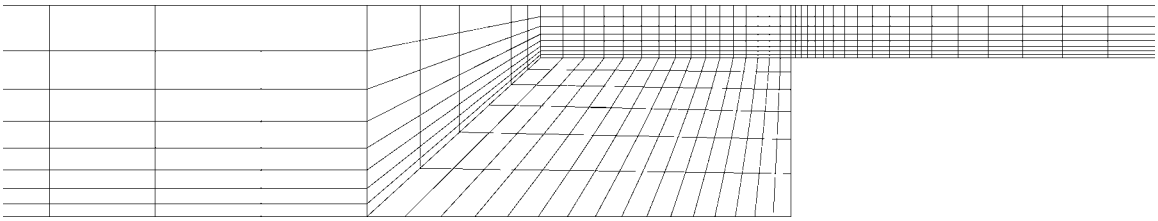

Mesh: s4.msh Nodes: 1138 Elements: 1819

(full view)

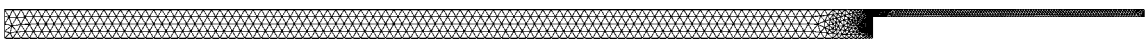

(10x view)

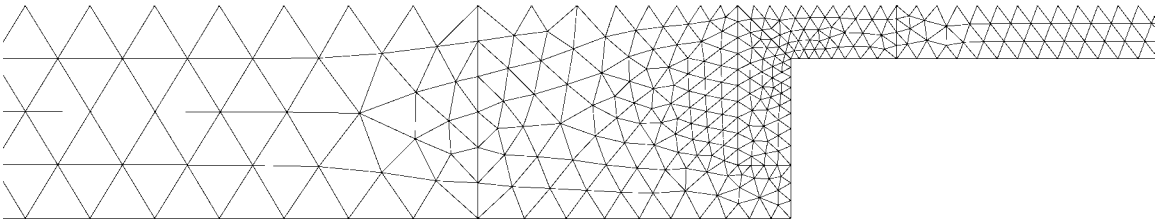

Mesh: sd.msh Nodes: 3896 Elements: 6878

(full view)

(10x view)

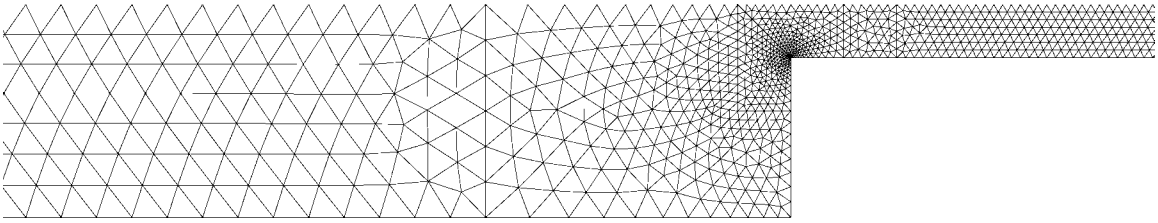

Mesh: sn.msh Nodes: 2396 Elements: 2200

(full view)

(10x view)

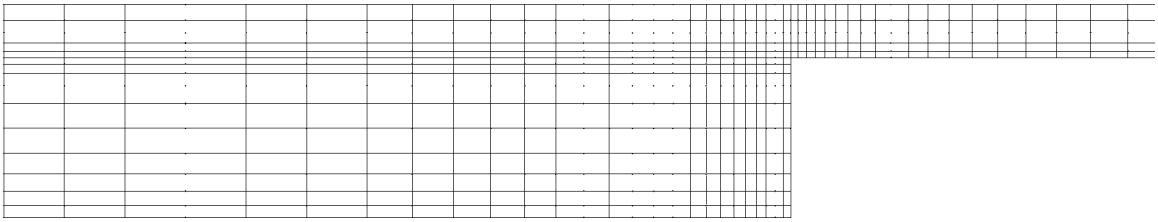

E.2. Mesh dependency comparisons

In order to establish confidence in the numerical predictions, the effects of mesh refinement were investigated. Initial predictions obtained using the `s1.msh` were subject to uncertainty due to the coarse nature of the mesh. As a result, `s2.msh` was generated to asses the influence that element size has on the numerical predictions of the hydrodynamic pressure, velocity in the primary flow direction, and normal stress in the primary flow direction. Figure E.1 – E.3 demonstrate the influence of mesh refinement on these predicted quantities.

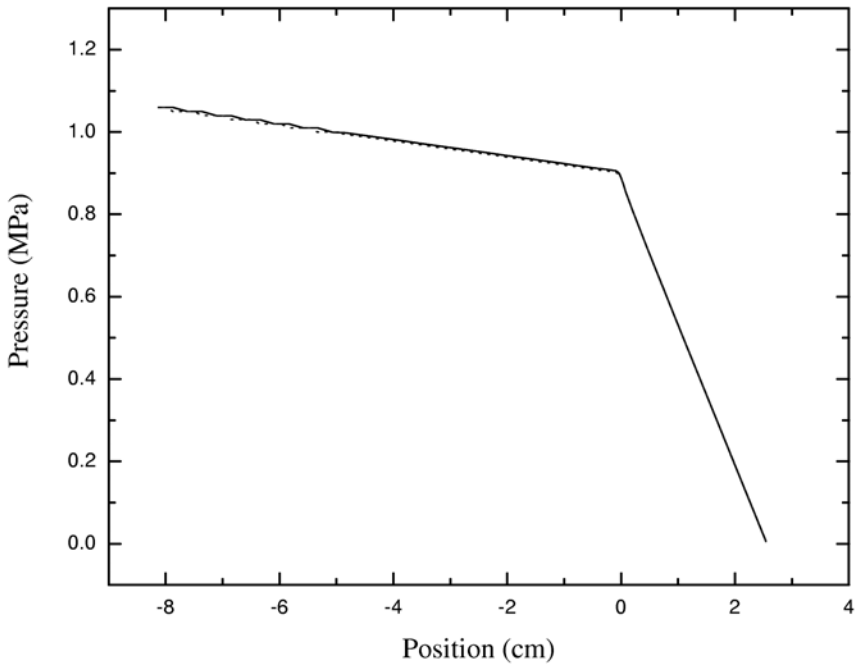

Figure E.1: Comparison of the predicted pressure profiles, $\dot{\gamma}_a$=4.8 s^{-1}. (——) s1.msh, (・・・) s2.msh

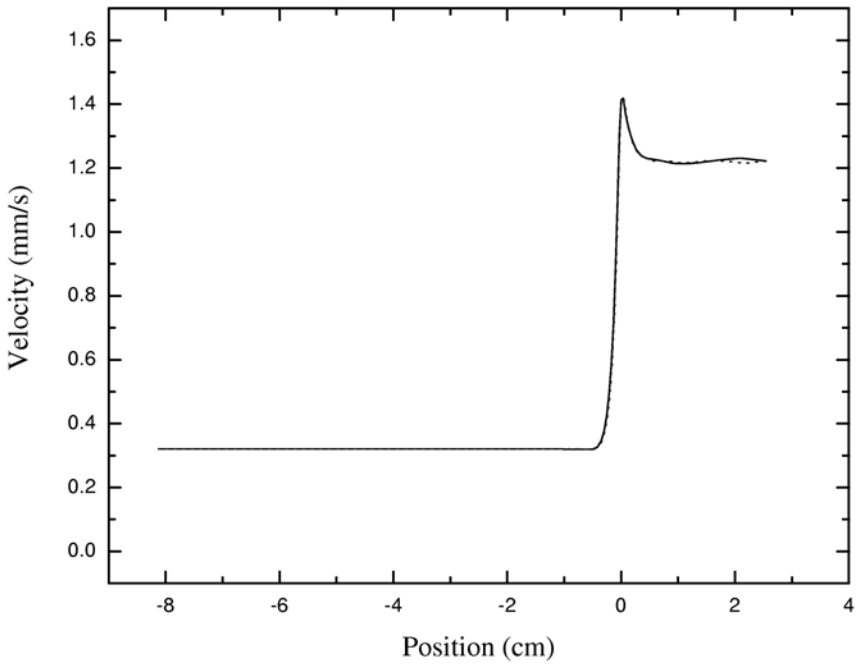

Figure E.2: Comparison of the predicted velocities (x-direction) along the plane of symmetry at $\dot{\gamma}_a$=4.8 s^{-1}. (——) s1.msh, (· · ·) s2.msh

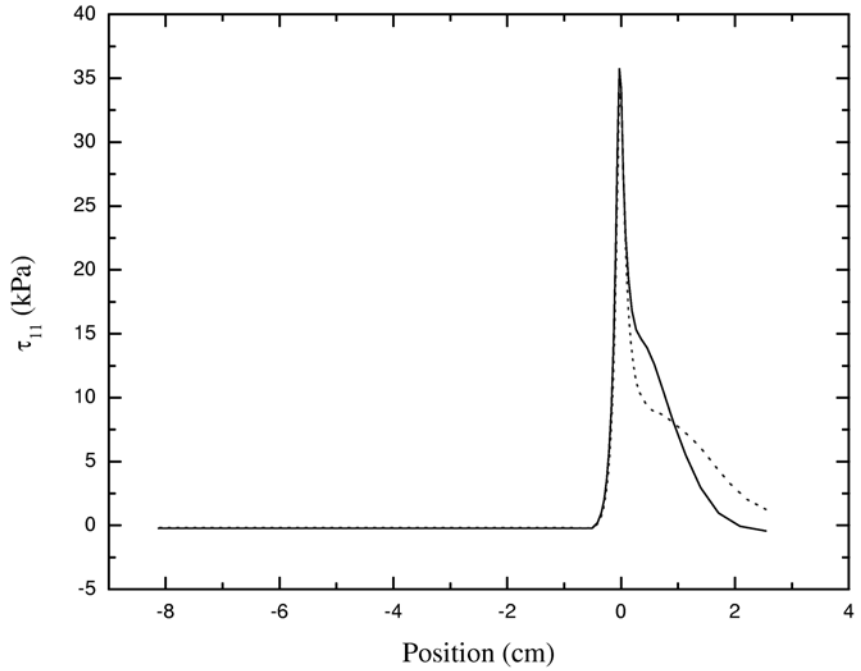

Figure E.3: Comparison of the predicted τ_{11} profile along the plane of symmetry at $\dot{\gamma}_a$=4.8 s^{-1}. (——) s1.msh, (· · ·) s2.msh

The results presented above demonstrate that additional mesh refinement does not significantly affect the predicted pressure profiles, which is significant for the study identified in Chapter 7, but appears to mildly affect the velocity profile and moderately affect the τ_{11} profile following the contraction. Surprisingly, additional efforts to further refine the computational mesh resulted in loss of convergence at lower apparent shear rates. As a result, the `s2.msh` was chosen for the study appearing in Chapter 7 because it presumably provides results that are more accurate and the additional spatial refinement along the plane of symmetry was desired.

E.3. Integration schemes for differential constitutive models

Three integration schemes are commonly used throughout literature and are available in Polyflow 3.8. These schemes are: the Galerkin, Streamline Upwinding (SU), and Streamline Upwinding/Petrov Galerkin (SUPG) formulations. In order to demonstrate the differences between these schemes we will begin by defining a one-dimensional representation of an arbitrary differential viscoelastic constitutive equation. This equation appears as:

$$\lambda u \frac{d\tau}{dx} + g\tau = f$$

where λ is a characteristic relaxation time, u is a characteristic velocity, $\mathrm{d}\tau/\mathrm{d}x$ is the spatial derivative of the stress τ, and g and f can be arbitrary functions of u and its spatial derivatives. The quantity $u\ \mathrm{d}\tau/\mathrm{d}x$ represents the convected derivative of τ and is usually the source of divergence in numerical simulations.

The Galerkin scheme represents the unaltered finite element formulation, which appears as:

$$\int_0^L \left(\lambda u \frac{d\tau^h}{dx} + g\tau - f \right) w\, dx = 0$$

Here the solution is determined by integrating the product of the constitutive equation and a test function *w* over the domain x=0 – L. The test function *w* is a simple function of *x* and is generally linear or quadratic in nature. τ^h represents the approximate numerical solution to the problem on a grid of size *h*. Although the Galerkin scheme can provide the most accurate solutions, it suffers from loss of convergence when the convective term becomes large. This is associated with a change of type of the differential equation from elliptic to hyperbolic in nature.

In order to circumvent the problem associated with the Galerkin formulation, Brooks and Hughes (*Comp. Meth. Appl. Mech. Eng*. **32**, 199-259,1982) developed what is known as the Streamline Upwinding/ Petrov Galerkin scheme (SUPG). This formulation treats the equation set differently by addressing the problems associated with the convective term, and appears as:

$$\int_0^L \left[w + \frac{\bar{k}}{u}\frac{dw}{dx} \right] \left(\lambda u \frac{d\tau^h}{dx} + g\tau - f \right) dx = 0$$

The primary difference between the SUPG and Galerkin formulations is the addition of the right-hand term in the bracket. k(bar) is a variable value that depends linearly on the size of the element and u. This term represents an artificial diffusion along the streamlines that serves to mitigate the effects of the convective term in parentheses. One major problem with the SUPG formulation is that the benefits of upwinding are lost in the presence of flow singularities (i.e. sharp corners) where the stress gradient can be very high. This arises from backward diffusion near the singularity that ultimately destabilizes the solution.

Finally, the inconsistent streamline upwinding (SU) technique developed Marchal and Crochet (*J. Non-Newt. Fluid Mech*. **26**, 77-114, 1987) partially addresses the problem of flow singularities by applying the diffusive component exclusively to the convective term. This inconsistent approach appears as,

$$\int_0^L \left(\lambda u \frac{d\tau^h}{dx} \right) \frac{\bar{k}}{u} \frac{dw}{dx} dx + \int_0^L \left(\lambda u \frac{d\tau^h}{dx} + g\tau - f \right) w dx = 0$$

As a result of this formulation, the diffusive term does not significantly affect the stability of the remaining elliptical components of the constitutive equation. Furthermore, in the limit of small element sizes the Galerkin formulation can be recovered. Of course, this inconsistent approach alters the nature of the problem and leads to error of order O(h). Unfortunately, substantial mesh refinement reverts back to the Galerkin limitation.

E.4. Convergence limits

Convergence studies were carried out using the `s2.msh` featured above in order to establish the maximum convergence range (shear rate range) attainable using either the Galerkin (G), Streamline Upwinding/Petrov Galerkin (SUPG), or Streamline Upwinding (SU) methods. The multi-mode PTT model using the fluid descriptions featured in Chapter 6 for LDPE and LLDPE was the constitutive model analyzed. The results are presented in the following table.

Table E.1. Convergence results for LDPE and LLDPE fluids

LDPE			
	G	SUPG	SU
We_{crit}	1.2	0.59	1.8
$\dot{\gamma}_{a,crit}$	0.76	0.04	12.4
$\tau_{w,crit}$	9.09	1.53	36.4
LLDPE			
	G	SUPG	SU[a]
We_{crit}	0.42	0.64	0.99
$\dot{\gamma}_{a,crit}$	1.52	0.35	37.0
$\tau_{w,crit}$	22.6	6.43	212

[a]: denotes limit of interest, no loss of convergence observed

Three different measures of convergence criteria have been presented. The first is the Weissenberg (We) number, defined as the ratio of the normal stress difference N_1 to the twice the wall shear stress τ_w. The second is the apparent wall shear rate $\dot{\gamma}_a$. The third is the wall shear stress τ_w. The results show that for LDPE description the SU method provides the highest convergence limits while the SUPG method provides the lowest. Conversely, the Galerkin method provides the lowest convergence limits in the case of LLDPE. Quite surprisingly, the fluid description has a significant influence on the convergence limits for each integration scheme. Comparing We_{crit}, higher values were attained for LDPE than LLDPE using the G scheme, similar values were observed using the SUPG scheme, and higher values were observed for LDPE than LLDPE using the SU scheme, but loss of convergence was not attempted for the LLDPE material.

E.5. Influence of ε parameter (PTT model) on flow predictions

Pressure Profile Predictions

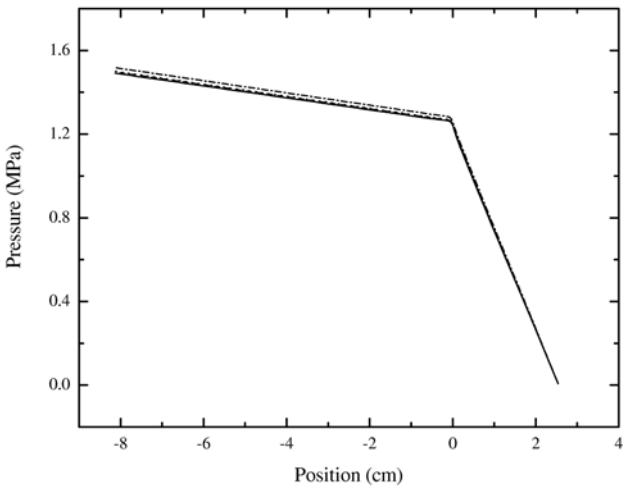

Figure E.4: Effect of ε parameter on predicted pressure profiles. (——) ε = 1.28E-6, (– – –) ε = 0.021, (· · ·) ε = 0.034, (—·—) ε = 0.100.

Streamline Patterns

ε=1.28E-6

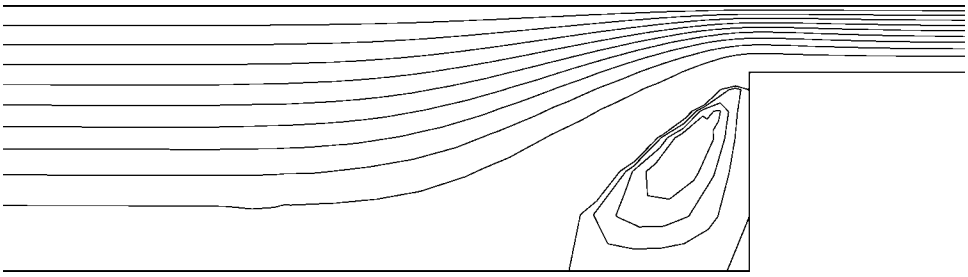

ε=0.021

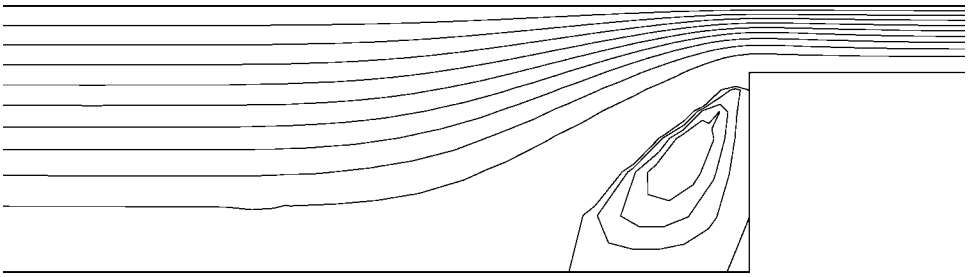

ε=0.034

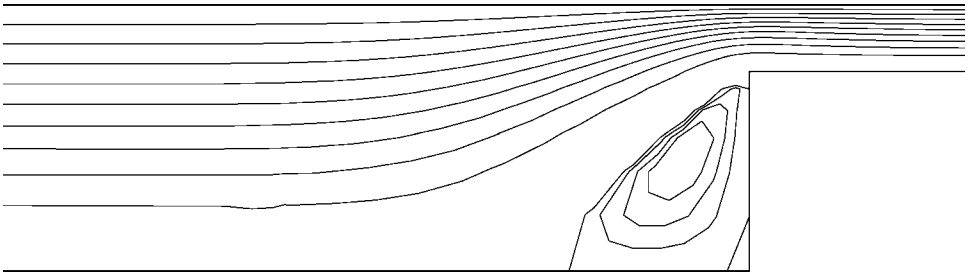

ε=0.100

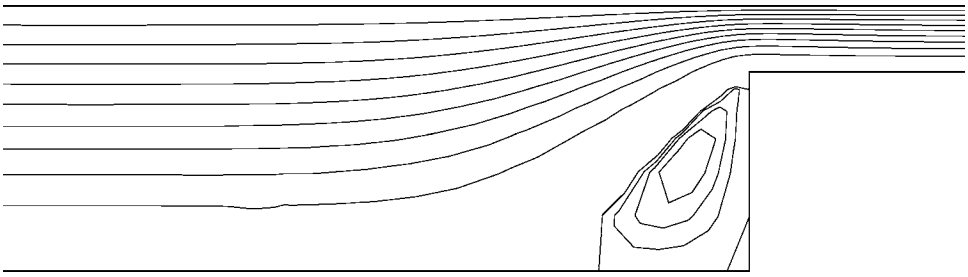

Appendix F. Transient Melt Fracture Data

F.1 Introduction

Initial investigations of the melt fracture behavior of metallocene polyethylenes identified several idiosyncrasies not seen before in conventional polyethylenes (see Chapter 2 or 6). One of the most interesting of these idiosyncrasies was observed by Hatzikiriakos *et al*. (1997). In their study, they found that sparsely branched metallocene polyethylenes produced by Dow Chemical exhibited long induction periods prior to steady-state flow during which surface melt fracture gradually disappeared. Surprisingly, this phenomenon is in fact universal, as it has been observed here as well.

F.2 Pressure trace during capillary extrusion

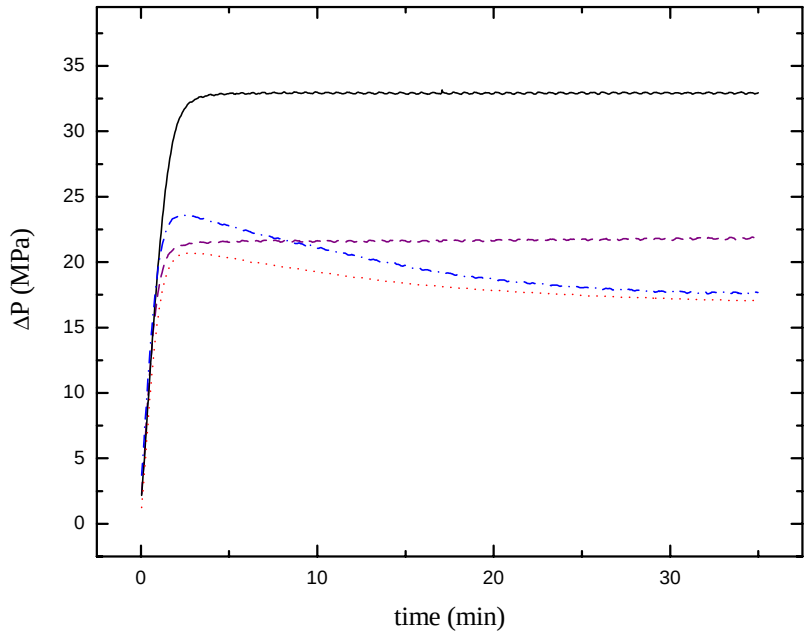

Figure F.1: Transient pressure measurements at T=150 °C, $\dot{\gamma}_a$=100 s^{-1}. (——) Exact 3132, (– – –) Exact 0201, (—·—) PL1880, (· · ·) PL1840.

F.3. FE-SEM micrographs

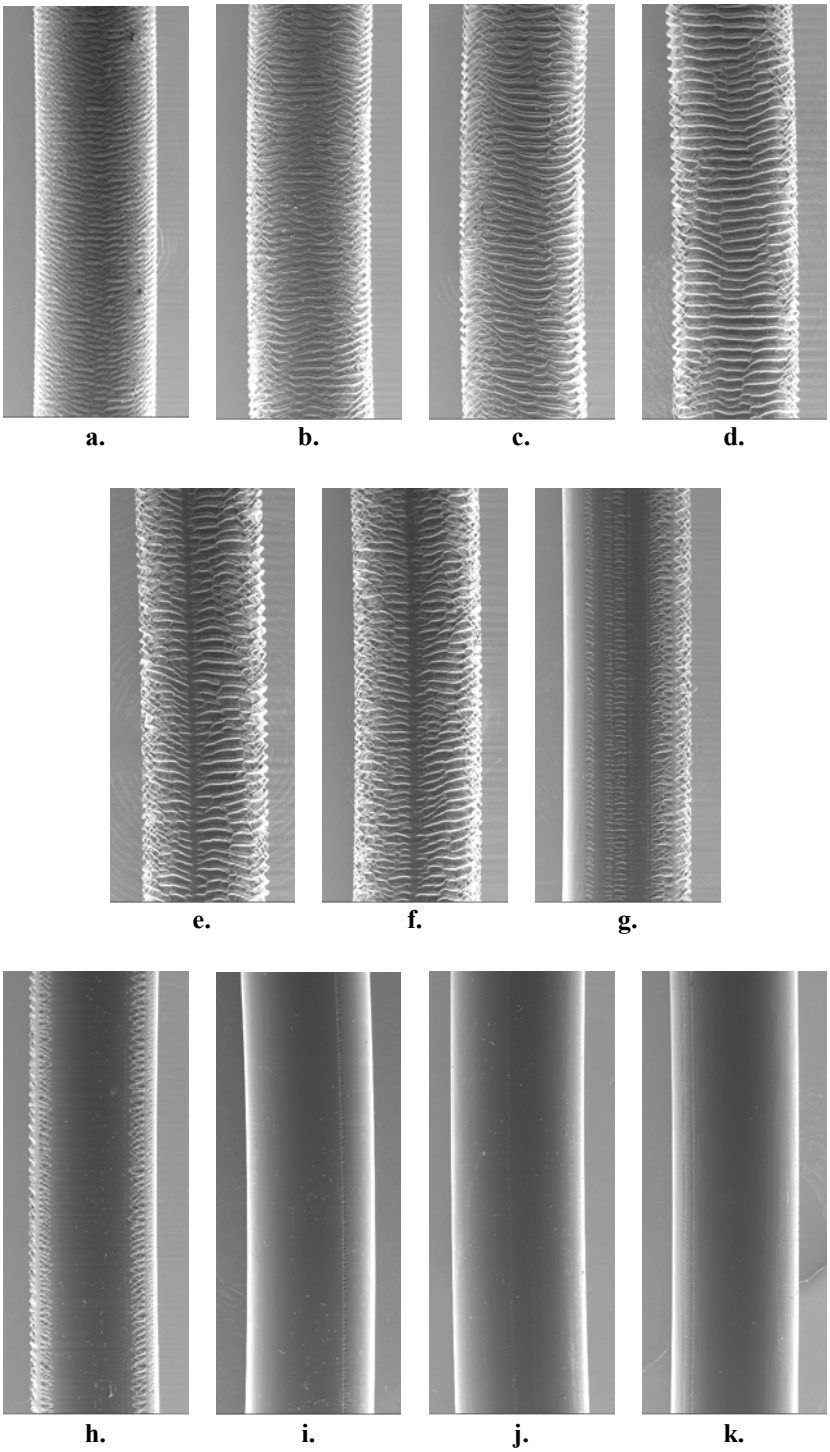

Figure F.2: FESEM micrographs obtained for PL1840 at T=150 °C, $\dot{\gamma}_a$=100 s^{-1}. Elapsed time (shear stress) at **a**. 10 s (0.042 MPa), **b**. 17.8 s (0.071 MPa), **c**. 31.6 s (0.098 MPa), **d**. 56.2 s (0.154 MPa), **e**. 100 s (0.197 MPa), **f**. 178 s (0.206 MPa), **g**. 316 s (0.202 MPa), **h**. 562 s (0.193 MPa), **i**. 1000 s (0.181 MPa), **j**. 1778 s (0.172 MPa), and **k**. 2650 s (0.164 MPa).

F.4 Discussion

The results presented above clearly demonstrate an induction period of over 30 minutes for the Dow Affinity resins. Conversely, the Exact resins produced by ExxonMobil do not exhibit an induction period and reach their steady-state pressure values within five minutes of imposing flow. Figure F.1 shows a 20% decrease in the pressure drop across the capillary for Affinity PL1840 and a 25% decrease for Affinity PL1880 from their maximum pressure drop values, respectively. Figure F.2 provides a visual demonstration of the disappearance of surface melt fracture (sharkskin) as a function time. Clearly, within the first 100s of the test surface melt fracture is evident. However, beyond 100 seconds small regions of distortion free extrudate grow to eventually encompass the entire circumference of the extrudate. Although Dow Chemical claims that no processing aids (fluoroelastomers) have been added to these resins, this response is typical of fluroelastomers.

Appendix G. Flow Birefringence Data

G.1 Flow Birefringence Theory

The optical properties of a polymer molecule are locally anisotropic along the chain, i.e. the refractive index along the chain axis is different from that orthogonal to the chain axis. Under quiescent conditions, the random orientation of the chains leads to globally isotropic optical behavior within the system. However, the application of stress under flowing conditions leads to global orientation of the molecules and anisotropic optical behavior. The method of flow birefringence takes advantage of this optical anisotropy to determine the level of stress in the melt under conditions of flow. In this appendix, a brief overview of the applied flow birefringence theory is presented.

There are three basic assumptions in the birefringence theory presented here: first, the flow field is assumed to be two-dimensional in nature; second, the real polymer chain in the melt is accurately described by a statistical chain; and third, only small deformations of the chain are occurring during flow. There are then two principal stresses, σ_I and σ_{II}, acting on the fluid at an angle χ relative to the local direction of flow. The principal stress difference, $\Delta\sigma = \sigma_I - \sigma_{II}$, is related to the extra stresses by,

$$\Delta\sigma \sin 2\chi = 2\tau_{12} \qquad \text{G.1}$$

$$\Delta\sigma \cos 2\chi = \tau_{11} - \tau_{22} \qquad \text{G.2}$$

In a similar fashion, the birefringence, Δn, is related to the components of the refractive index tensor, **n**, by

$$\Delta n \sin 2\chi = 2n_{12} \qquad \text{G.3}$$

$$\Delta n \cos 2\chi = n_{11} - n_{22} \qquad \text{G.4}$$

where χ is the extinction angle. Expressions for the refractive index behavior of a material in terms of the applied stresses can be obtained from the stress optic law. Specifically, these expressions are given by

$$n_{12} = C\tau_{12} \qquad \text{G.5}$$

$$n_{11} - n_{22} = C(\tau_{11} - \tau_{22}) \qquad \text{G.6}$$

where C is the material dependent stress optic coefficient. Combining all of the above equations gives the expression for the applied stresses in terms of birefringence,

$$\Delta n \sin 2\chi = 2C\tau_{12} \qquad \text{G.7}$$

$$\Delta n \cos 2\chi = C(\tau_{11} - \tau_{22}) \qquad \text{G.8}$$

In order to resolve the shear stress and the normal stress difference from the birefringence, it is necessary to also determine the extinction angle χ. This is generally performedy by generating isoclinic birefringence patterns using plane polarized white light. With respect to isochromatic patterns, equations G.7 and G.8 are combined to obtain the following expression for the state of stress in the fluid,

$$\Delta n = C\sqrt{4\tau_{12}^2 + (\tau_{11} - \tau_{22})^2} \qquad \text{G.9}$$

The final point to be made in terms of flow birefringence is in regard to the order of the observed fringes. The retardation, N, or phase difference is related to the birefringence by the following relationship,

$$N = \frac{\Delta n L}{\lambda} \qquad \text{G.10}$$

where L is the sample width and λ is the wave length of the incident radiation source.

G.2 Stress Patterns for an Abrupt 8:1 Planar Contraction

Isochromatic, Plane Polarized Patterns (N=0,1,2,…)

NA952 (LDPE)

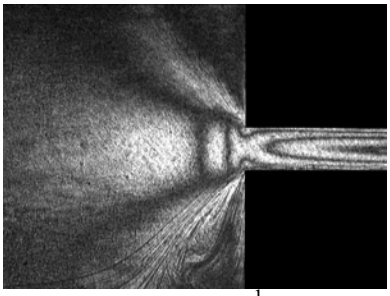

$\dot{\gamma}_a$=1.0 s^{-1}

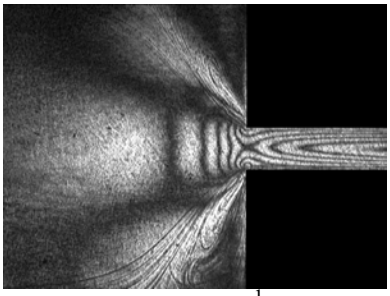

$\dot{\gamma}_a$=2.9 s^{-1}

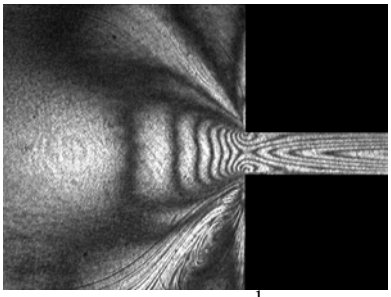

$\dot{\gamma}_a$=5.1 s^{-1}

NTX101 (LLDPE)

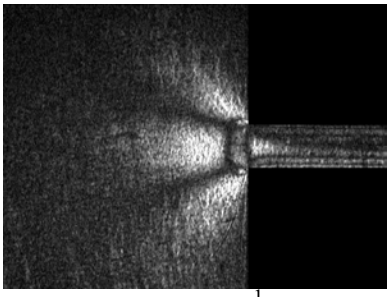

$\dot{\gamma}_a$=1.0 s^{-1}

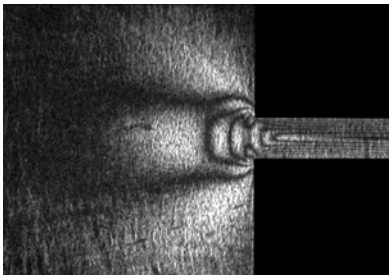

$\dot{\gamma}_a$=2.9 s^{-1}

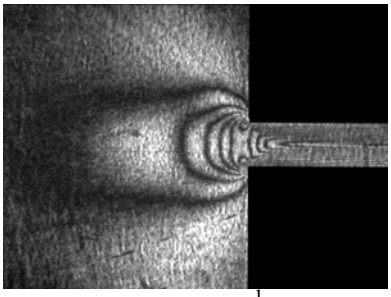

$\dot{\gamma}_a$=5.1 s^{-1}

PL1840 (mBLDPE)

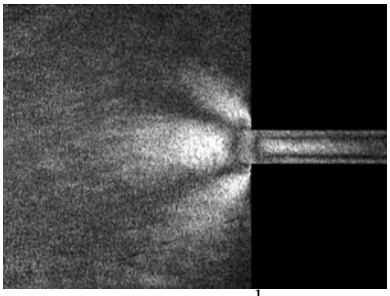

$\dot{\gamma}_a$=1.0 s^{-1}

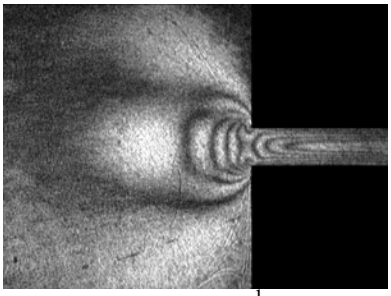

$\dot{\gamma}_a$=2.9 s^{-1}

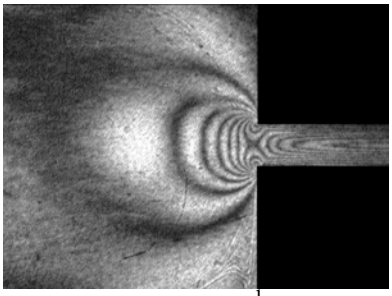

$\dot{\gamma}_a$=5.1 s^{-1}

PL1880 (mBLDPE)

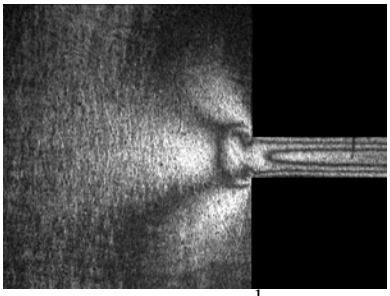

$\dot{\gamma}_a$=1.0 s^{-1}

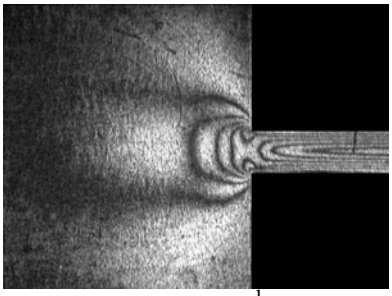

$\dot{\gamma}_a$=2.9 s^{-1}

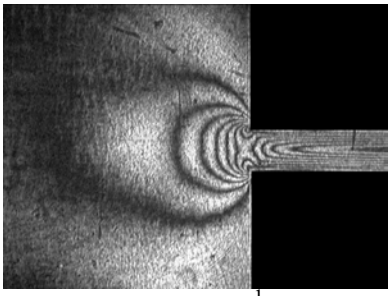

$\dot{\gamma}_a$=5.1 s^{-1}

The flow patterns presented above were obtained from an abrupt 8:1 planar contraction die identified in Chapter 3 using monochromatic light (λ=632.8 nm). The downstream width-to-height aspect ratio is 10:1 and the upstream aspect ratio is 10:8.

G.3 Sources of Error

The accuracy of the full-field flow birefringence patterns presented above can be adversely affected by equipment and material factors. The most predominant source of error is optical misalignment. Because the path length of the incident polarized light through a birefringent medium determines its optical retardation, any misalignment of the optical components (i.e. polarizer, analyzer) or flow cell can lead to erroneous birefringence patterns. In general, a net increase in the degree of retardation will occur. Therefore, careful alignment of all optically active components is critical for accurate stress field patterns.

In some cases, the flow domain itself can contribute to significant error in the birefringence patterns. For example, the flow domain used to generate the above patterns was an abrupt 8:1 planar contraction. The downstream aspect ratio (W:H) is 10:1, but the upstream aspect ratio is 10:8. This relatively low upstream aspect ratio can give rise to additional optical retardation near the face of the quartz window. This "parasitic" birefringent response occurs in the 1-3 plane and ultimately affects the response obtained from the desired 1-2 plane.

Finally, the material itself may affect the accuracy of the measured stress patterns. The only material dependency arising from flow birefringence is the value of the stress optic coefficient (SOC). It is well known that the SOC varies between polymer melts of different monomeric composition. For PE melts, the value of the SOC is approximately 2.0×10^{-9} Pa^{-1}. However, slight variations can arise from the effects of long-chain branch content, additives, and processing/thermal history. Therefore, independent measurements of the SOC is required to quantify the magnitude of the principal stresses and careful attention to melt degradation, and its effect on the SOC, must be observed.

Vita

The author was born in Tulsa, Oklahoma on April 15, 1975. Upon graduating from Jenks High School (Jenks, Oklahoma) on May 5,1993, he attended the University of Oklahoma. The degree of Bachelor of Science in Chemical Engineering was conferred on May 10, 1997. His undergraduate education was supplemented by several years of undergraduate research under the advisement of Professor Brian P. Grady. With an interest in polymer rheology and processing, the author began his graduate studies at Virginia Polytechnic Institute and State University in August, 1997. Under the direction of Dr. Donald G. Baird, he performed the research that has culminated in this dissertation, from which he received a Ph.D. in Chemical Engineering on August 8, 2002. He was offered and accepted a research and development position with Kraton Polymers in Houston, TX.

Phillip J. Doerpinghaus, Jr.